Technische Universität München

Max-Planck-Institut
für extraterrestrische Physik

Analysis and Operation of DePFET X-ray Imaging Detectors

Thomas Lauf

Vollständiger Abdruck der von der Fakultät für Physik der Technischen Universität München zur Erlangung des akademischen Grades eines

Doktors der Naturwissenschaften (Dr. rer. nat.)

genehmigten Dissertation.

Vorsitzender:		Univ.-Prof. Dr. Andrzej J. Buras
Prüfer der Dissertation:	1.	Hon.-Prof. Dr. Günther Hasinger
	2.	Univ.-Prof. Dr. Stephan Paul

Die Dissertation wurde am 02.02.2011 bei der Technischen Universität München eingereicht und durch die Fakultät für Physik am 28.04.2011 angenommen.

Zusammenfassung

Der Depleted P-channel Field Effect Transistor (DePFET) Pixelsensor gehört zu den neuesten Entwicklungen halbleiterbasierter Detektoren für die bildgebende Röntgenspektroskopie, der am Max-Planck-Institut Halbleiterlabor (HLL) entwickelt wird. Dieser Sensortyp besitzt einen integrierten Verstärker auf Pixelebene und zeichnet sich durch sehr gute Energieauflösung, geringes Rauschen bei schneller Auslese und niedrige Leistungsaufnahme aus. Einzelne Pixel dieser Detektorstruktur können direkt adressiert und ausgelesen werden. Desweiteren besitzt die Detektorstruktur alle Vorteile eines seitwärts verarmten Detektors, d.h. 100 % Füllfaktor und eine sehr gute Quanteneffizienz.

Im Laufe der DePFET-Entwicklung wurde der Bedarf für eine Datenanalysesoftware für DePFET-Detektoren deutlich. Im Rahmen dieser Arbeit wurde eine Software entwickelt, die es einerseits ermöglicht, DePFET Daten zu analysieren, andererseits flexibel genug ist, um an neue Detektorvarianten und Analyseanforderungen angepasst werden zu können.

Dabei wurde ein modulares Konzept umgesetzt: Ein Basisprogramm, welches die Analyse mittels einzelner Schritte durchführt. Diese Schritte, die die Algorithmen enthalten, können kombiniert und ausgetauscht werden. Damit wurde eine flexible, anpassbare und erweiterbare Analyse-Software geschaffen.

Die Software wurde genutzt, um verschiedene Strukturvarianten von DePFET-Detektoren zu untersuchen und zu qualifizieren. Für die Untersuchung und Korrektur von Detektoreffekten wurden Algorithmen und Methoden entwickelt und in die Software eingebaut. Auf diese Weise entstand eine Standard-Analyse für DePFET-Daten, welche jetzt am HLL eingesetzt wird.

Neben dem geplanten Einsatz für den Wide Field Imager des Röntgen-Observatoriums IXO werden DePFET-Dektoren auch als Fokalebenendetektor für das Mercury Imaging X-ray Spectrometer (MIXS) verwendet. MIXS soll an Bord der Raumsonde BepiColombo die Oberfläche des Merkur untersuchen. Die Analyse-Software wurde im Rahmen der Detektor-Entwicklung für dieses Projekt genutzt, um Test-Strukturen zu qualifizieren, Detektor-Effekte zu analysieren und experimentelle Ergebnisse auszuwerten.

Im Zuge dieser Entwicklung wurde die Linearität, Ladungssammlung und Detektionseffizienz von DePFET-Detektor-Prototypen am Synchrotron BESSY untersucht. Diese Messungen dienten auch als Test der für die Datenanalysesoftware entwickelten Algorithmen.

Abstract

The latest active pixel sensor for X-ray imaging spectroscopy developed at the Max-Planck-Halbleiterlabor (HLL) is the Depleted P-channel Field Effect Transistor (DePFET). This detector type unites detector and first stage amplification and has excellent energy resolution, low noise readout at high speed and low power consumption. This is combined with the possibility of random accessibility of pixels and on-demand readout. In addition it possesses all advantages of a sidewards depleted device, i.e. 100 % fill factor and very good quantum efficiency.

In the course of the development of DePFET detectors the need of a data analysis software for DePFET devices became apparent. A new tool was developed within the scope of this thesis, which should enable scientists to analyze DePFET data, but also be flexible enough so it can be adapted to new device variants and analysis challenges.

A modular concept was thus implemented: a base program running an analysis by individual steps encapsulating algorithms, which can be interchanged. The result is a flexible, adaptable, and expandable analysis software.

The software was used to investigate and qualify different structural variants of DePFET detectors. Algorithms to examine detector effects and methods to correct them were developed and integrated into the software. This way, a standard analysis suite for DePFET data was built up which is used at the HLL.

Beside the planned use as detector for the wide field imager in the space X-ray observatory IXO, DePFET matrices will be used as focal plane array on the Mercury Imaging X-ray Spectrometer on board the Mercury probe BepiColombo which is scheduled for launch in 2014. The developed analysis software was used in the detector development for this mission to qualify test structures, analyze detector effects and study experimental results.

In the course of this development, detector prototypes were studied in respect of linearity, charge collection and detection efficiency in an experiment at the BESSY synchrotron. These measurements also served as a test for the algorithms of the developed data analysis software.

Contents

1. Introduction

The exploration of the universe poses an ongoing, fascinating task to humanity. It began as a necessity to define space and time in the old ages, by charting the stars and planets and measuring their movement across the sky. Travelers on land and sea relied on the direction and position information retrieved from celestial positions, the periodicity of the sun and other astronomical objects defined the rhythm of life of the people.

Nowadays astronomy has become also some kind of archeology. The further away an object in space is, the longer the light coming from it needs to reach us. So every glance upon the night sky is a glance back in time. With modern telescopes scientist look further and further back towards the beginning of the universe.

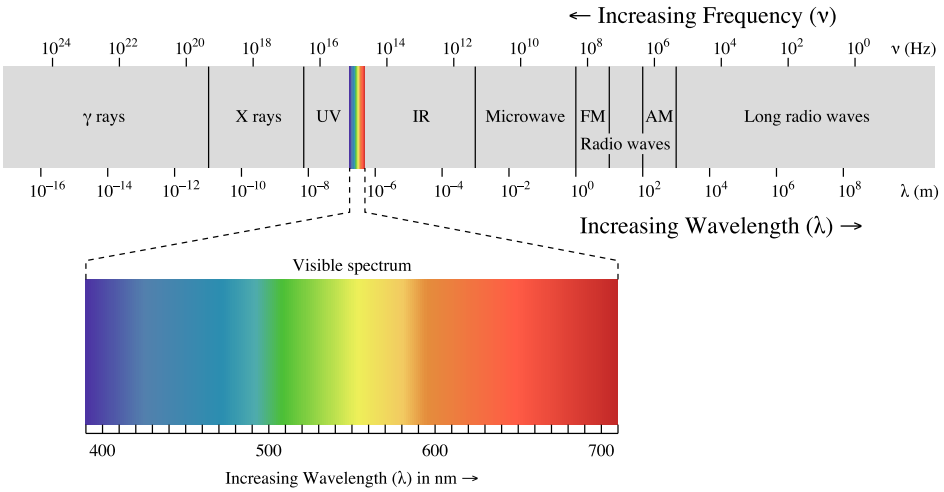

Figure 1.1: The electromagnetic spectrum. The visible spectrum occupies only a small fraction and is framed by the short-wave range with ultraviolet, X-ray and γ radiation and the long-wave range with infrared radiation, microwaves and radio waves [1].

The light reaching us from space comprises the whole electromagnetic spectrum of which figure 1.1 shows a graphical display. The optical light band is only a small fraction of the overall spectrum. For the first astronomers only this tiny optical range was accessible.

Thanks to modern developments, like space flight and radio science and others, today astronomy is able to harvest the whole range of the electromagnetic spectrum.

In the electromagnetic spectrum the X-ray band is framed by the γ-band and the UV light band. X-rays range in energy from approximately E=12 eV to E=120 keV. This can be translated according to Planck's formula

$$E = h\nu = \frac{hc}{\lambda} \tag{1.1}$$

to a wavelength range of approximately λ=100 nm to λ=0.01 nm[1].

X-rays are emitted from different sources in our universe. The nearest source is our sun, which emits a small portion of its energy in this energy band. More important sources are hot areas in our universe like black hole accretion discs, neutron stars and white dwarfs. These spots have temperatures from ten thousand up to several million degrees Kelvin. Also electrons deflected in very strong magnetic fields, as they are found around pulsars, can produce X-rays.

The study of these objects is the scope of X-ray imaging spectroscopy. The detector systems used here must deliver the energy of the photon (for spectroscopy) as well as its position of incidence (for imaging).

The first detectors for X-rays were photographic plates and scintillators (e.g. fluorescence screens). Photographic plates blacken depending on the number of impinging photons. This way (apart from the position) only the quantity of the photons could be measured, but not the energy.

In a scintillator, the incoming radiation energy is absorbed and re-emitted as light. The original radiation signal is thereby shifted into the visible range or a regime which lies better within the range of the detector (e.g. transform γ-radiation into an UV-signal). Still, a scintillator needs an extra device (e.g. a photomultiplier tube) or an observer to record the transformed photon signal.

Gaseous detectors were the first electrical devices developed for radiation detection [2]. These detectors use the ability of radiation to ionize the atoms in the absorber material, here a gas volume which is within an electric field. The electrons and ions separate in the electric field and drift towards their respective electrodes, where they create current pulses. With appropriate electronics the pulses can be counted. Also, the pulse height corresponds to the deposited energy, so the photon energy can be determined if the detector is calibrated.

[1] These limits are merely a rule of thumb. There are no exact borders between the individual energy or wavelength ranges, and each scientific field more or less defines its own wavelength/energy regimes. The actual differences are, however, minimal.

The simplest form of gaseous detectors are ionization chambers. Here the applied field voltage is high enough to separate electrons and ions before they recombine. By increasing the voltage of the electric field an amplification effect can be created.

The electrons are accelerated in the electric field until their kinetic energy is high enough to ionize other gas atoms[2]. This way the original number of electron-ion pairs created by the radiation is increased, amplifying the generated electric pulse proportional to the deposited energy. This is a proportional chamber.

In modern physics experiments gaseous detectors with more sophisticated designs, like in multi-wire proportional chambers, drift chambers, and time projection chambers have replaced simple ionization detectors.

With these devices particle trajectories can be located to less than a millimeter. They operate on the same basic principles as the proportional chamber, yet require more sophisticated electronics as well as data acquisition by computer.

The advent of semiconductor technology, especially in silicon semiconductors, created new possibilities and opportunities for detector technology. Among them are the use of semiconductors as detectors themselves, and the progress in semiconductor device fabrication, e.g. miniaturization, photolithography, chemical processing of silicon wafers.

Semiconductor detectors work just like gas-chambers: The radiation is converted into an electrical signal by ionization of the absorber material and separation of the charge cloud. Instead of gas, the absorber material here is the semiconductor crystal, and the radiation produces electron-hole pairs instead of electron-ion pairs.

In contrast to gas detectors, less energy (about 3.6 eV for silicon, 30 eV for gas) is required for ionization. Thus more charge carriers are produced per unit energy loss of the ionizing particle, which results in a higher energy resolution of semiconductor detectors compared to gas detectors [2].

Furthermore, the higher density of the detector material leads to a large energy loss (approximately 2 MeV to 4 MeV) per traversed length of the ionizing particle. This makes thin detectors possible that still produce large enough signals to be measured. Semiconductor detectors also show a higher position precision (few µm), because of the small range of δ-electrons. Another advantage is the high mobility of charge carriers within the material. Charge can be rapidly collected (~ 10 ns) which enables usage in high rate environments [3].

[2]Of course, also the ions are accelerated in the electric field. However, being much heavier than electrons, their gain in energy does not spawn further ionizations.

The excellent mechanical rigidity allows self-supporting structures, and by doping (see section 2.2.3) field configurations which are not possible in gas detectors can be created. Moreover, detectors and electronics can be both built out of silicon, which makes the integration into a single device possible.

Two disadvantages of semiconductor detectors are their sensitivity to radiation damage and the requirement of cooling during operation. The cooling overhead, however, is less with silicon detectors compared to germanium detectors. These require to be cooled down to liquid nitrogen temperature (77 K) while it is possible for silicon detectors to be operated at room temperature.

Also the readout electronics profited from the progress in semiconductor technology. First stage amplifiers for detectors can be tailored to their specific needs, increasing the sensitivity of the whole device. Another advantage came from the developments in computer technology. Since their invention these machines have become more and more powerful such that with each generation larger amounts of data could be stored and be handled in shorter time.

At the Max-Planck-*Halbleiterlabor* (HLL), different types of silicon detectors are produced: *Silicon Drift Detector*s (SDDs), p-n CCDs, and DePFET detectors. *Depleted P-Channel Field Effect Transistor* (DePFET) detectors and *Charge-Coupled Device*s (CCDs) are pixelated detectors, the sensitive area is divided into small units (pixels) which can be read out. These detector types can be used as imaging detectors.

To draw scientific conclusions from the data coming from a detector, it is important to know the various effects that influence the signal. By studying the data these effects can be uncovered and qualified, so they can be corrected which improves the final data. This is the task of data analysis.

Also, determining certain detector parameters helps to find optimal operation parameters for the detector, and to improve the detector design and production process. This gives data analysis a central role in the feedback cycle for both, detector production and operation, and scientific study.

This thesis focuses on DePFET detectors developed for use in X-ray imaging spectroscopy. The detectors described in this thesis were developed for space missions like *X-ray Evolving Universe Spectroscopy* (XEUS) [4], Simbol-X [5], *International X-ray Observatory* (IXO) [6], and BepiColombo [7].

Chapter 2 starts with a description of the interaction of radiation, especially X-rays, with matter. Afterwards, the evolution from a simple semiconductor detector to a DePFET detector is explained. At last, a typical data acquisition setup for such a detector is presented.

Chapter 3 starts with a description of various effects that contribute to the spectrum of a DePFET detector. Finally the data analysis software developed in this thesis is described.

Chapter 4 shows measurements that were evaluated using the developed data analysis software.

An overview of the space missions using DePFET detectors, which were mentioned above is given in chapter A.

2. The way of the photon

The very first (optical) detector humans used was the eye. Photons interact with the retina, this interaction creates a nerve pulse, which is processed in the brain and in the end the human observer writes down what he saw for further use and analysis.

With modern detectors, properties like processing speed, sensitivity, and accuracy may have improved, but the principle of the individual steps depicted above still remains: interaction, signal generation, signal processing, storage and analysis.

For spectroscopy, the central property of interest is the radiation energy. The detector setup represents a chain of transducers which transform the radiation energy finally into a digital number which is stored in a computer system.

Most common radiation detectors utilize the ionizing effect of radiation on matter to convert the radiation energy into a charge cloud, e.g. electron-hole pairs in semiconductor detectors. The charge cloud formation depends on the type of radiation and the properties of the absorber material. The detector then has to supply means to conserve this signal for readout. This can be achieved by an electric field which separates the differently charged particles and guides them towards readout electronics.

Additionally, detectors for X-ray imaging spectroscopy need to deliver not only energy but also position information. In semiconductor detectors this can be achieved by e.g. dividing the detector area in small subunits called pixels. The detector system then has to supply the necessary means to read out those pixels.

This chapter aims to trace the transformation of the radiation energy information into the final detector signal of a DePFET detector. As an introduction the interaction of radiation with matter is discussed.

From there the evolution from a simple p-n diode to a DePFET detector is shown. The DePFET principle and detector structure is explained, and followed by a description of how this device serves as building block for a detector array.

At last, the readout system itself is described. This includes the readout chip used, the description of the data acquisition system, the data format used for storage on hard disk, as well as the offline analysis system.

2.1 Interaction of radiation with matter

Radiation is detected by measuring its interaction with the detector medium. In the detector medium the energy of the radiation is converted into a measurable signal, usually a charge cloud which delivers a pulse to an appropriate readout electronic.

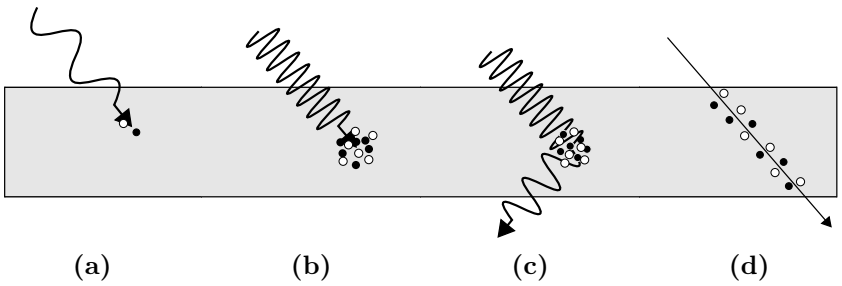

Figure 2.1: Different types of interaction between radiation and matter: (a) Photoelectric effect with an optical photon, (b) photoelectric effect with an X-ray photon, (c) Compton scattering, (d) MIP. The filled and empty circles stand for the electrons and holes created during the interaction.

Figure 2.1 shows a schematic overview of the most relevant forms of interaction between radiation and matter: photoelectric effect (for both, optical and X-ray photons), Compton scattering and *Minimal Ionizing Particle*s (MIPs).

To understand radiation detection it is important to understand the mechanisms of interaction between radiation and matter, which differ in whether the radiation consists of electromagnetic waves (i.e. photons) or massive particles. For the latter one can distinguish between charged (e.g. protons, electrons, muons) and neutral particles (e.g. neutrons).

2.1.1 Particle radiation

The way of interaction of particles[1] with matter depends on whether the particles are charged or not. Neutral particles, e.g. neutrons, usually interact by direct collision with the crystal lattice producing phonons or kicking lattice atoms out of their position, which then interact like charged particles. Since the ionizing potential of neutral particles is thus rather low, semiconductor detectors are usually not used for their detection.

[1]Photons are particles, too, but here the term is used synonymously for 'massive particles'

Charged particles, e.g. protons, muons or electrons, deposit their energy along their path through matter according to the Bethe-Bloch equation [8].

$$\langle -\frac{dE}{dx} \rangle = K z^2 \frac{Z}{A} \frac{1}{\beta} \left[\frac{1}{2} \ln \left(\frac{2 m_\mathrm{e} c^2 \beta^2 \gamma^2 T_\mathrm{max}}{I^2} \right) - \beta^2 - \frac{\delta(\beta\gamma)}{2} \right] \tag{2.1}$$

with

- $\beta = \frac{v}{c}$, v being the particle speed and c the speed of light
- $\gamma = 1/\sqrt{1-\beta^2}$, being the Lorentz factor
- $K = 4\pi N_A r_\mathrm{e}^2 m_\mathrm{e} c^2$
- N_A being Avogadro's number
- m_e being the electron rest mass
- $r_\mathrm{e} = e^2/(4\pi\varepsilon_0 m_\mathrm{e} c^2)$ being the classical electron radius
- $\varepsilon_0 = 8.85 \cdot 10^{-12}\,\mathrm{F/m}$ being the vacuum permittivity
- $z \cdot e$ being the charge of the incident particle
- e being the elementary charge
- Z being the proton number of the absorber material,
  A being its mass number
- E being the particle energy
- x being the path length
- I being the mean excitation energy of the material
- T_max being the maximum kinetic energy which can be imparted to a free electron in a single collision
- $\delta(\beta\gamma)$ being a density effect correction to ionization energy loss

Figure 2.2 shows the energy loss per path length with respect to the particle energy for muons, pions and protons in different media. The curve shows a minimum. For energies below, the energy loss is inversely proportional to the energy. Above, the energy loss rises (so-called relativistic rise) and then saturates due to polarization of the medium [3].

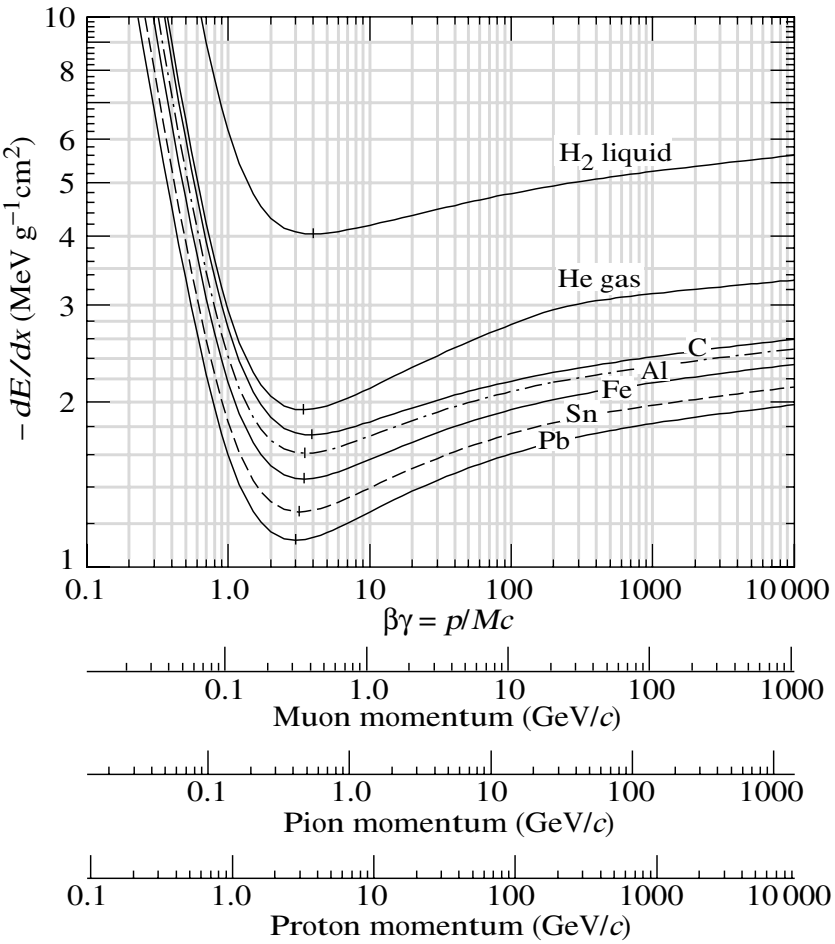

Figure 2.2: Mean energy loss rate in liquid (bubble chamber) hydrogen, gaseous helium, carbon, aluminum, iron, tin, and lead. Radiative effects, relevant for muons and pions, are not included. Picture from [8].

A particle with an energy above the minimum loses energy along its track in an approximately constant rate (Compare to fig. 2.1d). Such high energy particles, which are not stopped in the material, are called *Minimal Ionizing Particle*s (MIPs).

If the particle energy is reduced below the minimum, the energy loss increases drastically. The particle loses more energy when it gets slower. Thus the energy loss over depth of such a particle shows a distinctive peak at the end of the track, the so-called Bragg peak.

Another effect of particle radiation on the semiconductor bulk is the creation of defects. In contrast to the creation of an electron cloud, which is a transient effect, these defects can be stable – although a partial repair by annealing is pos-

sible. These defects generally deteriorate the electrical properties of the detector material.

When it comes to application in space, radiation damage on the detector is usually an issue. More information on radiation damage on silicon detectors can be found in literature [9].

2.1.2 Electromagnetic radiation

The attenuation of electromagnetic radiation follows the Beer-Lambert law:

$$I(x) = I_0 \cdot e^{-\frac{x}{\mu}} = I_0 \cdot e^{-\alpha x} \tag{2.2}$$

- I denotes the intensity, $I_0 = I(0)$
- x is the depth
- μ is the attenuation length, α the attenuation factor ($\mu = \frac{1}{\alpha}$)

The attenuation factor is an energy dependent material constant. Figure 2.3 shows α for silicon (Si) and aluminum (Al). One can see that there are steps in the graph's slope. These band edges occur whenever the photon energy is high enough to excite electrons from another shell.

The steps in figure 2.3 belong to the K-shell, therefore it is called the Si K-edge or Al K-edge, respectively. The K-edge of silicon has an energy of 1840 eV, for aluminum it has an energy of 1536 eV.

Figure 2.5 shows the cross sections for different interaction mechanisms. For electromagnetic radiation there are three main interaction paths:

- The photoelectric effect with cross section τ,
- Compton scattering with cross section σ_{incoh}, and
- pair production with cross section κ.

Other paths are either very rare (e.g. photo-nuclear absorption) or do not produce electron-hole pairs and thus no detectable signal charge (e.g. Rayleigh scattering). The cross section gives a measure of the probability for a reaction to occur. The total probability for photon interaction σ is the sum of the individual cross sections:

$$\sigma = \tau + \sigma_{\text{incoh}} + \kappa \tag{2.3}$$

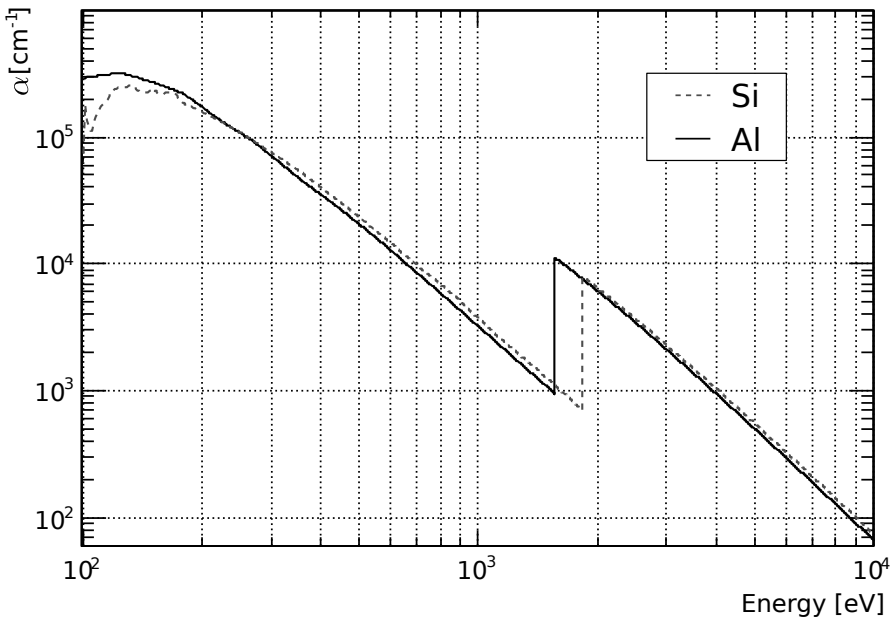

Figure 2.3: Attenuation factor α over energy for Si and Al. The K-edge for Si and Al is visible as a step in the slope of the respective graph. Data from [10].

The attenuation factor α, which is the probability per unit length for an interaction, is connected to σ via

$$\alpha = n \cdot \sigma \tag{2.4}$$

where n is the density of atoms for the respective material [2].

Pair production Pair production describes the process where a photon converts itself into an electron-positron pair according to Einstein's formula $E = mc^2$. For this process, the minimum photon energy has to be at least twice the electron's rest mass, i.e. $E \geq 2 \cdot 511\,\mathrm{keV} = 1.02\,\mathrm{MeV}$. This is far above the energy range of X-ray photons.

Compton scattering In the case of Compton scattering, only a part of the photon's energy is transferred to an electron, which - if it has enough kinetic energy - undergoes the same process as photoelectrons described below. After the scattering process, the primary photon has a lower wavelength and can either undergo another interaction or leave the detector (compare figure 2.1c). In the latter case the photon energy is only partially detected.

Photoelectric effect With the photoelectric effect the photon transfers its whole energy to an electron in the atomic hull. The atom is then ionized and the electron carries the photon energy minus the binding energy as kinetic energy.

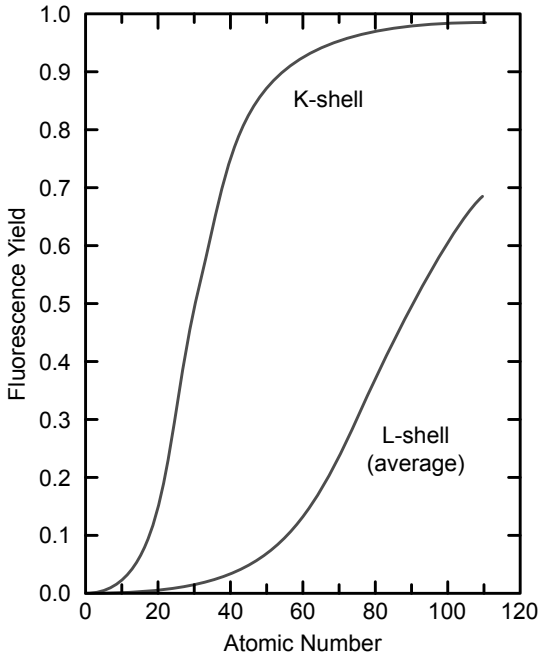

Figure 2.4: Fluorescence yield for K and L shells for $5 \leq Z \leq 110$. The plotted curve for the L shell represents an average of L_1, L_2, and L_3 effective yields. Picture from [11] based on data from [12].

X-ray photons usually ionize electrons from the inner shells of the atom. Electrons from outer shells then fill the gap. The energy freed in this process creates either a fluorescence photon or an Auger electron. The Auger process dominates for elements with low Z, fluorescence becomes more dominant with rising Z. For silicon the fluorescence yield is 4.29% for the silicon K-shell (see figure 2.4).

An electron produced in the ionization process carries kinetic energy. If this energy is large enough, the electron is itself capable of ionizing atoms, like the charged particles described in section 2.1.1. The same holds for the Auger electron or the fluorescence photon which also can excite further electrons. The absorption of a photon thus triggers a cascade of electron excitations in the vicinity of the interaction point.

From figure 2.5 one can see that the photoelectric effect is dominant for energies up to $5 \cdot 10^4\,\mathrm{eV}$, pair production for energies larger than $5 \cdot 10^7\,\mathrm{eV}$, and the Compton effect in the energy region between.

As this work deals mainly with X-ray imaging spectroscopy, the energy ranges

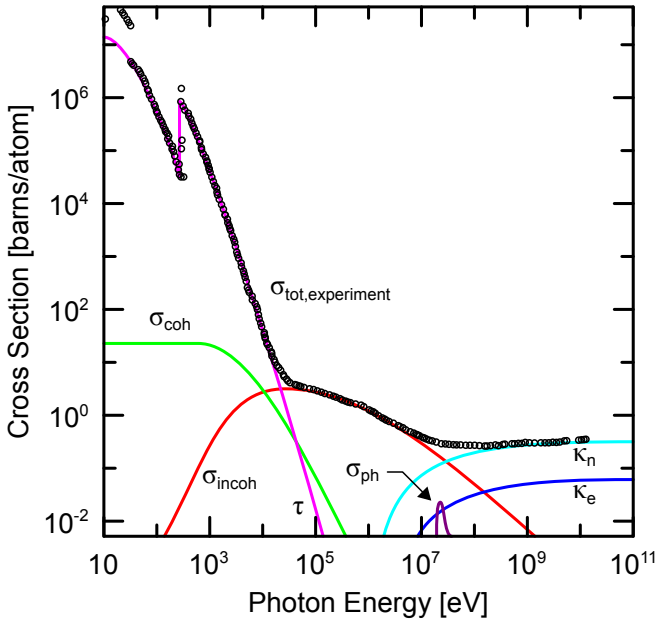

Figure 2.5: Total photon cross section σ_{tot} in carbon, as a function of energy, showing the contributions of different processes: τ, atomic photo-effect (electron ejection, photon absorption); σ_{coh}, coherent scattering (Rayleigh scattering - atom neither ionized nor excited); σ_{incoh}, incoherent scattering (Compton scattering off an electron); κ_{n}, pair production, nuclear field; κ_{e}, pair production, electron field; σ_{ph}, photonuclear absorption (nuclear absorption, usually followed by emission of a neutron or other particle). Picture adapted from [11].

discussed further will be limited up to 20 keV, meaning only photoelectric absorption is considered.

2.2 Semiconductor detectors

In a single atom the electrons are located at discrete energy levels. When bringing N identical atoms with the same energy levels together to form a crystal lattice, the interaction between the atoms causes the discrete energy levels to degenerate, forming energy bands when $N \to \infty$. These bands broaden, merge and split again with even closer spacing of the atoms [3].

In this simple picture, a *valence band* and *conduction band* is formed in a semiconductor crystal, separated by the *band gap* in which no electron state can exist. The valence electrons are bound to individual atoms whereas the conduction electrons can move freely within the atomic lattice.

The valence band is located energetically below the conduction band. To

enable conduction in a semiconductor an electron has to be excited from the valence band to the conduction band. This can happen e.g. by thermal excitation, or by irradiation as explained in section 2.1.

A more thorough discussion of the electronic band structure can be found in literature [13]. As this thesis deals with DePFET detectors, which are silicon devices, the following discussion is mostly limited to silicon as detector material. The following sections will discuss how silicon can be used as a radiation detector. Further details on other semiconductors can be found in literature [14].

2.2.1 Silicon as detector material

Silicon is a standard material for semiconductor detectors. There are other materials that also serve as detector crystals such as germanium and compound materials like gallium arsenide and cadmium telluride, but being the most commonly used material in electronics industry, silicon has the advantage of a highly developed technology. This makes silicon a material whose processing is quite deeply understood, which is important for producing homogeneous large area detectors.

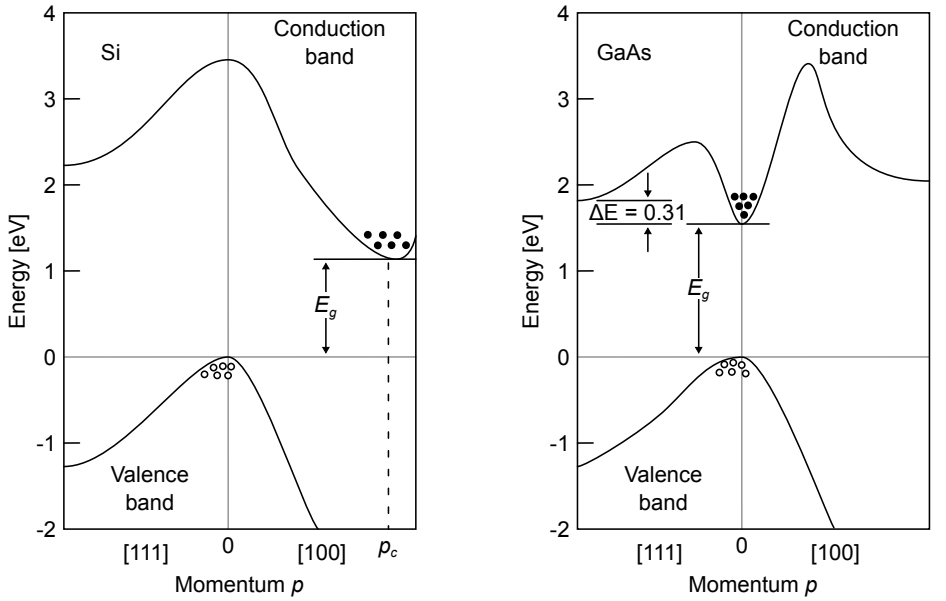

(a) band structure of silicon **(b)** band structure of gallium arsenide

Figure 2.6: Schematic view of the band structure in (a) silicon and (b) gallium arsenide. One can see the difference between the indirect semiconductor Si and the direct semiconductor GaAs. Pictures from [14].

Figure 2.6a shows a simplified schematic view of the band structure of silicon. The lower line is the valence band which is filled with electrons at zero temperature, the upper line is the conduction band which is then empty.

The bandgap is found between the maximum of the valence band and the minimum of the conduction band. Silicon has a band gap energy of $E_g = 1.12\,\mathrm{eV}$. To enable conduction in a semiconductor an electron has to be excited from the valence band to the conduction band. This can happen e.g. by thermal excitation or irradiation as explained in section 2.1.

In silicon the valence band maximum and the conduction band minimum are not situated at the same momentum like in gallium arsenide (see figure 2.6b) but shifted. This is called an *indirect band gap* (and silicon thus an *indirect semiconductor*), meaning that an electron needs an additional momentum from a phonon to reach the conduction band when absorbing a photon with an energy $E = E_g$.

Of course, electron excitation without phonon interaction is possible, but then a larger energy (the difference between conduction and valence band at $p = 0$, approximately 3.5 eV) is needed.

The band gap energy E_g poses a lower limit to the detectable photon energy. This means that silicon becomes transparent at a photon energy equal to or below the band gap, i.e. there is a maximum wavelength λ_g

$$E_{ph} = \frac{hc}{\lambda_g} = E_g \Rightarrow \lambda_g = \frac{hc}{E_g} = 1107\,\mathrm{nm} \tag{2.5}$$

for the electromagnetic radiation which can be detected.

During the electron excitation cascade, a part of the electron energy is lost in the production of phonons, therefore the average energy per electron-hole pair is higher than the band gap energy. For silicon, the mean electron-hole pair creation energy w is about 3.65 eV [15, 16]. More information about silicon as detector material can be found in standard literature [3, 14].

2.2.2 Fano statistics

The conversion of photon energy into electron-hole pairs by the cascade described in section 2.1.2 is a statistical process. The average number of electron-hole pairs $\langle N \rangle$ created by a photon with energy E_{ph} is given by

$$\langle N \rangle = \frac{E_{ph}}{w} \tag{2.6}$$

with w being the mean energy for creating an electron-hole pair.

The single steps in the electron cascade are independent of each other, but the overall energy available – namely the photon energy E_{ph} – is fixed. This leads to a deviation from Poisson statistics [15].

The phenomenological Fano factor F [17] describes the ratio between the variance $\langle \Delta N^2 \rangle$ of the number of electron-hole pairs and their mean value $\langle N \rangle$

$$\langle \Delta N^2 \rangle = F \cdot \langle N \rangle = F \cdot \frac{E_{ph}}{w} \tag{2.7}$$

There is a dependency of both, F and w, on photon energy and temperature. In the case of silicon, it is sufficient for most calculations to calculate with a constant electron-hole pair creation energy of $w = 3.65\,\text{eV}$ and a Fano factor of $F = 0.12$. More about the Fano factor and its dependency on temperature and photon energy can be found in literature [15].

As already mentioned above, the electron-hole pair creation energy w for silicon is higher than its band gap energy E_g, because some of the photon energy is lost to phonons during charge cloud creation.

The variance of the number of electrons created in photon absorption poses a lower limit to the energy resolution resulting from the fundamental properties of silicon as detector material.

The energy resolution is usually expressed by ΔE, the *Full Width at Half Maximum* (FWHM) of the peak in the pulse-height spectrum taken from monochromatic radiation. For a Gaussian peak, ΔE is connected to the variance σ by

$$\Delta E = 2\sqrt{2\ln 2}\,\sigma \approx 2.355 \cdot \sigma \tag{2.8}$$

The *Fano noise* or *Fano limit* ΔE_{Fano}, the minimal reachable FWHM[2] at an energy E, is thus given by

$$\Delta E_{\text{Fano}}(E) = 2.355 \cdot \sqrt{w \cdot F \cdot E} \tag{2.9}$$

with the Fano factor F and electron-hole pair creation energy w.

A commonly used source of X-ray radiation in a laboratory is ^{55}Fe, which decays by electron capture to ^{55}Mn with a half life of 2.7 years. The resulting manganese has a vacancy in the K-shell which is then filled by electrons from upper shells; the energy difference is emitted as an X-ray photon.

The two prominent lines of the ^{55}Fe source are the Mn-K$_\alpha$ and Mn-K$_\beta$ lines,

[2] Effects from leakage current and electronics noise broaden the peak further (see section 2.3).

which have energies of 5.9 keV and 6.5 keV respectively. The Fano limit for the K_α line is thus

$$\begin{aligned} \Delta E_{\text{Fano}}(5.9\,\text{keV}) &= 120\,\text{eV} \\ \Delta E_{\text{Fano}}(6.5\,\text{keV}) &= 126\,\text{eV} \end{aligned} \tag{2.10}$$

2.2.3 Doping

Figure 2.7a shows a simplified schematic of a silicon lattice. A bond has been broken, e.g. by radiation, and an electron-hole pair has formed. The electron can move in the conduction band, thus enabling conduction in the semiconductor until it finally recombines again with a hole in the valence band.

The broken bond can be filled by an electron from a neighboring bond. This way a hole can move through the semiconductor in the valence band, contributing to conduction until it recombines with an electron from the conduction band. A semiconductor without any – in practice very few – impurities is called an *intrinsic semiconductor*.

A way to alter the properties of a semiconductor is to deliberately introduce impurities, i.e. other atoms, into the crystal lattice. This process is called *doping*, the result is called an *extrinsic semiconductor*. Dopants change the way conduction takes place in a semiconductor.

For silicon, which is a member of group IV of the periodic table, the elements used for doping are in group III (acceptors) and group V (donors), with boron (group III) and phosphor (group V) being the most common materials.

Figure 2.7b shows a silicon lattice with a boron atom implanted. Boron acts as an *acceptor*, has one valence electron less than silicon. This creates an unsatisfied bond to a silicon neighbor which can be easily occupied by an electron from another bond. This means that the hole is moving through the semiconductor as the electrons jump from bond to bond, which enables conduction.

Phosphor has one surplus valence electron compared to silicon, it acts as a *donor*. Figure 2.7c shows a schematic view of this case. The surplus electron is easily excited into the conduction band where it can move, i.e. enabling conduction.

An *acceptor* creates additional empty states close to the valence band, a *donor* filled states close to the conduction band. Less energy is required to excite electrons from donor states to the conduction band, or from the valence band to acceptor states.

The doping of a semiconductor usually defines its *majority charge carrier*.

Figure 2.8 shows a simplified band model for intrinsic, n- and p-doped semiconductors. In the intrinsic case, shown in figure 2.8a, conduction takes place equally by electrons and holes, if an electron is excited from the valence band into the conduction band.

Figure 2.8b shows a semiconductor doped with acceptor atoms. The acceptors create additional states close to the valence band (45 meV in the case of boron in silicon). Electrons are easily excited into these states, creating a fixed negative ion with the acceptor. The holes created in the valence band can move and enable conduction. A semiconductor doped with acceptor atoms is called *p-doped* and has holes as its majority charge carrier.

Figure 2.8c depicts the analogous situation in a semiconductor doped with donor atoms. The donor electrons are in states close to the conduction band (45.3 meV for phosphor in silicon) and are thus easily excited into the conduction band. This leaves a fixed positive donor ion. A semiconductor doped with donor ions has extra electrons for conduction. It is called *n-doped* and electrons are the majority charge carrier here.

When an electron is excited from the valence band to the conduction band both, the electron and the hole, contribute to conduction. In contrast to this, only one kind of charge carrier contributes in case of excitation of an electron

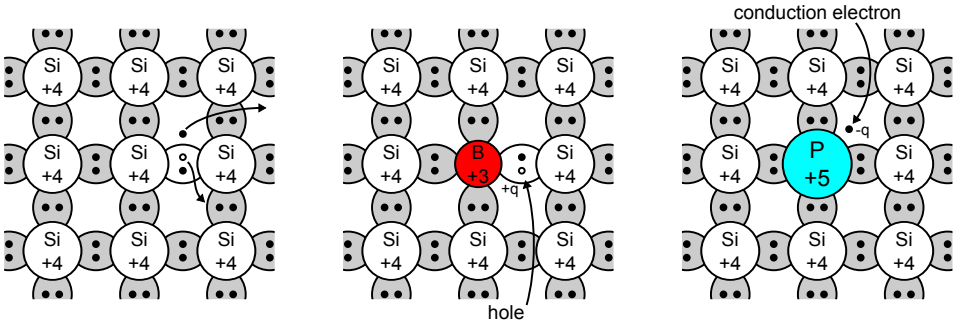

(a) intrinsic semiconductor **(b)** p-doped **(c)** n-doped

Figure 2.7: (a): For conduction in an intrinsic semiconductor an electron has to be excited from the valence band to the conduction band. This leaves a broken bond, a hole, which can be filled by an electron from a neighboring bond. This way the hole moves through the semiconductor. (b): In a p-doped semiconductor an acceptor (here: boron) creates an unsatisfied bond. This bond is filled by electrons from neighboring bonds making the hole move through the semiconductor. (c): In an n-doped semiconductor a donor (here: phosphor) adds an extra electron which can be excited into the conduction band much easier than the silicon valence electrons. Pictures adapted from [14].

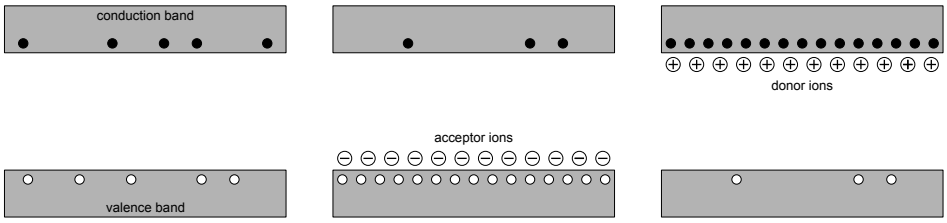

(a) intrinsic semiconductor **(b)** p-doped **(c)** n-doped

Figure 2.8: Simple band models of intrinsic, n-type and p-type semiconductors. (a) In an intrinsic semiconductor conduction is only possible when electrons from the valence band are excited into the conduction band, leaving holes in the valence band. Both, electrons and holes, contribute to the conduction. (c) A n-doped semiconductor adds extra electrons to the conduction band, (b) a p-doped semiconductor provides extra holes in the valence band making electrons, respectively holes, the majority charge carrier in the semiconductor.

from a donor state or to an acceptor state, while an ionized donor or acceptor atom fixed to the crystal lattice is left behind.

2.2.4 The p-n junction

Bringing p-doped and n-doped material in contact creates a *p-n junction*. Figure 2.9 shows the three stages of this process. The left column shows a simplified view of the doped crystal lattice, with the acceptor and donor atoms shown as squares, and the electron and holes shown as circles. At the right side, the band model view is shown. Note that the Fermi level E_F of the p-doped semiconductor is closer to the valence band, for an n-doped semiconductor it is closer to the conduction band.

When bringing the two in contact, the majority charge carriers of each part diffuse into the other leaving behind a fixed ion of the opposite charge. The electrons from the n-doped area and the holes from the p-doped area recombine, which creates a region depleted of free charge carriers, the *depletion zone*.

As this zone contains charge coming from the fixed ions left behind during the diffusion process, it is also called the *space charge region*. The fixed ions create an electric drift field counteracting the diffusion current with a drift current. In thermal equilibrium these two contributions cancel each other.

Of course, a p-n junction cannot be created by pressing n-doped and p-doped semiconductors together. Usually, a p-n junction is produced by applying a high density p-doping to a n-type silicon substrate. For an asymmetric doping

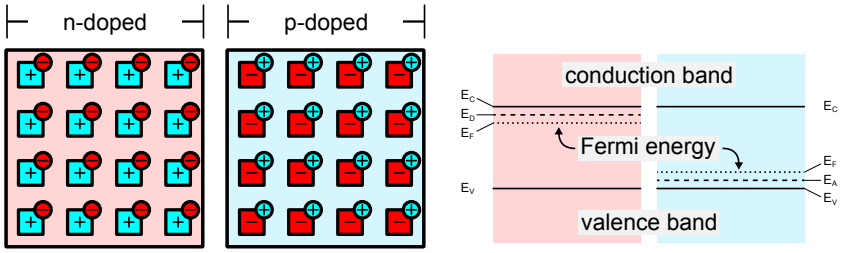

(a) before contact

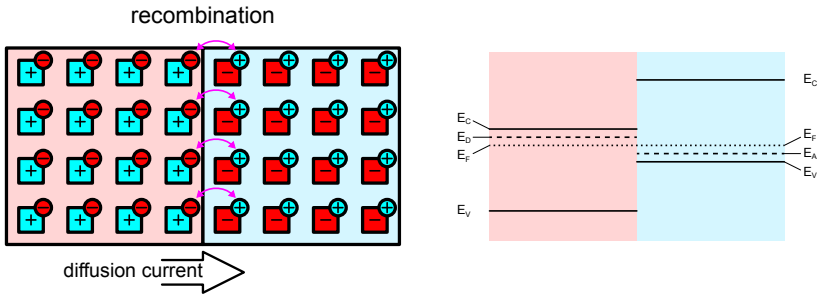

(b) at contact

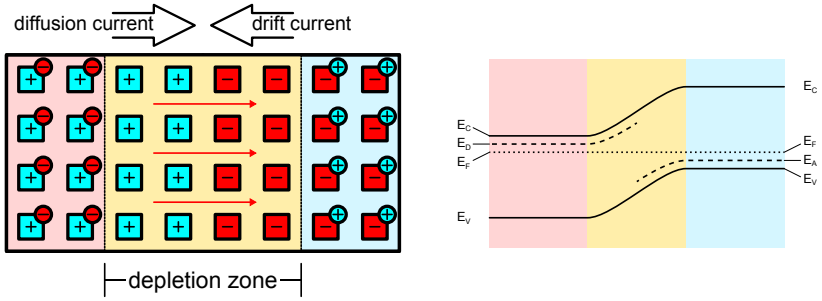

(c) after contact

Figure 2.9: A p-n junction. The left column shows a schematic view of the semiconductor, the right column a simplified band model. (a): The n-doped semiconductor has positive ions carrying extra electrons, the p-doped negative ions making holes the majority charge carrier here. E_D is the donor state energy, E_A the acceptor state energy. The semiconductors have different values of the Fermi level E_F because of their doping. (b): When in contact the majority charge carriers of each region start to drift to the opposite side and recombine with each other, leaving behind an ion of the opposite charge. (c): The drift process continues until the force from the electric field (red arrows) of the ions creates a drift current which counteracts the diffusion current. A *depletion zone* or *space charge region* has formed.

profile, the space charge region extends more into the region with the lower doping density. If the p and n doping had the same density, the space charge region would extend symmetrically into both regions.

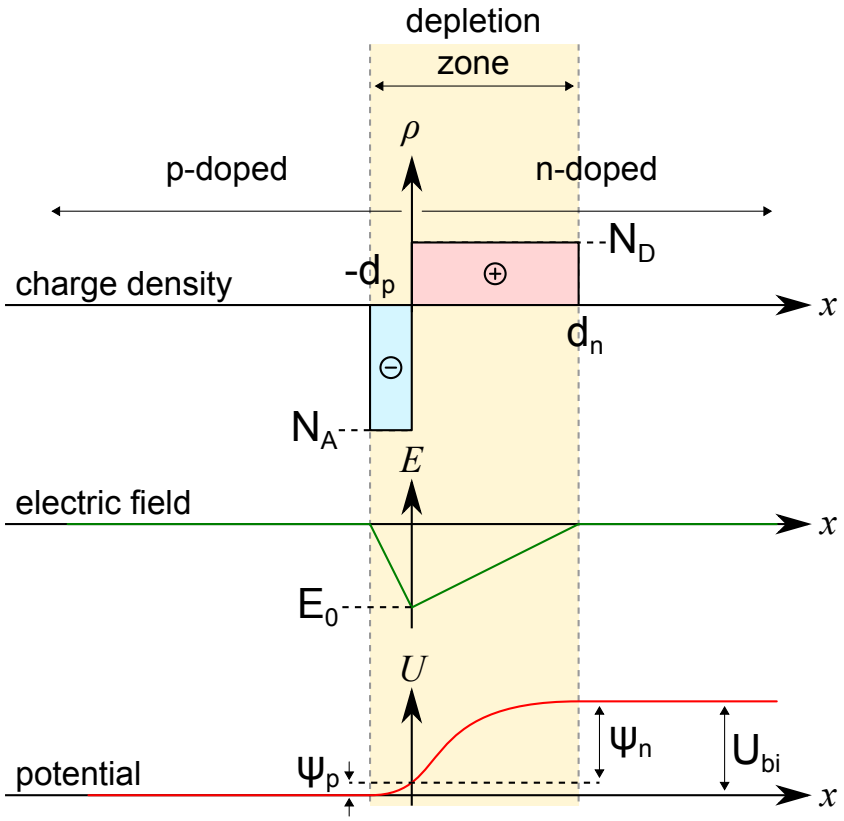

Figure 2.10: Charge density, electric field and potential of an abrupt p-n junction in thermal equilibrium. Picture adapted from [14].

The width of the space charge region can be determined by solving Poisson's equation for the potential field ψ inside the wafer:

$$\nabla^2\psi = -\frac{\rho}{\varepsilon\varepsilon_0} \tag{2.11}$$

Where ρ is the charge density, and ε and ε_0 are the vacuum permittivity and the relative permittivity of the semiconductor respectively.

A simple one-dimensional model[3], in which a sharp doping profile is assumed and the thermal generation of charge carriers is neglected is shown in figure 2.10.

In the space charge region, the total ionization of acceptors and donors is assumed. In thermal equilibrium the total negative charge per unit area in the

[3]A thorough calculation for this can be found in chapter B.

p-side must be precisely equal to the total positive charge per unit area on the n-side [14]:

$$N_A \cdot d_p = N_D \cdot d_n \tag{2.12}$$

where N_A and N_D are the acceptor and donor concentrations, and d_p and d_n are the widths of the positive and negative space charge regions respectively.

Integrating over equation 2.11 delivers for the maximum electric field E_m at $x = 0$, i.e. the interface between n-doped and p-doped material.

$$|E_m| = \frac{qN_D d_n}{\varepsilon\varepsilon_0} = \frac{qN_A d_p}{\varepsilon\varepsilon_0} \tag{2.13}$$

Integrating twice over equation 2.11 delivers the potentials for the p- and n-side

$$\begin{aligned} \psi_p &= \frac{qN_A d_p^2}{2\varepsilon\varepsilon_0} \\ |\psi_n| &= \frac{qN_D d_n^2}{2\varepsilon\varepsilon_0} \end{aligned} \tag{2.14}$$

which add up to the *built-in voltage* U_{bi}:

$$U_{bi} = \psi_p + |\psi_n| \tag{2.15}$$

The width of the depletion layer $d = d_n + d_p$ is this model is then given

$$d = \sqrt{\frac{2\,\varepsilon\varepsilon_0}{q}\frac{N_A + N_D}{N_A\,N_D} \cdot U_{bi}} \tag{2.16}$$

In the case of a thin high density p-implantation upon a n-type bulk, one obtains a one-sided abrupt p^+-n junction ($N_A \gg N_D$). The width of the depletion layer d then can be simplified to

$$d = \sqrt{\frac{2\,\varepsilon\varepsilon_0}{q\,N_D} \cdot U_{bi}} \tag{2.17}$$

For a very highly doped ($N_A = 1 \cdot 10^{16}\,\mathrm{cm}^{-3}$) p-type junction on n-type detector-grade material ($N_D = 1 \cdot 10^{12}\,\mathrm{cm}^{-3}$), this model returns for the width of the natural space charge region approximately $d \approx 25.3\,\mu\mathrm{m}$ [3].

As shown above, doping creates a space charge in a depleted semiconductor. Thus, by altering the concentration of the dopant, doping can also be used to create sophisticated field configurations in semiconductor detectors. Examples

for this will be given in the section 2.6 and section 2.7.

2.2.5 The p-n junction as radiation detector

A p-n junction as described in section 2.2 presents the simplest form of a silicon radiation energy detector. Irradiation creates electron-hole pairs in the semiconductor, which are separated by the natural space charge region. They generate a photocurrent, if the contacts of the p-n junction are shortened. If the contacts are open a voltage drop is generated, such that the change in voltage compensates the photocurrent by increasing the diffusion current across the junction.

The most sensitive region of a p-n junction is the space charge region where electron-hole pairs are separated by the electric field. In the neutral regions the efficiency drops exponentially with the distance from the space charge region [3].

A p-n junction can be operated either unbiased or with a bias applied. Unbiased diodes have a lower sensitivity due to the smaller sensitive volume (space-charge region), but have the advantage of producing no signal offset (dark current) in the absence of radiation. Such devices are used e.g. for radiation-level measurements [3].

By applying an external voltage U, the size of the space charge region can be enlarged or diminished. Substituting $(U_{bi} - U)$ for U_{bi} in equation 2.16 yields the depletion layer width as a function of the applied voltage

$$d = \sqrt{\frac{2\,\varepsilon\varepsilon_0}{q}\frac{N_A + N_D}{N_A\,N_D}\cdot(U_{bi} - U)} \approx \sqrt{\frac{2\,\varepsilon\varepsilon_0}{q\,N_D}(U_{bi} - U)} \tag{2.18}$$

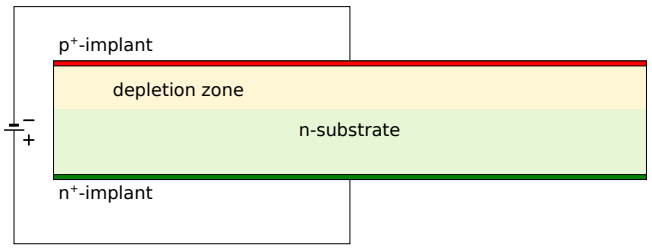

Figure 2.11: A p-n diode. The color green denotes n-doping, red p-doping. The color intensity corresponds to the doping concentration. The yellow part marks the space charge region. Within the space charge region, the electron-hole pairs are separated by the electric field. The electrons drift towards the p^+-junction, the holes towards the n^+-junction.

Figure 2.11 shows a p-n diode in reverse bias. The p-type junction is connected

to the negative terminal and the n-type to the positive (i.e. U in equation 2.18 is negative). Because of this, the electrons and holes are pulled away from the junction, increasing the size of the depletion zone. The depletion region is free of mobile charge and thus forms a capacitor. The capacitance C is defined by the width of the depletion region d and the detector area A:

$$C = \varepsilon\varepsilon_0 \frac{A}{d} \tag{2.19}$$

With enough voltage, the depletion layer can be extended over the whole volume of the wafer, which is then *fully depleted*. To fully deplete a detector has the advantage that the detector has no noteworthy dead layers, thus the whole detector volume is sensitive to radiation. Also the capacitance drops with increasing width of the depletion region.

A downside of such a p-n diode detector becomes visible when the influence of detector noise is considered. Section 2.3 will explain different sources of noise (section 2.3.1 to section 2.3.3) and finally discuss their impact on the detector readout in section 2.3.4.

Based on these considerations the motivation for more sophisticated semiconductor devices like SDDs, p-n CCDs and DePFET detectors is then shown.

2.3 Detector readout & noise

A detector working with the ionization principle converts the photon energy into a charge cloud which is then processed by appropriate electronics. In section 2.2.2 the Fano noise was introduced as the physical limit for a photon signal in such a device.

The processing electronics converts the original photon signal to voltages and/or currents in the detector system. Voltages and currents in electronic devices are not constant in time but show small statistical fluctuations. Together with the Fano noise, these fluctuations, called *electronic noise*, define the lower limit and the resolution for signals such a detector system can measure.

There are three main electronic noise sources, thermal noise, 1/f-noise, and shot noise, which will be described in the next sections. To incorporate noise in the models the ideal circuits are equipped with additional voltage or current sources which deliver the effective noise voltage or current.

2.3.1 Thermal noise

Due to thermal movement the electrons in the conductor create small current and voltage fluctuations. This *thermal noise* was first investigated and studied by J. B. Johnson [18] and H. Nyquist [19] in 1928. Its power spectrum, the distribution of $\overline{U_n^2}$ over frequency f, is given by

$$\frac{\partial \overline{U_n^2}}{\partial f} = 4 k_B T R \,, \tag{2.20}$$

with

- $k_B = 1.38 \cdot 10^{-23}\,\mathrm{J/K}$ being the Boltzmann constant,
- T the absolute temperature,
- R the resistance

In analogy to optics this noise is also called *white noise* as all frequencies are equally represented.

In field effect transistors thermal noise is caused by the resistance of the transistor channel. The modulation of the channel current I_{DS} is represented by a noise voltage source at the gate [3]

$$\frac{\partial \overline{U_n^2}}{\partial f} = 4 k_B T \, \Gamma \, \frac{1}{g_m} \tag{2.21}$$

g_m is the transconductance of the field effect transistor; see section 2.7 for its definition. The factor Γ depends on the transistor type and manufacturing process. For a *Metal-Oxide-Semiconductor* (MOS) field effect transistor in saturation it can be assumed as $\Gamma = 2/3$ [3].

2.3.2 1/f-noise

1/f-noise is also called low-frequency noise or *pink noise* (as low frequencies dominate the spectrum). The 1/f dependence is only approximately and there are several mechanisms for this noise type [3].

In field effect transistors the 1/f-noise is due to traps in the transistor channel. These traps bind moveable charge carriers which then become temporarily fixed charges and induce mirror charges in the channel, thus modulating the channel conductivity. The amplitude of modulation of the transistor current depends on the position of the trap with respect to the channel. The frequency of trapping

and emitting depends on the depth of the trap and on the temperature. This has been studied systematically by Kandiah et al. [20].

In the gate of a *Field Effect Transistor* (FET) most traps reside at the interface between silicon bulk and the oxide. The 1/f-noise is therefore reduced if the channel is located in the bulk in a distance to the interface [3].

For practical purposes, $1/f$ noise can be described by a gate noise voltage with a spectral power density expressed by

$$\frac{\partial \overline{U_n^2}}{\partial f} = \frac{k_{1/f}}{f} \tag{2.22}$$

with $k_{1/f}$ a parameter that incorporates the influence of e.g. gate width, gate length, oxide thickness, but also properties of the specific device production process [3].

2.3.3 Shot noise

Shot noise occurs due to the quantization of charge. A constant current I implies a charge ΔQ crossing a boundary in a (short) time interval Δt. This corresponds to a mean number of ΔN electrons

$$I = \frac{\Delta Q}{\Delta t} = \frac{\Delta N \cdot e}{\Delta t} \tag{2.23}$$

With a statistical fluctuation of $\delta \Delta N = \sqrt{\Delta N}$ the mean-square variation of the current is

$$\langle \delta I^2 \rangle = \frac{e^2 (\delta \Delta N)^2}{\Delta t^2} = \frac{e^2 \Delta N}{\Delta t^2} = \frac{I\, e}{\Delta t} \tag{2.24}$$

From these considerations the frequency spectrum of the noise current can be derived:

$$\frac{\partial \overline{I^2}}{\partial f} = 2Ie \tag{2.25}$$

with e being the elementary charge.

In deriving equation 2.25, it was assumed that the probability of an electron crossing the boundary is independent of the status of all other electrons. This approximation is fulfilled to a very large degree in a reverse-biased detector. The shot noise of a reverse-biased diode is given by

$$\frac{\partial \overline{I^2}}{\partial f} = 2I_L e \tag{2.26}$$

where I_L is the leakage current.

In contrast to thermal noise, which is also present when no external voltage is applied, shot noise requires a current flow caused by an external power source [21, 3].

2.3.4 Equivalent Noise Charge

Figure 2.12 shows an equivalent circuit of a simple detector system, e.g. a diode as presented in section 2.2.5, connected to an amplifying and filtering stage. The noise sources are modeled as a current source for the leakage current I_L (shot noise) and a voltage source for the voltage noise U_n (thermal and 1/f-noise).

The detector has a capacitance C_det, the amplifier an internal capacitance C_int. All other capacitances present in the system, e.g due to cables and connectors, are combined as stray capacitances in C_stray. The sum of these is the total capacitance C_tot, which is used below.

The amplifier has a filter stage attached with a time dependent filter function $F(j\omega)$ which describes the ratio of input and output amplitude as a function of frequency. This function is also called the *frequency transfer function* (in the frequency domain) or *weighting function* (in the time domain) of the filter. The frequency transfer function is the Fourier transform of the weighting function. The filter stage can improve the signal-to-noise ratio S/N by restricting the input bandwidth of the detector. A simple example is an integrator which integrates the over the input signal, thus high frequency noise is cancelled out.

Depending on the type of filter, there are one or more filter frequencies characterizing the behavior of $F(j\omega)$. Usually these filter frequencies, or their characteristic time constants τ_i can be combined into a single constant τ.

The electronic noise contribution to the signal is usually described by the *Equivalent Noise Charge* (ENC). In the following the ENC for this example will be derived; some steps are abbreviated, details can be found in literature [22, 23, 24].

If amplification is assumed 1 and thermal and 1/f-noise are assumed uncorrelated, the noise power density u_n is given by [25]

$$u_\mathrm{n}^2 = \frac{\partial U_\mathrm{n}^2}{\partial f} = \frac{\partial U_\mathrm{th}^2}{\partial f} + \frac{\partial U_\mathrm{1/f}^2}{\partial f} = k_\mathrm{th} + \frac{k_\mathrm{1/f}}{f}\,. \tag{2.27}$$

The noise power density of the leakage current can be deduced from equa-

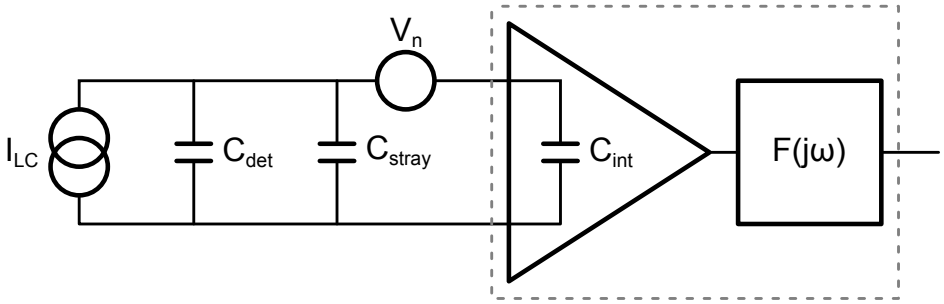

Figure 2.12: An equivalent circuit for a simple detector system with amplifier and filtering stage. Leakage current noise of the detector diode is represented by the current source I_{L}. Capacitances of detector diode C_{det}, amplifier C_{int}, and stray and cable capacitances C_{stray} are shown. The voltage noise of the amplifier is represented by the voltage source U_{n} which combines thermal and 1/f-noise.

tion 2.26, with the assumed amplification of 1, to be [22]

$$u_{\mathrm{L}}^2 = 2I_{\mathrm{L}}e\frac{1}{(\omega \cdot C_{\mathrm{tot}})^2}\,, \tag{2.28}$$

which is added to u_{n}^2.

The square of the noise signal at the filter output is given by the integral over the positive part of the noise power spectrum taking into account the filter function:

$$U_{\mathrm{noise}}^2 = \frac{1}{2\pi}\int_0^\infty (u_{\mathrm{n}}^2 + u_{\mathrm{L}}^2)\cdot|F(j\omega)|^2\,d\omega \tag{2.29}$$

If the charge collection time is small compared to the signal processing time, the signal charge at the detector input can be described by a Dirac current pulse $Q \cdot \delta(t)$. The output voltage U_{sig} generated by this pulse is

$$U_{\mathrm{sig}}(t) = \mathcal{L}^{-1}\left(\frac{Q}{(j\omega)C_{\mathrm{tot}}}F(j\omega))\right) = \frac{Q}{C_{\mathrm{tot}}}\mathcal{L}^{-1}\left(\frac{F(j\omega)}{(j\omega)}\right)\,. \tag{2.30}$$

where $\mathcal{L}^{-1}$ denotes the inverse Laplace transform [23].

The ENC corresponds to the amount of electrons that would create the same signal amplitude in a noiseless device as the noise source. It is thus the quotient of the noise signal U_{noise} and the maximum signal $\max(U_{\mathrm{sig}})$ created by the charge of a single electron.

$$\mathrm{ENC}^2 = \frac{U_{\mathrm{noise}}^2}{\max(U_{\mathrm{sig}}(e))^2} = \frac{\frac{1}{2\pi}\int(u_{\mathrm{n}}^2 + u_{\mathrm{L}}^2)\cdot|F(j\omega)|^2\,d\omega}{\left[\frac{e}{C_{\mathrm{tot}}}\cdot\max\left(\mathcal{L}^{-1}\left(\frac{F(j\omega)}{(j\omega)}\right)\right)\right]^2} \tag{2.31}$$

To study the influence of τ on the detector noise the substitution $\omega = x/\tau$ is applied. Inserting equation 2.27 and equation 2.28, equation 2.31 can be rearranged and split up depending on the individual contributions:

$$\begin{aligned}
\mathrm{ENC}^2 = & \frac{C_{\mathrm{tot}}^2 \cdot k_{\mathrm{th}}}{e^2 \cdot \tau} \cdot \frac{\int |F(jx)|^2 \, dx}{2\pi \cdot \left[\max\left(\mathcal{L}^{-1}\left(\frac{F(j\omega)}{(j\omega)}\right)\right)\right]^2} \\
& + \frac{C_{\mathrm{tot}}^2 \cdot k_{1/\mathrm{f}}}{e^2} \cdot \frac{\int \frac{|F(jx)|^2}{x} \, dx}{\left[\max\left(\mathcal{L}^{-1}\left(\frac{F(j\omega)}{(j\omega)}\right)\right)\right]^2} \\
& + \frac{2I_{\mathrm{L}} \cdot \tau}{e} \cdot \frac{\int \frac{|F(jx)|^2}{x^2} \, dx}{2\pi \cdot \left[\max\left(\mathcal{L}^{-1}\left(\frac{F(j\omega)}{(j\omega)}\right)\right)\right]^2} \\
= & \ \mathrm{ENC}_{\mathrm{th}}^2 + \mathrm{ENC}_{1/\mathrm{f}}^2 + \mathrm{ENC}_{\mathrm{LC}}^2
\end{aligned} \tag{2.32}$$

Namely the contribution by thermal noise ($\mathrm{ENC}_{\mathrm{th}}$), 1/f-noise ($\mathrm{ENC}_{1/\mathrm{f}}$), and leakage current ($\mathrm{ENC}_{\mathrm{LC}}$) to the equivalent noise charge.

The right part of each contribution only depends on the properties of the chosen filter. From the left parts the following dependencies can be deduced:

$$\begin{aligned}
\mathrm{ENC}_{\mathrm{th}}^2 & \propto C_{\mathrm{tot}}, \ \propto \frac{1}{\tau} \\
\mathrm{ENC}_{1/\mathrm{f}}^2 & \propto C_{\mathrm{tot}} \\
\mathrm{ENC}_{\mathrm{LC}}^2 & \propto \tau
\end{aligned} \tag{2.33}$$

It becomes clear from above considerations that to optimize the signal-to-noise ratio, the detector and amplifier system (with the filtering stage) have to be adjusted to each other – in the above example by choosing an optimal shaping time τ.

Another way to minimize noise is to reduce the leakage current I_{L} by cooling the detector, and to minimize the total capacitance C_{tot} by reducing the detector capacitance C_{det}.

2.3.5 Impacts on detector design

The capacitance of a p-n diode, like the one shown in figure 2.13a, is connected to its area. Dividing the detector area in small sub-detectors, e.g. strips (see figure 2.13b) or pixels (see figure 2.13c), reduces the capacitance for each. However, the number of required readout nodes rises and charge splitting between the sub-detectors becomes more and more prominent.

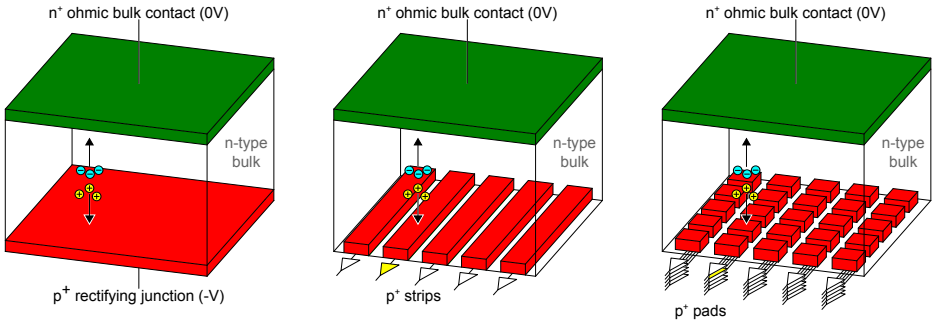

(a) p-n diode **(b)** strip detector **(c)** pad detector

Figure 2.13: Different detectors based on a p-n junction. (a): A simple diode, (b): a strip detector and (c) a pad detector. Electron-hole pairs created in the n-type bulk are separated in the electric field. The electrons drift towards the n^+-contact, the holes towards the p^+-contact. With the latter two also position resolution is possible. All detectors have a reverse bias applied.

An alternative way to reduce detector capacitance, which decouples the detector capacitance and its size, is given by the principle of sidewards depletion which is presented next in section 2.4.

2.4 Sidewards depletion

In 1984 Ghatti and Rehak proposed the principle of sidewards depletion [26]. Sidewards depletion makes it possible to deplete the same detector with less voltage and to decouple the size of the readout anode from the detector size. As the anode capacity is linked to its size (shown in section 2.3), this reduction also decreases the readout noise.

The principle of sidewards depletion is depicted in figure 2.14. A wafer of thickness l can be thought of as split in two wafer with thickness $l/2$, each with its own p^+-junction. Figure 2.14b shows the internal potential when reverse bias is applied.

The depletion zone expands from both sides towards the n^+-junction which merely serves as a contact. If omitted, the potential curve stays the same (see figure 2.14c). The n^+-junction thus can be made arbitrary small and placed on the device border while the undepleted semiconductor in the middle acts as a conductor. When fully depleted, the depletion zones from both sides meet and the potential shows a parabolic shape with the potential minimum in the middle of the wafer (figure 2.14d) [26].

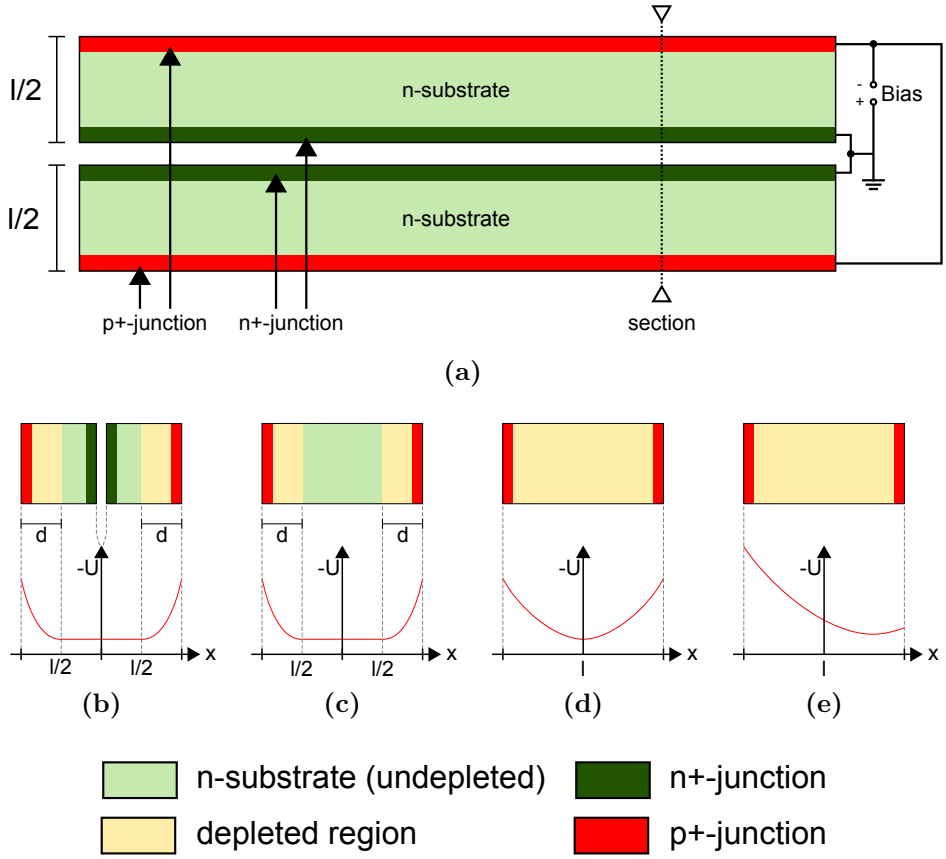

Figure 2.14: Principle of sidewards depletion. A wafer can be thought of as split in two wafers of the half size, each with its own p^+- and n^+-junction. (b): the potential at the section. (c): the n^+-junction merely serves as a contact and can be placed at the border. (d): parabolic potential curve when fully depleted. (e): applying asymmetric bias voltages shifts the minimum towards a wafer surface. Pictures adapted from [26].

If a wafer with thickness D is depleted the traditional way, thickness and depletion voltage U' are connected in the following manner according to equation 2.18 ($|U'| \gg U_{bi}$):

$$D = \sqrt{\frac{2\varepsilon \cdot |U'|}{q \cdot N_D}} \tag{2.34}$$

As described above, a sidewards depleted wafer with thickness D can be thought of as split into two wafers with thickness d depleted traditionally with voltage U. For each half, equation 2.34 holds and thus

$$D = 2d = 2\sqrt{\frac{2\varepsilon \cdot |U|}{q \cdot N_D}} = \sqrt{\frac{2\varepsilon \cdot 4|U|}{q \cdot N_D}} \tag{2.35}$$

Equations 2.35 and equation 2.34 set equal delivers for the sidewards depletion voltage U:

$$4U = U' \Rightarrow U = \frac{1}{4}U' \tag{2.36}$$

So the wafer is depleted with a quarter of the traditional depletion voltage.

Figure 2.15 shows schematics of a sidewards depleted device. For symmetric bias voltages, the potential minimum is in the middle of the wafer (see figure 2.15a). When applying asymmetric bias voltages as in figure 2.15b, the potential minimum moves towards a wafer surface (compare also to figure 2.14e). Electrons generated in the bulk move to this potential minimum while the holes drift towards the p-implantation.

For the devices shown in figure 2.15, the electrons reach the anode only by diffusion. For use as detector, the depletion field has to be overlaid with a transport field which drives the electrons towards the anode (see section 2.5). The transport field also continuously sweeps thermally generated electrons towards the anode and thus stabilizes the depletion against thermal generation of electron-hole pairs [26].

For a sidewards depleted device, the capacitance of the anode, which is important for the noise behaviour of the detector, only depends on the size of the anode. The readout anode of the devices shown in figure 2.15 spans along one

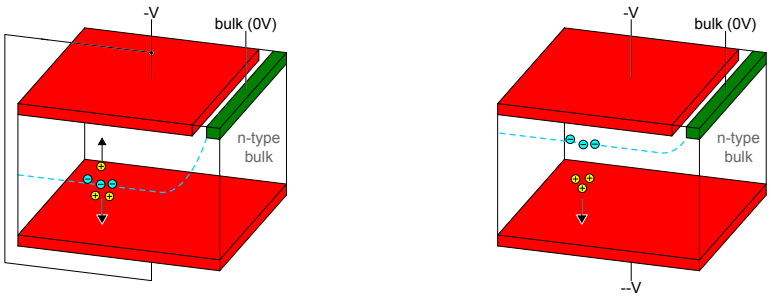

(a) symmetric bias **(b)** asymmetric bias

Figure 2.15: In a sidewards depleted p-n junction, the n^+ bulk contact (shown in green) can be made arbitrarily small. This reduces the capacitance of the readout node and decouples the readout capacitance from the detector surface. Like in a p-n junction, electron-hole pairs are separated by the electric field. The holes drift towards the p^+-contacts (shown in red), the electrons towards the potential minimum (dashed blue line). When symmetric bias is applied (figure 2.15a), the potential minimum is in the middle of the wafer. By applying asymmetric bias voltages (figure 2.15b), the potential minimum can be moved towards a wafer surface.

edge of the device. With the appropriate transport field applied, the anode can be reduced to a point anode to create a detector with smallest possible capacitance [26].

Thus the decoupling of the detector size and the capacitance of the readout node makes it possible to increase the detector size, while keeping the readout node capacitance constant. The leakage current of such a device still rises with the detector volume, but this can be compensated by cooling.

The asymmetric bias has the side effect that the potential becomes shallower towards the detector surface (compare to figure 2.14e). To prevent charge loss to the surface, the potential can be deepened by an additional n-doping in this layer [27]. Additionally, this n-doping can be structured to form special field configurations as applied in both, the p-n CCD (shown in section 2.6) and the DePFET detector (shown in section 2.7).

2.5 Silicon drift detectors

To enhance and to speed up electron collection in a sidewards depleted device, one can overlay the depletion field with an additional lateral drift field. This can be established by segmenting the p-implantation and connecting these segments to a voltage cascade. Such a *Silicon Drift Detector* (SDD) is shown in figure 2.16.

In a linear SDD as shown in figure 2.16a, one-dimensional position resolution can be obtained by using the drift time of the electrons. In a matrix SDD

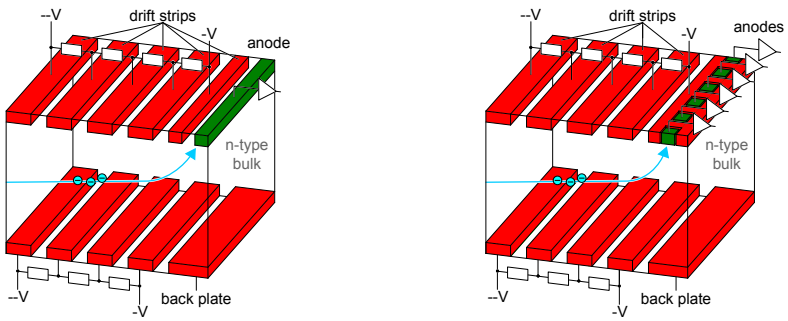

(a) linear SDD **(b)** matrix SDD

Figure 2.16: Silicon drift detectors. By segmenting the p-implantation and connecting the segments to a voltage cascade, the depletion field is overlaid with a lateral drift field. (a): In a linear SDD, one-dimensional position resolution can be obtained by drift time measurement. (b): In a matrix SDD, two-dimensional position resolution is achieved by segmenting the readout anode and drift time measurement.

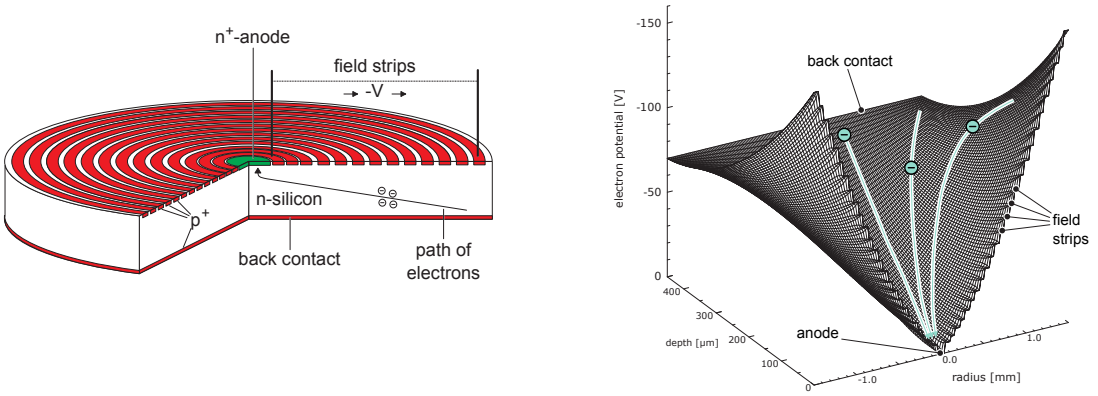

(a) Circular SDD schematic **(b)** Theoretical drift field

Figure 2.17: (a): Schematic of a circular silicon drift detector. The front contact is segmented into several rings (p^+-implantations) which are connected to a voltage cascade. This overlays the depletion field with an additional lateral drift field guiding the electrons generated in the bulk into the center of the detector. (b): Simulation of the potential formed by the circular field strips on the front side. The back contact is a homogeneous p^+-implantation [28].

(figure 2.16b), in which the readout anode is segmented, two-dimensional position resolution can be achieved. Here the coordinates are obtained from the pad on which the signal appears and the drift time measurement.

The finite length of the drift strips and the continually rising potential of transport field leads to very high voltages which have to be applied to the field strips (several hundred to few thousand, depending on drift length). Therefore proper termination of the field strips is necessary in such devices [3].

A circular SDD, which is produced at the HLL, is shown in figure 2.17. Because of the circular drift rings, the problem of proper termination of the field-shaping strips does not occur.

These radial SDDs are especially interesting for energy measurements. The point-like readout anode with small capacitance is located at the center of the detector surrounded by circular p^+ field strips which create the drift field shown in figure 2.17b.

For detector sizes smaller than approximately $1 \times 1\,\mathrm{cm}^2$, it is sufficient to segment the p-electrode only on one side of the device and to have a common potential on the large, undivided p^+-implantation on the other side [3]. As this implantation is homogeneous and can be made flat, it is ideally suitable as radiation entrance window.

Such a detector has a near Fano-limited energy resolution of 125 eV at 5.9 keV (Mn K_α) and a peak-to-background ratio of approximately 10 000. They have been used in several applications, among them space missions like the Mars Exploration Rovers "Spirit" and "Opportunity" [29], both missions run by the the *National Aeronautics and Space Administration* (NASA).

The side of the detector with the readout anode is usually referred to as its *front side*. Radiation enters the detector then through the homogeneous *back side*, coining the name *back side illuminated devices* for these detectors. This naming scheme is applied to all sidewards depleted devices at the HLL and also used in this thesis.

The detector shown in figure 2.17 can be equipped with a FET processed next to the readout anode (*first FET*). Charge collected in the anode flows onto the gate, modulating the transistor current which is then processed by readout electronics (see section 2.8.1 and section 2.8.2 for examples). This establishes a first amplification of the detector signal.

As the charge pulses created by absorbed photons immediately drift towards the readout anode, the detector needs to be read out permanently to avoid signal loss. This means each detector cell needs a dedicated amplifier and readout electronics. A device with controlled readout, i.e. readout-on-demand, which is better suited for imaging detectors, is presented next in section 2.6: the p-n CCD.

2.6 p-n CCDs

Another type of sidewards depleted devices are p-n CCDs, which are CCDs which exceed the capabilities of MOS CCDs in sensitivity, response uniformity and operation speed [3]. They are also capable of charge storage and transport like the MOS-devices. The p-n CCD working principle can be explained from the drift chamber.

Figure 2.18 shows a schematic of such a p-n CCD. Like the sidewards depleted device shown in figure 2.15b, the potential minimum is lifted towards the front side by applying asymmetric bias.

In contrast to the SDD already shown in figure 2.16b, the front side strips are no longer connected to a voltage cascade. Instead, every third is connected to a common voltage node, Φ_1, Φ_2, and Φ_3, turning them into *shift registers*. Applying a more negative voltage to e.g. Φ_1 and Φ_3 than to Φ_2 forms a potential minimum for electrons below Φ_2.

To avoid spreading of the charge cloud below the shift register, an additional,

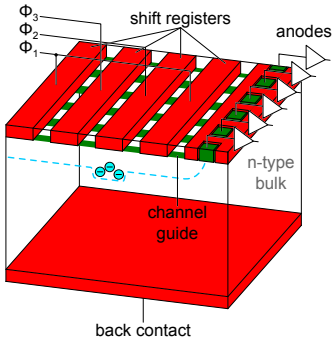

Figure 2.18: Schematic of a p-n CCD. Like the SDD, a p-n CCD is a sidewards depleted device. The potential minimum is shifted towards the wafer surface by asymmetric bias voltages. By applying appropriate voltages to the shift registers (Φ_1, Φ_2, and Φ_3) and the channel guides, the detector area is divided into pixels where the electrons created in the bulk are collected. The channel guides are an additional, striped n^+-doping perpendicular to the shift registers (shown as green stripes). By applying a voltage sequence to the shift registers, the collected charges can be transported to the readout nodes.

striped, n^+-doping in the surface region, perpendicular to the shift registers, forms *channel guides*. The channel guide doping is indicated by the green strips in figure 2.18.

The potentials of the shift registers and the channel guides divide the detector area into pixels. The pixel size of the p-n CCD is defined by the shift registers (usually three registers per pixel) and the channel guide [30].

Electrons generated in the bulk drift to the potential minimums (see figure 2.18), where they reside until readout. Thus, a p-n CCD is an integrating detector with readout-on-demand. Readout is accomplished by periodically raising and lowering the voltages of the shift registers such that the potential minimum moves towards the readout anode. The position information for a collected charge can be deduced from the number of potential shifts applied.

It is important to point out that the potential minimum is located not at the surface but at a distance (approximately 5 µm to 10 µm) in the bulk. The surface interface usually contains defects which can trap electrons and lead to charge loss if the charge is transported close to the surface. This is avoided by the channel guide implantation.

Like circular SDD shown in figure 2.17, the back contact of a p-n CCD is formed as a homogeneous large-area structure. This gives the p-n CCD the same excellent quantum efficiency. P-n CCDs also have an integrated first FET connected to the readout anode for first amplification.

In this section, only a coarse description of p-n CCD devices is given. A thorough description of p-n CCDs can be found in literature, e.g. in [30], [3], [31], [32] or [33].

2.7 DePFET detectors

The DePFET was introduced by Lutz and Kemmer in 1986 [9]. DePFET detectors combine detector and first stage amplification. Like the SDD and the p-n CCD, DePFET detectors are sidewards depleted devices.

In the course of detector evolution presented in the sections above, the DePFET is the next logical step. While a CCD transports the collected charge from the individual pixels to the readout node, a DePFET detector has a readout node at each pixel. This merges the first amplification stage with the place of charge collection.

Figure 2.19 shows a cut through a circular DePFET pixel cell along with the equivalent circuit. Basis of the DePFET device is the sidewards depleted structure with asymmetric bias shown in figure 2.15b. The potential minimum described in section 2.4 is laterally formed by an additional n^+-implantation, creating potential minimum pockets for electrons.

Right above these pockets, the gate of a MOS field effect transistor is pro-

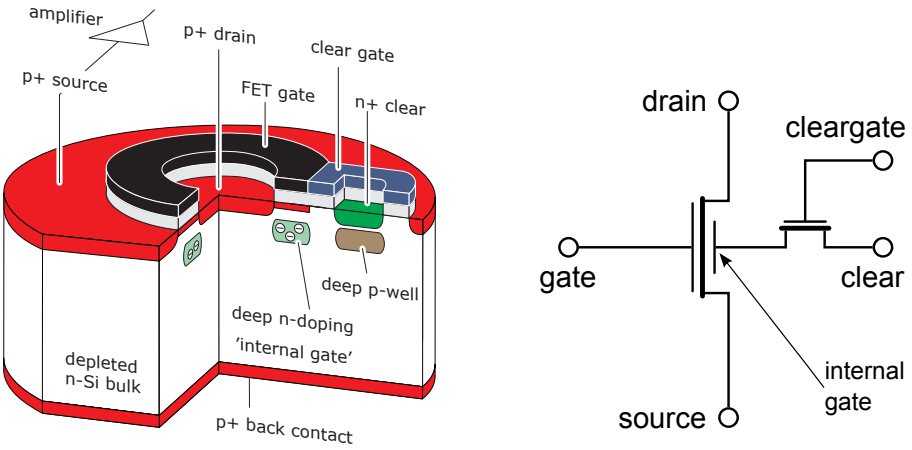

(a) DePFET pixel cell **(b)** Equivalent circuit

Figure 2.19: A DePFET pixel cell and its equivalent circuit. The current between source and drain is modulated by both, the external and internal gate. The charge from the internal gate is removed by the additional nMOS structure attached to the internal gate, the clear. The cleargate shields bulk and internal gate from the clear contact preventing electron injection or charge loss [28].

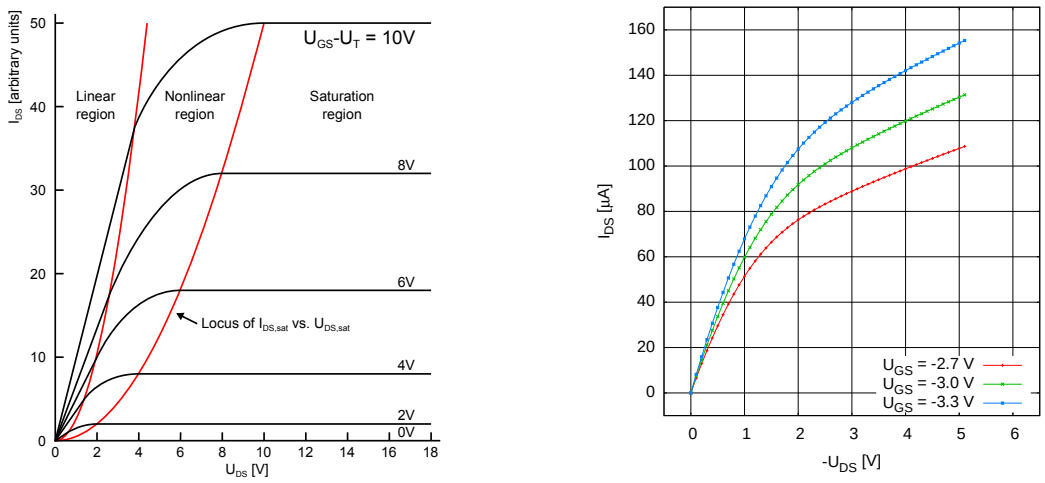

(a) ideal MOSFET **(b)** DePFET

Figure 2.20: (a): Idealized drain characteristics (I_{DS} vs. U_{DS}) of a n-channel MOSFET. The red lines separate the linear, nonlinear, and saturation regions. Picture from [14]. (b): Measured drain characteristic of pixels from a real DePFET detector for different gate-source voltages U_{GS} [34]. The rise in the saturation region ($|U_{\mathrm{DS}}| > 2\,\mathrm{V}$) is clearly visible.

cessed. Electron-hole-pairs generated in the bulk are separated by the depletion field, the electrons drift towards the potential minimum below the transistor gate where they influence mirror charges in the transistor channel. This alters the channel conductivity in the same way as electrons on the transistor gate do. Thus the potential minimum is referred to as the *internal gate* of the DePFET.

A DePFET pixel thus consist of a MOS field effect transistor processed upon the sidewards depleted bulk, with an external MOS-gate, and an internal gate made up by a potential minimum for electrons.

The drain characteristic of an ideal *Metal-Oxide-Semiconductor Field Effect Transistor* (MOSFET) is shown in figure 2.20a. The plot shows a linear region where the drain-source current I_{DS} rises linearly with U_{DS} and a saturation region where there is (ideally) no change of I_{DS} with respect to U_{DS}.

DePFETs are usually operated in the saturation region, where ideally only the gate has influence on the transistor current.

For a real transistor there is still a dependency of the drain-source current on the drain source voltage due to effects like channel-length modulation [14]. In figure 2.20b the measured drain characteristic of selected pixels of a DePFET matrix is shown. The measurement was performed for different gate voltages

U_{GS}. The drain current also rises linearly at first and then saturates. But in contrast to the ideal MOSFET, a real one (like the DePFET) still has a slope in the saturation region.

The characteristics of a DePFET are described by the two small signal parameters g_m and g_Q.

The *transconductance* g_m is defined as the derivative of the drain-source current I_{DS} with respect to the gate-source voltage U_{GS}. It describes the influence of the gate-source voltage on I_{DS}:

$$g_m = \left.\frac{\partial I_{DS}}{\partial U_{GS}}\right|_{U_{DS}=\text{const}} \tag{2.37}$$

The influence of the charge Q_{int} in the internal gate on I_D is expressed by the g_Q parameter. It is defined as the change of I_{DS} with respect to the charge in the internal gate:

$$g_Q = \left.\frac{\partial I_{DS}}{\partial Q_{\text{int}}}\right|_{U_{GS}=\text{const},U_{DS}=\text{const}} \tag{2.38}$$

For circular DePFET structures g_Q-values of $300\,\text{pA}/\text{e}^-$ have been measured.

The value of g_Q depends on several properties of the DePFET, e.g. the distance of the internal gate to the channel, gate width and length, doping concentrations, detector biasing [35].

So, with the two small signal parameters g_m and g_Q, the drain source current I_{DS} can be described by

$$I_{DS} = I_0 + \Delta U_{GS} \cdot g_m + \Delta Q_{\text{int}} \cdot g_Q\,. \tag{2.39}$$

DePFET detector models can be found in literature [3] [23]. These predict a linear response to the charge for typical operation parameters, $U_{GS} \approx 3\,\text{V}$ and a charge of $O(10^4 e)$ [36].

To remove the charge from the internal gate, a positive pulse is applied to the structure next to the transistor gate. This *clear* contact is an n^+-implantation surrounded by a MOS-structure, the *cleargate* (compare to figure 2.19b). To prevent unwanted charge loss to the clear contact, it is shielded towards the bulk by a deep p-implantation below.

A DePFET can be designed in many shapes, there are circular designs[4] as depicted in figure 2.19a, but also rectangular DePFETs designs exist, e.g. as detectors for particle physics [37].

[4] An overview of different circular designs can be found in [27]

The internal gate persists regardless of the transistor's state. Therefore, the gate of the transistor can be turned off during integration. Current flow is only necessary during readout, which decreases the power consumption of the detector.

The charge storage capability of internal gate of course depends on the layout and design of the DePFET. Measurements performed hint that a pixel in the current circular design is capable to store up to 300 000 electrons [34].

2.7.1 DePFET macropixels

X-ray imaging spectroscopy often desires detectors which cover a large field of view, i.e. to have a large detector area. The resolution of X-ray optics ranges in the region of 1 mm which makes it desirable to adapt the pixel size to the optic's resolution. This reduces the oversampling which – especially an advantage on satellite missions – also reduces the power consumption of the device, as less pixels need to be read out.

A *DePFET macropixel* combines a silicon drift detector with the DePFET amplifier/detector structure. This creates a device whose pixel size can scale up to 1 cm^2.

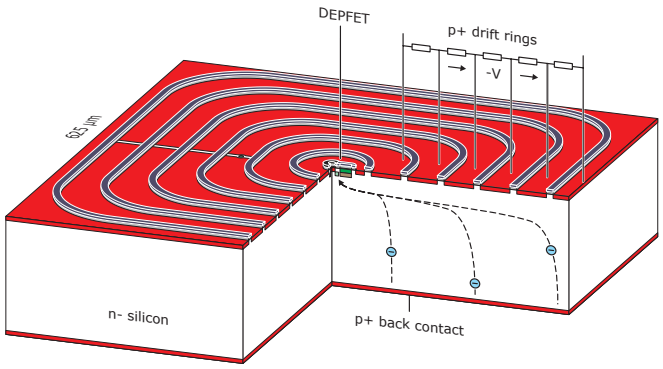

Figure 2.21: Cut through a DePFET macropixel cell. A DePFET macropixel combines a silicon drift detector with the DePFET structure. The drift rings are connected to a voltage cascade creating a drift field which guides the electrons into the internal gate of the DePFET in the center. Pixel sizes up to 1 cm^2 are possible [28].

Figure 2.21 shows a cut through a DePFET macropixel cell. The DePFET structure presented in section 2.7 is surrounded by a set of drift rings connected to a voltage cascade, like in the SDD shown in figure 2.17. These form an electric field guiding the electrons created in the bulk towards the internal gate of the DePFET in the center.

The SDD technology decouples the noise of the detector from its size while the DePFET adds features like charge storage and readout on demand.

2.8 DePFET readout

A DePFET pixel is read out by sampling the channel conductance, removing the charge from the internal gate by the clear contact and sampling the conductance again.

The first measurement yields the baseline plus the collected charge while the second one only measures the baseline. The pixel signal is the difference between these two measurements. This is referred to as *correlated double sampling*.

Figure 2.22 is a schematic of the principle of DePFET readout. In the present design, DePFETs are p-channel field effect transistors which require a negative gate voltage to switch it on.

After the first readout, sampling baseline and signal (compare to figure 2.22),

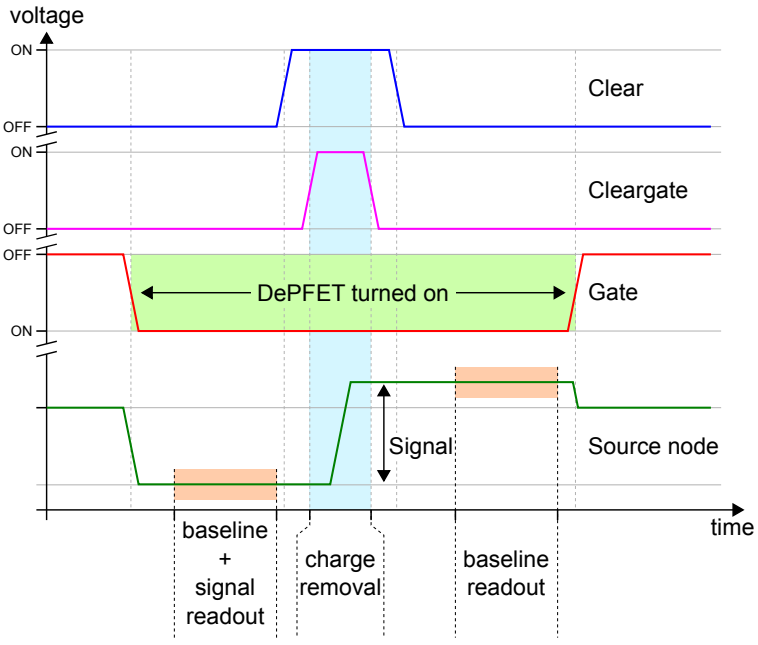

Figure 2.22: Principle of DePFET readout. The pixel conductance is sampled before and after the clear pulse. The signal which corresponds to the charge collected in the internal gate is the difference between the two measurements. The pixel is turned on only during readout, the charge is removed by applying a positive voltage to the clear and cleargate contact. Here, source-follower readout is shown: the pixel conductance is measured by sampling the source node voltage.

the clear process applies a positive voltage to the clear contact and then opens the cleargate for a certain period to remove the charge in the internal gate. Then the cleargate is closed and the clear contact is switched to a more negative off voltage to prevent charge loss into the clear. At the end, the second readout samples the baseline alone and the DePFET is then switched off by applying a positive voltage to the gate.

DePFET pixels are commonly read out by two methods, source-follower readout and drain-current readout. Both methods will be presented briefly in the next sections, a detailed discussion can be found in literature [38, 39].

The 'signal' fed to the readout electronics is created by the change in channel conductance created due to the charge removal during the clear process. Depending on the readout method this is either a voltage step at the source node or a change in drain-source current.

For correct signal processing, the charge deposition has to take place during integration time, before the readout. The effects of charge deposition during detector readout will be discussed in section 3.1.6.

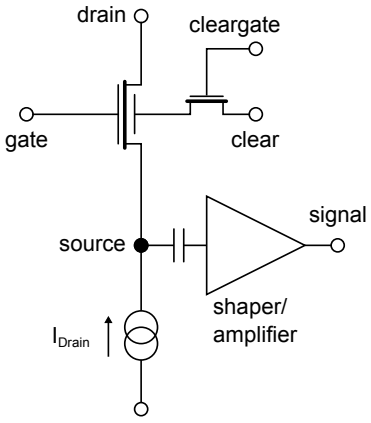

(a) source-follower readout

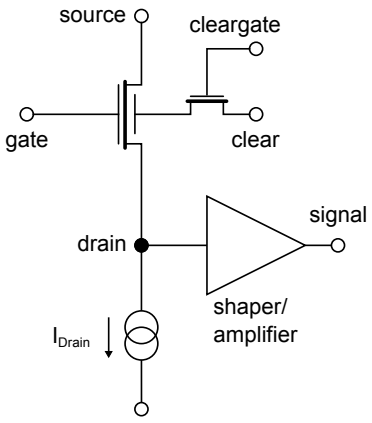

(b) drain-current readout

Figure 2.23: DePFET readout methods. Note that the positions of source and drain are switched between (a) and (b)! (a): At source-follower readout, the current source supplies a constant current which defines the voltage at the source node depending on the conductance of the DePFET channel. (b): For drain-current readout, the current source supplies a subtraction current such that the dynamic range of the shaper/amplifier can be used optimally. The current fed into the shaper/amplifier depends on the charge within the internal gate of the DePFET.

2.8.1 Source-follower readout

Figure 2.23a shows a schematic representation of DePFET readout in source-follower configuration. In source-follower readout the DePFET is biased with a constant drain-source current I_{DS} by a current source.

One can think of the DePFET in this setup as a variable resistor. The charge deposited in the internal gate changes the channel conductance of the DePFET. As the current source provides a constant current between source and drain, the change in channel conductance causes a change in the voltage drop over the transistor channel thus altering the potential of the source node. This changes the gate-source voltage U_{GS}.

According to equation 2.39, the constant drain-source current I_{DS} before the clear process is determined by the charge in the internal gate, while after charge removal the change of the source node potential compensates for it.

$$\begin{aligned} I_{DS,\text{before}} &= I_{DS,\text{after}} \\ I_0 + 0 \cdot g_m + \Delta Q_{\text{int}} \cdot g_Q &= I_0 + \Delta U_{GS} \cdot g_m + 0 \cdot g_Q \\ \Delta U_{GS} &= \frac{g_Q}{g_m} \cdot Q_{\text{int}} \end{aligned} \tag{2.40}$$

The change of the source node potential ΔU_{GS} is proportional to the charge which has been accumulated in the internal gate. By capacitive coupling an amplifier can measure this voltage step.

Being AC-coupled, the source-follower configuration has the advantage of easy coping with inhomogeneities of a pixel matrix and easy compensation of threshold voltage shifts. After switching to a row and application of the clear pulse, a settling time ranging from 0.8 µs to 1.5 µs is needed. This decreases the effective measurement time if the readout time stays constant.

2.8.2 Drain-current readout

Figure 2.23b shows a schematic representation of a DePFET readout in drain-current configuration. Here the drain is directly connected to the input of a current amplifier. To use the dynamic range of the amplifier optimally, a constant current equal to the typical drain-source current of the DePFET (30 µA to 100 µA) is subtracted by a current source [27].

The amplifier measures the current step ΔI between the drain-source current before and after the clear pulse, which is proportional to the deposited charge

Q_{int}:

$$\begin{aligned}\Delta I &= I_{DS,\text{before}} - I_{DS,\text{after}} \\ &= (I_0 + 0 \cdot g_m + \Delta Q_{\text{int}} \cdot g_Q) - (I_0 + 0 \cdot g_m + 0 \cdot g_Q) \\ &= \Delta Q_{\text{int}} \cdot g_Q\end{aligned} \tag{2.41}$$

The DePFET matrices investigated within the scope of this thesis were all read out in source-follower configuration. A study of a DePFET drain-current readout can be found in literature [39, 40, 41].

2.9 DePFET matrices

DePFET pixels are used as building block for imaging detectors. In section 2.8 the retrieval of the pixel signal, which is equivalent to the charge stored in the internal gate, was described. This correlated double sampling procedure requires a set of voltages to be applied to the DePFET pixel synchronously to the sampling of the internal gate (see figure 2.22).

A direct connection between each pixel and a readout channel would be possible. In the context of the free electron laser XFEL, new technologies are currently explored to achieve fast parallel readout for large matrices. Here, each pixel bump bonded to dedicated channel of a readout *Application Specific Integrated Circuit* (ASIC) [42]

However bump bonding is not an option if the DePFET detector matrix is used as low-energy detector in front of a high-energy detector. Besides, a larger number of readout nodes increases the overall power consumption of the device and high energy radiation passing the detector can cause fluorescence radiation in the bump bonds creating additional background in the detector.

A simple interconnection scheme, which allows fast readout (currently down to 4 µs/row) with a minimum number of readout nodes, will be presented below. Figure 2.24 shows a sketch of the matrix readout scheme in source follower mode. It sums up to the following features:

- The drains are connected to a global drain contact.
- The DePFET terminals gate, cleargate and clear are connected row-wise to steering *Integrated Circuit*s (ICs), which allow to select one row at a time.
- The sources are connected column-wise to a readout ASIC, which does column parallel readout

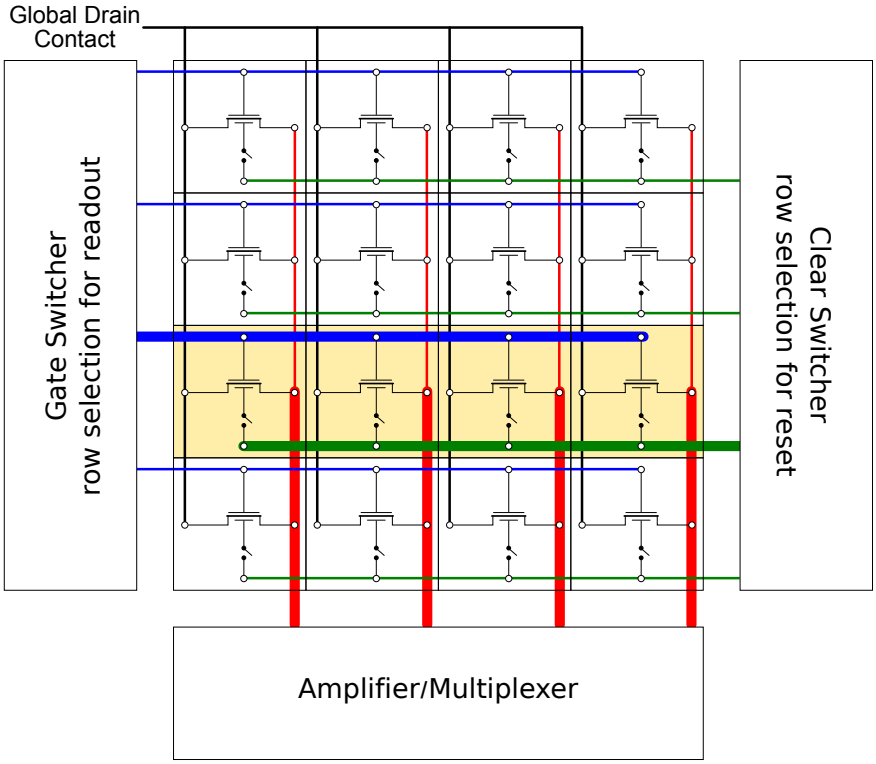

Figure 2.24: A schematic of the matrix interconnection scheme in source-follower configuration. A 4×4 matrix with each pixel represented by its simplified equivalent circuit is shown. The drain is connected globally, the sources are connected column-wise to the readout ASIC. The row selection is made by the two Switcher ICs, while the readout ASIC performs column parallel readout. The currently active row is colored, the respective connection lines are drawn thick.

The two sample measurements and their subtraction to retrieve the pixel signal are performed by a readout ASIC optimized for this task. Such an ASIC usually has a number of channels which can readout pixels in parallel as well as a multiplexer which serializes the data. In section 2.9.2 the current readout ASIC used with DePFET matrices, the ASTEROID ASIC, is described in detail.

A commonly used readout mode is to activate one row at a time, measure the collected charge as described in section 2.8, and proceed to the next. While one row is read out, the remaining pixels are integrating, i.e. accumulating charge. The integration time t_{int} of a pixel in a matrix with N_{rows} rows is

$$t_{\text{int}} = (N_{\text{rows}} - 1) \cdot t_{\text{readout}} \tag{2.42}$$

with t_{readout} being e.g. defined by equation 2.43.

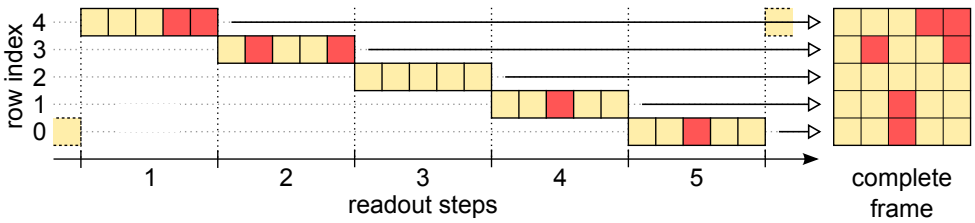

Figure 2.25: Rolling shutter readout of a 5×5 pixel matrix. Pixels with photon signals are marked red, else yellow. A complete frame comprises all readouts of a single pass of the shutter through the matrix. The columns are read out in parallel by the readout ASIC and then serialized into a single analog output. The rolling shutter traverses the matrix from top to bottom. After the readout of the row with index 0, a new frame is started with the readout of row index 4. All rows have the same integration time, but different starting points.

Figure 2.25 shows an illustration of this *rolling shutter readout*[5] on a 5×5 pixel matrix. The active row passes through the matrix from top to bottom. When it reaches the last row, restarts at the first. The combination of the readouts of one pass through the matrix is called a *frame*.

The interconnection scheme also allows readout modes such as windowing, i.e. selected readout of smaller parts of the matrix. This is useful if there are exceptionally bright objects in the field of view which require faster readout than the rest of the matrix.

For row selection and voltage application also an ASIC, called *Switcher IC*, is used. Both, Switcher IC and readout ASICs have to be programmed or controlled such that row selection and readout can happen in the manner described above. More about the Switcher ICs can be found in section 2.9.1

An example for the imaging capabilities of a DePFET pixel matrix is shown in figure 2.26. The picture in figure 2.26a was created by shielding the detector an ^{55}Fe source with the 450 µm silicon baffle shown in figure 2.26b. The detector used was a 64×64 DePFET macropixel matrix with $300 \times 300\,\mu m^2$ pixel size, designed for the space mission BepiColombo.

Apart from their imaging capabilities, DePFET detectors are a good choice for applications like X-ray imaging spectroscopy:

- As semiconductor detectors, DePFET detectors have a good energy resolution compared to gas detectors.
- As sidewards depleted devices, the detector capacitance is very small giving

[5] The active row is thus also referred to as the *shutter*

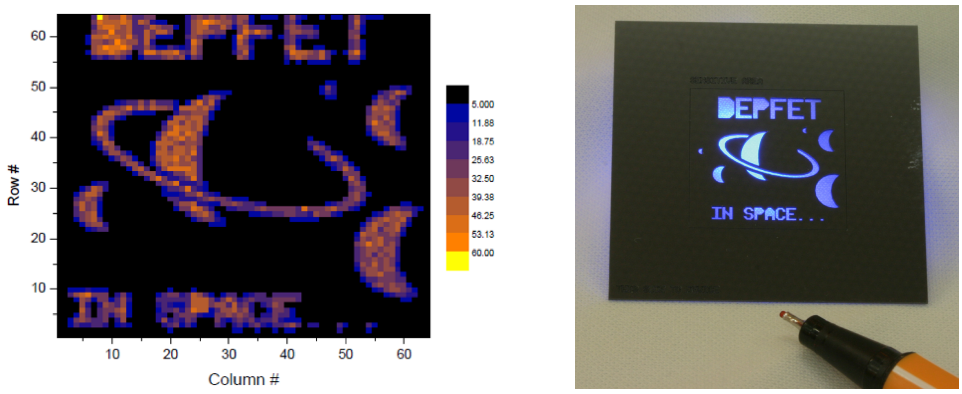

(a) detector image **(b)** silicon baffle

Figure 2.26: (a): Image obtained by shielding a 64×64 DePFET macropixel matrix with $300 \times 300\,\mu m^2$ pixel size with Si baffle. (b): The baffle made out of silicon with $450\,\mu m$ thickness. The image in the center has the same size as the active area of the DePFET matrix. It is surrounded by a 1 cm border used for fastening.

DePFET detectors excellent noise properties.

- Compared to p-n CCDs, DePFET show a better radiation hardness, as the signal is only broadened by higher leakage current. Furthermore, there is no need for charge transfer to the readout node during which charge loss can occur.
- With DePFET detectors, which are not limited by the charge transfer speed as CCDs, higher readout rates are possible.
- The possibility of random access to pixels allows flexible readout modes, e.g. windowing.
- Arbitrary pixel sizes up to $1\,cm^2$ are possible with macropixel structures, which allows adaption of pixel size to the resolution of the X-ray optics.
- Special DePFET designs allow *repetitive non-destructive readout* and thus ultra-low noise measurements of the charge in the internal gate. With such devices ENC values of $0.18\,e^-$ for readout noise have been achieved [27].

2.9.1 The Switcher steering IC

The purpose of the Switcher ICs is to

- activate the matrix rows consecutively (*rolling shutter*),

- apply a voltage sequence to the active row for readout.

The voltage sequence which is applied to gate, cleargate and clear of the DePFET comprises switching on the pixel, clearing the pixel, switching off the pixel. This was described in section 2.8.

A Switcher IC has two ports (A and B) and a number of channels. Each port has two inputs (e.g. A_{HIGH} and A_{LOW}), and one output for each channel (e.g. $A_{out,i}$ for channel i). This means each channel has two outputs, one for each port. The voltages for the input levels (HIGH and LOW) are supplied externally.

Each output can take two states, ON and OFF. A so-called *polarity bit* defines to which input level (HIGH or LOW) the output is set at which state.

For an active channel, the output of a port can be switched between the ON and OFF state using dedicated input signals. This way the voltage sequence for DePFET readout is applied. When a channel is deactivated, the respective outputs are automatically set to their OFF state.

The Switcher ICs are produced in an *Austria Microsystems* (AMS) high voltage *Complementary Metal Oxide Semiconductor* (CMOS) process. There are currently two variants of these chips in use with matrices designed for X-ray imaging spectroscopy: Switcher II[6] and Switcher S.

Figure 2.27 shows a simplified schematic view of a Switcher II ASIC to illustrate the working principle of a Switcher IC. This chip has 64 high voltage channels, a channel selection counter, a *Random Access Memory* (RAM) sequencer and two *direct pins* (Direct A and Direct B).

Both, the RAM sequencer and the direct pins can set the state of the port outputs of the currently active channel. The RAM sequencer is not used with the current DePFET matrices at the HLL, the signals for voltage level shifting are supplied externally via the direct pins by the sequencer in the X-Board (see section 2.10.2).

The channel selection counter is a 6-bit counter which selects exclusively one channel after another. When reaching the last channel number, the counter starts again at the first. The counter can also run in reverse direction.

In contrast to the Switcher II design, the Switcher S is simpler, having only a shift register to select outputs, and the sequence for switching between voltage levels is supplied externally. It also has a revised high voltage part which is able to switch voltage spans of up to 30 V (Switcher II: up to 20 V) and is radiation tolerant up to > 100 krad [44]. Switcher S was designed for space application

[6] A variant, called Switcher IIb, has extra test pads but is else identical.

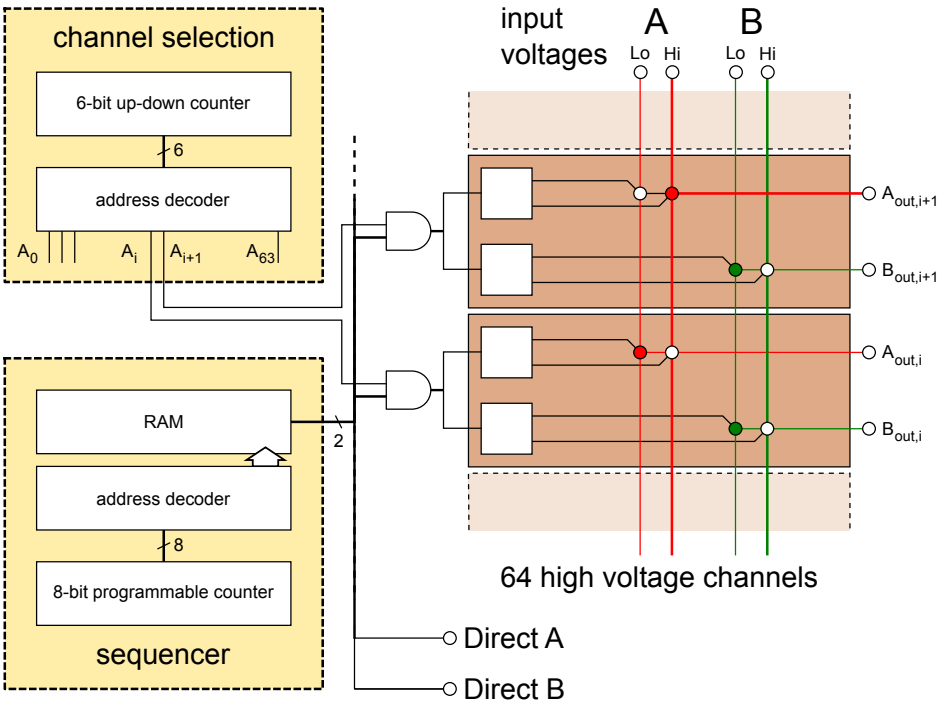

Figure 2.27: Schematic view of a Switcher II ASIC with 64 high voltage channels, a channel selection counter and a RAM sequencer. The channel selection selects one row at a time (rolling shutter). The output voltages of the selected channel can be set either by an internal RAM sequencer or externally via the pads Direct A and Direct B. Current DePFET matrices use the external variant where the pattern is supplied by the X-Board sequencer. Picture adapted from [43].

and will be used to steer the DePFET matrix on the mission BepiColombo (see section A.2).

For DePFET operation, gate, cleargate and clear need one switcher port each. Therefore, a DePFET matrix needs three ports in total, i.e. at least two Switcher ICs.

One Switcher IC is dedicated to the clear contact, because the voltage span (difference between lowest and highest voltage applied at all port inputs) is maximal for it (around 20 V for the clear contact, less than 10 V for gate and cleargate contact). Gate and cleargate are thus steered by the other Switcher IC. The former is called the *clear switcher* while the latter is referred to as the *gate switcher*.

The Switcher II and Switcher S ASICs have both 64 output channels. For operation of larger matrices, the chips can be connected in a daisy chain [43, 44] forming a switcher group. A matrix with 128 rows is then steered by two clear switchers and two gate switchers. Here, each Switcher IC of each group controls

half of the matrix rows.

2.9.2 The ASTEROID readout IC

The ASTEROID[7] ASIC has been developed at the HLL for DePFET readout in source-follower configuration. The ASTEROID is a 64 channel shaper/amplifier IC. It features trapezoidal shaping, serial analog readout and an integrated shaping sequencer for flexible application of different filter timing [45, 46].

Figure 2.28a shows a picture of the trapezoidal weighting function of the ASTEROID readout ASIC. The weighting function describes the impact of the detector signal onto the amplifier output as a function of the time of arrival of the signal with respect to the operational state of the filter. The detector signal is the voltage step at the source node due to the charge removal during the clear process (compare to section 2.8.1). The amplifier output is maximal if the signal coincides with the "plateau". The Fourier transform of the weighting function, the frequency transfer function, is shown in figure 2.28b. If folded with the noise power spectrum, the impact of the different noise contributions (thermal, 1/f, shot noise) on the output signal can be deduced.

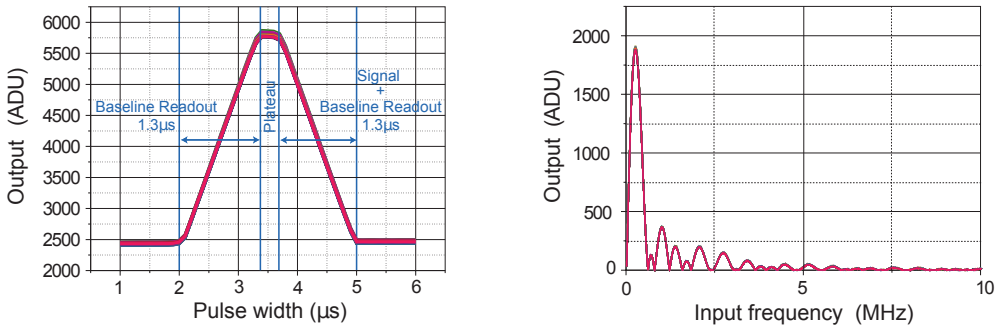

(a) weighting function **(b)** frequency transfer function

Figure 2.28: Weighting function and frequency transfer function of the ASTEROID readout IC [45]. The weighing function (a) describes the impact of the input signal of the ASTEROID onto its output signal as a function of the time of arrival of the signal with respect to the operational state of the filter. The input signal is the voltage step created at the DePFET source node by the charge removal during the clear process. The frequency transfer function (b) is the Fourier transform of the weighting function. If compared to the noise power spectrum, the impact of the different noise contributions (thermal, 1/f, shot noise) on the output signal can be deduced.

[7] ASTEROID = **A**ctive Current **S**witching **T**echnique **R**eado**u**t **I**n X-ray Spectroscopy with **D**ePFET

Figure 2.28 shows the superimposed weighting function of all 64 channels. It can be noticed that the ASTEROID readout ASIC shows a very good homogeneous response. Its relative non-linearity is about 0.4 % for all channels, the gain dispersion, the quotient of gain variance and mean gain, is 0.4 % [45].

The ASTEROID is the successor to the CAMEX[8] [47]. The CAMEX was originally designed and optimized for CCD readout. Like ASTEROID it performs source follower-readout but uses eight-fold multi-correlated double sampling instead of an integrating shaper.

Figure 2.29 shows a simplified overview of the ASTEROID readout chain in one channel. The readout chain consists of a preamplifier stage which also serves as a voltage to current converter, an integration stage, a second amplification stage, and a *Sample and Hold* (S/H). Not shown in figure 2.29 is the multiplexer which serializes the signals from the 64 channels to the common differential output buffer.

The individual stages have a number of switches which are controlled by an internal sequencer. Both, sequencer and multiplexer are controlled by the sequencer on the X-Board from which they receive a dedicated clock signal each.

The sequences for the amplifier and the multiplexer can be run in succession (*simplex mode*) or in parallel (*duplex mode*). In simplex mode the active row is first read out and then serialized to the output buffer. In the duplex mode the multiplexer serializes the previous row read out, while the active row is processed.

As presented above in section 2.8 the DePFET pixel column is connected to a current source which provides a constant current through the column. The current flows from the source through the currently active DePFET pixel to the global drain contact.

In the following the ASTEROID readout sequence, which is also shown in figure 2.29 above the channel schematic will be described. Figure 2.29 shows the channel in an initial state where

- S_{in}, the input switch, is open,
- S_{Pre}, the preamplifier reset, is open,
- S_{G1}, connecting the preamplifier output to ground, is closed,
- S_1, connection preamplifier and integrator, is open,
- S_{R1}, the integrator reset, is open,

[8] CAMEX = **C**harge **A**mplifier **M**ultipl**EX**er

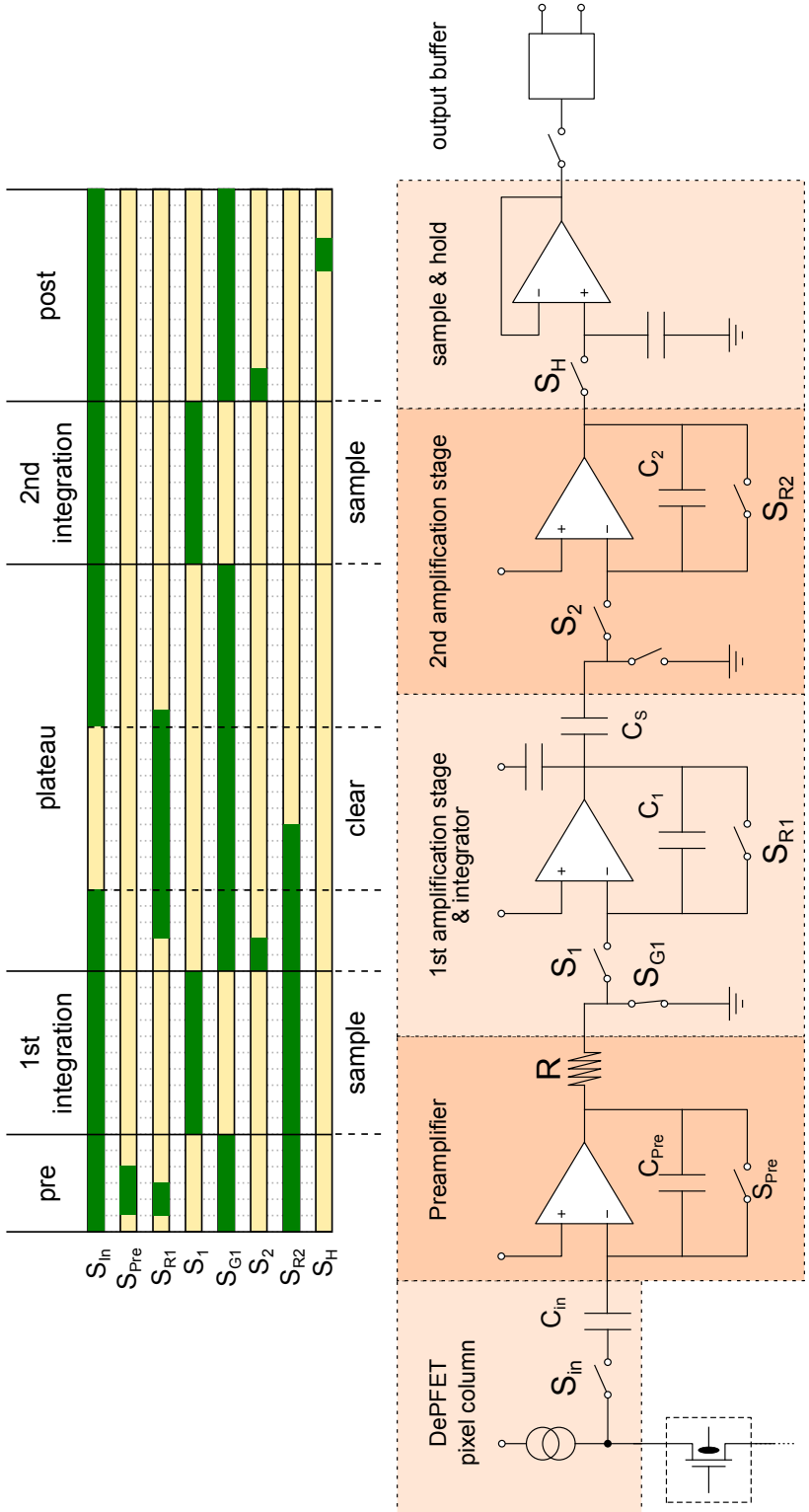

Figure 2.29: Simplified ASTEROID readout channel. The main components are shown with necessary detail. The charge collected in the DePFET pixel causes a change in the source node voltage. The source node voltage is converted to a current in the preamplifier stage. The current is integrated in the 1st amplifier stage before and after the clear pulse. The difference of the two integrations is stored in the sample and hold. The signal is finally converted to a pseudo-differential signal at the output buffer. Above the channel schematic, a switching sequence is shown. The green bars mark the time period during which the respective switch is closed.

- S_2, connecting integrator and 2nd amplifier, is open,
- S_{R2}, the 2nd amplifier reset, is open,
- S_H, connecting 2nd amplifier and S/H, is open.

The ASTEROID readout sequence can be divided into the following stages: preprocessing, first integration, plateau, second integration, postprocessing. The total readout time t_{readout} is the sum of the duration of these stages:

$$t_{\text{readout}} = \tau_{\text{pre}} + \tau_{\text{int}} + \tau_{\text{plateau}} + \tau_{\text{int}} + \tau_{\text{post}} \tag{2.43}$$

Preprocessing After the input switch S_{in} is closed, the ASTEROID channel is reset at first. This is accomplished by closing S_{Pre}, S_{R1}, and S_{R2}.

This procedure defines the current voltage level at each operational amplifier input as its zero level. The output voltage of the respective amplifier then depends on the difference ΔU to this input level. While S_{Pre} and S_{R1} are opened before the first integration, S_{R2} stays closed until the plateau stage.

After opening S_{Pre} the output voltage U_{pre} is defined by

$$U_{pre} = \Delta U_{in} \cdot \frac{C_{in}}{C_{pre}} \tag{2.44}$$

which is converted to a current I by the resistor R. So the preamplifier is also a voltage-to-current converter which output current is defined by

$$I = \frac{U_{pre}}{R} = \Delta U_{in} \cdot \frac{C_{in}}{R \cdot C_{pre}} \tag{2.45}$$

First integration For the first integration S_{G1} is opened and at the same time S_1 closed. The current of the preamplifier is now fed into the integrator. At the end of the integration period the output voltage U_{int} of the integration stage is

$$U_{int,1} = \frac{1}{C_1} \int I \, dt = \frac{1}{R\,C_1} \int U_{pre,1} \, dt \tag{2.46}$$

The total capacitance of the feedback capacitance C_1 can be changed to set the gain level of the ASTEROID. At the end of the integration S_1 is opened while simultaneously closing S_{G1}.

S_1 and S_{G1} are always switched complementary, so the current produced by the preamplifier either flows to ground or into the integrator thus preventing charge buildup.

As described in section 2.8 the first integration samples the *filled* state of the DePFET.

The Plateau At the beginning of the plateau, S_2 is closed. Because S_{R2} is still closed the second amplifier acts as a voltage follower. This defines the output level of the integrator as the zero level of the second amplifier (like the reset procedure in the preprocessing stage). Afterwards, S_2 is opened again.

Now the charge is removed from the internal gate of the pixel. During application of the clear pulse S_{in} is opened. Although the clear process takes currently only around 600 ns, the length of the plateau is longer to give the source node voltage time to settle.

Also within the plateau, the integrator is reset by opening and closing S_{R1}, and S_{R2} is opened (this is important for the postprocessing stage).

Second integration After the plateau comes the second integration, which samples the *empty* state of the DePFET. Again the preamplifier current is redirected to the integrator by opening S_{G1} and closing S_1. After τ_{int}, once more, S_1 is opened and S_{G1} is closed. The second integration sets the output voltage U_{int} of the integrator to

$$U_{int,2} = \frac{1}{C_1} \int I \, dt = \frac{1}{R\,C_1} \int U_{pre,2} \, dt \tag{2.47}$$

Postprocessing At the beginning of the postprocessing the input of the second amplifier is at $U_{int,1}$ (set after the first integration), the output of the integrator is at $U_{int,2}$ after the second integration. After closing S_2 the voltage $\Delta U = U_{int,2} - U_{int,1}$ is applied to capacitor C_S. This sets the output U_{out} of the second amplifier to

$$\begin{aligned} U_{out} &= \frac{C_S}{C_2} \cdot \Delta U = \frac{C_S}{C_2} \cdot (U_{int,2} - U_{int,1}) \\ &= \frac{C_S}{C_2} \cdot \frac{1}{RC_1} \int (U_{pre,2} - U_{pre,1}) \, dt \\ &= \frac{C_S}{C_2} \cdot \frac{C_{in}}{C_{pre}} \cdot \frac{1}{RC_1} \int (U_{in,2} - U_{in,1}) \, dt \\ &= \frac{C_S}{C_2} \cdot \frac{C_{in}}{C_{pre}} \cdot \frac{\Delta t}{RC_1} \cdot \Delta U_{in} \, . \end{aligned} \tag{2.48}$$

The input voltage step ΔU_{in} is the source node voltage change as defined in equation 2.40; it is caused by the charge removal during the clear process.

As a final step, S_H is closed and opened, thus transferring the resulting signal onto the S/H capacitance. Triggered by the multiplexer clock from the X-Board, the ASTEROID multiplexer transfers the signals from the channel S/H stages to the output buffer. This can happen in parallel to the ASTEROID sequencer (duplex mode) or successively (simplex mode). When the sequence for the current row is finished, the Switcher IC selects the next row and the readout sequence starts over.

The trapezoidal weighting function of the shaper represents the optimum time-limited filter for white series noise which is the dominant electronics noise at the DePFET readout speed (approximately $5\mu s$ per row) chosen for the current missions (e.g. BepiColombo) [46].

The DePFET matrix presented in chapter 4 was read out with a $t_{\text{readout}} = 6.9\,\mu\text{s}$ per line. The integration time there was 1 µs each, the length of the plateau 2.5 µs. The length of the pre- and post-intervals were 0.6 µs and 1.3 µs respectively. With detector setups designated for the space mission BepiColombo even faster readout times of 4.8 µs per row have been achieved [48].

The output buffer delivers a differential analog signal and is connected to an *Analog-to-Digital Converter* (ADC). Figure 2.30 shows oscilloscope images of the analog output of the ASTEROID. The pixel signals are visible as steps in the respective channel of the oscilloscope. Although the pixels of the active row are read in parallel, their readout values are sent serially to the output by the

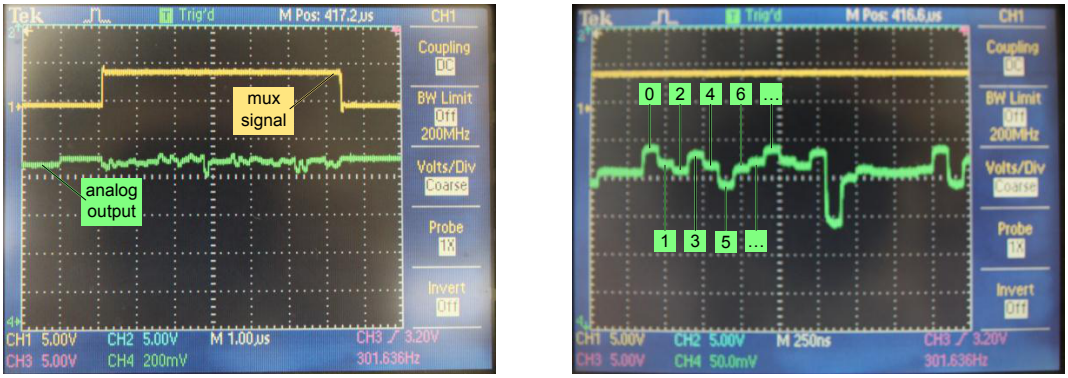

(a) oscilloscope image **(b)** zoom

Figure 2.30: Images of the analog output of the ASTEROID. The yellow curve signals the state of the multiplexer, the green curve shows the individual pixel signals. (a) shows the signals of a complete line of the DePFET matrix. In the zoom (b), the individual pixel signals are visible as steps. The first ones are labeled to help visualization.

multiplexer. This defines a *readout direction*.

Digitization and storage of the ASTEROID output signals is explained in detail in section 2.10 where a DePFET data acquisition system is presented.

2.9.3 Readout sectors and hemispheres

To increase readout speed, a matrix can be divided into *hemispheres* and *sectors*. This is just a logical subdivision of the detector matrix, which assigns the individual pixels to the steering and readout ASICs. The division does neither affect the pixels themselves nor introduce inefficiencies like "blind spots" at the sector borders.

A matrix $C \times R$ pixels has C columns and R rows. If the matrix is divided into hemispheres, each hemisphere contains C half-columns with $R/2$ pixels in each. A sector comprises all pixels which are read out by the same readout ASIC. In the simplest case (one sector, no hemispheres), there is one readout ASIC for the whole matrix as shown in figure 2.24.

During readout, the active row passes through the sectors. Depending on the programming of the Switcher ICs (see section 2.9.1) the active row can pass through a sector from top to bottom or from bottom to top. Together with the readout direction of the readout ASIC (see section 2.9.2) this establishes an order among the pixels of the matrix in the data stream coming from the output buffer of the readout ASIC.

Figure 2.31 shows an overview of different matrix readouts and how they affect the pixel order in the data stream. The order in which the readout values of the 6×6 pixel matrix are finally stored is indicated by the index in the respective pixel. Comparing figure 2.31a and figure 2.31b one can see that the pixels with the same position in the data stream (same index value) are at different positions on the matrix. For later image reconstruction it is thus vital to know how the matrix was read out.

In contrast to the running direction of the rolling shutter, there is only one running direction for the multiplexer of the readout ASIC. However the relative position of the ASIC in relation to the matrix can result in the pixel columns being addressed either from left to right or from right to left.

The effect of the positioning of the readout ASIC can be seen in figure 2.31c: Although both readout chips have the same multiplexer running direction (relative to the same edge of the ASIC chip), the running direction on the matrix is in opposite direction (left to right for the lower half, right to left for the upper).

If more than one readout ASIC is used for a matrix, eventually, the data

streams of the individual ASICs have to be combined. This can either be accomplished by interleaving them before writing to file, or by writing the data streams into individual files and merging them later. More detail on this can be found in section 2.11.

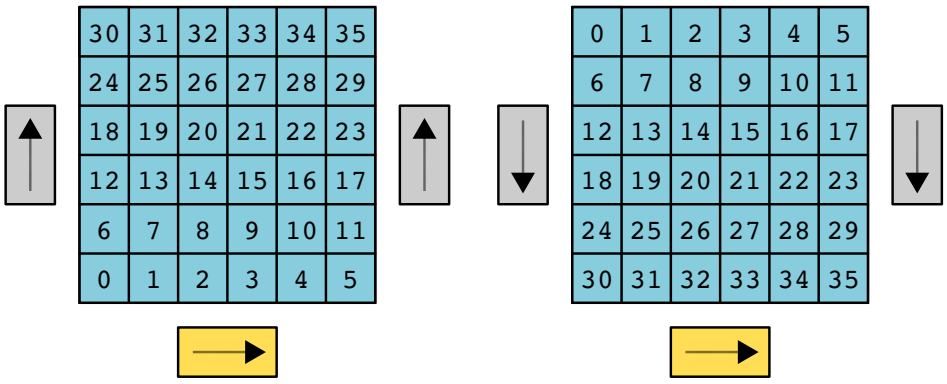

(a) single sector readout, up direction

(b) single sector readout, down direction

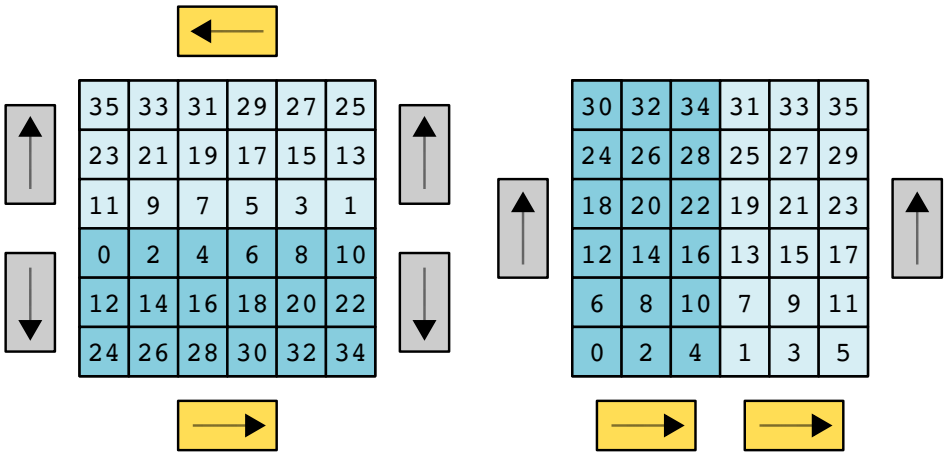

(c) two hemispheres

(d) double sector readout, up direction

Figure 2.31: Different matrix readout schemes. The numbers in the pixel cells give the readout order of the signals in the data stream. The readout ASICs are colored golden, the Switcher ICs silver. The matrix area can be subdivided into hemispheres as in (c), sectors as in (d), or both. For the matrices with two readout chips ((c) & (d)) the order of the pixel signals in the data stream is also depending on the multiplexing in the readout chain.

Interleaving means the data streams of two readout ASICs are merged into one by alternately writing out the pixel values of the individual streams. The effect of this is shown figure 2.31c and figure 2.31d: one sector has only even indices and the other only odd indices. Also here, the information about how the matrix was read out is important for a correct image reconstruction.

The active row traversing the matrix and the multiplexer of the readout ASIC thus convert the signals from the two-dimensional matrix into a one-dimensional data stream. The data stream and its further processing is described in section 2.10 and section 2.11.1.

For X-ray imaging spectroscopy several devices have been developed. An overview of their sizes and logical subdivision is given in Table 2.1. Figure 2.32 shows a size comparison of the active areas of the listed matrices. Images of these detector matrices can be found in section 2.10, figures 2.36 to 2.39.

Name	Size (pixels)	Readout	Type
XEUS-Small	64×64	1 sector	75 µm DePFET
BepiColombo	64×64	2 sectors, hemispheres	300 µm macropixel
Simbol-X	64×64	1 sector	500 µm macropixel
XEUS-Large	256×256	4 sectors	75 µm DePFET
IXO	1024×1024	16 sectors, hemispheres	100 µm macropixel

Table 2.1: Overview of DePFET matrices. The "XEUS-Large" device is currently the largest (in terms of pixel count) DePFET device which has been operated. The IXO device is presently in the prototyping stage.

The "XEUS[9]-Small" devices are the smallest matrices, with a pixel size of $75 \times 75\,\mu m^2$ and an active area of $4.8 \times 4.8\,mm^2$. They have a pixel count of 64×64 pixels.

The "XEUS-Large" devices have the same pixel size but a higher pixel count (256×256) and thus an active area of $19.2 \times 19.2\,mm^2$. In terms of pixel count, the "XEUS-Large" is at present the largest DePFET device which has been operated. The matrix is divided into four sectors.

Of the two macropixel matrices, the BepiColombo matrix has the same active area size as the "XEUS-Large" device, but due to a pixel size of $300 \times 300\,\mu m^2$ this is achieved with a pixel count of 64×64 pixels. The matrix is divided into two hemispheres. Because each hemisphere has its dedicated readout ASIC, the

[9]The **X**-ray **E**volving **U**niverse **S**pectroscopy (XEUS) space observatory was planned by the *European Space Agency* (ESA) as successor to the XMM-Newton X-ray satellite telescope [4]. Developments for XEUS were then merged into the mission for IXO.

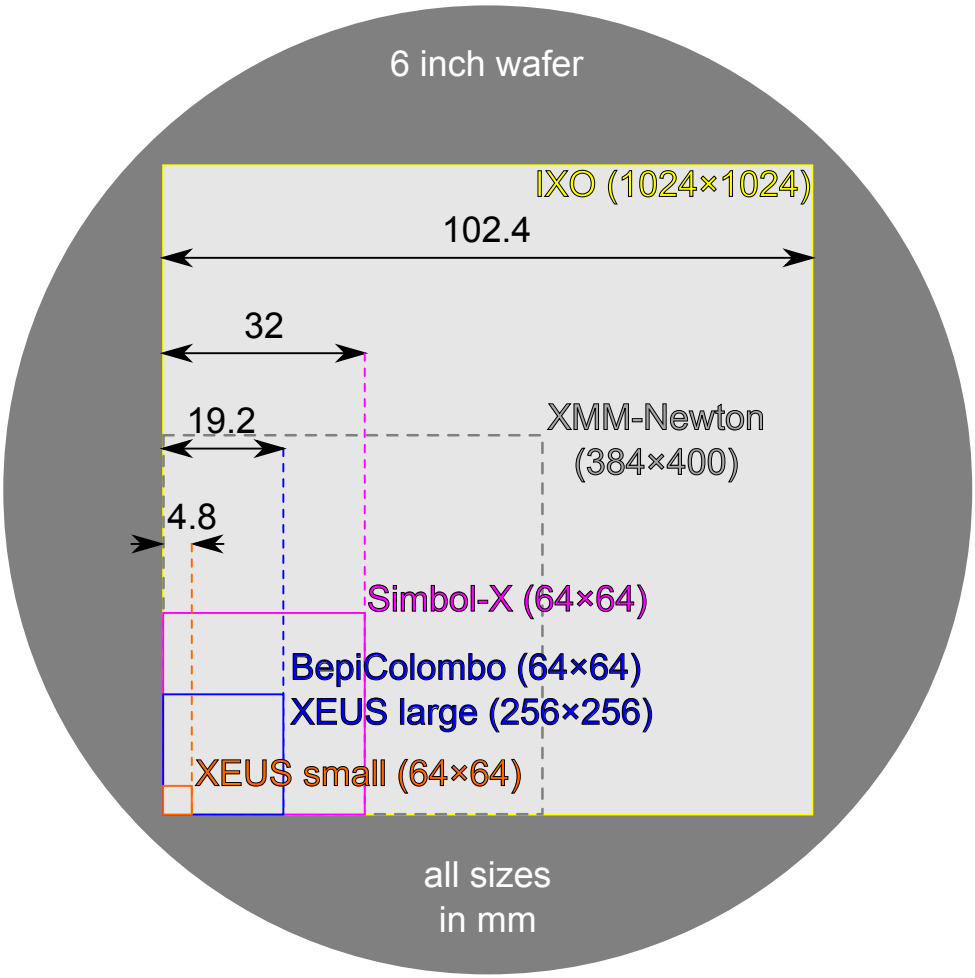

Figure 2.32: Comparison of active area sizes of different DePFET matrices. The pixel count of each matrix is shown in parentheses. Also the size of the – until recently – largest p-n CCD, which is on board the XMM-Newton space telescope, is shown. This detector has an active area of $60 \times 60\,\mathrm{mm}^2$ with a pixel count of 384×400.
The "XEUS-Small" devices are the smallest DePFET matrices, followed by the "XEUS-Large" devices, which have the same pixel size ($75 \times 75\,\mu\mathrm{m}^2$) but a higher pixel count of 256×256. The macropixel detector for the space mission BepiColombo has the same active area size as the "XEUS-Large" matrix. Because of a pixel size of $300 \times 300\,\mu\mathrm{m}^2$ this is already achieved with a pixel count of 64×64. The Simbol-X quadrant matrix has the same pixel count as the BepiColombo device, but a pixel size of $500 \times 500\,\mu\mathrm{m}^2$ and thus an active area size of $32 \times 32\,\mathrm{mm}^2$.
All devices will be outranged, both in pixel count and active area size, by the proposed focal plane detector for the IXO wide field imager. This detector will have a pixel count of 1024×1024, a pixel size of $100 \times 100\,\mu\mathrm{m}^2$ and an active area of $102.4 \times 102.4\,\mathrm{mm}^2$.

BepiColombo matrix has two sectors.

The Simbol-X quadrant matrix has an even larger pixel size of $500 \times 500\,\mu m^2$ and therefore an active area size of $32 \times 32\,mm^2$. This makes the Simbol-X quadrant the DePFET device with the largest active area in operation at present.

For comparison, the size of the XMM-Newton p-n CCD detector is also shown in figure 2.32. The detector with a pixel count of 384×400 and an active area of $60 \times 60\,mm^2$ was until recently the largest X-ray CCD detector ever built[10].

However, the proposed focal plane detector for the space telescope IXO will outrange all these with a pixel count of 1024×1024 and an active area size of $102.4 \times 102.4\,mm^2$. The detector will have a pixel size of $100 \times 100\,\mu m^2$ and be built monolithically on a 6 inch wafer. The detector matrix here is planned to be divided into two hemispheres with eight sectors each, which also means the readout ASIC for each sector here is designed to have 128 channels, unlike the ASICs used with the devices above which have 64 channels [6].

Except for the IXO device, which is still in the prototyping stage, all DePFET matrix types have been successfully realized and tested at present time.

2.10 The data acquisition system

Depending on the application's requirements the data acquisition setup can look different. It is also subject to constant evolution and improvement. Here, the current setup used in the HLL test lab is described as a prototype for DePFET data acquisition. This setup was also used for the measurements shown later in this thesis (see chapter 4).

Figure 2.33 shows a schematic of the measurement setup. On top, there is the vacuum tank which contains the detector *hybrid ceramic* which is fastened in a cooling mask (not shown) and connected to a *Printed Circuit Board* (PCB), the *inner PCB*.

The hybrid is a multilayer ceramic to which the detector as well as the steering and readout ASICs are glued. Besides support to the detector chip and signal routing, it also provides thermal coupling to the cooling mask. The hybrid ceramic is described in detail in section 2.10.1.

The inner PCB is connected by flexleads through the vacuum flange to the *outer PCB* (also called the *PixBoard*). The inner and outer PCBs route the signals from the hybrid to the outside and the supply voltages and timing signals from outside to the hybrid.

[10] p-n CCDs developed for the free electron laser XFEL [49] have outranged the XMM CCD.

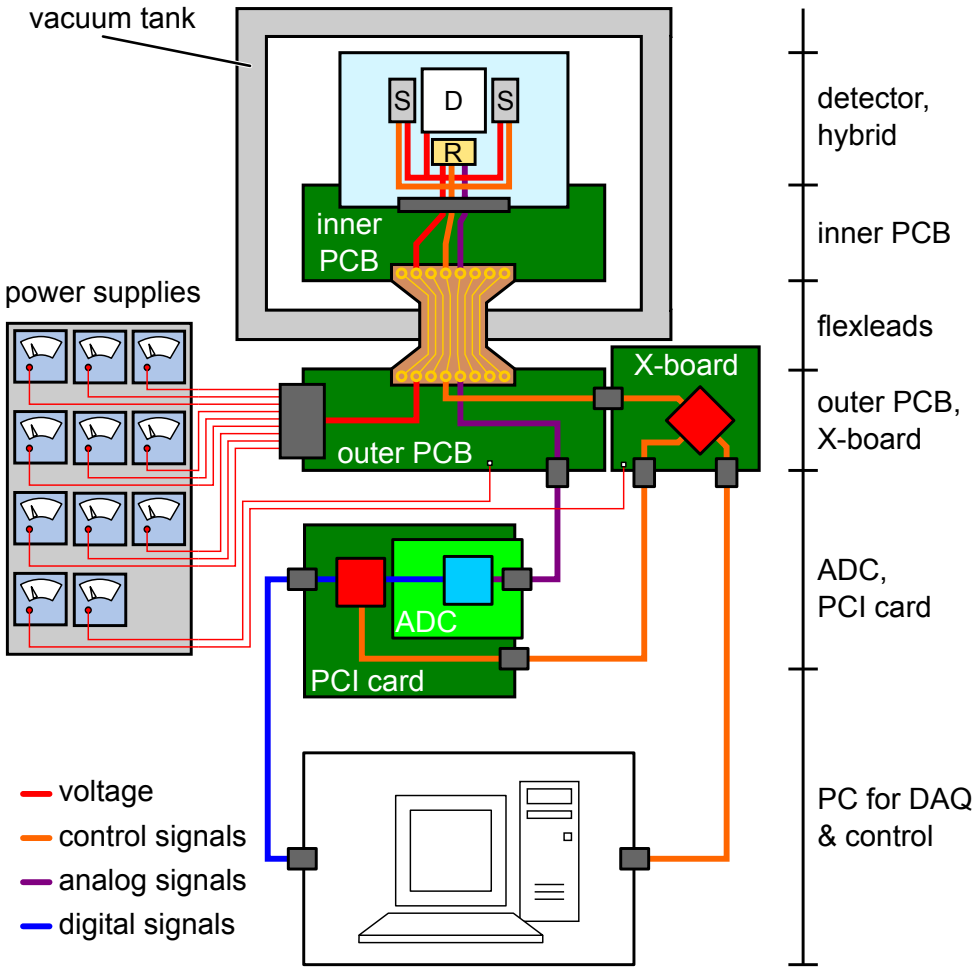

Figure 2.33: Schematic of the DePFET test setup. Inside the vacuum tank is the detector hybrid ceramic with the detector matrix (D), and the steering (S) and readout ASICs (R). The hybrid is connected to the inner PCB, which is connected to the outer PCB via flexleads through the vacuum flange. The required voltages for DePFET operation (red lines) are routed through the PCBs and the hybrid to the ASICs and the detector, as well as the analog output from the readout ASIC (violet line), and the control and programming signals (orange lines). Connected to the outer PCB is the X-Board which contains the sequencer controlling the DePFET operation. The analog output is connected to an ADC which converts the analog signals along with timing signals from the X-board into a digital formatted data stream (blue line). The data stream is finally recorded by the acquisition PC, which is also used to program the X-board.

The hybrid, inner PCB, and the PixBoard contain filter capacitors and buffers for the various input and output signals, the outer PCB also provides a galvanic separation of the detector signals by optocouplers.

Connected to the PixBoard is the *X-Board*, which contains the pattern generator responsible for the operation of the hybrid (see section 2.10.2). Also the power supplies which provide the different voltages needed on the detector hybrid are connected to the PixBoard. PixBoard and X-Board have themselves dedicated power supplies.

DePFET matrices usually have a temperature diode processed in a corner of the chip, well outside the active area. With this diode the temperature of the detector can be monitored by measuring the voltage drop of a 100 nA forward bias current across the diode. The voltage drop changes with temperature approximately by $-2.7\,\mathrm{mV/K}$.

The PixBoard provides an output for the differential analog signal from the detector which is connected to an ADC. The ADC sits on an ADC card which is mounted onto a multi-purpose *Peripheral Component Interconnect* (PCI) card. This PCI card houses a *Field-Programmable Gate Array* (FPGA) which processes the digitized detector output signal coming from the ADC and converts it to a digital formatted data stream which is finally stored by the acquisition computer.

The computer usually also contains the control programs for programming the steering and readout chips as well as the sequencer on the X-Board.

Figure 2.35 shows a simplified schematic of the three main components of the acquisition setup: the DePFET hybrid, the X-Board and the PCI/ADC card. These will described in the next sections.

2.10.1 The detector hybrid ceramic

The detector chip and its steering and readout ASICs are mounted on a *hybrid ceramic*. These are ceramic PCBs made up of an AlO_2 carrier ceramic onto which circuits are silkscreen printed with AgPd or Au paste. Glass insulator layers are used to create multi-layer PCBs.

The hybrid ceramic serves as support for the detector chip and the readout and steering ASICs, but also provides good thermal coupling to the cooling mask due to its excellent thermal conductivity. It also distributes the different voltages and programming signals to the individual chips.

Steering, readout and detector chips are glued to the hybrid ceramic. Electrical contact between the chips and between the chips and the hybrid is established via bond wires.

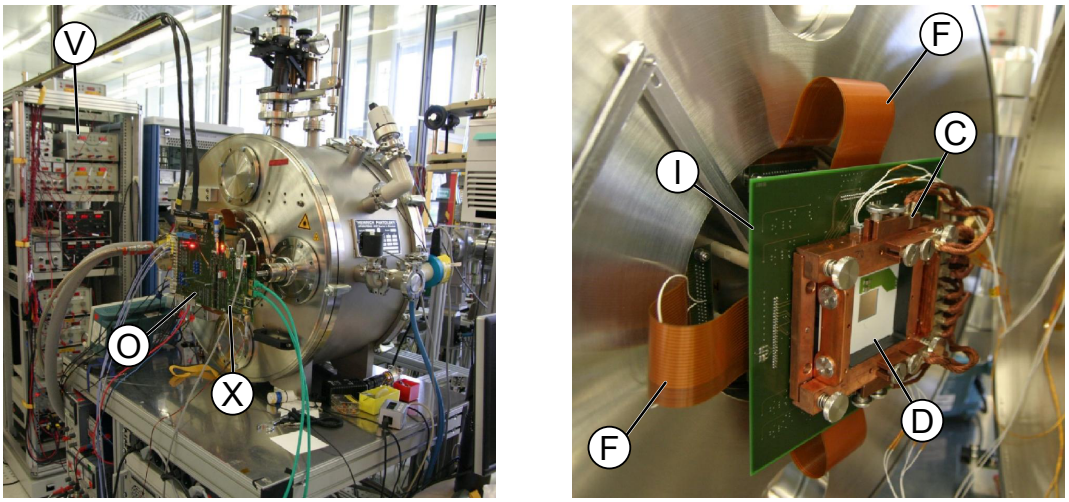

(a) (b)

Figure 2.34: (a): Picture of the vacuum tank. The voltage supplies (V) can be seen in the background. The outer PCB (O) and the X-Board (X) are attached to the tank door. (b): Picture shows the copper cooling mask (C), the inner PCB (I), and the flexleads (F) attached to the inside of the door to the vacuum tank. The detector ceramic (D) can be seen from its back side.

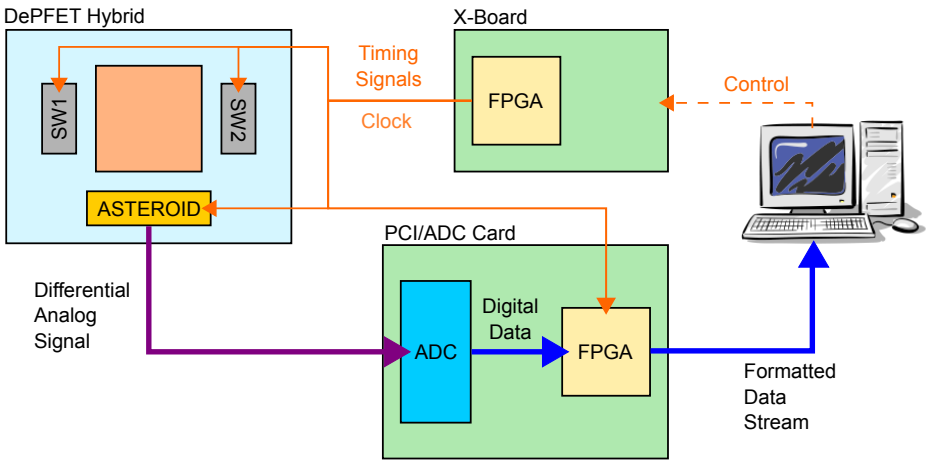

Figure 2.35: Main components of the DePFET data acquisition setup: The detector hybrid with the ASTEROID readout ASIC and the two Switcher ICs (SW1 and SW2), the PCI/ADC card, and the X-Board. The X-Board generates clocks and timing signals which steer the DePFET readout process. The ADC digitizes the analog signals coming from the ASTEROID readout. These are then combined with timing information from the X-Board and converted into a formatted data stream.

All ceramics have a central square hole over which the detector matrix is positioned, such that the detector back side is unobstructed. The fastening and

thermal contact between DePFET matrix and hybrid is established over the detector border (1 mm to 2 mm) which is sufficient for cooling.

Each DePFET matrix type has its own hybrid ceramic as there are size differences between the matrices. There is also a difference in the way the matrix is connected to the inner PCB. Figures 2.36 to 2.39 show an overview of different hybrid ceramics.

"XEUS Small" hybrid ceramics, shown in figure 2.36, have connector legs attached, which are fixed in a so-called *Zero Insertion Force* (ZIF) socket. Hybrids ceramics are brittle and ZIF sockets reduce the mechanical stress on inserting.

Hybrid ceramics designed for carrying Simbol-X matrices (see figure 2.39), as well as those for "XEUS Large" matrices (see figure 2.37), have connector pads which are pressed against a spring socket on the inner PCB. These two hybrid ceramics have the same size, but differ in electrical assignment of the individual pads.

Hybrid ceramics for the BepiColombo space mission (shown in figure 2.38) have special space-qualified plugs which are connected via flexlead to the hybrid ceramic. The flexlead is glued to the ceramic for mechanical contact, and bonded for electrical contact.

2.10.2 The X-Board

The X-Board (short for XILINX®-Board) is a multi-purpose digital interface card holding an XILINX® Spartan® II FPGA. This FPGA is used to implement a sequencer which sends timing and control signals to the single components of the acquisition setup. The sequencer runs at a working frequency of 80 MHz, which can be reduced by setting a *clock divider ratio* n, resulting in only the $(n+1)$th clock signal triggering progress.

From the working frequency ($= 80\,\mathrm{MHz}/(n+1)$) a clock signal for both, the ASTEROID pattern generator and the multiplexer, is generated. Also the pattern for the Switcher ICs is generated here, defining the states (ON or OFF) of the three DePFET steering voltages, gate, cleargate and clear (compare to section 2.9.1

The pattern generator in the latest design is now programmable itself, meaning complicated readout schemes can be implemented easily and – more important – efficiently with help of conditionals.

The X-Board also sends timing signals to the PCI/ADC card which are used there to generate the formatted data stream (see next section).

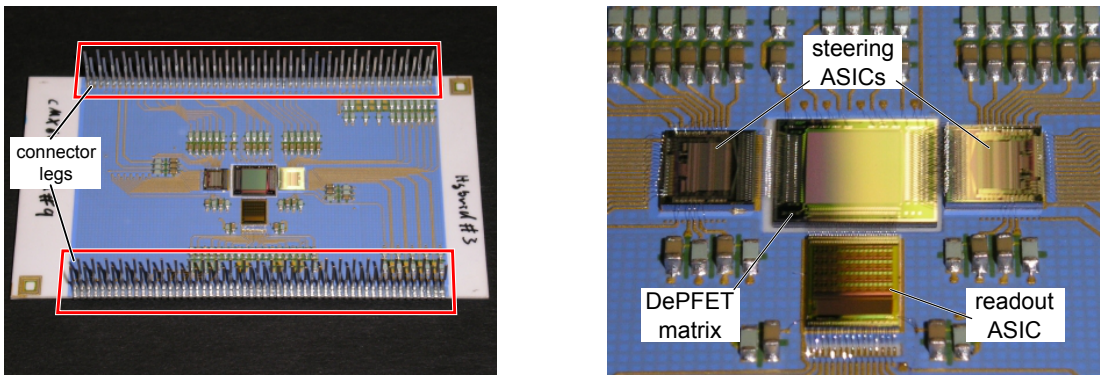

(a) hybrid ceramic **(b)** close-up view

Figure 2.36: The "XEUS Small" hybrid ceramic carries a 64×64 DePFET pixel matrix with $75 \times 75\,\mu m^2$ pixel size. Figure (a) shows the hybrid ceramic. The 102 connector legs, which are inserted into a ZIF socket, are framed in red. Figure (b) shows a close-up view. Two Switcher ICs and one readout ASIC are needed for matrix operation. Both images show the detector front side.

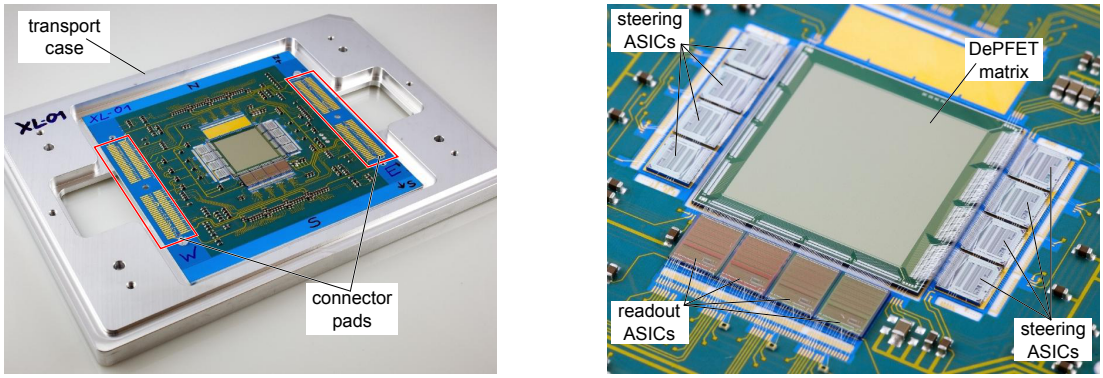

(a) hybrid ceramic **(b)** close-up view

Figure 2.37: The "XEUS Large" hybrid ceramic carries a 256×256 DePFET matrix with $75 \times 75\,\mu m^2$ pixel size. Figure (a) shows the hybrid ceramic in its transport case. In contrast to the "XEUS Small" hybrid ceramic, the "XEUS Large" hybrid ceramic has connector pads which are pressed against a spring socket on the inner layer PCB. (b): The active area of the detector is 4×4 times the one of the "XEUS Small" detector matrix. Therefore, four readout ASICs and eight Switcher ICs are needed for matrix operation. Both images show the detector front side.

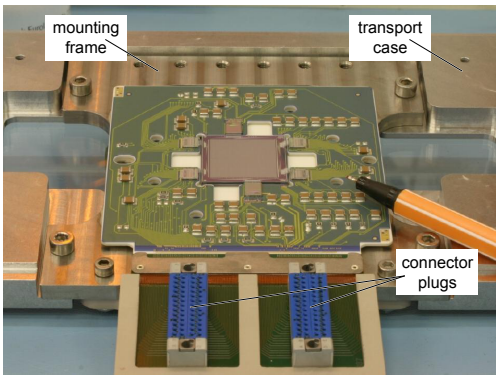

(a) hybrid ceramic

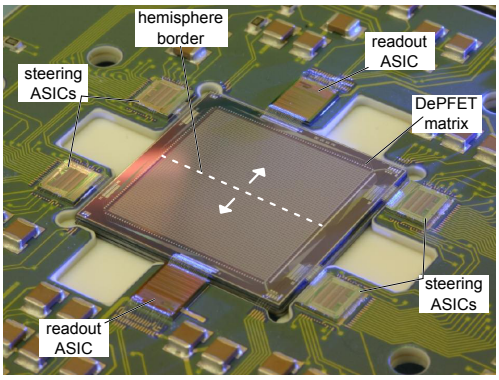

(b) close-up view

Figure 2.38: The "BepiColombo" hybrid ceramic carries a 64×64 DePFET macropixel matrix with $300 \times 300\,\mu m^2$ pixel size. Figure (a) shows the hybrid ceramic which is glued to a mounting frame. The mounting frame here is screwed to a transport case. The two connector plugs are connected to a flexlead which is glued to the ceramic for mechanical contact. Electrical contact between the flexleads and the hybrid ceramic is established via bondwires. Figure (b) shows a close-up view. The detector matrix has two hemispheres, for each two Switcher ICs and one readout ASIC are needed for operation. The hemisphere border is marked by the dashed line, the two errors show the readout direction. Both images show the detector front side.

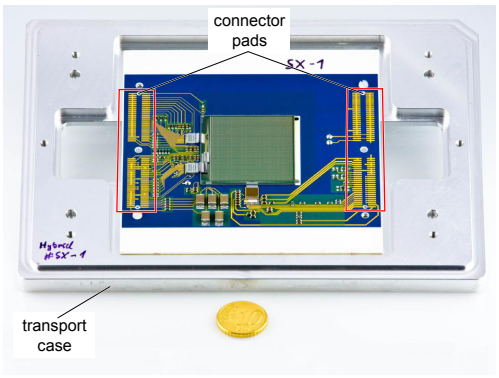

(a) hybrid ceramic

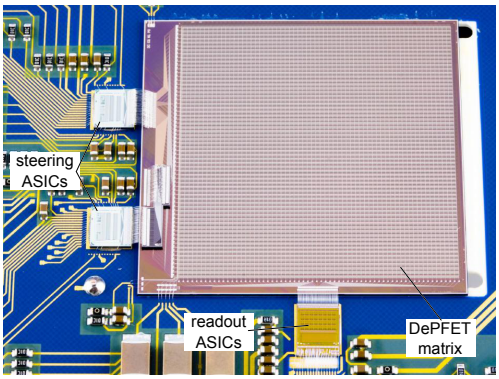

(b) close-up view

Figure 2.39: The "Simbol-X quadrant" hybrid ceramic carries a DePFET macropixel matrix with $300 \times 300\,\mu m^2$ pixel size. Figure 2.39a shows the hybrid ceramic it its transport case. The hybrid ceramic has connector pads (framed red) which are pressed against a spring socket on the inner layer PCB. The detailed view in figure 2.39b shows the two Switcher ICs and the readout ASIC needed for operation. Due to design specifications, the steering ASICs are on the same side and not on opposite sides of the matrix, as it is the case on the "XEUS Small" detector hybrid (compare to figure 2.36). Both images show the detector front side.

2.10.3 The ADC card

As mentioned above the readout chip measures the charge within the pixels of one row and multiplexes these signals to a single output. At the end of the output buffer chain there is an ADC which translates the voltage signal to *Analog-to-Digital Unit*s (ADUs).

Figure 2.40 shows a schematic of the ADC card. The ADC is mounted on an in-house developed ADC module. The module itself is piggy-backed onto a SIS1100-cCMC compact PCI card from Struck Innovative Systeme (SIS). The card also contains a FPGA which is used for processing of the digitized data. The term *ADC card* is used to refer to the union of the PCI card and the attached ADC module.

The ADC used is an AD9245 from Analog Devices which has a 14 bit width. The FPGA on the ADC card converts the values into 16 bit integers using the upper two bits tag over- and underflow values and special keywords.

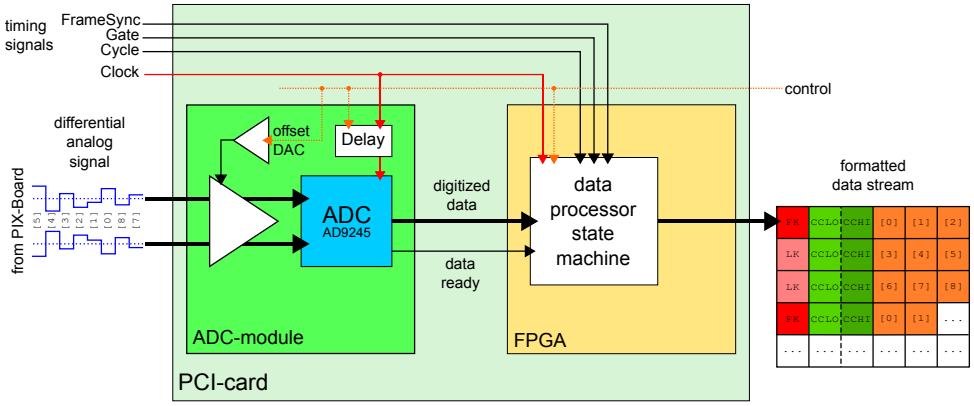

Figure 2.40: Schematic of the ADC card. The differential analog signal is constantly sampled by the ADC. When receiving a clock signal, which can be modified by a programmable delay, the sampled value is handed over to the FPGA. There, the digitized data is combined with timing information (e.g. start of a new frame, start of a line) and converted into a formatted data stream.

The ADC sampling is triggered by the internal clock of the X-Board which is fed in. This clock runs at a frequency of 80 MHz as already stated above.

With the offset *Digital-to-Analog Converter* (DAC) one can align the dynamic ranges of the readout ASIC and the ADC by adding a constant voltage value to the signals coming from the readout ASIC multiplexer.

The clock signal from the X-Board can be shifted in time with a programmable delay to synchronize sampling moment and signal settling time. The gate signal determines the point when the ADC sample is handed over to the FPGA.

Parallel to the signal the ADC card receives digital signals from the PixBoard which indicate the FPGA the beginning of a new line or frame. Together with the digitized data from the ADC this information is used to construct the formatted data stream shown on the right side of figure 2.40.

The data is written out in two-byte blocks, with *keywords* marking the beginning of a new line or the beginning of a new frame (= beginning of the first line). Along with each keyword, the current value of the *conversion counter* is written to the data stream.

The *conversion counter* is a four byte long unsigned number which is incremented by the X-Board sequencer clock. When reaching its maximum value it starts again at 0. The change of the conversion counter value from line to line (or from frame to frame) has to be regular, so the conversion counter serves as a checksum for the sanity of the data stream. Irregular values are hints for data loss or clock irregularities. The *line increment*, the increment of the conversion counter between two lines, depends on the number of fields read out and the sequence length used. The *frame increment*, the increment between two frames is the product of the line count with the line increment.

The *line data* are the individual pixel signals of a single row as they have been processed by the readout ASIC and sent to the ADC (compare to section 2.9.2). Currently, they are stored as two byte unsigned integers. More information about the formatted data stream is given in section 2.11.1.

The ADC board has a *First In, First Out* (FIFO) buffer with 200 byte length to buffer the data stream. If there is a delay in the data transfer such that the FIFO fills up, all further data is discarded. If the transfer process continues, these 200 byte are transferred first in front of the new data.

The ADC card is placed in a compact PCI rack which is connected to the acquisition PC. The formatted data stream is written to hard disk via *Direct Memory Access* (DMA) (see section 2.10.4).

The ADC card described here has two channels which can be used in parallel. When both channels are used the readings of each channel is interleaved in the data stream (see section 2.11.1 for details on this). This is applied when using DePFET matrices that are read out by two instead of one readout chip. One example is the BepiColombo matrix, which has a readout ASIC for each hemisphere.

When more readout ASICs are used, e.g. the "XEUS-Large" matrix which has 4 ASTEROID chips, several ADC-cards can be used (in this case two, one card for two readout ASICs). Currently, the data stream from each ADC card is

written to an individual file. When using more than one ADC card in the *Data Acquisition* (DAQ) setup, these files have to be merged afterwards if one wants to analyze the whole matrix at once.

2.10.4 DMA transfer

Direct Memory Access (DMA) is a feature of modern computers and microprocessors that allows certain hardware subsystems within the computer to access system memory for reading and/or writing independently of the central processing unit.

The DePFET data acquisition has two different ways for DMA transfer, sketched in figure 2.41. Both ways work with a set of buffers which are reserved in memory, to which a *producer* thread writes data and from which a *writer* thread reads and writes it on hard disk. One method is called *Scatter Gather List* (SGL) the other *Multiple Buffer Structure* (MBS).

Using the SGL, the producer writes to a buffer and sends an interrupt signal whenever it finishes a buffer. Figure 2.41a shows a schematic. Concurrently, the writer thread reads the filled buffers and writes their data to hard disk. It also sends an interrupt signal whenever a buffer is processed. A third thread, *interrupt control*, monitors the interrupt signals. If the producer thread becomes faster than the writer thread, there is the danger of data loss. In this case, an error is issued and the DMA process stops.

The SGL records the data lossless, but is unstable when encountering high data rates which reach the limit of the computer system. The transfer of data to hard disk is a bottleneck which defines the maximum data rate.

The MBS also has a producer and a writer thread, but in this case each buffer can be locked by a *mutex*. A mutex is a program object that is similar to a baton. Only the thread which has the baton has access to the buffer, the other one has to wait until the mutex is released.

This means, in MBS the producer requests the mutex for a buffer, writes data into it, releases the mutex and requests the mutex for the next buffer and so on. Similarly, the writer thread also requests the mutex for a buffer and writes its data to hard disk, releases the mutex and requests the mutex of the next buffer. If a mutex is not yet free when requested, the thread pauses until the mutex is released.

MBS is more stable, when writing to hard disk is slower than the data rate from the ADC card. But the data then contains gaps, which has to be considered when analyzing.

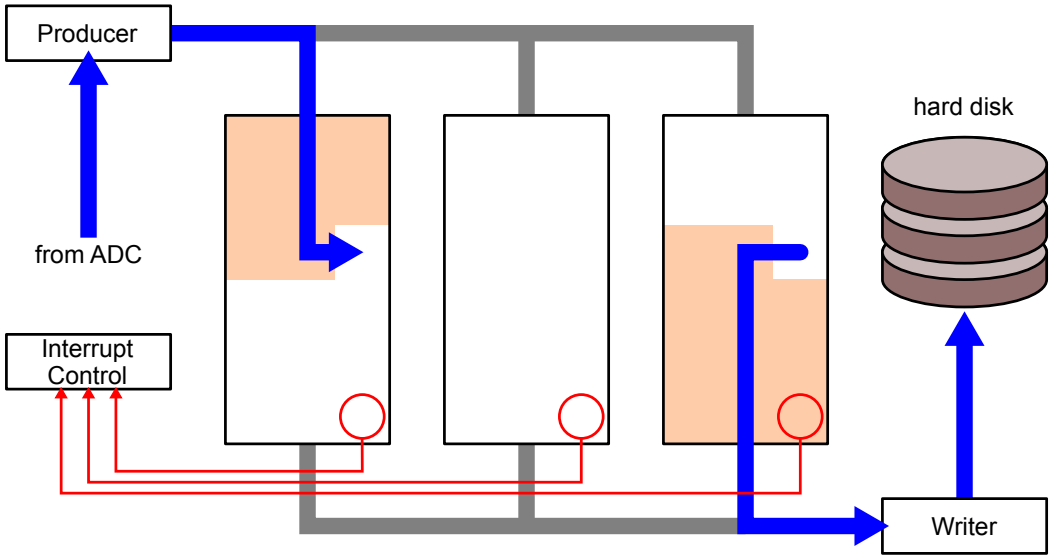

(a) SGL DMA transfer

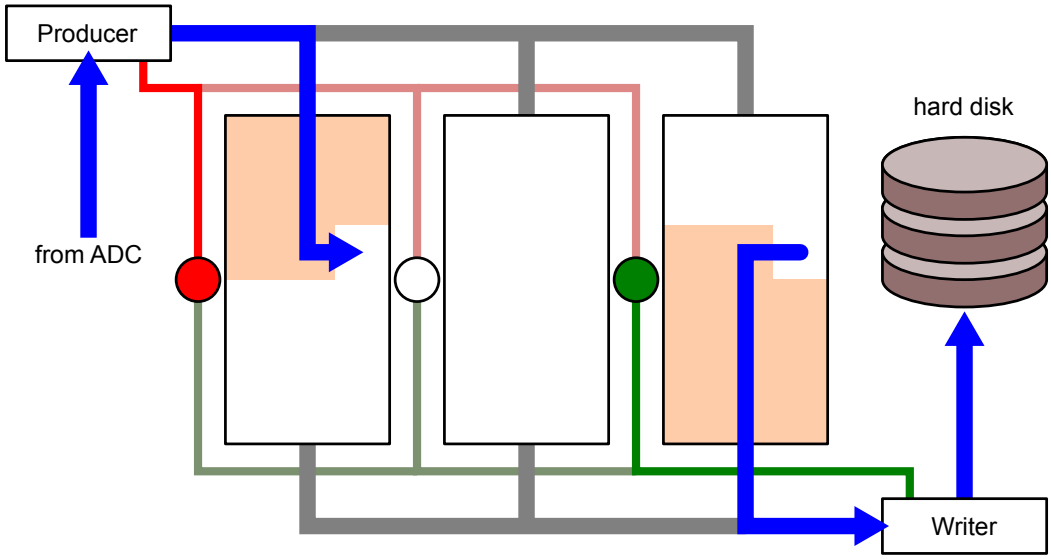

(b) MBS DMA transfer

Figure 2.41: There are two different methods of DMA transfers currently implemented in the DePFET data acquisition: SGL and MBS. Both work with a set of buffers (e.g. 3) and two threads called *producer* and *writer*. The producer writes the data coming from the ADC to the buffer, the writer writes the data from the buffer to hard disk. The buffers are needed to cover latencies of the hard disk.

2.11 File formats

There are two in-house developed data formats used with DePFET data acquisition and analysis: the *rawfile format* and the *frames file format*. The former is used to store the data coming from the ADC on hard disk, the latter is the data format used in the offline analysis. Both formats will be described briefly in the next sections.

For data analysis the framesfile format is used. Therefore the data is converted from rawfile format to framesfile format.

The data analysis software is in principle capable of processing the raw data format directly. One reason for the conversion step is that the raw data can contain incomplete frames as explained in section 2.10.4. The conversion step thus serves as a filtering step for these incomplete frames.

The other reason is that the data is sorted to correspond to a common coordinate system (see section 3.2.3) used in the analysis. In section 2.9 different readout schemes for DePFET matrices have been discussed. The order of the pixel signals in formatted data stream thus depends on the applied readout scheme, i.e. number of matrix columns, readout hemispheres, running directions of the Switcher IC. Sorting the data removes these dependencies and thus makes the analysis independent of the used DePFET chip.

2.11.1 The rawfile format

A *rawfile* contains the formatted data stream coming from the ADC board (described in section 2.10.3) directly written onto hard disk. The data from each ADC card in the setup is stored in an individual rawfile.

The *rawfile format* describes the layout of a rawfile. There are two variants, the *standard rawfile format*, in which the data of a single ADC channel is stored, and the *interleaved rawfile format*, in which the data of the two ADC channels of the ADC card is stored in a single file.

Figure 2.42 shows a schematic of a rawfile for a 4×4 pixel matrix. The rawfile format comprises the signal data, plus additional keywords and conversion counter values. Shown is the representation of a single frame in the two format variants, standard and interleaved. Each block in the data stream has a width of two bytes. The red blocks FK and LK are the frame keyword and line keyword respectively, the green blocks LO and HI are the low and high bytes of the conversion counter value. The orange blocks are the pixel signals, which are marked with the respective pixel index in figure 2.42.

Figure 2.42a shows the standard rawfile format. The data is stored line-wise, each line starts with a keyword, followed by the conversion counter and the signal values of the respective pixels. The first line starts with the frame keyword, the other lines with the line keyword.

The interleaved rawfile format is used if a matrix is divided in sectors and/or hemispheres and thus read out by two or more readout ASICs. In figure 2.42b the matrix is divided into two hemispheres, each read out by an individual readout ASIC. Both ASICs are connected to the same ADC card.

As with the standard rawfile format, the data is stored line-wise, each line starts with a keyword, which is followed by the conversion counter and the pixel signal values. Each line in the file now contains the signal values of both lines

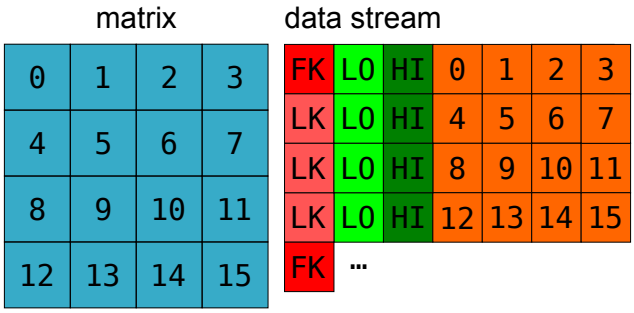

(a) standard rawfile format

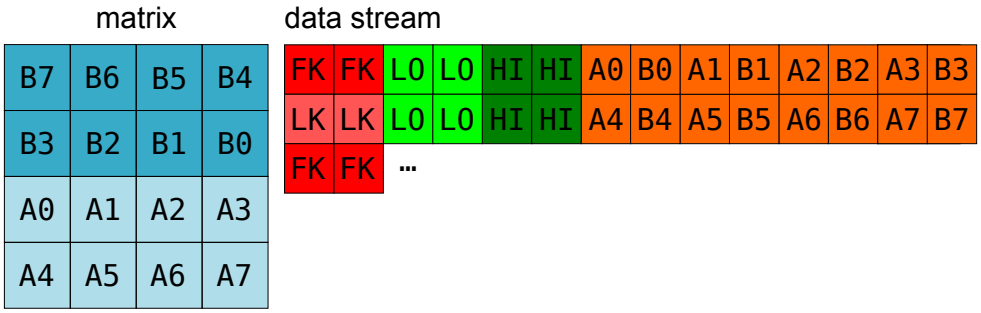

(b) interleaved rawfile format

Figure 2.42: Schematic of the rawfile format variants. Each example shows the representation of a single frame of a 4×4 matrix. The keywords are shown in red, the conversion counter values in green and the signal values in orange. The matrix to the left shows local affiliation of the pixel signal values for each variant. (a): The matrix is read out by a single readout ASIC. The data is stored line-wise, each line starts with a keyword, followed by the conversion counter and the signal values. The first line is marked with the frame keyword, the others with the line keyword. (b): The matrix is divided into two hemispheres, each with a dedicated readout ASIC. Again the data is stored line-wise, but now each line contains the signal values from both readout ASICs in alternating order.

read by the readout ASICs in alternating order. Due to implementation issues, the keywords, as well as the high and low bytes of the conversion counter appear doubled in the data stream.

2.11.2 The framesfile format

The framesfile format is also a binary file format developed and used at the HLL. There are different versions of the framesfile format.

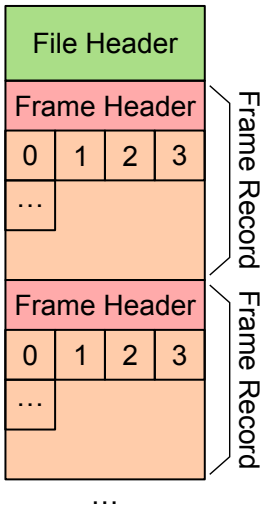

Figure 2.43: A framesfile starts with a file header, which is followed by the frame records. Each frame record comprises a frame header and the frame data of the respective frame. The headers contain additional information, like column and row count of the matrix (file header), or the frame number (frame header).

Figure 2.43 shows a schematic of the general layout of a framesfile. All framesfiles start with a file header, which is then followed by the individual frame records, each comprising a frame header and the frame data.

The individual format versions of the framesfile format differ in the layout of these headers. All framesfile formats store the signal data as an array of two byte unsigned integers.

A detailed overview of the different versions of the framesfile format can be found in section C.

2.12 Data reduction & analysis

The last stage is the data reduction and analysis. This takes place offline upon the saved data. For this purpose a data analysis software has been developed. This software was written to serve as a common platform for data analysis, not only for DePFET data at the HLL. The analysis software is explained in detail within the next chapter.

3. DePFET data analysis

To draw scientific conclusions from the recorded data it is necessary to analyze it. Among the tools of data analysis are filtering of data, calibration of values, calculation of certain figures from a data set, fitting of functions, creation of histograms.

These things can be done with commercial software, e.g. Origin®, to name a prominent example. Such software has the benefits of already providing a large set of tools for data analysis.

The drawback is that such environments only provide standard analysis, which is sometimes difficult to adapt to a specific analysis task. Also the use of non-standard input data can be cumbersome as it can require to convert it to other formats, like e.g. ASCII[1], first.

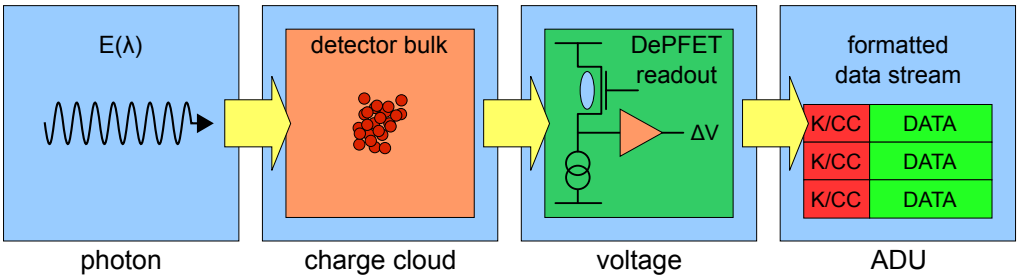

Figure 3.1: Conversion chain of a detector setup. The photon information is transformed into a data value by several in-between steps. The task of data analysis is to retrieve the original photon information from the data. To achieve this the effects of the conversion steps have to be determined and corrected – or at least to be known, so a correct interpretation of the data is possible.

The previous chapter described how a photon is converted into a data point by the detector signal. The task of data analysis is to retrieve the original photon information from the data. The detector system shown in chapter 2 represents a conversion chain which converts the photon information between different "formats" (as sketched in figure 3.1), e.g.:

- a charge cloud when absorbed in the detector,

[1] American Standard Code for Information Interchange, i.e. a normal text file

- a electrical signal when read out,
- a data point when digitized.

To retrieve the original information, the effects of the conversion steps have to be determined (preferred from the data itself) and corrected – or at least to be known, so a correct interpretation of the data is possible.

In the context of this thesis a new data analysis software framework was developed. With the intention to serve as a long term solution for data analysis at the HLL, it was designed to be modular and expandable, so it can be adapted to new tasks and thus let the user analyze unencountered problems by extending the available analysis system. Although primarily used with DePFET data, the design of the framework allows it also be used to analyze data from other detectors like p-n CCDs or SDDs.

This chapter starts with a description of the individual effects that have influence on the signals coming from the detector and thus define the shape of the resulting spectrum. Afterwards, the analysis framework developed will be described. At first at a structural level, depicting its way of working, at last algorithms developed for the analysis of DePFET pixel data are presented.

The examples shown in the following sections are mostly taken from measurements performed with the same matrix which was used for the measurements presented in chapter 4. The discussion of effects is therefore also done in the face of the results presented there.

3.1 The DePFET detector spectrum

The interaction of radiation with the detector bulk defines the basic shape of the spectrum. As shown in chapter 2, the energy of a photon is first converted into a charge cloud. This charge cloud is separated by the depletion field of the detector and guided into the internal gate of the DePFET detector where it generates a signal. This signal is amplified, first by the DePFET transistor, then by the readout electronics. The amplified signal is finally digitized and stored.

If fed into a histogram, these data represent the *raw data spectrum* of a DePFET detector. Figure 3.2 shows such a histogram taken from a measurement with a monoenergetic source.

The *raw data spectrum* shows all ADC values of all pixels of all frames. Figure 3.2 shows an example which was recorded with a DePFET macropixel detector with $500 \times 500\,\mu m^2$ pixel size. The same device was used for the measurements

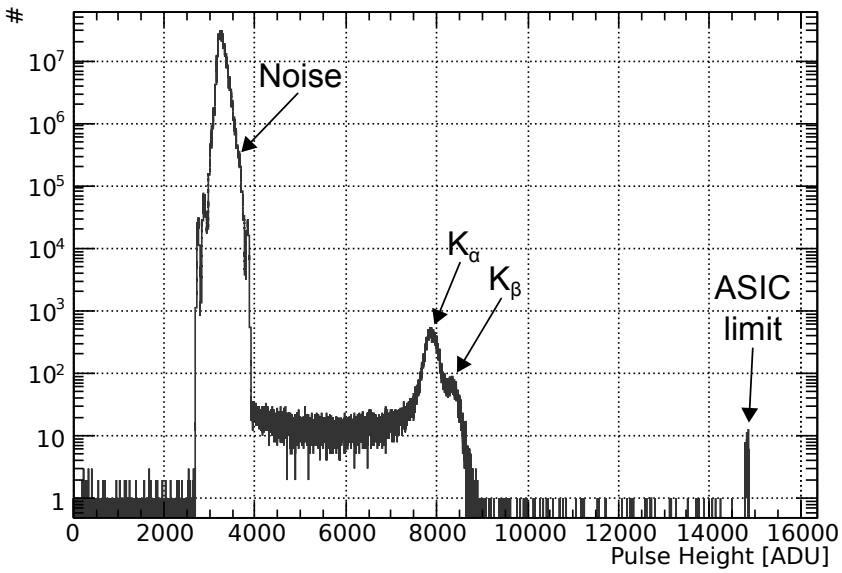

Figure 3.2: Raw data spectrum of a measurement with an ^{55}Fe source. The most prominent features are from left to right: the noise peak, which is broadened by pixel offsets. Next is the signal peak, also broadened by detector effects. The Mn-K$_\alpha$ and Mn-K$_\beta$ are almost blended into each other. The thin peak on the very right is caused by signal pulses exceeding the maximum range of the readout ASIC which accumulate here.

presented in chapter 4. The most prominent features are the noise peak and the signal peak. Both show detector effects coming from the single elements of the readout chain.

The contribution coming from the readout electronics is mainly the noise presented in the previous chapter. Other effects are possible inhomogeneities between the single channels and possible non-linearities in the gain of the amplifier.

The detector's contributions can be coarsely divided into those coming from the absorption of radiation in silicon, those coming from inhomogeneities of the pixel matrix, and those resulting from the pixelation of the detector matrix.

In the next sections different effects that contribute to the spectrum will be presented. How the spectrum can be corrected for these effects will be shown in section 3.3 where the individual algorithms of the DePFET data analysis are presented in detail.

3.1.1 Offset

In section 2.7 a single DePFET pixel and the methods of its readout were explained. Even if no photons hit the detector the internal gate is accumulating charge from the always present leakage current. Between two readouts the detector is thus integrating a constant amount charge ΔQ_{LC}, which modulates the channel current. The collected charge depends on the leakage current and the integration time.

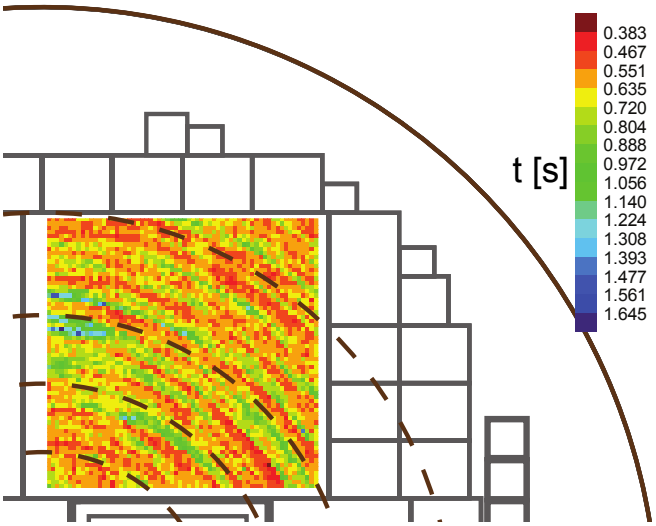

Figure 3.3: Approximate fill time of the internal gate by leakage current. The measurement was performed upon an undepleted matrix. Individual circular structures can be observed. The matrix is drawn at its position on the processing wafer, which is only partially shown. The grey areas indicate the layout regions. The brown lines are concentric rings, the outmost ring being the wafer circumference. The circular structures correspond nicely to the concentric rings [34].

The leakage current is not necessarily constant over the detector matrix. Direct measurements of DePFET matrices revealed that there are circular regions within a DePFET matrix which have different leakage current rates [34].

This can be seen in figure 3.3, which shows the approximate fill time for the internal gate of the individual pixels. The measurements were performed on a Simbol-X matrix which was contacted by a needle mask on a probe station. The matrix was not depleted, so this measurement gives only an estimate for the situation of matrix operation.

The circular regions with different fill times correspond nicely with concentric rings drawn on the wafer surface. The reasons for these rings are currently still discussed. A possible explanation are resistivity fluctuations in the wafer coming from the crystallization process.

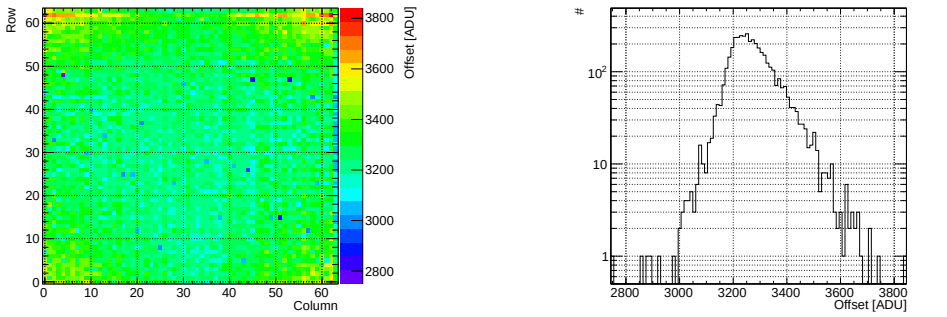

(a) Offset map **(b)** Offset map value histogram

Figure 3.4: Offset map of a DePFET matrix. The offset is defined pixel-wise by differences in the detector and ASIC layout. (a) shows the color coded pixel values, (b) a map value histogram of the offset values.

Also the modulation effect of the internal gate can differ between the individual DePFET pixel cells. This can be due to gate width variations, differences in thickness of the gate oxide, or other effects which arise from processing.

These can influence e.g. the small signal parameters g_Q and g_m (see section 2.7) of the respective pixel. It is – of course – desired and tried to keep these variations at a minimum.

In source follower readout, the difference between the samples from the pixel before and after the clear pulse is transformed into a voltage step ΔU (see section 2.23a). This *pixel offset* o_{pix} of a DePFET pixel can thus be modeled by

$$o_{\text{pix}} = \Delta U = \frac{g_Q}{g_m} \Delta Q_{\text{LC}} \tag{3.1}$$

where k is parameter that incorporates effects that are not affected by the leakage current.

As discussed above, the amount of leakage charge and the small signal parameters can vary for the respective pixel. So there is an individual pixel offset $o_{\text{pix},c,r}$ for each pixel, where c and r are the column and row coordinates respectively.

The pixel offset is amplified by the respective readout channel of the ASTEROID ASIC. As stated in section 2.9.2, the ASTEROID amplifier can be assumed linear. Each output channel has a pedestal p_c and a gain $g_{\text{amp},c}$, where c is the channel number which is identical to the column coordinate of the DePFET pixel. The pedestal is the output voltage of the amplifier, when zero input voltage is applied.

The *offset* $o_{c,r}$, the analog output voltage of the readout ASIC when no photon

signal is recorded, for a pixel is thus[2]

$$o_{c,r} = p_c + g_{\mathrm{amp},c} \cdot o_{\mathrm{pix},c,r} + A_{c,r} \,. \tag{3.2}$$

The term $A_{c,r}$ in equation 3.2 accounts for artifacts dueto the relaxation time of the pixel source voltage after the clear operation (see section 2.9.2). This is a systematic error which depends on the input capacitance (contributions of all transistors within a column) and the input resistance (inverse of transconductance of the transistor). Of course, the variances in gain and pedestal between the individual channels, which arise from the design, are kept minimal [45].

The last step of readout, the digitizing in the ADC, adds another offset to the signal. Here the signals from the readout ASIC channels, i.e. voltage levels, are converted into numbers.

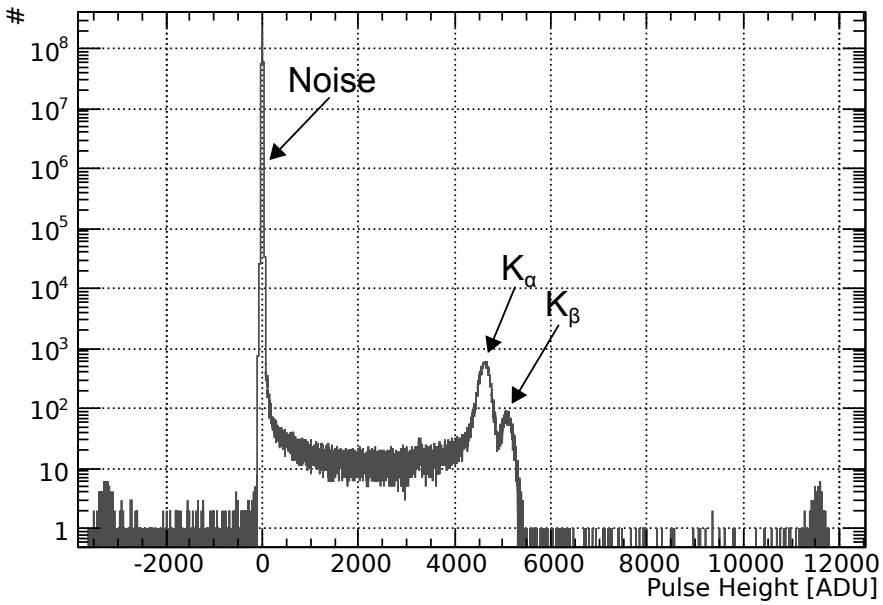

Figure 3.5: Offset corrected data spectrum. This histogram shows the same data as figure 3.2, but now the signal from each pixel has been corrected for the pixel offset. Compared to the raw data spectrum (figure 3.2) the structures in the noise peak have vanished which now shows a more Gaussian shape. Also the Mn-K$_\alpha$ and Mn-K$_\beta$ peaks from the ^{55}Fe source have become more distinguishable. The small peaks on the very left and very right are artifacts created by the offset subtraction.

[2] $o_{c,r}$ is pixel dependent, but it must not be confused with the pixel offset $o_{\mathrm{pix},c,r}$. The latter is the voltage step of an empty pixel, the former is the combined offset of pixel and readout ASIC.

The ADC has a fixed output range, usually ranging from 0 to $2^n - 1$, which then corresponds to a minimal and maximal voltage. To use the dynamic range of the ADC optimally, the signal voltage can be shifted (see section 2.10.3), such that the signals from empty pixels are not too high above the minimal ADC voltage, and the gain of the readout ASIC changed (see section 2.9.2), such that the maximum signal voltage is not too much below the maximum ADC voltage.

Figure 3.4a shows a so-called *offset map* where the offset value of each pixel is shown as a color coded value. The offset *map value histogram* in figure 3.4b shows the frequency of the values in the offset map. The structure here can also be found in the noise peak of the raw data spectrum.

By determining the offset of each pixel and subtracting it from the respective signal value on can compensate the shifts in the raw data spectrum. Figure 3.5 shows the same data as shown in figure 3.2, but now corrected for the offset. The noise peak is now clearly visible and has a Gaussian shape as expected. How the offset of a pixel is determined is shown in section 3.3.1.

3.1.2 Event discrimination

As discussed above, there is always a signal coming from the DePFET detector. If no source of radiation is present these signals are generated by the noise sources in the acquisition setup.

To discriminate between noise signals and those generated by radiation, a threshold is applied to the signals. Signal values below the threshold are discarded, a pixel signal above the threshold is called a *hit*. The threshold thus sets a lower bar for the minimal detectable energy.

Ideally, each hit is connected with an *event*, a photon absorbed in the detector bulk. The validity of this assumption also depends on the threshold value.

3.1.2.1 Noise hits

The threshold value T is usually set for each pixel as a multiple of its offset signal variance, its noise σ. The noise distribution is assumed to have Gaussian shape. The probability for a noise signal to exceed the threshold value and create a hit with energy E is given by the integral

$$P(E \geq T) = \int_T^\infty p(E)\, dE = \frac{1}{\sigma\sqrt{2\pi}} \int_T^\infty e^{-\frac{1}{2}\left(\frac{E}{\sigma}\right)^2} dE = 1 - \Phi\left(\frac{T}{\sigma}\right) \tag{3.3}$$

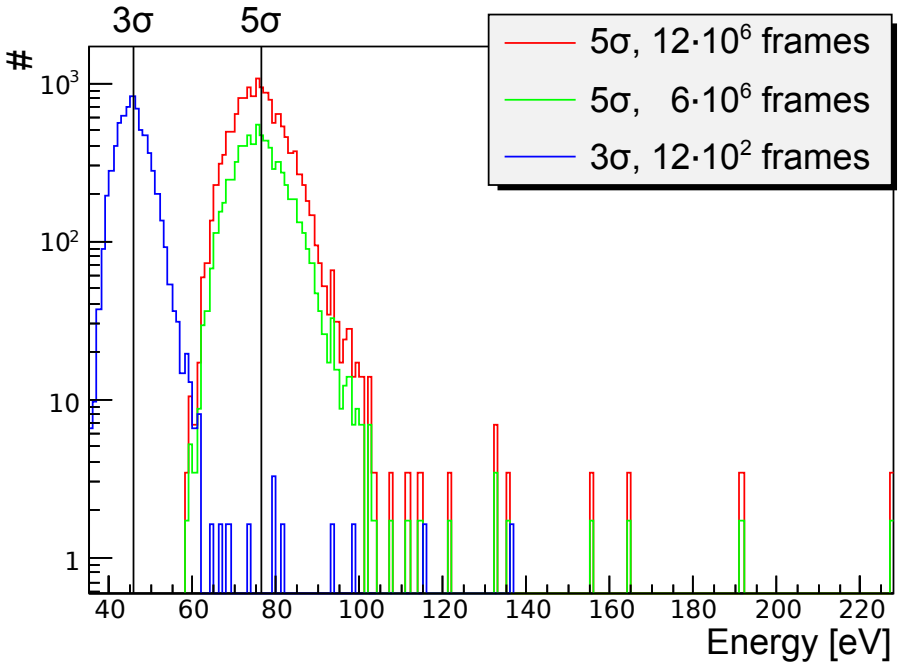

Figure 3.6: Simulated noise hit spectrum for a 64×64 pixel DePFET matrix based upon the noise distribution of a real DePFET matrix with a mean pixel noise of 15.1 eV. The mean threshold values are thus 45.3 eV for $T = 3\sigma$ and 75.5 eV for $T = 5\sigma$. Due to the variation of the pixel noise over the matrix the peak is broadened.

with Φ being the *Cumulative Distribution Function* (CDF) of the normal distribution $p(E)$

$$\Phi(x) = \frac{1}{\sqrt{2\pi}} \int_{-\infty}^{x} e^{-t^2/2}\, dt \tag{3.4}$$

For a threshold value of $T = 3\sigma$ only 0.14 % of all readouts of this pixels will result in a hit which is not connected to a photon event. A usual value for the threshold is 5σ. This reduces the probability of a noise hit P_{noise} to $2.87 \cdot 10^{-5}$ %. A noticeable number of noise hits in the spectrum is only accumulated in very long measurements with a low matrix occupancy then.

Figure 3.6 shows an estimation for noise hits in a spectrum. The mean number of noise hits was calculated for different frame numbers and threshold values. The simulation is based on a real noise distribution from a DePFET detector with a mean noise of 15.1 eV over the 64×64 pixel matrix.

The mean energy of the noise hit $\overline{E}$ which is given by

$$\overline{E} = \frac{\int_T^\infty E \cdot p(E)\, dE}{\int_T^\infty p(E)\, dE} \approx T \tag{3.5}$$

was approximated with the threshold energy T, which is in reality lower than $\overline{E}$ but close enough for this rough estimation of the noise peak.

For each pixel a Gaussian distribution was assumed with the pixel noise as its variance. From this the mean number of noise hits for this pixel was calculated and this number entered in the spectrum at the respective energy. The broadening of the peaks shown in figure 3.6 results from the dispersion of the detector noise over the matrix.

With a lower threshold, a noise peak of the same height is already achieved with a much lower number of frames. For long measurements the number noise hits can exceed the detector background create an extra peak in the spectrum (compare to figure 3.15).

3.1.2.2 Split events

The absorption of a photon within the detector bulk creates a charge cloud consisting of electron-hole pairs. Deduced from the range of electrons in matter the charge cloud has an initial size of about 0.3 µm [15].

In the depletion field the charge cloud is separated and the electrons drift towards the detector front side. During drift the electron cloud widens because of diffusion (for small electron numbers) and/or electrostatic repulsion (larger electron numbers) [30].

The electron cloud is assumed to have a Gaussian radial density. When reaching the detector front side, the electron cloud has a σ of around 10 µm [30]. If the 5σ range of the density function is taken as the diameter of the whole charge cloud, this means the charge is distributed over an area with 100 µm diameter.

The exact size of the charge cloud when reaching the internal gate depends on several parameters like the photon energy, drift time, charge carrier mobility, and others [30].

Depending on the pixel edge length and the lateral position of the charge cloud, the charge can end up in more than one pixel. DePFET pixels used for X-ray imaging spectroscopy have edge lengths from 75 µm (e.g. "XEUS-Small" DePFETs) to 500 µm (Simbol-X macropixels).

If the charge cloud diameter is smaller than twice the pixel edge length, it is valid to assume for these devices that the charge is at most split between four pixels forming a 2×2 square. This is definitely the case for the macropixel detector presented in chapter 4 which has a pixel size of $500 \times 500\,\mu m^2$.

The charge splitting between pixels is influenced by the position of the charge cloud with respect to the pixel. If a charge cloud has a maximum radius r, charge

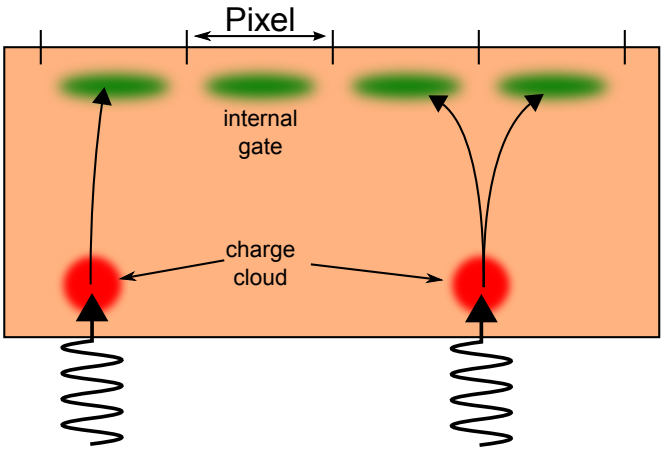

Figure 3.7: Formation of split events. A photon is absorbed in the detector bulk, creating a charge cloud which is separated in the depletion field. The electrons drift towards the detector front side where they end up in the internal gates of the matrix. Depending on the lateral impact position of the photon and the size of the generated charge cloud the electrons end up in one or more internal gates.

splitting can only occur if the center of the charge cloud is in the region less than r away from the pixel border. Charge splitting between more than two pixels is then restricted to a $r \times r$ square in the pixel corners [30].

Charge splits can be reconstructed by combining pixel hits to patterns. This is discussed in section 3.1.2.3. If the charge flowing to a neighbouring pixel is little, it will not necessarily create a signal above the event discrimination threshold. The influence of the event discrimination threshold is discussed in section 3.1.2.4.

3.1.2.3 Patterns

When hits share a common border it is likely that they have a common origin, i.e. a split event. In this case the energy information about the event is distributed over several pixels. In order to reconstruct the original information they have to be recombined. Such a combination of hits is called a *pattern*.

Patterns are named according to their multiplicity, i.e. the number of hits they comprise. The most commonly appearing patterns are *Single*s (SNGs), *Double*s (DBLs), *Triple*s (TRPs) and *Quadruple*s (QUDs).

Additionally, the patterns are divided into *valid* and *invalid* types, according to their shape. As shown in section 3.1.2.2, patterns that extend over more than 3 pixels in a dimension (this does not affect SNG and DBL patterns) are not created by real photon events if the charge cloud diameter is less than twice the pixel edge length.

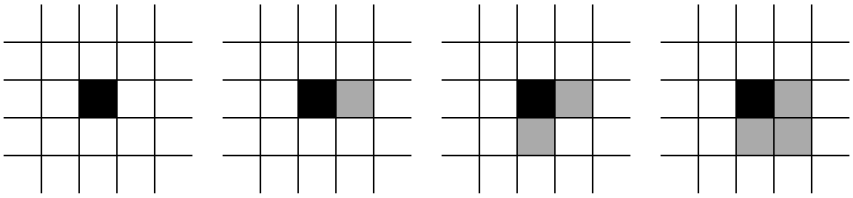

(a) Single **(b)** Double **(c)** Triple **(d)** Quadruple

Figure 3.8: Overview of valid patterns. Hits are shown in grey, the respective maximum pixel in black. Patterns are named after their multiplicity, i.e. the number of hits which make it up. Rotating a pattern around its maximum pixel creates a valid representative of the same group, except for SNG.

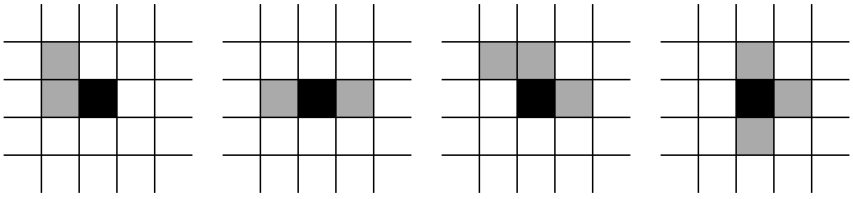

(a) Invalid TRP **(b)** Invalid TRP **(c)** Invalid QUD **(d)** Invalid QUD

Figure 3.9: Selection of invalid patterns. The pattern shown in (a) is invalid, because the maximum pixel does not share a border with each of the two other hits. The pattern in (b) does not fit into a 2×2 pixel box, as well as those depicted in (c) and (d).

The TRP and QUD patterns have therefore extra constraints to count as valid: The whole pattern must fit into a 2×2 field and the maximum pixel must share a border each with two other hits.

Figure 3.8 shows the basic valid patterns used in DePFET data analysis. The SNG pattern is the simplest one, it consists of a single hit. The other patterns have 4 different representations each, which can be obtained by rotating the shown pattern around their maximum pixel. A selection of invalid TRP and QUD patterns is shown in figure 3.9. Patterns with a multiplicity of 5 are always regarded as invalid.

The combination of hits to patterns is carried out in the data analysis during the event filtering procedure which is explained in section 3.3.2.

Figure 3.10 shows a pattern statistic for the DePFET macropixel detector which was used in the measurements presented in chapter 4 which has a pixel size of $500 \times 500\,\mu m^2$. This large area compared to the diameter of the charge cloud

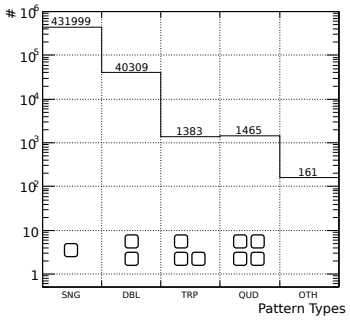

Figure 3.10: Pattern statistic for a DePFET macropixel detector. The measurement was made with an ^{55}Fe source. Due to the large pixel size of $500 \times 500\,\mu m^2$ most of the photon events result in SNG patterns. These are followed by DBL patterns, while TRP and QUD patterns occur only marginally. The column OTH comprises all invalid pattern types.

which is around 100 µm (compare to section 3.1.2.2) results in a high probability for the charge to be collected in a single pixel. As expected, most patterns are SNG patterns, followed by DBL patterns. TRP and QUD patterns are the rarest. *Other* (OTH) patterns comprise invalid patterns like those shown in figure 3.9. The resulting spectrum of this measurement is shown in figure 3.12 in section 3.1.2.4.

3.1.2.4 Threshold effects

Combining hits to patterns reconstructs the original signal of the event in case of charge splitting. Ideally, the mean pixel signal corresponds to the mean charge deposited. However, to count as a hit the pixel signal has to be above the event discrimination threshold. This "selection" distorts the connection between signal and detected charge, especially if the signal – or its charge equivalent – is close to the threshold.

The charge deposited in a pixel is assumed to be Gaussian distributed around the mean value q_0 with the detector noise σ as its variance. The respective probability distribution function $p(q, q_0)$ is therefore

$$p(q, q_0) = \frac{1}{\sigma\sqrt{2\pi}} e^{-\frac{1}{2}\left(\frac{q-q_0}{\sigma}\right)^2}. \tag{3.6}$$

To count as a hit, the signal produced by the charge in the internal gate has to be above the event discrimination threshold T which corresponds to a threshold charge q_T. The mean charge $\overline{q}$ detected if q_0 is deposited in a pixel is therefore

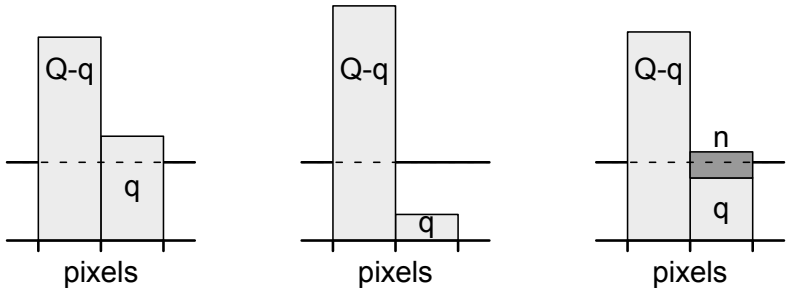

(a) DBL pattern **(b)** pseudo-SNG **(c)** noise-DBL

Figure 3.11: Threshold effects on patterns shown exemplarily for a charge split between two pixels. (a): If both signals are well above the threshold the result is a DBL pattern where the signal sum of the major $(Q-q)$ and minor (q) part represents the original charge Q deposited. (b): If the minor part is below the threshold, the charge split produces a pseudo-SNG pattern. Compared to the case where the whole charge is deposited within a single pixel, the signal here is reduced by the minor portion of the charge split, hence smaller. Such a pseudo-SNG pattern is also produced, if q is above the threshold but pixel noise "pushes" it below the threshold. (c): If a pixel signal is close to the event discrimination threshold, the pixel noise affects the final pattern. Although the signal produced by q is below the threshold, additional noise (n) creates a signal above it. The sum of both pixel signals $((Q-q)+(q+n)=Q+n)$ is larger than the signal representing the original charge Q deposited.

given by [50]

$$\overline{q}(q_0) = \frac{\int_{q_T}^{\infty} q \cdot p(q,q_0)\,dq}{\int_{q_T}^{\infty} p(q,q_0)\,dq} = q_0 + \frac{\sigma}{\sqrt{2\pi}} \cdot \frac{e^{-\frac{1}{2}\left(\frac{q_T-q_0}{\sigma}\right)^2}}{1-\Phi\left(\frac{q_T-q_0}{\sigma}\right)} \tag{3.7}$$

with Φ being the CDF of the normal distribution (see equation 3.4).

For large signals $(Q \gg q_T)$ the event discrimination threshold has no influence on the mean detected charge, thus $\overline{q}(Q) \approx Q$. The mean signal represents the full deposited charge.

However for signals close or below the threshold, there is a deviation from the ideal linear case. This is because for small charges close to the threshold charge the pixel noise strongly influences whether the signal is above or below the discrimination threshold.

If a charge (including the noise contribution) is below the threshold, it is not detected. If it is part of a charge split it means that the remaining signals represent a smaller charge than actually deposited (see figure 3.11b).

If e.g. the charge Q is split between two pixels and the signal of the minor

portion (q) is discarded, the remaining hit signal represents the major charge portion ($Q-q$). The resulting pattern is then a SNG pattern although the charge was split upon two pixels. This *sub-threshold charge loss* produces here a *pseudo*-SNG patterns which have a lower signal than "real" SNG patterns, thus shifting the average SNG signal to lower values.

The detector noise has influence on the mean detected charge, especially if the deposited charge q is close to the threshold charge q_T. If such a hit signal is part of a pattern also the overall signal is affected. On the one hand the noise can "push" signals below the threshold producing pseudo-patterns as shown above. On the other hand the noise can add extra "charge", lifting an otherwise discarded signal over the threshold (see figure 3.11c). Due to this effect the mean detected charge is higher than the deposited charge.

Assuming again a charge split between two pixels as above, but now both hits are above the threshold. The mean detected charge for both portions ($(Q-q)$ and q) is given by equation 3.7. If the minor portion q is close to the threshold charge q_T, the mean charge sum $\overline{Q}_{\mathrm{dbl}}$ for this case is

$$\overline{Q}_{\mathrm{dbl}} = \overline{q}(Q-q) + \overline{q}(q) \approx Q + \frac{\sigma}{\sqrt{2\pi}} \cdot \frac{e^{-\frac{1}{2}\left(\frac{q_T-q}{\sigma}\right)^2}}{1-\Phi\left(\frac{q_T-q}{\sigma}\right)} \geq Q \tag{3.8}$$

utilizing the fact that equation 3.7 is linear for $Q-q \gg q_T$. Such *noise*-DBL patterns have a larger signal than expected for the original charge. They thus cause a peak shift of the average signal of DBL patterns to higher signals.

Figure 3.12 shows the non-calibrated spectra for an ^{55}Fe measurement. The measurement was made with the $500 \times 500\,\mu\mathrm{m}^2$ macropixel detector which was also used for the measurements presented in chapter 4. The event discrimination threshold for this device was set to 5σ. One can see that SNG patterns are the predominant pattern type for this macropixel matrix.

The peak positions of the Mn-K$_\alpha$ for SNG and DBL patterns do not differ much (less than 2 ADU), so the influence of pseudo-SNG and noise-DBL patterns is not very prominent for this measurement. Apparently, the pseudo-SNG patterns are compensated by the large amount of true SNG patterns from the central area of the pixel.

The deviation of noise-DBL signals also depends on the chosen event discrimination threshold (see equation 3.8). A higher threshold decreases the probability and thus the impact for noise-DBL patterns on the spectrum, but it increases the sub-threshold charge loss.

For DBL patterns the influence of noise is also only relevant for charge splits

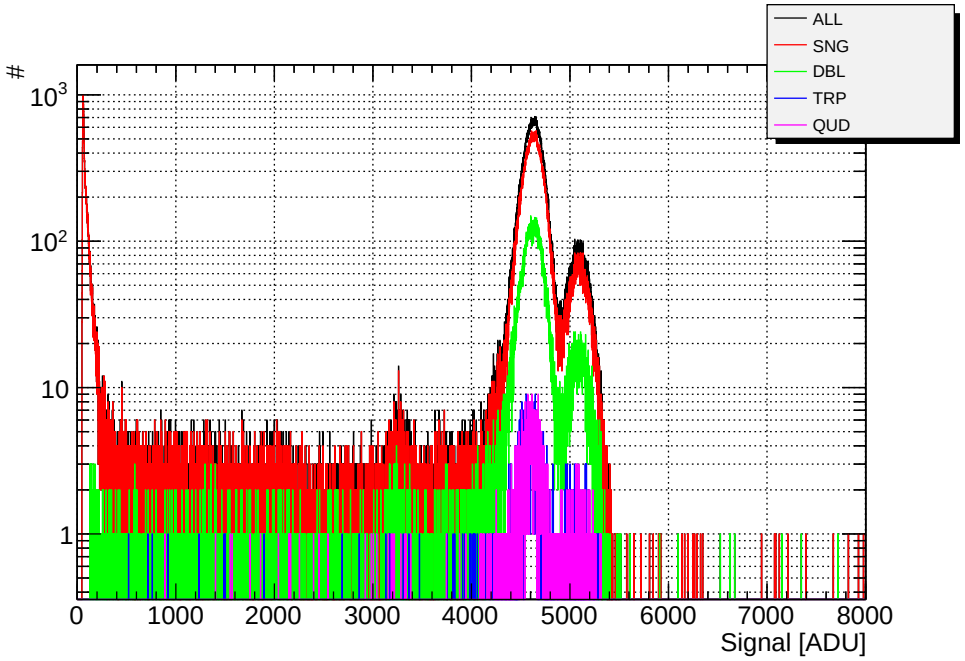

Figure 3.12: Non-calibrated spectra for valid SNG, DBL, TRP, and QUD patterns, and their combined spectrum (ALL). The spectra show a measurement of an ^{55}Fe source with a DePFET macropixel detector with $500 \times 500\,\mu m^2$ pixel size. The K_α and K_β peak can be seen around 5000 ADU, as well as the Si-escape peak around 3100 ADU. The reason for the peak at 0 ADU in the spectrum for SNG patterns is not yet fully resolved.

with a charge portion close to the threshold charge. For larger photon energies there is also a share of charge splits in which the charge portions are both far enough above the threshold so there is no influence of noise. These charge splits compensate the distorted signals from noise-DBL patterns in the spectrum.

The effect of noise-DBL patterns is therefore expected to be higher for lower photon energies, at which most of the detected split patterns have a signal corresponding to a charge close to the threshold charge. For the matrix presented in chapter 4, this would be the range approximately below 500 eV. However, in this energy range the charge collection is also strongly affected by influences from the entrance window (see section 3.1.4), the peak shift due to threshold effects was therefore neglected.

Especially for pixel sizes which are in the same range as the charge cloud size (compare to section 3.1.2.2) the sub-threshold charge loss is expected to be more dominant, because the area where the charge cloud is completely contained within a pixel is smaller for those pixel sizes. For such pixel sizes the peak shift for SNG patterns would also affect the calibration of the detector which is based

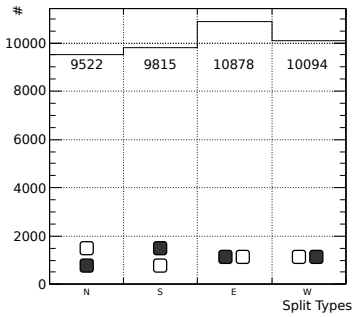

Figure 3.13: Distribution of DBL-pattern types. The pictogram in each column shows the location of the major (filled square) and minor (empty square) portion of the charge split. The east-DBL patterns notably stick out. This surplus can be attributed to multiplexer crosstalk. The deviations between the vertical DBL types (north- and south-DBL patterns) are still subject of investigations.

upon the assumption that the signal from SNG patterns represents the full charge deposited by the photon from the calibration source [51].

3.1.2.5 Multiplexer crosstalk

Figure 3.13 shows the distribution of the different DBL-pattern types. The pattern types are named according to the position of the minor signal with respect to the major signal. For the naming of the patterns the ROAn coordinate system is applied (see section 3.2.3).

Ideally all four DBL patterns should occur with the same frequency. However, in figure 3.13 there is a deviation between the individual types. There is also a difference between the average number of vertical (north- and south-DBL patterns) and horizontal (east- and west-DBL patterns) DBL patterns.

The effects behind these fluctuations is not yet fully understood and subject of investigations. The surplus of east-DBL patterns can be qualitatively explained by crosstalk in the multiplexer of the readout ASIC. Figure 3.14 shows an illustration of the situation.

The display style in figure 3.14 was chosen to match the display at the oscilloscope (compare to figure 2.30, on which the DePFET pixel signals show up as negative voltage steps. The pixels of a row are multiplexed out by the ASIC from west to east, which is indicated by the rising indexes from left to right on top of the respective pictures.

The ASTEROID readout ASIC was described in section 2.9.2. When a matrix row is read out, the results of each pixel are stored in the S/H of the respective

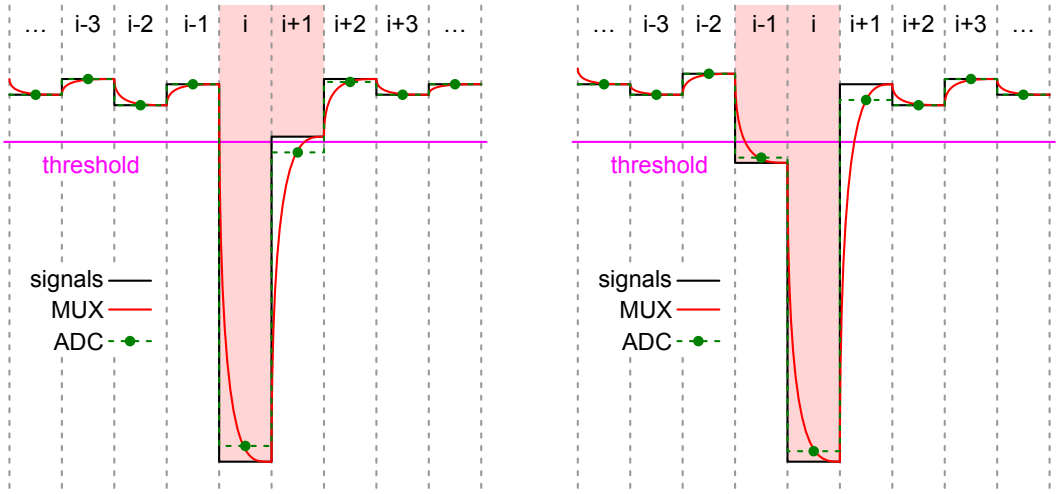

(a) east-DBL pattern **(b)** west-DBL pattern

Figure 3.14: Multiplexer crosstalk effect on horizontal DBL patterns. The illustration shows only a qualitative picture. Three components are shown: The signal value (black line), as it is stored in the S/H of the respective channel of the ASTEROID readout ASIC, the signal of the output buffer (red line), which is affected by rise time, and the samplings of the ADC (green dots), which happen at fixed points in time. Due to the rise time of the signal, there is an influence of a signal on its successor. (a): For an east-DBL pattern this increases the chance for the minor signal portion to be lifted over the event discrimination threshold. (b): A west-DBL pattern is less affected, because of the smaller rise time effect on the smaller portion of the split pattern.

channel. In figure 3.14 these values are shown as black lines. The pixel signals are then multiplexed to a single output buffer. This adopts the single values for a certain period in which they are sampled by the ADC.

The signal of the output buffer needs a certain time to reach the applied signal level of the S/H. Multiplexer crosstalk is an influence between the signals via the rise time of the output buffer. The value of the output buffer is shown as red line in figure 3.14 (the effect of the rise time has been exaggerated for better visibility).

The output buffer value is finally sampled by the ADC. Depending on the influence of the rise time, the signal value sampled by the ADC and the original pixel signal differ. In simple terms, a low signal pulls the following high signal down, a high signal drags the following low signal up.

An east-DBL pattern is defined as having the lower pattern signal east of the pattern's maximum signal, i.e. the lower signal is multiplexed out *after* the maximum signal. The west-DBL pattern is defined analogous as having the lower pattern signal west of the maximum, i.e. the lower signal is multiplexed out *before*

the maximum. The signals belonging to the DBL patterns are shown as filled areas in figure 3.14a and figure 3.14b.

So an east-DBL pattern with a minor signal close to the event discrimination threshold profits from the crosstalk of the major signal which is multiplexed out before, while for west-DBL patterns this is not the case. This way more east-DBL patterns than west-DBL patterns are detected when the event discrimination threshold is applied (see section 3.3.2).

3.1.2.6 Pile-up

Pile-up occurs when photons hit the detector in close proximity between two detector readouts. In that case their split charges can meet or overlap such that their hits form a pattern together. As a pattern is usually associated to a single photon event, this results in a wrong energy measurement.

Pile-up can be detected and filtered out, if an invalid pattern (compare to figure 3.9) is created by the individual patterns. If the photons hit the detector in a manner that a valid pattern is formed, the pile-up can be detected when using a monoenergetic source. Here, such a pile-up can be seen as an additional peak in the spectrum at higher energies, e.g. at twice the original energy if two photons coincided.

In the case of multi-line measurements, pile up can create additional peaks which can overlap or coincide with existing peaks in the spectrum. Here, pile-up models [52, 50] have to be applied to correct for these effects.

3.1.3 Amplification

The energy of the photon absorbed in the detector bulk is converted several times until it is finally stored as an *Analog-to-Digital Unit* (ADU) value. This includes transformation between different information carriers (charge cloud, current modulation, voltage step) as well as amplification.

On closer analysis of the readout chain, the conversion of the photon energy can be split up into two steps:

- Amplification in the DePFET and
- amplification in the readout ASIC

which can be treated independently. Moreover, the signals from pixels of a matrix column are subject to the same amplification. To calibrate the detector means to establish a connection between the signal $s_{c,r}$ coming from a pixel in column c

and row r, with the photon's energy E which deposited the corresponding charge into this pixel's internal gate.

$$s_{c,r}(E) = f_{\text{amp},c}(f_{\text{pix},c,r}(E)) \tag{3.9}$$

Here, $f_{\text{pix},c,r}$ is a function describing the transformation of the photon energy into a channel modulation in the DePFET pixel, and f_{amp} is a function describing the transformation of this channel modulation into the recorded signal s in the readout ASIC.

A usual approach to reconstruct the energy of the photon from the signal value is to illuminate the detector with a source of known energy E_{clb}. Together with the noise peak ($E = 0$) one has two measurements with known energies:

$$\begin{aligned} s_{c,r}(0) &= f_{\text{amp},c}(f_{\text{pix},c,r}(0)) = o_{c,r} \\ s_{c,r}(E_{\text{clb}}) &= f_{\text{amp},c}(f_{\text{pix},c,r}(E_{\text{clb}})) \end{aligned} \tag{3.10}$$

where $o_{c,r}$ is the offset of the pixel $[c, r]$ as introduced in equation 3.2.

The offset correction subtracts $o_{c,r}$ from $s_{c,r}$ resulting in the offset corrected signal value $s'_{c,r}$ and transforms equation 3.10 into

$$\begin{aligned} s'_{c,r}(0) &= f_{\text{amp},c}(f_{\text{pix},c,r}(0)) - o_{c,r} = 0 \\ s'_{c,r}(E_{\text{clb}}) &= f_{\text{amp},c}(f_{\text{pix},c,r}(E_{\text{clb}})) - o_{c,r} \end{aligned} \tag{3.11}$$

This leaves the question how the functions f_{amp} and f_{pix} behave at values aside these two fixed points.

Ideally, both functions are assumed to be linear: $f = g \cdot E + t$, where g is the slope and t the y-intercept of the amplifier-functions for amplifier channel and DePFET pixel respectively.

For the ASTEROID, slope and y-intercept correspond to the channel gain $g_{\text{amp},c}$ which can be derived from equation 2.48, and the channel pedestal p_c as defined in section 3.1.1. For the DePFET pixel, the slope is the gain $g_{\text{pix},c,r}$, which can be derived from equation 2.40, and the y-intercept is the pixel offset from equation 3.1.

Thus equation 3.9 transforms into

$$\begin{aligned} s_{c,r}(E) &= g_{\mathrm{amp},c} \cdot (g_{\mathrm{pix},c,r} \cdot E + o_{\mathrm{pix},c,r}) + p_c \\ &= g_{\mathrm{amp},c} \cdot g_{\mathrm{pix},c,r} \cdot E + (g_{\mathrm{amp},c} \cdot o_{\mathrm{pix},c,r} + p_c) \\ &= g_{\mathrm{amp},c} \cdot g_{\mathrm{pix},c,r} \cdot E + o_{c,r} \\ &= g_{c,r} \cdot E + o_{c,r} \end{aligned} \tag{3.12}$$

where $g_{c,r}$ is the combined gain of readout ASIC channel and DePFET pixel and $o_{c,r}$ the already known offset.

Inserting equation 3.12 into the equation system 3.11 delivers

$$\begin{aligned} s'_{c,r}(0) &= 0 \\ s'_{c,r}(E_{\mathrm{clb}}) &= g_{c,r} \cdot E_{\mathrm{clb}} \end{aligned} \tag{3.13}$$

which can be resolved to E, delivering the measured photon energy E against pixel signal $s_{c,r}$

$$E(s_{c,r}) = \frac{1}{g_{c,r}} \cdot s'_{c,r} = \frac{1}{g_{c,r}} \cdot (s_{c,r} - o_{c,r}) \tag{3.14}$$

The ASTEROID readout ASIC has been shown to be linear within 0.4 % over a dynamic range of 800 mV which corresponds to 18 keV [45]. The linearity of the DePFET has to be determined, e.g. by monoenergetic measurements at different energies, as shown in chapter 4.

As each DePFET pixel is a transistor with its own amplification properties it is clear that each pixel in a DePFET matrix has to be calibrated individually. A method to determine the gain is shown in section 3.3.3

3.1.4 Detector response function

Until now it was assumed that the absorption of a photon in the detector bulk leads to the same signal for photons with the same energy. Only the variance of the signal due to Fano and electronics noise was considered which leads to a Gaussian broadening of the detector response. This view does not take into account any effects that lead to charge loss. Especially if a photon is absorbed close to the surface or in the entrance window, the energy can only be detected partially. These effects are modeled by a detector response function.

In a DePFET detector radiation enters at the back side which consists of a homogeneous back contact with an optional entrance window processed upon it. DePFET detectors for space missions produced at the HLL typically have a thick-

ness of 450 µm. The transmission of photons with energies from 0 keV to 10 keV for this thickness is below 10 %. So for energies within that range absorption at a depth where the pixel structure of the matrix has no influence can be assumed. The effects forming the signal spectrum can thus be described globally by a detector response curve.

There are several models to calculate detector response curves. Among these are empirical functions, Monte-Carlo simulations and analytical approaches.

Empirical functions Empirical functions like the HYPERMET function [53] are easy to fit to the measured spectra. They consist of simple constituents like Gaussian peaks or error functions which are combined to trace the shape of the spectrum. The disadvantage of empirical functions is the difficulty to assign physical meaning to their parameters.

Monte-Carlo simulations As the absorption and electron cloud creation in the detector bulk is a statistical process it seems that they are best modeled by Monte-Carlo simulations. Their disadvantage is that they often require long calculation times depending on their level of detail and fitting them to measured spectra is thus a cumbersome task. Monte-Carlo models for SDDs have been developed in [54] and [15].

Analytical functions Analytical functions use approximations to account for the statistical effects. These approximations often turn out to be sufficient to achieve a good agreement with the measurement data. Different models have been developed by authors, for example for Si(Li) detectors with a gold contact [55] or for p-n CCDs with an aluminum entrance window and a silicon oxide layer [50]. Opposite to empirical functions only physical parameters are used.

3.1.4.1 The detector model

Within the scope of this thesis a simple detector model has been developed which is applied later to measurements presented in chapter 4. It is based on the model by M. Popp [50], which was developed for p-n CCDs and which is itself an analytical version of the model developed by P. Lechner [15].

The model describes the charge collection in the detector bulk and influences of the entrance window but does not recognize influences of the detector pixels (split events, threshold effects) or the readout electronics (apart from the detector noise).

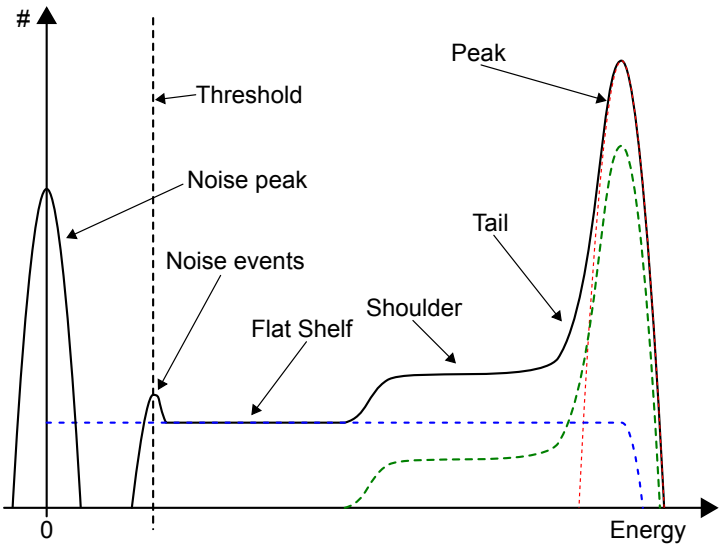

Figure 3.15: Features of a DePFET spectrum. It comprises the peak along with tail and shoulder and a flat shelf. Tail and shoulder are attributed to incomplete charge collection in depth, while the flat shelf is ascribed to electrons being lost to or injected from the entrance window. If the measurement is long enough, there is a chance to collect a significant number of noise events. The threshold shown here is the average threshold for the whole detector matrix. Because each pixel as an individual threshold depending on its noise, the spectrum shows a broadening around the average threshold value. The noise peak (drawn scaled) is normally not visible.

Figure 3.15 shows schematic of a typical spectrum. The main components are shown as dashed lines. These are the main peak, along with a tail and shoulder, and the flat shelf. Tail and shoulder are ascribed to incomplete charge collection in the detector. The flat shelf represents a more or less homogeneous background which is attributed to the loss of primary electrons to the entrance window and injection of primary electrons from the entrance window.

Not shown in figure 3.15 is the escape peak which is created when a fluorescence photon is emitted after the absorbed photon has transferred its energy onto an electron from the inner shell. There is a chance for this photon to escape from the detector before being absorbed again. In this case the energy deposited in the detector is the original photon energy minus the energy of the fluorescence photon.

The fluorescence photon energy is fixed, for silicon the most prominent line is Si-K_α which has an energy of 1740 eV. These events thus create a secondary peak which is shifted to lower energies by the fluorescence photon energy (the *escape peak*, see section 3.1.4.4).

Figure 3.16 shows a model of an infinitely thick silicon detector that is used

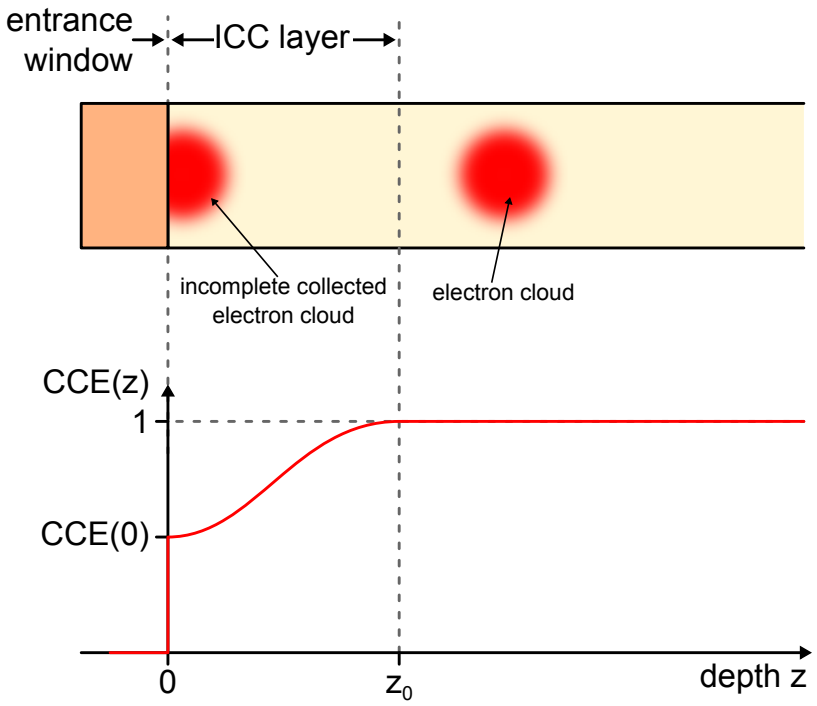

Figure 3.16: Detector model used for calculating the response function. The detector consists of an infinitely thick volume of silicon which is covered by an entrance window (e.g. aluminum). Close to the entrance window the charge cloud is only partially collected, deep in the detector volume the charge collection efficiency reaches 1. Below the model, the CCE function is shown.

in calculating the shape of the detector response curve. The detector volume is covered by the entrance window. The origin of the used coordinate system is put at the interface between entrance window and detector bulk. Places in the entrance window have thus a negative depth coordinate z.

Directly below the entrance window, a region $0 \leq z \leq z_0$ where the generated charge is not totally collected is assumed. This is referred to as the *Incomplete Charge Collection* (ICC) layer. Within the ICC layer the *Charge Collection Efficiency* (CCE) rises monotonously from its initial value CCE(0) at the interface to unity at $z = z_0$. The CCE within the entrance window is assumed to be zero. For photons absorbed below z_0 the charge loss leads to a signal pulse of reduced height which causes the peak in the spectrum to be shifted to lower energies.

The CCE is merely an approximation of the photon absorption process as it does not take into account the diffusion of electrons, their kinetic energies or the extent of the charge cloud. The idea behind the CCE is that of an effective function which describes the mean behavior during charge collection [55].

3.1.4.2 The shape of the peak

From the CCE function the shape of the peak with shoulder and tail can be derived. Details can be found in literature [50].

The spectrum $P(E, E_0)$, i.e. the number of counts dN per channel dE is connected to the CCE by

$$P(E, E_0) = \frac{dN(E, E_0)}{dE} = \frac{dN}{dz} \cdot \frac{dz}{dE} \tag{3.15}$$

where the left part of the product is the probability for absorption as defined by the Beer-Lambert law and the right part is the derivative of the inverse of CCE(z) with respect to E.

$$P(E, E_0) = \frac{dN}{dz} \cdot \frac{d}{dE}\mathrm{CCE}^{-1}(E) \tag{3.16}$$

The charge collection efficiency with respect to depth z is described close to the surface by a polynomial expression, in depth by an exponential function:

$$\mathrm{CCE}(z) = \begin{cases} 0 & z < 0 \\ S + B\left(\frac{z}{l}\right)^c & 0 < z < l \\ 1 - A\, e^{-\frac{z-l}{\tau}} & l < z < D \end{cases} \tag{3.17}$$

At $z = 0$ the CCE has a value of $\mathrm{CCE}(0) = S$ and rises to 1 in depth. D is the detector thickness. The two parameters A and B can be determined from the constraints of steadiness and differentiability of CCE(z) at the junction point $z = l$.

$$\begin{aligned} A &= (1 - S) \cdot \left(\frac{\tau c}{l + \tau c}\right) \\ B &= (1 - S) \cdot \left(1 - \frac{\tau c}{l + \tau c}\right) \end{aligned} \tag{3.18}$$

This leaves four parameters which describe the CCE.

- S, the minimal fraction of the charge which is detected, if a photon is absorbed in the detector. S can take values from 0 to 1
- c, describes the curvature in the region $0 \leq z \leq l$
- l, the width of the transition region.
- τ, rise constant of the exponential function.

The signal E as a function of the depth z is given by

$$E(z) = E_0 \mathrm{CCE}(z) \tag{3.19}$$

with E_0 being the photon energy. From there

$$\mathrm{CCE}(z) = \frac{E}{E_0} \Rightarrow z = \mathrm{CCE}^{-1}(\frac{E}{E_0}) \tag{3.20}$$

can be derived. Combining equation 3.16 and equation 3.20 delivers [50]

$$\frac{dN}{dE} = \begin{cases} \frac{N_0 \alpha l}{c E_0 B} \left(\frac{B E_0}{E - S E_0}\right)^{(1-\frac{1}{c})} \cdot e^{-\alpha l \left(\frac{E - S E_0}{B E_0}\right)^{\frac{1}{c}}} & E_0 S \leq E \leq E_0 (S+B) \\ \frac{N_0 \alpha \tau}{E_0 A^{\alpha\tau}} \cdot e^{-\alpha l} \cdot \left(1 - \frac{E}{E_0}\right)^{\alpha\tau - 1} & E_0 (S+B) \leq E \leq E_0 \end{cases} \tag{3.21}$$

N_0 is the number of photons *counted* in the detector, not the *total* number of photons. So the model does not take the quantum efficiency into account! The function contains two singularities (at $E = S \cdot E_0$ and at $E = E_0$) which are integrable.

3.1.4.3 The flat shelf

When a photon is absorbed, its energy is at first transferred to a single primary electron. The atom itself emits either a fluorescence photon or an Auger electron during its de-excitation process (see section 2.1.2). At the beginning of the charge cloud creation cascade there is thus either a primary electron and a fluorescence photon or a primary electron and an Auger electron.

The fluorescence photon has a certain probability to leave the detector without being absorbed (compare figure 3.17a). The energy of the photon is then missing in the detector signal, resulting in a peak which is located below the main peak in the spectrum. The difference between the main peak and the escape peak is the energy of the fluorescence photon. The escape peak is handled in section 3.1.4.4.

As a complementary process a fluorescence photon created by absorption in the entrance window can enter the detector medium and be detected (compare figure 3.17b). This creates a fluorescence peak at the fixed characteristic energies of the front layer material.

The probability for a fluorescence photon from the entrance window P_{fe} can be roughly estimated. The primary photon has to be absorbed within the entrance window thickness, the absorbing atom has to release a fluorescence photon into the direction of the detector bulk and this photon has to be absorbed there.

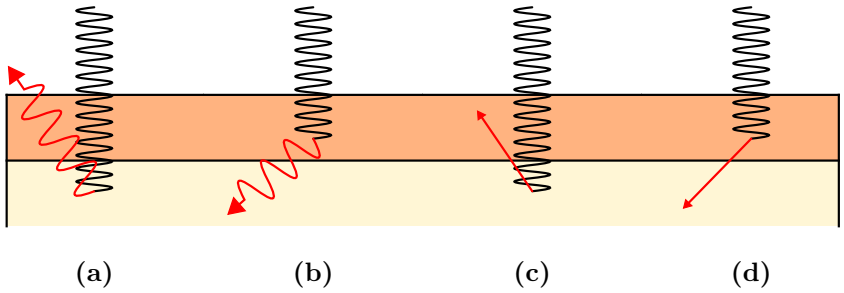

Figure 3.17: Effects creating different features of the detector response: (a) Photon escape, (b) fluorescence (photon injection), (c) electron escape and (d) electron injection. The darker area is the entrance window, below is the detector bulk. Photon escape and fluorescence create additional peaks, while electron escape and injection are responsible for an approximately homogeneous background between zero and the photon peak energy.

The first probability, $P_{abs,e}$, depends on the energy of the radiation impinging the detector and the entrance window material, the second, P_{fl}, depends only on the entrance window material. The emission of fluorescence photons is assumed to be isotropic, i.e. about half of the photons are emitted into the direction of the detector bulk. The probability of absorption in the detector bulk $P_{abs,b}$ can be assumed to be 1, because of the much higher thickness of the bulk compared to the entrance window.

$$P_{fe} = P_{abs,e} \cdot P_{fl} \cdot \frac{1}{2} \cdot P_{abs,b} = P_{abs,e} \cdot P_{fl} \cdot \frac{1}{2} \tag{3.22}$$

The absorption probability can be deduced from the Lambert-Beer law, P_{fl} is given by the fluorescence yield of the entrance window material which can be looked up, e.g. in the Elam database [56].

The detector used for measurements (see chapter 4) has an Al entrance window with thickness d of 50 nm is assumed. Fluorescence photons from the K-shell have the highest energy. To excite them the energy for the absorbed photon has to be above the Al-K edge energy of 1.56 keV. Above this energy the transmission probability is larger than 94.5 % [10].

The maximum probability for a fluorescence photon from the entrance window is thus

$$P_{fe} = \frac{1}{2} \cdot (1 - 0.945) \cdot 3.297\,67 \cdot 10^{-2} = 0.91 \cdot 10^{-3} \tag{3.23}$$

and lower for higher energies. Entrance window fluorescence is thus not handled specifically in this model.

Distinctive fluorescence peaks in DePFET spectra show up when the detector is e.g. illuminated from the front side where Al is present in thicker layers as power lines for the DePFET operation.

Like for the fluorescence photon in the case of the escape peak, there is also a chance that the primary and the Auger electron leave the detector (see figure 3.17c), resulting in charge loss. In contrast to a photon, an electron deposits its energy along its path through the medium, while a photon either deposits all of its energy or nothing. The primary and Auger electron can thus deposit an energy ranging from zero to the starting energy of the respective electron E_0 in the detector medium.

Hence, electrons originating from absorption in the bulk create a signal ranging from the full photon energy to the photon energy minus the kinetic energy of the electron. If the photon was absorbed in the front layer, the signal resulting from electron injection (see figure 3.17d) ranges from zero to the starting energy of the respective electron [55, 54].

These effects are assumed to create a more or less homogeneous flat shelf in the spectrum ranging from 0 to photon energy E_0. N_{fs}, the number of events in the flat shelf is calculated by

$$N_{\text{fs}} = k_{\text{fs}} \cdot N_0 \tag{3.24}$$

which are equally distributed over the energy range. The flat shelf is thus given by the function

$$\text{FS}(E, E_0) = \frac{k_{\text{fs}}}{E_0} \cdot N_0 \tag{3.25}$$

How the parameter k_{fs} is treated when applying the model, see section 4.2.6.

3.1.4.4 The escape peak

As stated above, during absorption of a photon with energy E_0 a fluorescence photon can be created which has a certain probability to leave the detector without being absorbed. This results in a peak which is located at $E_0 - E_{\text{esc}}$ the main peak in the spectrum. For silicon E_{esc} is 1740 eV.

The escape peak is modeled by applying the same calculations above to a photon with energy $E_0 - E_{\text{esc}}$ and adding the peak to the spectrum rescaled to the number of events in the escape peak. The number of events in the escape peak N_{esc} is calculated by

$$N_{\text{esc}} = k_{\text{esc}} \cdot N_0 \tag{3.26}$$

where k_{esc} is the energy dependent escape rate.

N_{esc} is subtracted from the counts in the main peak. The parameter k_{esc} is energy dependent, for energies below the Si K-edge energy it is 0. The parameter k_{esc} is modeled by an exponential function [50] when applying the detector model later (see section 4.2.6).

3.1.4.5 Contribution of noise

The contribution of noise is introduced by convolution with the noise function, a normalized Gaussian with variance σ_{noise}

$$\begin{aligned} \sigma(E) &= \frac{1}{\sqrt{2\pi}\,\sigma_{\text{noise}}} e^{-\frac{E^2}{2\sigma^2_{\text{noise}}}} \\ \sigma^2_{\text{noise}} &= \sigma^2_{\text{det}} + \sigma^2_{\text{Fano}} \end{aligned} \tag{3.27}$$

The noise comprises both, the electronics noise σ_{det} and Fano noise σ_{Fano}. The latter can be calculated, the former has to be determined. The final shape of the spectrum is thus given by

$$P(E, E_0) = \int_{-\infty}^{+\infty} \frac{dN}{dE}(E - \epsilon, E_0) \cdot \sigma(\epsilon)\, d\epsilon \tag{3.28}$$

In this equation the function $\frac{dN}{dE}(E, E_0)$ comprises the sum of the contribution from the main peak, the escape peak (if excited) and the flat shelf.

3.1.5 Clear-correlations

At normal pixel readout (see section 2.8) the internal gate is empty after the clear pulse and the pixel signal is the difference between the source node voltage of the filled and the empty pixel. Yet there are some pixel which show signals after a primary signal without a new deposit of charge in the internal gate. Such a sequence of signals is called a *clear-correlation (cluster)*.

Such a sequence can of course happen due to coincidence. As shown above in section 3.1.2.1 there is a probability for a hit signal to be generated by the electronics noise of the pixel. For a signal threshold of 5σ the probability to have a tail of n noise events after a hit is

$$P(\text{Tail} = n) = (1 - \Phi(5))^n = \left(2.87 \cdot 10^{-7}\right)^n , \tag{3.29}$$

with Φ being the CDF of the normal distribution:

$$\Phi(x) = \frac{1}{\sqrt{2\pi}} \int_{-\infty}^{x} e^{-\frac{1}{2}t^2}\, dt \tag{3.30}$$

If the extra constraint is applied that the signal decreases from frame to frame the probability becomes

$$P(\text{Tail} = n) = \frac{1}{n!}\left(1 - \Phi(5)\right)^n = \frac{1}{n!}\left(2.87 \cdot 10^{-7}\right)^n \tag{3.31}$$

which is even lower[3].

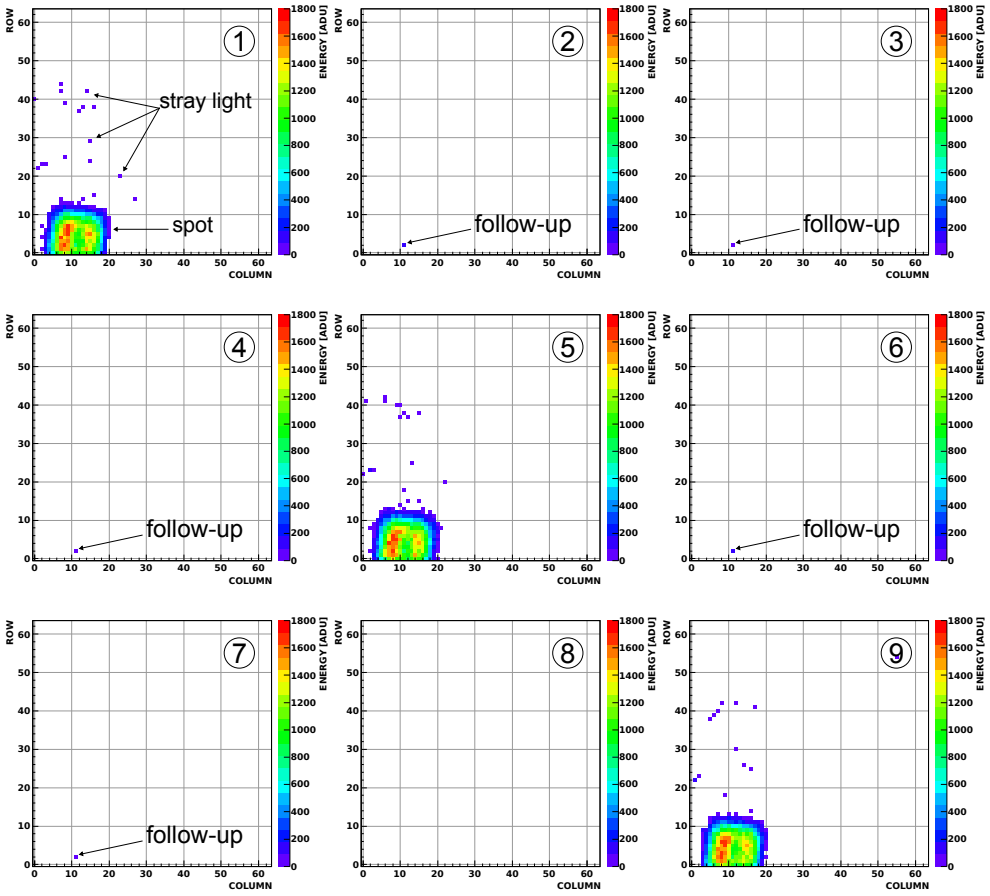

Figure 3.18: Nine frames out of a larger series of a measurement with a triggered light source (infrared LED). The number within the circle shows the order of the individual frames. The source was collimated and directed to the lower left part of the matrix. The light spot can be clearly seen in three of the nine frames. The clear-correlation signal shows up in the frames following the light pulse, except for the eighth.

[3] A proof for this formula can be found in chapter E.

Because of the low probabilities, one would expect only be few accidental follow-up signals for a real photon signal. However, measurements with a pulsed infrared light source showed that for some pixels these are not accidental coincidences. However, the reason why some pixels show clear-correlations is still investigated.

Here, a *Light Emitting Diode* (LED) creating a spot on the detector matrix was triggered by the chip readout, i.e. it illuminated the matrix synchronized with the readout. It emitted a short (250 ns) light pulse which created a signal in the detector. Then the chip was read out for a number of cycles without illumination before another light pulse was triggered.

Figure 3.18 shows a series of frames from such a measurement. Here, at every fourth frame the LED illuminated the detector, during the remaining three frames the light source was off. The illumination spot in the lower left corner can be seen clearly, the pixel signals above are probably caused by stray light.

When the light source is switched off, no pixel show a signal, except for one with coordinates $[11, 2]$. This one shows a signal both in the illuminated and non-illuminated frames. The signal in the non-illuminated frames is low, only just above the threshold. The reason that there is now follow-up signal in the next to last frame in figure 3.18 is probably that the pixel noise pushed the clear-correlation signal below the threshold.

If there is no illumination at all, pixel $[11, 2]$ shows no signal except for rare noise events. So the follow-up signals are correlated to the applied light pulse.

Such follow up signals are also present when the detector was illuminated with a ^{55}Fe-source as shown in figure 3.19. Figure 3.19a shows the total number of hits that was accumulated in each pixel, figure 3.19b the clear-correlation clusters found for each pixel. The ratio of clear-correlation clusters over the number of all hits per pixel is shown in figure 3.19c.

In contrast to the measurement before, the whole matrix was illuminated and the source was no longer triggered, also the photon energy was higher. Nevertheless, the follow up pixel shows up in figure 3.19c with a rate of 0.7, i.e. 70 % of the hits in this pixel were clear-correlations. Also other pixel peak out with high clear-correlation rates.

Additionally, circular regions can be seen which resemble the ones shown in figure 3.3. The illumination (figure 3.19a) has a circular structure with the center in the **top right** corner, but the circular regions in figure 3.19b and figure 3.19c have their center in the **bottom right** corner. This shows that these two structures are not correlated.

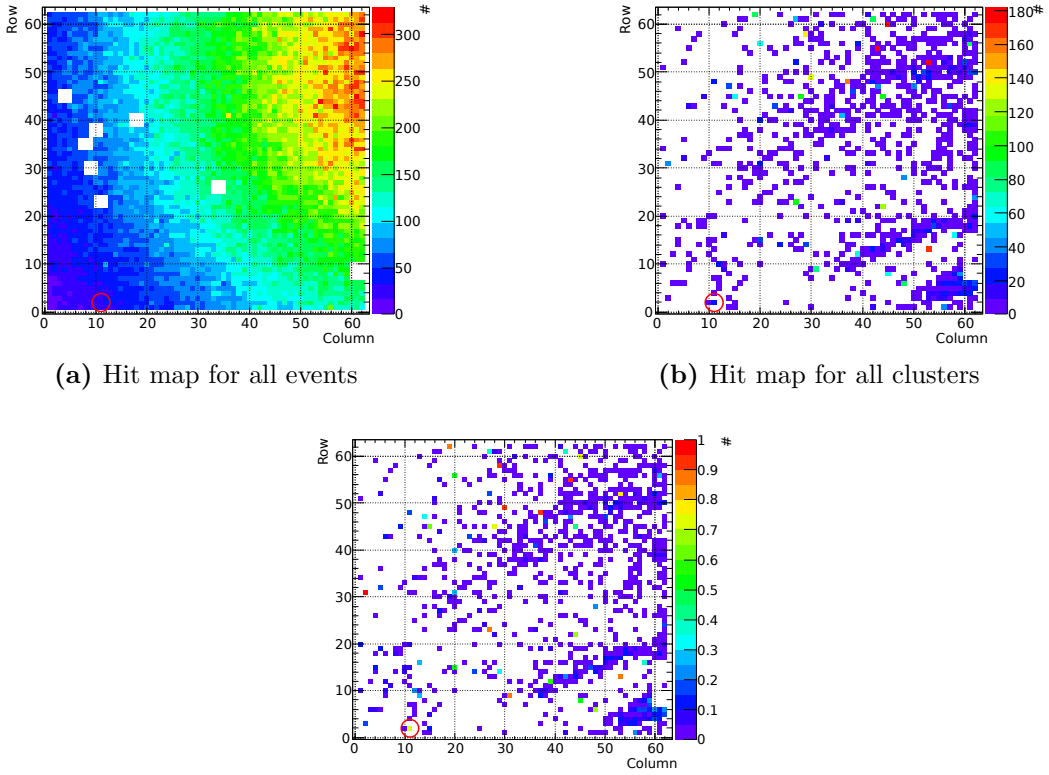

(a) Hit map for all events

(b) Hit map for all clusters

(c) Cluster rate

Figure 3.19: Result of clear-correlation filtering of a measurement with an ^{55}Fe source. (a) shows the number of hits accumulated in each pixel, (b) the number of clusters detected in each pixel. Because the radiation source was not centered, the hit map (a) shows a gradient. (c) shows the pixel cluster rate, which is the number of clusters divided by number of total hits. The white squares in (a) are pixels masked as 'bad'; also the border pixels have been masked out. The clear-correlation pixel that was in the focus of the pulsed light measurements is in the center of the red circle at the bottom left of the maps. It shows a higher rate (0.7) than the surrounding pixels. Also other pixels with higher rates (> 0.7) are visible. The circular regions visible in (b) and (c) resemble the regions shown in figure 3.3.

The position of the matrix shown in figure 3.19 on the wafer is left to the matrix from figure 3.3, so the circular regions in figure 3.19 also seem to match the concentric rings in figure 3.3. Also here, the reason for their occurrence is still subject of discussion, with resistivity fluctuations within the silicon crystal being a possible explanation.

Clear-correlation pixels return a lower signal as the remaining charge reduces the difference between the two sample measurements. Also, the follow-up signals create a low energy background. How clear-correlation clusters are detected is shown in section 3.3.6.

3.1.6 Misfits

DePFET detectors are always sensitive to radiation. The operation of a DePFET detector can be divided into an *accumulation phase*, in which the pixel is accumulating charge, and a *readout phase*, in which the pixel is read out.

A "normal" signal is generated when radiation hits the detector during the accumulation phase. If charge is deposited into a pixel during readout, the output signal is altered. Such a signal is called a *misfit*.

The generation of misfits is illustrated in figure 3.20. As the ASTEROID readout ASIC which is used for DePFET readout performs source-follower readout (see section 2.8.1), the following discussion is limited to this method. Of course, misfits can also occur when using drain-current readout. They result from the fact that the internal gate of the DePFET is unshielded to the detector bulk, i.e. charge can be deposited at any time.

The correlated double sampling implemented in the ASTEROID readout ASIC integrates a current proportional to the source node potential (see section 2.9.2). Two integrations, i_1 and i_2, are performed, before and after the clear process respectively. The difference $s = i_1 - i_2$ is returned as the pixel signal. For a given charge, this signal s depends on the point in time the charge deposition takes place.

In figure 3.20 time diagrams for four cases are shown. Apart from the case of no charge deposition (figure 3.20a), or normal charge deposition, i.e. charge deposition before readout (figure 3.20b), there are two cases which create a misfit signal: charge deposition during first integration (positive misfit, figure 3.20c) and charge deposition during second integration (negative misfit, figure 3.20d). For each case the integrator result is drawn above in red, the source node voltage is drawn below in green. The two sample periods during which the integrations take place are marked as colored areas.

No charge deposition When the detector is not illuminated, no charge is deposited in the pixel and the source node voltage stays constant[4]. The integrator first integrates the current, leading to a rising result in the first sampling period in figure 3.20a, and then subtracts the same integral, which is illustrated by the falling result in the second sampling period. The two integrations, i_1 and i_2, thus cancel each other, the resulting signal $s = i_1 - i_2$ is zero.

[4]Charge deposition by leakage current is neglected. On average, leakage current adds the same amount of charge in each integration, which cancel each other when taking the difference. The variance of the leakage current only adds noise to the resulting signal.

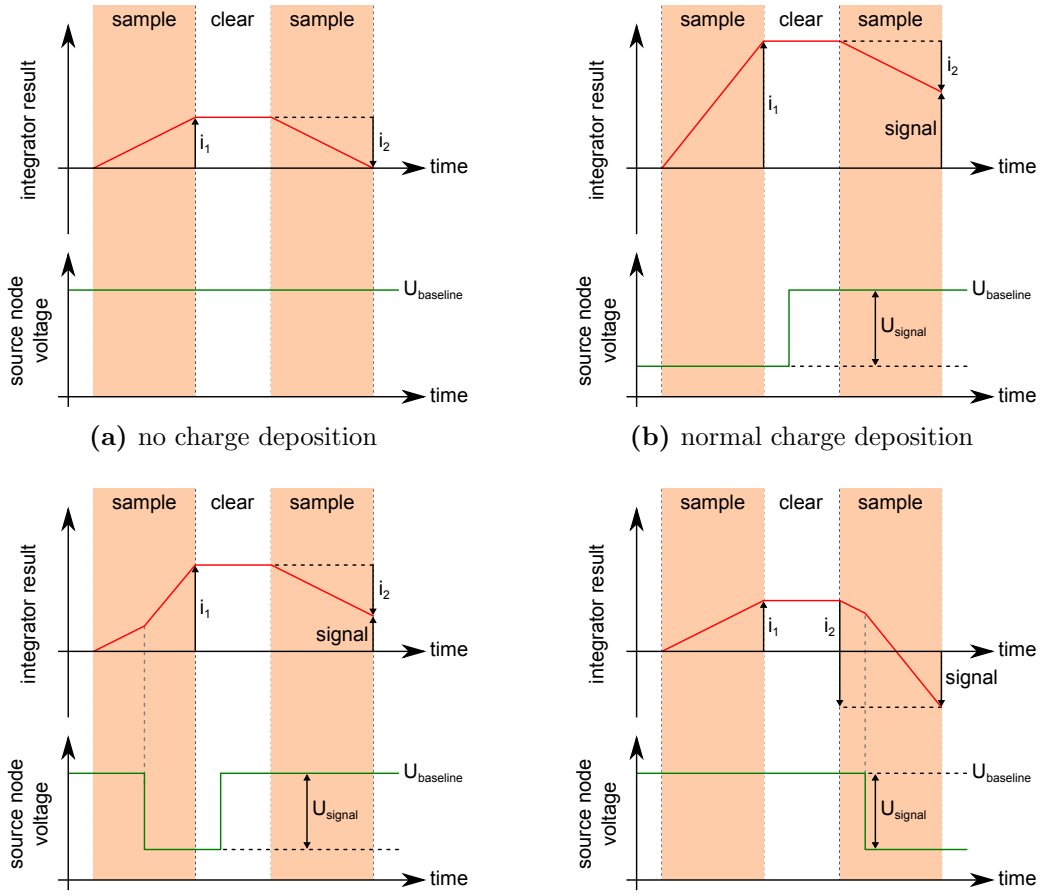

(a) no charge deposition

(b) normal charge deposition

(c) positive misfit

(d) negative misfit

Figure 3.20: The pixel signal depends on the point in time of charge deposition in the pixel. The correlated double sampling implemented in the ASTEROID readout ASIC integrates a current proportional to the source node voltage and returns the difference as the signal.
(a): If no charge is deposited, these two integrations, i_1 and i_2, cancel each other.
(b): If charge is deposited before pixel readout, the first integration, i_1, samples the signal plus baseline, the second integration, i_2, just the baseline. The signal is the difference.
(c): If charge is deposited during first integration, it contributes only partially to i_1. As i_2 is the integral over the same baseline as in (b), the resulting signal is smaller, but still positive. This is a *positive misfit*.
(d): The first integration is done with an empty pixel, thus i_1 is equal to the baseline. The charge deposited during second integration contributes partially to the second integration, depending on the point in time when it happened. i_2 is now larger than i_1, thus the difference, i.e. the signal, is negative. This is a *negative misfit*.

Normal charge deposition When charge has been deposited into the pixel before readout it alters the conductance of the DePFET which results in a low source node voltage. As the preamplifier is inverting, a lower voltage creates a higher current. Therefore, during the first integration the integrator result rises faster in figure 3.20b. The clear process removes the charge from the internal gate, the source node voltage rises to its baseline value, the current thus drops. The baseline integral i_2 is subtracted from the integral over signal plus baseline i_1, thus returns the pixel signal $s = i_1 - i_2$.

Charge deposition during 1st integration When charge deposition happens within the first sampling period, the integrator result i_1 is a combination of the integration over the low baseline current and the high baseline-plus-signal current. Depending on the point in time the charge deposition takes place only a fraction of the signal current is integrated (see figure 3.20c). After the clear process, the baseline is subtracted and the result is thus a lower signal – ranging from s to 0 – for the same amount of charge compared to the above case. This is called a *positive misfit*.

Charge deposition during 2nd integration The internal gate is at first empty. Therefore the integrator integrates over the baseline current during the first sampling period. The charge deposition increases the current during the second sampling period. Therefore a larger second result is subtracted from the first, resulting in a negative signal. Depending on the point in time the charge deposition takes place, the signal value can vary from $-s$ to 0. In contrast to the other cases, the charge remains in the internal gate and is read out at the next readout process. The *negative misfit* is thus followed by the nominal signal in the next frame.

Loss of signals If the charge is deposited in the pixel after the first integration but before the clear pulse, there is no effect on the output signal (This case is not shown in figure 3.20). The clear process removes the signal charge before it is detected, the integrations i_1 and i_2 thus represent only the baseline. Also, if the charge is deposited at a point in time close to the end of one of the sampling periods, its influence on the output signal is small. The resulting signal s is then lost during event discrimination, if it is below the threshold (see section 3.1.2)

Effect on frames If the effects described above are combined with charge splitting, it can lead to a modification of the resulting pattern. Apart from

SNG patterns, valid patterns can be seen as combinations of a horizontal and a vertical split between two pixels (see section 3.1.2.2). Therefore, the discussion of the effect of misfits is limited to these two cases. The case for SNG patterns is analog to a horizontal charge split.

Figure 3.21 shows the case for a horizontal charge split. The boxes on the left show a 4×4 matrix during readout. The rolling shutter is marked yellow passes through the matrix from top to bottom. For each row the readout procedure – sample (S), clear (C), sample (S) – is applied. For each period the current state of the matrix is drawn, except for the clear period for which the matrix is "compressed" to a single column.

Charge deposition within a pixel is symbolized by a black circle, charge removal by a green box in the respective clear period. To the right of the readout representation, the resulting frame composed of the 4 readouts is shown. A black circle here symbolizes the nominal signal, a green circle if only a part of the charge is measured. This is a *positive misfit* (compare to figure 3.20c). A red "×" is a *negative misfit* (compare to figure 3.20d).

If the charge is deposited during the accumulation phase, it is read out correctly when the shutter passes the respective pixels and the resulting frame contains the full nominal signals (figure 3.21a).

If the photon hits the pixel during the first sample period (before the clear pulse), the resulting signal in the frame represents only a fraction of the original charge. Such a positive misfit is shown in figure 3.21b. Such a signal cannot be distinguished from a partial event, as e.g. by charge loss (see section 3.1.4).

Additionally, if one or both signals are lower than the threshold for event discrimination, the pattern can be converted to a lower multiplicity or get lost totally.

The case when the photon hits the detector during the clear pulse is not shown. The charge is then removed from the internal gate and no signal is measured. The resulting frame is thus empty.

Figure 3.21c shows what happens if the photon hits the detector after the clear pulse, during the second sampling. The deposited charge makes the readout chip subtract a higher value than usual resulting in a negative (i.e. below offset) signal in the first frame. The charge remains in the internal gate and is read out normally during the next frame readout. The original signal is then shown in the following frame.

All or parts of the negative misfit signal pattern could also fall below the event threshold. However, in contrast to the positive misfit the deposited charge is not

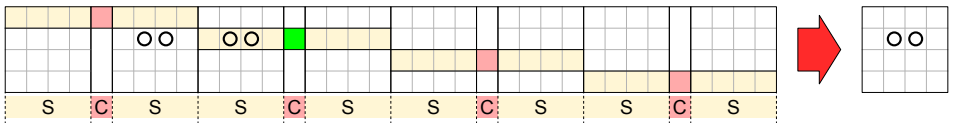

(a) event during accumulation phase

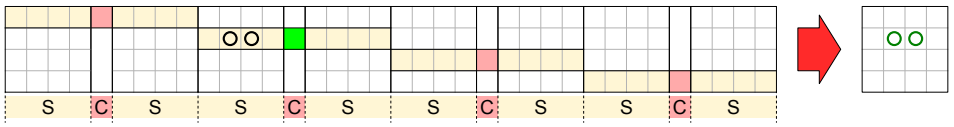

(b) event before clear pulse, during first integration

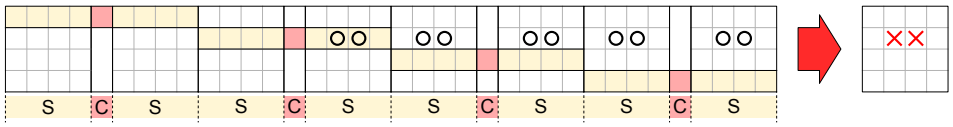

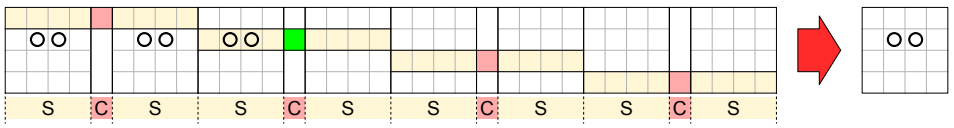

(c) event after clear pulse, during second integration

Figure 3.21: Influence of misfits on horizontal split events. The boxes on the left show a 4×4 matrix during readout. The rolling shutter is marked yellow. For each row the readout procedure – sample (S), clear (C), sample (S) – is applied. A black circle here symbolizes charge deposition, a green box charge removal.
On the right the resulting frame composed of the 4 readouts is shown. A black circle here symbolizes the nominal signal, a green circle a *positive misfit*. A red "×" is a *negative misfit*. (a) shows the case of charge deposition during the accumulation phase. The charge is read out during the pass of the shutter and the resulting frame shows the nominal signal. A positive misfit is shown in (b). The charge is only partially detected, the signals in the resulting frame thus lower. (c) shows a negative misfit. When the charge is deposited during the second sampling period it creates a negative signal in the resulting frame. In contrast to the positive misfit, the signal remains in the internal gate and is read out during the next pass of the rolling shutter. The nominal signal then shows up in the next frame.

lost and the original signal not altered then.

Figure 3.22 shows an example in which the charge of a photon event is split vertically between two pixels in the detector. The display style is the same as in figure 3.21.

If charge deposition happens in both pixels during the accumulation phase, such an event would normally create a DBL pattern. This case is not shown in figure 3.22 as well as the case of charge deposition during the clear process, in which the signal is lost and the resulting frame empty.

In the first case (figure 3.22a) the upper part of the split charge is deposited in the active row during the first integration, which means it is only partially detected. The lower part is read out normally when the shutter proceeds. If the charge loss due to the partial detection is that large that the hit signal is pushed below the threshold, the resulting DBL pattern can also be converted to a SNG pattern which consist only of the lower part of the original photon event. This can especially be the case, if the lower part contains the major share of the charge split.

In the second case (figure 3.22b) the upper part is deposited during second integration which creates a negative hit signal in this pixel. The south part is again read out normally. As the charge of the north part remains in the pixel, it is read out during the next pass of the shutter. If the misfit signal is lower than the respective threshold (compare to section 3.3.2), the result is a DBL pattern in the first frame comprising a negative and a positive hit signal, and a SNG pattern in the second frame. If the negative signal cannot be detected, the event is split between two frames and thus regarded as two separate signals.

In the third case (figure 3.22c) the lower part of the split charge is deposited during the first integration and thus only partially detected. The north part is read out at the next pass of the shutter and the charge is attributed to the next frame. The original event is thus split between to frames. Like the first case, this cannot be distinguished from other signals.

In the fourth case (figure 3.22d) the south part of the split event is in the active row during second sampling, creating a negative signal. The charge remains in the internal gate and the complete pattern is read out during the next pass of the shutter. In contrast to the second case the event is not split between the frames. The misfit in the first frame thus is here merely an indicator for the “improper” charge deposition.

As shown in figure 3.21, all parts of a horizontal split event are affected similarly by misfits. Therefore, if a frame contains a negative misfit next to

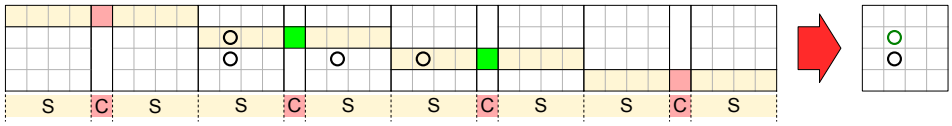

(a) north part hits pixel before clear pulse, during first integration

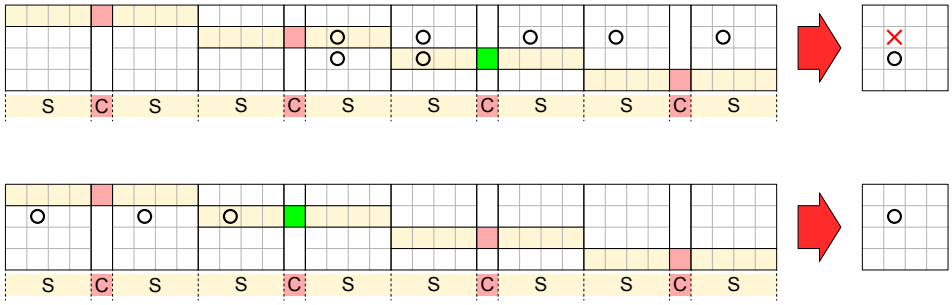

(b) north part hits pixel after clear pulse, during second integration

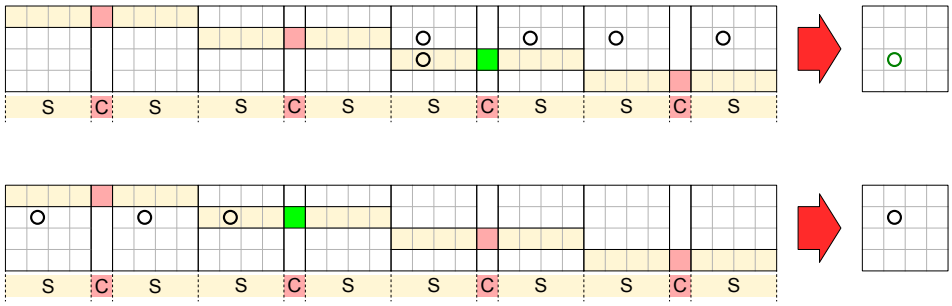

(c) south part hits pixel before clear pulse, during first integration

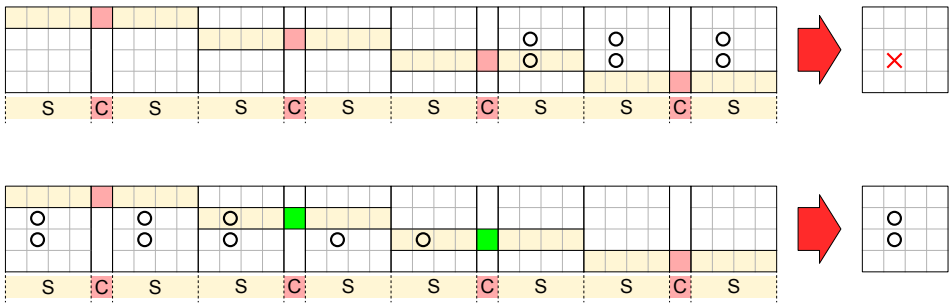

(d) south part hits pixel after clear pulse, during second integration

Figure 3.22: Influence of misfits vertical split events. The display style is the same as in figure 3.21. Depending on point in time the charge is deposited, the pattern can be split between two frames like shown in (b) and (c). In contrast to the case shown in figure (b), the split shown in figure (c) can be reconstructed if the negative signal is detected.

a positive hit signal within the same row, they stem from different photon events and must not be combined to a pattern then.

Looking at figure 3.22, one can see that for vertical split events a pattern comprised of a negative misfit and a positive hit signal is only created in figure 3.22b. The position of the misfit signal relative to the positive hit signal depends on the running direction of the shutter.

In figure 3.22 the shutter runs from top to bottom, the positive hit signal is located *in running direction* of the shutter, i.e. below. Therefore, negative misfit signals may only be combined with positive signals to a pattern if these are located next to them in the running direction of the shutter.

The last two conclusions have been implemented in the pattern search algorithm of the event filtering (see section 3.3.2). The detection of negative misfit clusters is discussed in section 3.3.7.

3.2 ROAn – The ROOT based Offline Analysis software

This section will present the software package ROAn, the *ROOT based Offline Analysis*, which has been developed in the context of this thesis. As already outlined at the beginning of this chapter, the main requirements to the software package were to be flexible and extensible which lead to a modular design of ROAn.

ROAn is written in C++, a powerful language which allows various programming paradigms and low level programming as well as high abstraction. ROAn itself is written object orientated. This programming paradigm facilitates modularity and the definition of interfaces.

ROAn makes heavy use of the data processing framework ROOT [57], which itself is object oriented and written in C++. ROOT has its roots in the field of high energy physics but has spread its use also to other fields. It is developed at the *European Organization for Nuclear Research* (CERN[5]) since 1994.

CERN has a comprehensive web page offering a complete documentation of the ROOT framework [58]. Some of its advantages are presented here:

- ROOT is developed at and also used by CERN, and a large number of institutes and users. This means it is widespread and thus likely to be widely used in the future.

[5] CERN = **C**onseil **E**uropéen pour la **R**echerche **N**ucléaire

- ROOT is open source. Hence, its code can be viewed and checked by the developers. This reduces dependency compared to proprietary software, where the user often has to rely on the vendor to answer questions about implementation details and errors. Also no license fee is involved.

- ROOT is developed to be portable and to run on different platforms and systems. Adhering to the frameworks programming paradigm ensures portability for the analysis software package.[6].

- Being rooted in the field of high energy physics, ROOT offers means to store large amounts of data and to access them quickly and flexibly.

The ROOT framework comprises the C++ script and command line interpreter CINT. The use of CINT has certain advantages:

- CINT interprets C/C++. Hence new algorithms can already be developed here in the same language the analysis software is written. There is no need to port the code later.

- CINT is capable of running macros, i.e. external files containing instructions in C/C++. This also eases development of algorithms and allows the user to reuse code. CINT also offers the possibility to load macros as compiled code which makes them run faster.

- CINT can load external libraries. The loading of external libraries makes the software flexible in use.

ROAn uses ROOT to store the analysis results and for their graphical presentation. Also, adhering to the frameworks standards ensures portability of the software package.

3.2.1 Object oriented programming

The sections below may require a certain knowledge of the principles of *Object Oriented Programming* (OOP). To explain OOP is clearly beyond the scope of this thesis. A thorough overview is given in literature [59], here only some aspects are clarified for a better understanding of the following sections.

[6] Critical elements in portability are usually the graphical output (system dependent) and the size of number formats like integers, shorts, floating point numbers, etc. (platform dependent).

Objects and classes In object oriented programming the problem is divided into *objects* which interact with each other. An object encapsulates data and the functions to manipulate them. The description of such an object is called a *class*. A simple image for this would the recipe for a cake: The recipe (the class) describes how the cake (the object) is built. By following the recipe several cakes can be created.

Inheritance Classes can be derived from each other. The new class inherits all functions and data members from the old class. It can then add new members or functions, or alter the existing functions. This way, common routines can be centrally defined in a base class, which also represents an *interface*. Specific routines are modeled in the subclasses. To stay with the image of the cake: Inheritance means same dough, different frosting.

Interfaces By defining interfaces, a simple base system can be set up which deals with other objects via their common interface. This way new objects can be easily used with such a system, when they comply with the interface definition. The base system also does not depend on internal details of these objects then. This makes the system modular and expandable. In the cake analogy: For a waiter it is sufficient to know how to carry a cake to the customer. The frosting (internal implementation details) is irrelevant for completing this task. As long as a new product from the kitchen is a cake (i.e. complies with the interface), he can carry it to the customer.

3.2.2 Internal mechanics

This section will sketch the principles incorporated in ROAn. The source code of the ROAn analysis software, as well as a documentation of the analysis parameters can be found on its website [60].

- During data analysis results are produced. These results themselves can be used to calculate other results, which establishes a dependency between them. The results needed for calculation of a result are called its *dependencies*.

- To calculate a result an *algorithm* is used. There may be several algorithms to calculate a result, so it should be possible to interchange them. These algorithms are steered by *parameters* which can modify the calculation.

- If a result depends on another one, it has to be calculated after it. To keep track of calculation order, a *timestamp* is assigned to the result. The timestamp of the result has to be larger than the timestamp of its dependencies.

- Parameters which steer the algorithm to produce the result thus define the result itself. A change of a parameter can lead to a change in the result. Therefore, the parameter set has to be stored along with the result so it can be reproduced. The same holds of course for the result's dependencies. Therefore the parameter set of a result must not be only the parameters controlling its algorithm, but the union of these and the parameter sets of all its dependencies.

Above considerations lead to a set of basic features the data analysis software should provide:

- For each result, the analysis software has to know by which step it is calculated, which results are needed for its calculation, and which parameters steer the algorithm.

- If a result is re-calculated, it sets results depending on it out-of-date. The software must have the means to discover out-dated results.

- The same holds for a change of parameter values. The software must also detect these changes.

- As there are several possible ways to calculate a result, the software should provide a common interface for algorithms. This way they can be interchanged easily.

- Parameters and results also need a defined interface, such that the analysis software can handle them knowing about their internal details

The ability to discover out-dated results can increase the speed of the analysis process (only the results out-of-date are recalculated) and ensures that the complete set of results is coherent.

A common interface to implement algorithms frees the user from being pinned to a rigid set of predefined algorithms. In ROAn this interface is called a *step*. This makes the software flexible, so the user can easily test new algorithms and thus adapt the software to future tasks.

There are four basic components within ROAn:

- Results, which are uniquely identified by their name and derived from the same base class (interface).
- Steps, which house an algorithm and produce results. Steps provide a common interface to interact with the software. Some also take results from other steps as input. The algorithm can be steered by parameters.
- Parameter pools, where the parameters defining the calculation of the results are stored. Each parameter has a unique key.
- The analysis program, which offers a user interface, manages access to files and other objects, keeps track of outdated results and triggers calculations.

Figure 3.23 shows a schematic overview of an analysis step. This scheme is implemented by simple steps which only open a file, as well as steps which perform more sophisticated calculations. This common scheme has proved to deliver the desired flexibility to the analysis software.

Each result has a storage location (in memory or a file), a timestamp, and a set of parameters, the *parameter pool*, associated with it. From the timestamp it can be retrieved *when*, from the parameter pool *how* the result was produced.

Parameter pools are databases, which store parameter values under a unique key. Each parameter has a default value. If a parameter is queried, either the

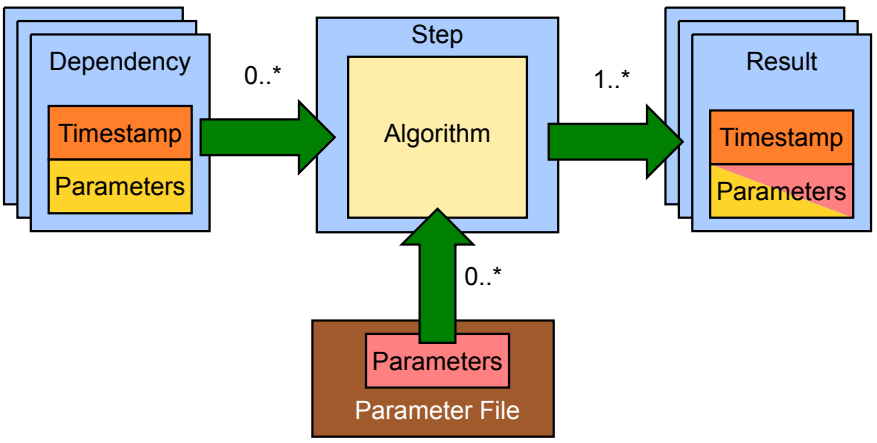

Figure 3.23: Schematic overview of an analysis step. A step calculates at least one result. A result can be calculated from other results, these are called *dependencies*. The algorithm can be steered by a set of parameters, the *parameter pool*. To ensure that results are up to date, each result is stored along with a timestamp and a parameter pool. The parameter pool of the result is the union of the parameter pools of the algorithm and the pools of all results.

value stored is returned or – if not available – the default value. This way it is ensured that the analysis always runs with a defined parameter set.

The parameter pool of a result is the union of the parameter pools of the result's dependencies and the parameter pool of the used step. Because the parameter keys are unique identifiers, this requires that pools are only merged if common keys have the same value. The functions for merging parameter pools make sure that pools are only merged, if their common parameters match, i.e. the common keys have the identical associated value.

A typical analysis run starts with the initialization. A user loads a parameter file where the analysis to be performed is described by a set of parameters. This includes at least a list of steps. The according step objects are generated and each step registers its result in a central list.

For each result, the name storage location, the step producing it, and a timestamp are stored. The timestamp shows when the calculation took place. In this way the analysis knows which results can be calculated and which step is responsible for it.

If the user requests the calculation of a *target result*, the analysis first checks the stated storage location whether the result is available. If this is the case, a check is performed to ensure the result is up to date.

This check first looks up the step responsible for the result in question. Each step has a function which returns a list of dependencies which are needed for the calculation. For each the respective step is looked up and its dependencies queried as well. With this recursive procedure a dependency graph is created. Figure 3.24 shows such a graph. The arrow between the elements of the graph reads as "*depends on*".

It is important to keep in mind that the dependency graph is built *bottom up*. A step which produces a result in the dependency graph may also produce other results in parallel. But these results play no role in when it comes to investigate the dependencies of the target result. Another important remark is that circular dependencies have to be avoided.

The dependency graph is then investigated *top down*, from the top nodes ('Photon Frames' and 'Dark Frames' in figure 3.24) down to the target result ('Sng Resolution'). The timestamps of each result has to be older than the ones of its dependencies, and the parameter pool of the result has to be the union of the pools of its dependencies. Any mismatch here is a hint that a result in the graph is outdated.

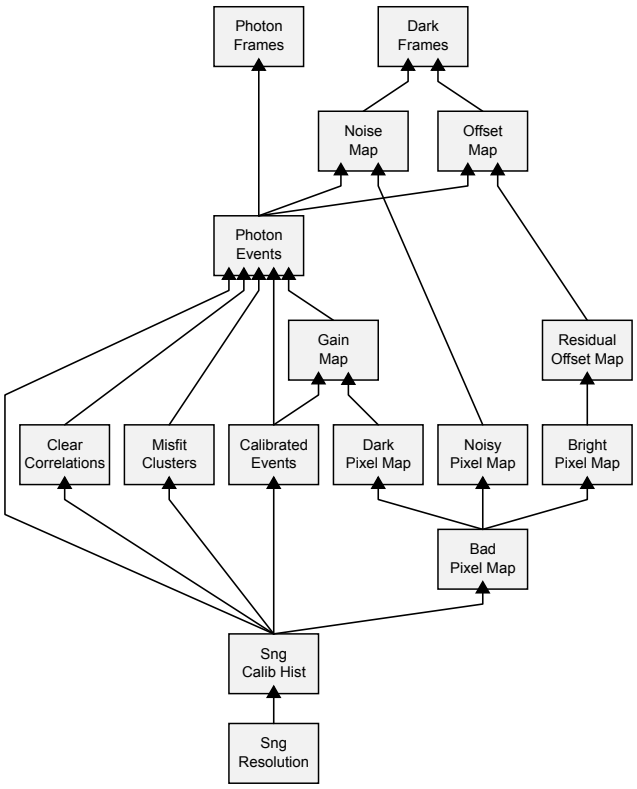

Figure 3.24: Dependency graph for the result 'Sng Resolution' which shows the energy resolution calculated from the calibrated histogram for SNG-events. The arrows between the elements are read as "*depends on*". This graph shows only the dependencies for the result 'Sng Resolution', not for all results calculated during an analysis run.

If the check is successful for the target result, i.e. all dependency timestamps and parameter pools match, it is returned. If a mismatch is detected, a recalculation is triggered.

If a result, the target result or a result from the dependency tree, does not exist, it triggers a recalculation just like a mismatch in the check routine described above. This way only necessary recalculations are performed.

How the software behaves if run with erroneous input is beyond the scope of this thesis will not be presented here. ROAn has, of course, means to handle these cases. The default behavior is that no calculation is executed if an error is detected.

3.2.3 Definitions

Before proceeding, a summary of terms which can help the understanding of the following sections will be given here Some have already been introduced in the

previous chapters, some will be explained in detail in the following sections.

Rolling shutter DePFET matrices are read out by switching on the transistors of one matrix line and doing parallel readout to all pixels in this active line. This is called a *rolling shutter*, with the active line being the shutter moving over the matrix. (see section 2.9)

Frame The complete set of pixel signals from one pass of the shutter through the matrix is called a frame. In the software, a frame is internally handled as an array of data values (e.g. with the current DAQ integer numbers with a size of 2 bytes). (see section 2.9)

Front side, back side The side of the DePFET detector, on which the transistors are located is called the *front side*. The *back side* is produced as a homogeneous entrance window through which radiation can enter with least obstruction. (see section 2.5)

Event An *event* describes the process of a photon being absorbed in the detector and producing an electron-hole cloud (see section 2.1). The electrons drift toward the front side of the detector where they are distributed among one or several pixels.

Hit A pixel delivering a signal above threshold produces a *hit*. One event can produce several hits (charge splitting), not every hit is produced by an event because pixel noise can also generate signals above threshold. (see section 3.1.2 and section 3.3.2)

Pattern Hits from pixels which share a common edge can be combined to *patterns*. The simplest pattern is a single hit. Patterns can comprise an arbitrary number of signals and have arbitrary shapes. However, because the charge cloud created by a photon can only create specific patterns, there is a discrimination between valid and invalid patterns (see section 3.1.2.3).

Cluster Hits from the same pixel which appear in consecutive frames can be grouped to *clusters*. The first hit in a cluster is called the *precursor*, the following signals *successors*. The number of hits within a cluster defines its length. A hit with no successors is a cluster with length 1.

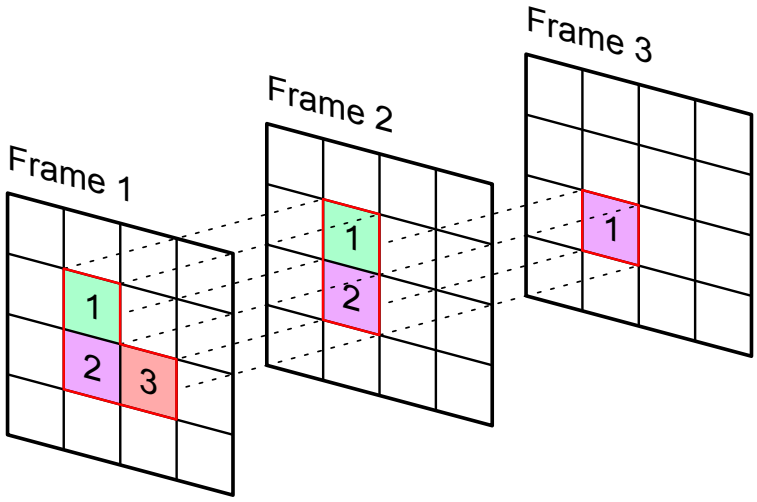

Figure 3.25: Illustration of hits, patterns and clusters. Three frames are shown. The hits in each frame are numbered consecutively. The patterns are framed red, the clusters marked by different colors. The hit in frame 1, which has the number 3 is a cluster on its own (marked red) with length 1. The other two hits in the same frame belong to longer clusters (marked green and purple). All three hits of frame 1 belong to the same pattern. Same holds for the hits from frame 2 and frame 3.

Figure 3.25 shows a simple example illustration of hits, patterns and clusters. Three frames are shown, which contain a number of hits numbered consecutively. The hits within a frame are grouped to patterns framed in red. Also, the hits have been grouped to clusters which are marked by different colors.

There are three clusters in figure 3.25: One is colored green and comprises the hits in 'frame 1' and 'frame 2' which have both the number '1'. This cluster has the length 2. The other cluster has length 3 and is made up by the three events colored purple. The last one has length 1 and is colored red.

By this definition, a hit is always part of both, a cluster and a pattern. In the simplest case both, pattern and cluster, are made up by a single hit. More on clusters, see section 3.1.5 and section 3.1.6.

Coordinate system In computer systems, multi-dimensional data is usually stored as a one-dimensional array. The position within the array then encodes the coordinates of the data point. For DePFET detectors and other imaging detector this concerns first of all two-dimensional data, like frames or representations of pixel values (see **Map** further below).

ROAn uses a common convention for the representation of all two-dimensional data, shown in figure 3.26. In a two-dimensional display, a pixel can be addressed

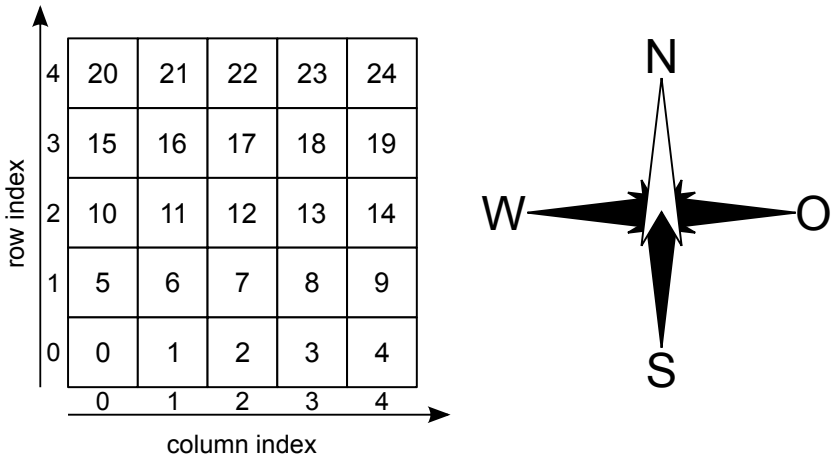

Figure 3.26: The ROAn coordinate system applied to a 5×5 pixel matrix. The number within the pixel is the position index i_p. When e.g. reading a frame from a framesfile, the pixel signals are stored as an array. The first signal has the index 0, the last the index $N_{\text{pixels}} - 1$, where N_{pixels} is the number of pixels in the matrix. For directions and positions with respect to the detector matrix, ROAn uses a nomenclature based on the four cardinal points. The column index c thus rises here from west to east, the row index from south to north.

by its column and row index $[c, r]$. In the one-dimensional array in which such data is stored, it is addressed by its position i_p in the array.

The position index i_p can be calculated from c and r:

$$i_p = c + r \times N_c \,, \tag{3.32}$$

where N_c is the column count, i.e. the overall number of columns of the two-dimensional array. By this convention, $i_p = 0$ denotes the bottom left pixel $[0, 0]$ in a map. The index i_p rises with the column index c from left to right and with the row index r from bottom to top.

Vice versa column and row index can be calculated from the position index i_p by

$$\begin{aligned} c &= i_p \mod N_c \\ r &= \lfloor i_p / N_c \rfloor \end{aligned} \tag{3.33}$$

The fact that all data adheres to a common coordinate system makes comparison between them simpler. Also, the algorithms used are simpler and more universal if they do not have to deal with the complexity of different data representations.

Additionally, the (relative) position and orientation of the detector matrix is of interest. ROAn uses a nomenclature based on the four cardinal points (see figure 3.26). In this system, the column index rises from west to east, the row index from south to north. Here the front side of the matrix faces the viewer, the back side the source of radiation.

The placement of readout and steering ASICs depends on the used detector hybrid. An overview of the positions of Switcher ICs and readout ASICs with respect to the detector matrix can be found in the section D.

Histograms, Spectra A *histogram* – sometimes called *spectrum* – shows the frequency distribution of data. Those histograms are usually one-dimensional. Often they summarize the data of all pixels of a DePFET matrix.

During creation of histograms, filtering can be applied to remove data from e.g. erratic pixels, or to select only specific events, e.g. by an energy cut.

Map DePFET detectors are imaging devices. Properties of a pixel (like offset, noise, gain, etc.), but also detector images can be shown as two-dimensional histograms, called *maps*. According to the ROAn coordinate system, the origin is in the bottom left corner, the columns are plotted left to right, the rows bottom to top.

Map value histogram A *map value histogram* shows the frequency of values within a map. While the color coded two-dimensional display of a map has advantages to detect localized effects on the DePFET matrix, a map value histogram offers a better evaluation of the general distribution of values.

3.3 Description of analysis steps

After the general description of the developed analysis software, this section is focused on a detailed overview of the analysis of DePFET data, and the algorithms developed for it. Most of the algorithms presented in the following sections target the effects presented in section 3.1.

The following sections address the analysis of DePFET data, but it should be pointed out once more that the flexible structure of ROAn makes the framework also useable for the analysis of data from e.g. CCDs or drift detectors.

The basic analysis steps in DePFET data analysis are:

- Determination of pixel offset and noise

- Filtering of events from frame data
- Determination of pixel gain
- Calibration of events
- Tagging of events
- Analysis of events

Additional analysis can be easily implemented by adding new steps and other modules, or by using the scripting capabilities of CINT. Implementation details on the algorithms described in the following sections can be found in the ROAn reference guide [60].

3.3.1 Offset and noise map calculation

The offset and noise is determined from a set of so-called *dark frames*, i.e. frames taken without any illumination of the detector. The offset $o_{c,r}$ of pixel $[c,r]$ is determined by calculating the average detector signal from this set.

$$o_{c,r} = \overline{s_{c,r}} = \frac{1}{N_{\mathfrak{F}}} \sum_{i \in \mathfrak{F}} s_{i,c,r} \tag{3.34}$$

$\mathfrak{F}$ in above equation is the set of dark frames used, which contains $N_{\mathfrak{F}}$ frames, i is the index of the respective frame.

To filter line and column effects from the offset, the so-called *residual offset* $\hat{o}_{c,r}$ is calculated by first subtracting the median of each column $\tilde{o}_c$ and then the median of the resulting row-values $\widetilde{o'}_r$ from $o_{c,r}$.

$$\begin{aligned} o'_{c,r} &= o_{c,r} - \tilde{o}_c \\ \hat{o}_{c,r} &= o'_{c,r} - \widetilde{o'}_r \end{aligned} \tag{3.35}$$

The residual offset map can reveal pixel dependent variations of the offset which can e.g. arise from fluctuations in the wafer processing (etching, sputtering, etc.).

Figure 3.27 shows an example offset map and residual offset map with the respective map value histograms. The residual offset map can be used later to detect pixels with too high offset values (see section 3.3.5).

The pixel noise $\sigma_{c,r}$ is drawn from the same set by determining the standard deviation of the signals from the offset $o_{c,r}$. The noise of the detector is comprised of two contributions: pixel noise and *common-mode noise*.

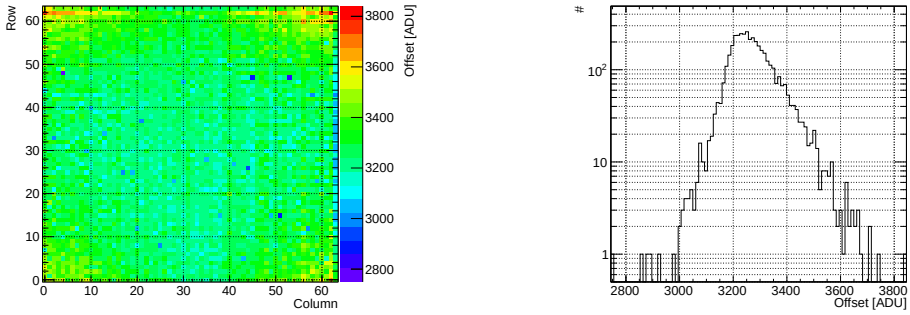

(a) offset map **(b)** map value histogram

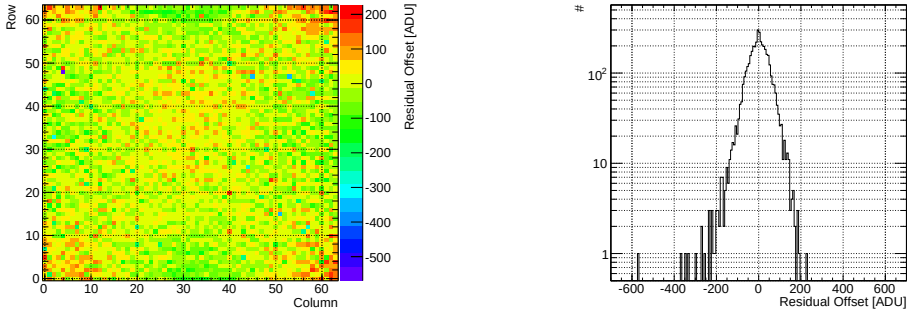

(c) residual offset map **(d)** map value histogram

Figure 3.27: Offset map (a) and residual offset map (c) of a DePFET macropixel matrix. To the right, the respective map value histogram is shown. In the residual offset map, the influence from column and row effects are filtered out by subtracting the respective median value from the pixel value.

Common-mode noise affects all readout channels equally. It is created for example by pickup which couples on the DePFET gates, leading to a change in transistor conductance, or by effects in the readout ASIC which affect all channels similarly [36].

The common-mode noise is corrected by subtracting the respective row median $\widetilde{s'_{i,r}}$ from the difference between the pixel signal $s_{i,c,r}$ and the offset $o_{c,r}$.

$$\begin{aligned} s'_{i,c,r} &= s_{i,c,r} - \overline{s_{i,c,r}} = s_{i,c,r} - o_{c,r} \\ s''_{i,c,r} &= s'_{i,c,r} - \widetilde{s'_{i,r}} \end{aligned} \tag{3.36}$$

This *common-mode correction* is also applied when photon frames (i.e. frames containing photon signals) are analyzed. Using the median makes the method robust to the presence of single photon signals within the row.

As long as within a row the number of photon signals is small compared to the

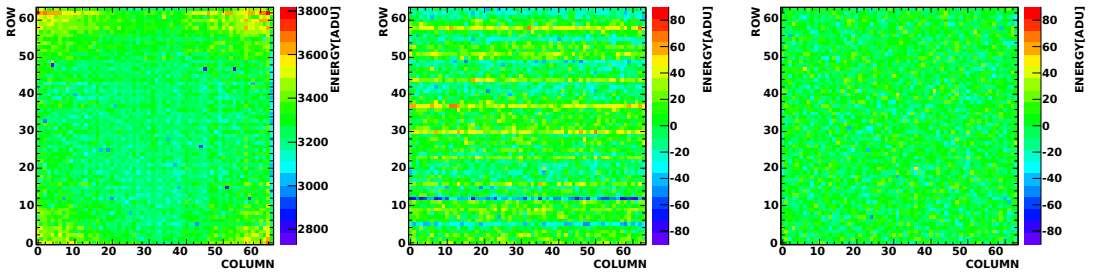

(a) raw frame **(b)** offset corrected **(c)** common-mode corrected

Figure 3.28: Effect of offset and common-mode correction on a frame. (a): The original non-illuminated frame. The pixel values are dominated by the offset values (compare to figure 3.27a). Structures like e.g. higher values in the corners can be observed. (b) The same frame after offset subtraction. The image now shows the matrix noise, especially the common-mode noise, which appears as horizontal stripes. (c): When applying the common-mode correction, the matrix shows the pixel noise only.

number of pixels, the median presents a good estimator for the common-mode noise. An alternative would be e.g. the use of a truncated mean [36].

Figure 3.28 shows the effect of the offset subtraction and common-mode correction. Figure 3.28a shows the original non-illuminated frame, in which the signal values are dominated by the offset values.

When subtracting the offset values, the noise becomes visible. It is clearly dominated by the common-mode, which appears as horizontal stripes in figure 3.28b. When correcting the common-mode noise as well, the frame presents only the pixel noise (figure 3.28c).

The pixel noise $\sigma_{c,r}$ is calculated from the common-mode corrected values $s''_{i,c,r}$ of the same frame set $\mathfrak{F}$ as the offset $o_{c,r}$:

$$\sigma_{c,r} = \sqrt{\frac{1}{N_{\mathfrak{F}} - 1}\left(\sum_{i\in\mathfrak{F}} s''^{2}_{i,c,r} - N_{\mathfrak{F}} \cdot \overline{s''_{c,r}}^{2}\right)} \tag{3.37}$$

The frames shown in figure 3.28 were taken with a "Simbol-X quadrant" macropixel matrix. More on its noise and offset characteristic can be found in section 4.2.1.

3.3.1.1 Correction for MIP events

As mentioned above, offset and noise are calculated from a set (a usual number are 200 frames) of dark frames, i.e. there is no source illuminating the detector. As it is quite easy to switch off an X-ray tube or to move away a radioactive source, there is a source of radiation that cannot be shielded easily: cosmic rays.

This radiation – which mainly consists of muons – deposits charge into the detector which creates a signal that can alter the result of offset and noise calculation. The offset as the mean over the data set is less affected than the noise, because the MIP signal presents an extremely large variation in the data set. Therefore these events have to be avoided or filtered out.

As they impinge from above, a vertical positioning of the detector helps to reduce MIP events as this reduces the cross section. But still, these events can happen and in this case they affect more pixels along their track through the detector volume compared to a horizontal positioning.

A rough estimate with a muon rate r of 100 to 200 muons per second and square meter gives for a vertically positioned macropixel detector with 3.2 cm edge width and 450 µm thickness a rate r of 0.1 to 0.2 muon hits per minute. The probability that the detector is hit by at least one MIP is given by

$$P(X \geq 1) = 1 - P(X = 0) = 1 - \frac{\lambda^0 e^{-\lambda}}{0!} = 1 - e^{-\lambda} \tag{3.38}$$

assuming MIPs are Poisson distributed.

With $\lambda = r \times t$ and a measurement time t of two minutes we get a probability of 25 %. If we increase t to 8 minutes the probability becomes even 80 %.

This estimate is only for particles with vertical incidence. But the detector can also be hit by particles with slightly inclined paths which cross the detector somewhere in-between, meaning the hit probability is thus higher.

For 200 frames, which is the usual sample size for the dark-frame set, a measurement time of only 80 ms is needed. This of course gives a very low probability for a MIP hit (0.02 %) during that time with the above assumption. However, MIPs create a large amount of charge when hitting the detector and thus distort the calculated values for offset and noise of the affected pixels.

An approximate value for the stopping power is 2.3 MeV/cm, the muons have an average energy of 3 GeV at sea level. If we assume that the muon passes through 2 cm of the detector material we get an energy deposit of approximately 5 MeV. With an electron-hole pair creation energy of 3.65 eV this means $1.4 \cdot 10^6$ electron-hole pairs.

Along its path there are roughly 40 pixels so each pixel gets an average charge of 35000 electrons. For comparison: A photon from an ^{55}Fe source which is usually used for calibrations has an energy of 6 keV and deposits thus 1650 electrons in one pixel. These high signals can falsify the offset and noise of the affected pixels if they are not taken out. So, though they are rare it is desirable to filter them out.

There are two methods to filter MIP events: *frame rejection* and *min/max rejection* [61], which will be described in detail next in section 3.3.1.2 and section 3.3.1.3.

The min/max-rejection algorithm stems from the in-house CCD data analysis software "HLLSAS" and was re-implemented within the scope of ROAn and adapted to the needs of DePFET pixel analysis. The frame-rejection algorithm was developed within the scope of this thesis.

The next two sections will describe the two MIP filtering methods. For investigation they have been applied to a simulated data set. The data set comprises frames with 64×64 random pixel signals, in which all values have a Gaussian distribution with a mean of 1000 ADU and variance of 12 ADU.

Each algorithm returns an offset map and a noise map for this data set. From each map the mean and the variance can be retrieved, which serve as a measure for how precisely the algorithm can reproduce the real offset or noise value respectively.

The number of frames can be varied to test the algorithm results with respect to the sample size. To test the behavior of the algorithm to the presence of MIP signals, frames with very high signal values (15 000 ADU) are introduced into the data set. Their impact on the mean offset and noise values and their respective uncertainties can be studied then.

3.3.1.2 Min/max rejection

The min/max rejection method discards a certain amount (N_{MIP}) of smallest and largest signal values for each pixel regardless of the presence of a MIP event. The number of extremal pixel values N_{MIP} is called the *cutoff*. With this method (3.34) becomes

$$o_{c,r} = \frac{1}{N_{\mathfrak{F}} - 2 \cdot N_{MIP}} \left(\sum_{i \in \mathfrak{F}} s_{i,c,r} - \sum_{i \in \mathfrak{L}_{c,r}} s_{i,c,r} - \sum_{i \in \mathfrak{H}_{c,r}} s_{i,c,r} \right) \tag{3.39}$$

with $\mathfrak{L}_{c,r}$ and $\mathfrak{H}_{c,r}$ being the set of indices of the lowest and highest signal values of pixel $[c, r]$ respectively. Both sets have N_{MIP} entries which have to be subtracted from the overall number of frames used.

These values must also be excluded when calculating the noise:

$$\sigma_{c,r} = \sqrt{\frac{1}{N_{\mathfrak{S}} - 1} \left(\sum_{i \in \mathfrak{S}_{c,r}} s''^2_{i,c,r} - N_{\mathfrak{S}_{c,r}} \cdot \overline{s''_{c,r}}^2 \right)} \tag{3.40}$$

Here $\mathfrak{S}_{c,r}$ is the set of all frame indices used to calculate the noise for pixel $[c, r]$ except for its N_{MIP} highest and lowest values. Each set contains $N_{\mathfrak{S}} = N_{\mathfrak{F}} - 2 \cdot N_{MIP}$ indices.

Figure 3.29 shows mean offset and noise values over the different number of frames from the simulated data set. The data set contained no MIP signals in this case. Results for two different cutoff values are shown.

The calculated mean offset is stable over the number of frames used and close to the simulated value of 1000 ADU. The uncertainty reduces the more frames contribute. The value for the cutoff has no strong impact on the mean offset and

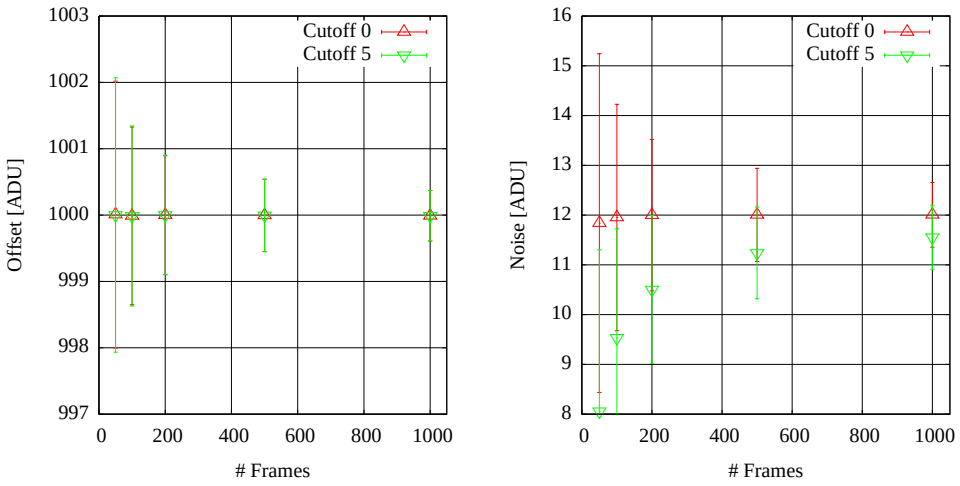

(a) offset values **(b)** noise values

Figure 3.29: Offset and noise calculated with min/max-rejection method for data sets with different number of frames. Data for two cutoff values are shown. The mean offset (a) shows no dependence on the cutoff and reaches the simulated value of 1000 ADU. When a non-zero cutoff is applied, the mean noise (b) does not reach the simulated value of 12 ADU and shows a dependence on the number of frames in the data set. For a cutoff of 0, the algorithm reproduces the simulated noise value. The slight decline of the mean noise for ≤ 100 frames is more likely due to the sample size.

its uncertainty, the points and error bars for both results overlap closely.

With a cutoff of 0, the calculated mean noise value matches the simulated one. The slight decline for small frame numbers ($\leq$ 100 frames) is more likely because of the small data set. Like for the mean offset, the uncertainty declines the more frames are within the sample.

For a non-zero cutoff, the calculated noise shows a strong dependency with respect to the number of frames. Also the noise is underestimated; the simulated value of 12 ADU is not reached even with 1000 dark frames. This is no surprise, because by filtering the smallest and largest values from the data set for each pixel, those values which contribute most to the variance are removed.

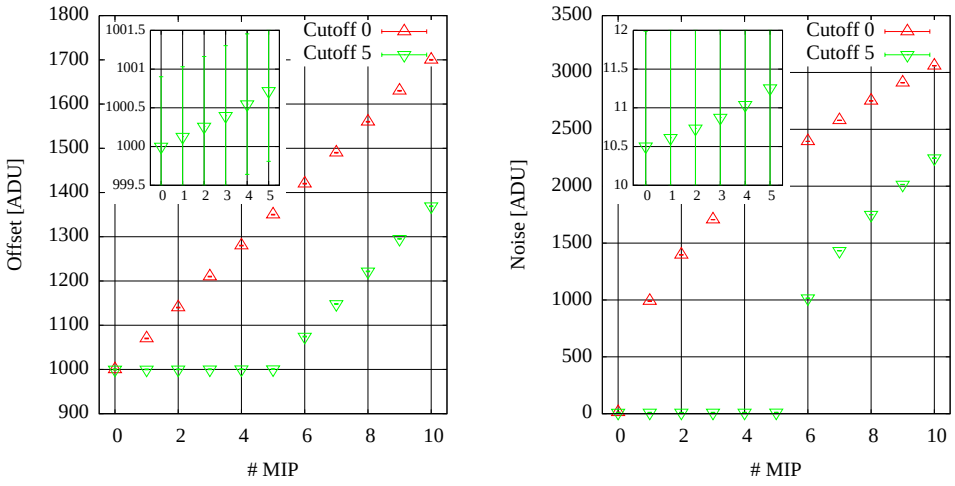

(a) offset values **(b)** noise values

Figure 3.30: Mean offset and noise calculated with min/max-rejection over number of MIPs. The mean offset is affected by the presence of MIP signals, even if they are filtered (see zoom in figure 3.30a). The noise values are stable. However, the original mean noise of 12 ADU is not reproduced when filtering is applied.

Figure 3.30 shows the calculated offset and noise over the number of MIPs within the sample. The total number of frames in the set was 200.

With no filtering (cutoff 0) - or when the filter is full - the offset increases the more MIPs are within the sample (see figure 3.30a). But also when the number of MIPs is smaller than the chosen cutoff, there is an influence on the offset value as shown in the zoom in figure 3.30a. However, the change is less than 1 ADU for 5 MIPs.

The rise of the offset for a filtered MIP signal can be explained as follows: For the assumed Gaussian noise extreme values are rare. Therefore a MIP will most likely replace a signal close to the distribution center than one from the border.

When a MIP event is within the sample it thus "pushes" a high value out of the filter back into the sample set, but the set of filtered low values stays the same. This means there is now a higher value within the set the offset is calculated from. Therefore the offset rises, even if the MIPs are filtered out.

For the noise a similar behavior as for the offset can be observed (see figure 3.30b). The noise rises when MIP signals are filtered out (see zoom in figure 3.30b), also here the change is less than 1 ADU for 5 MIPs.

When the filter is full or in case of no filtering, the drastic impact of MIP signals on the noise value can be observed. The calculated uncertainty rises slightly the more MIPs are within the sample, yet the change stays below ±2 ADU.

3.3.1.3 Frame rejection

The frame rejection method applies a threshold to each pixel to detect MIP events. Whenever a pixel signal exceeds the threshold the current frame is discarded. This way (3.34) and (3.37) are now calculated upon a set of frames where no pixel exceeds the threshold and thus can be assumed to contain no MIP signal.

The threshold for each pixel is calculated by adding a fixed step to its first-frame signal. The first frame of a set thus serves as a prototype for the pixel offset (as shown in figure 3.28a, the raw frame is dominated by the offset).

Of course, it has to be checked that it contains no MIP signal. Currently, this is done manually by visual inspection. Later this could be automatized as well. The threshold has to be chosen large enough (e.g. 500 ADU) such that only MIP events exceed the threshold, yet normal pixel noise stays below it.

Figure 3.31 shows the offset and noise over the number of frames. The algorithm was applied to the same data set as the min/max-rejection method in figure 3.29. The retrieved mean values for both, offset and noise, are close to the simulation input and stable with respect to the number of frames used for calculation.

There is only a slight decrease in mean noise for small frame sets ($\leq$ 100 frames), which can be again attributed to the small sample size. This has also been observed with the min/max-rejection method. A number of 200 frames delivers a result for noise and offset with a deviation of approximately ±1 ADU.

Figure 3.32 shows again offset and noise calculated upon a data set of 200 frames with the same input parameters as above, but now with different numbers of MIP events within the sample. The mean offset and noise show no significant dependency upon the number of MIP events.

Of course, due to the way the frame-rejection algorithm works, the sample

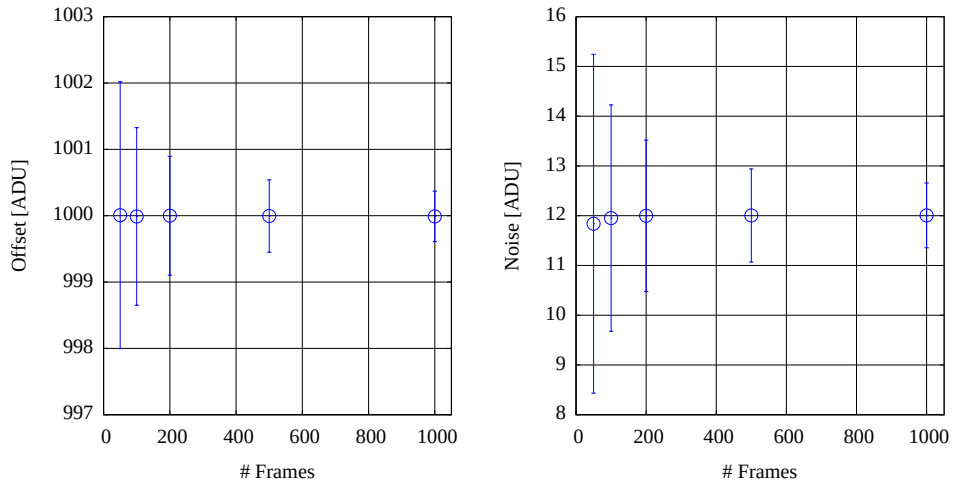

(a) offset values **(b)** noise values

Figure 3.31: Mean offset and noise calculated with frame rejection upon the simulated data set. The data set contained no MIP signals. The calculated mean offset and noise reproduce the original values (offset 1000 ADU, noise 12 ADU) very well. The slight decline of the mean noise values for small data sets (< 100 frames) can be attributed to the small sample size.

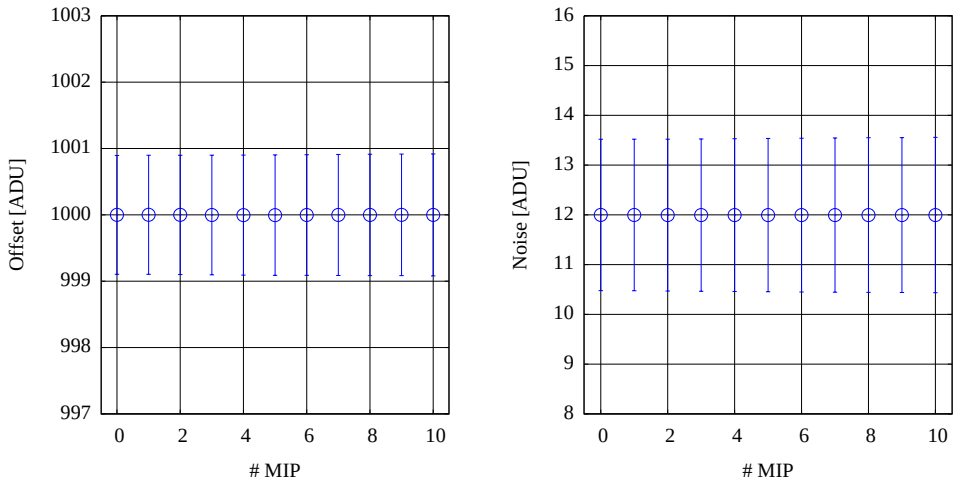

(a) offset values **(b)** noise values

Figure 3.32: Mean offset and noise calculated with frame rejection upon 200 frames. The offset and noise values show no dependency upon the number of MIP signals in the simulated sample.

size upon which offset and noise are calculated is decreased by the number of MIP signals. In the case of 10 MIPs, offset and noise are calculated from 190

instead of 200 frames then.

The results presented in figure 3.32 also show that the reduction of the dark-frame set by 10 frames has no apparent effect for a total sample size of 200 frames. However, given the rareness of MIP signals the expected number of discarded frames will be more in the range of 0 to 1.

3.3.1.4 Comparison

The frame-rejection method discards a whole frame whenever a MIP event is detected. This reduces the data set the offset and noise is calculated from, but makes the calculation of offset and noise more stable with respect to the number of frames used and the number of MIPs within the sample. As MIP signals are rare, only a minimal number of frames (0 to 1) is expected to be discarded at all, and the reduction showed no apparent effect for a total sample size of 200 frames.

The min/max-rejection filters a fixed number of signals per pixel from the data set offset and noise are calculated from. This introduces a strong dependency on the number of frames and MIPs, especially for the noise. Also the noise is underestimated when a non-zero cutoff is applied.

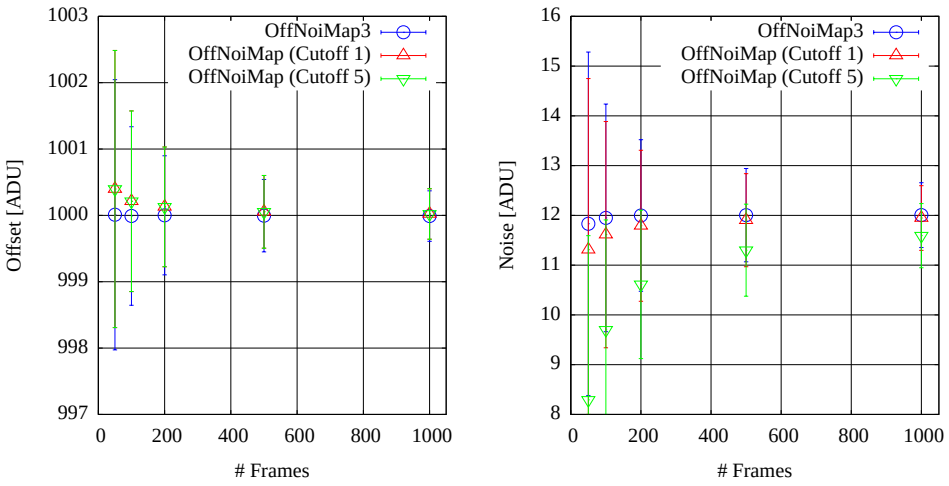

(a) offset values **(b)** noise values

Figure 3.33: Comparison of algorithms results for offset (a) and noise (a). The results were calculated from a simulated data with an offset of 1000.0 ADU and a noise of 12.0 ADU and which contained a single MIP signal. The calculated offset values differ for small sample sizes ($\leq$ 200 frames). The strongest difference is the underestimation of noise by the min/max-rejection algorithm.

Figure 3.33 shows a comparison of the two calculation methods for the simulated dark-frame set containing a single MIP signal. Figure 3.33a shows the mean offset, figure 3.33b the mean noise with respect to the number of frames used for calculation.

The offset is less affected by the filtering method, the values differ for only for dark-frame sets with less than 200 frames. The min/max-rejection method underestimates the noise the larger the cutoff value is, for dark-frame sets with more than 400 frames this underestimation is less than 1 ADU even for a cutoff of 5.

So, by using enough frames and choosing a small cutoff value the disadvantage of the min/max-rejection algorithm can be reduced, but then the algorithm has to be adapted to each measurement.

The advantage of the min/max-rejection algorithm is that it is still applicable in the presence of a photon field, e.g. when no dedicated dark frame measurement is possible and all frames in the set contain signals.

However, the frame-rejection algorithm presents the better, flexible solution for laboratory conditions where dark frame measurements can be taken. It is also applicable when a weak source is disturbing the dark frame measurement ("weak" in this case means that still most of the frames within the set are empty, i.e. contain only detector noise).

If (MIP) signals are present, they are detected and filtered out. Otherwise the complete frame data set is used and the offset and noise values are calculated with best accuracy. Frame rejection was also applied to the measurements presented in chapter 4.

Figure 3.34 shows the effect of such a MIP hit on a noise map and the results of the filtering methods. These maps were calculated from real detector data.

The MIP is the red streak in the bottom right quadrant of the map shown in figure. The limits for the noise values have been limited to 7 to 18 for better visibility (the actual values of the MIP pixels are much higher) and to make the images comparable.

Figure 3.34c shows the filtered noise map when applying the frame-rejection method, figure 3.34e the filtered noise map with min/max-rejection method with a cutoff of 5. The respective map value histogram (figure 3.34f) reveals that the min/max rejection returns a lower mean noise than the frame rejection method. The distribution of noise values for the frame-rejection method (figure 3.34d) is similar to the distribution in the unfiltered map (figure 3.34b).

For further applications, especially in environments where offset and noise are

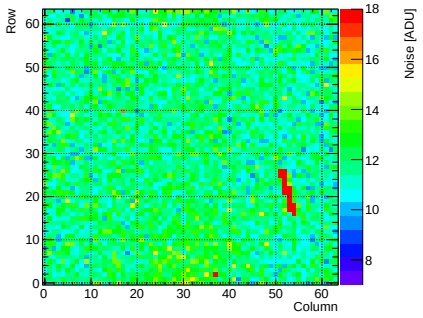

(a) no MIP filter

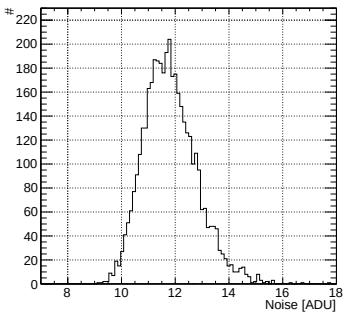

(b) map value histogram

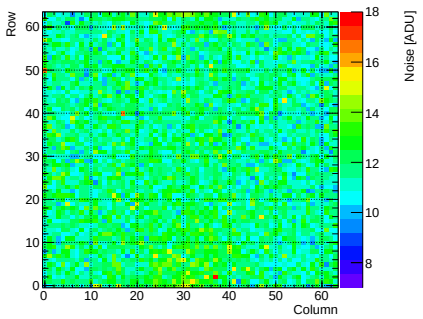

(c) frame rejection

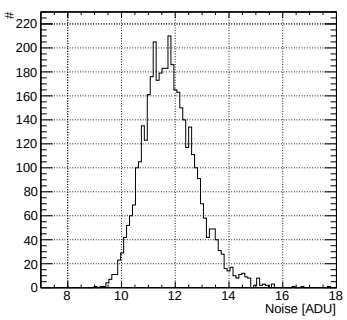

(d) map value histogram

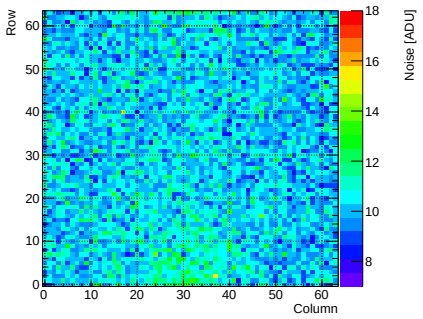

(e) min/max rejection

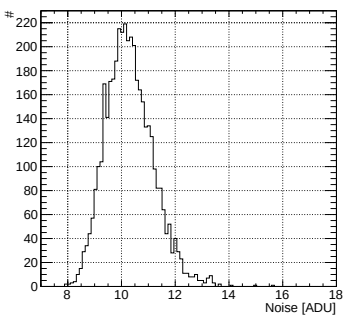

(f) map value histogram

Figure 3.34: Effect of a MIP on the noise map. All noise maps were calculated upon a set of 200 dark frames. The z-axis on all noise maps has been set to a range from 7 ADU to 18 ADU for better comparison. Figure (a) shows the noise map if calculated without any filtering applied. The MIP is the red streak in the bottom right quadrant. The range of the respective map value histogram (b) has been limited to exclude the high noise values of the pixels affected by the MIP. Figure (c) shows the noise map calculated with the frame-rejection method. The algorithm returns an equal distribution of noise values, comparing the map value histogram of this algorithm with the one without any filtering. Figure (e) shows the noise map calculated with the min/max-rejection method (with a cutoff of 5). Like the frame-rejection method, it filters the MIP signal from the data, but looking at the map value histogram it can be seen that the min/max rejection method returns a lower mean noise.

expected to change with time, new methods to determine offset and noise of the matrix will have to be investigated. A running average combined with signal detection could pose a possible solution in such cases.

3.3.2 Event filtering

The event filtering process reduces the raw data from the detector (the frames) to its essence, the photon events. It is clear that one has to take care that the right data is filtered and not accidentally thrown away. The process described here comprises three stages: filtering, pattern search, and tagging.

Filtering In the filter stage the offset and noise determined for each pixel (e.g. like shown in section 3.3.1) are used. The frame is first offset corrected by subtracting the pixel-wise offset. After that, the data is corrected for common mode noise (see also section 3.3.1), and pixel-wise thresholds for event filtering are applied.

The filtering operates with three thresholds, a *primary threshold* $T_P(c,r)$, a *secondary threshold* $T_S(c,r)$ and a *negative threshold* $T_N(c,r)$. The thresholds are individual for each pixel with column index c and row index r, but – for the sake of simplicity – from here on the thresholds are referred to only as T_P, T_S and T_N.

The primary threshold is larger or equal to the secondary, which is larger than the negative threshold.

$$T_P \geq T_S > 0 > T_N \tag{3.41}$$

The threshold are calculated for each pixel from the respective noise value σ. Usually, for the primary threshold a value of 5σ is chosen. The secondary threshold can be set lower (e.g. 3σ) to minimize sub-threshold charge loss. However, with a lower secondary threshold the chance of noise hits increases which can then falsify the primary hit signal they are clustered with.

For the macropixel matrix used at the measurements presented in chapter 4 best results were obtained when the secondary threshold was set to the same level as the primary threshold.

Everything below T_S but above T_N is discarded. A pixel signal passing this stage is called a *hit*. Pixels signals above T_P are stored in a list which is used in the clustering stage. Pixels signals below T_N – a usual value for T_N is -3σ – are an indicator for *misfit events* (compare to section 3.1.6). These pixels are handled specially in the clustering and tagging stage.

Pattern search The pattern search stage serves to improve energy resolution by recombining split events (see section 3.1.2.2). During pattern search, adjacent hits are combined to a *pattern*.

The pixels which exceeded T_P serve as starting points for the pattern search. For each pixel, the edges are searched for neighbors with positive content. If found, these pixels are added to the pattern and serve themselves as starting point for the next search round. If no new pixels are added, and all pixels have been searched, the pattern is complete. Figure 3.35 shows a visualization of the search process. Pattern search is only applied along pixel edges, not diagonally.

The pattern search for misfits is slightly different from the process described above. The nature of misfit creation forbids certain patterns (see section 3.1.6). The pattern search is modified accordingly. Negative hits are only combined to patterns when they are in the same row, combination of negative and positive hits to patterns only occurs in running direction of the rolling shutter.

Tagging The last stage of the event filtering is tagging. Although all patterns are in principle equal, there are some that stick out. The tagging stage assigns a set of flags to each pattern, which denote certain properties for later analysis. These are:

- *Overflow* and *underflow*. These flags are set whenever one of the signals contributing to the pattern exceeds the range of the ADC.

- *Invalid*. The invalid flag is set whenever the signal exceeds a limit set by the user. This is can be used to tag patterns which are within ADC range but exceed the dynamic range of the readout chip.

- *Border*. Patterns which contain a border pixel have the border flag set. It is important to tag border pixels, because undetected charge loss to the surrounding can happen here.

- *Misfit*. This flag is set for patterns which contain a negative signal. These patterns serve as a starting point when searching for misfit clusters (see section 3.3.7).

The tagged patterns are finally stored. The tagging can be refined later by additional diagnosis steps (e.g. section 3.3.6 or section 3.3.7). The pattern data is then used for detector calibrations and qualification.

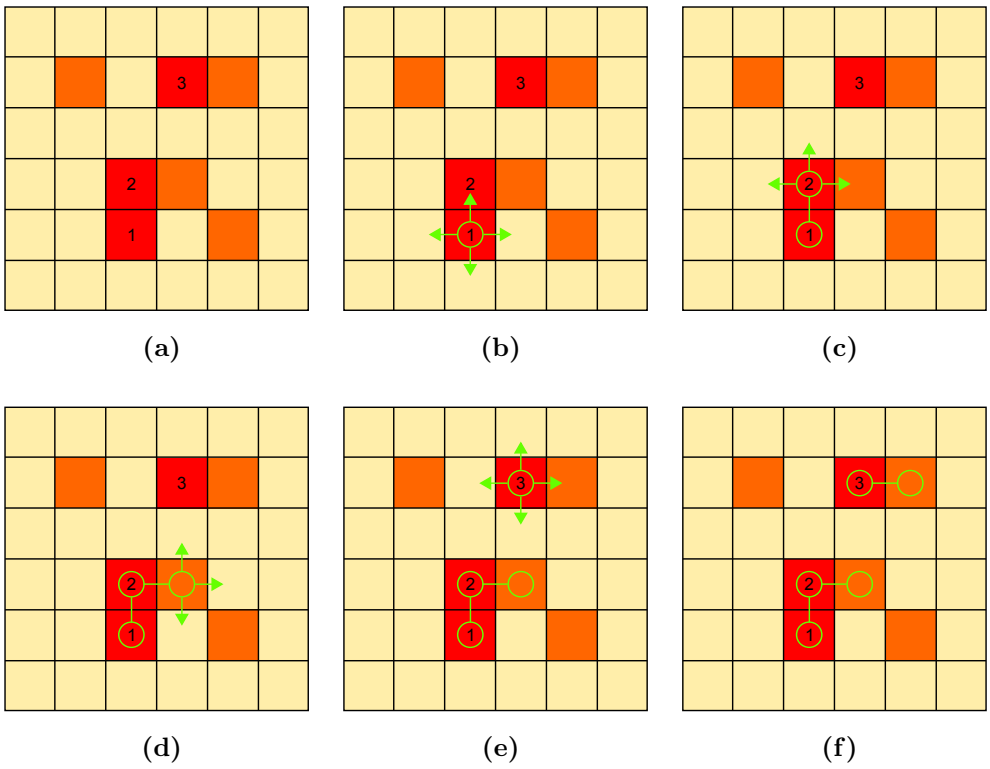

Figure 3.35: The pattern search process: (a) Initial state. The pictures show a 6×6 frame with an arbitrary hit pattern. Red pixels are above the primary threshold, orange above secondary. The pixels above the primary threshold are numbered according to their position in the search list. (b) Search starts from pixel 1, finding one adjacent pixel. (c) Search is continued, another pixel found. The pixel number 1 is marked as searched, therefore the search goes only into the remaining three directions. (d) Last pixel is searched, no more adjacent pixels found. The pattern is complete. Note that the search is performed along pixel edges, not corners. The orange pixel bottom right is therefore not detected as belonging to the pattern. (e) Because pixel 2 is already part of a pattern the next pixel searched is pixel 3. (f) Final state, 2 patterns found. Two pixels (orange, top left & bottom right) below primary threshold are discarded because they are not part of a pattern.

3.3.3 Gain map calculation

In contrast to CCDs, where only the readout ASIC is amplifying the signal, each DePFET pixel with its FET presents an amplifier on its own. Therefore each pixel has to be calibrated individually.

DePFET matrices used for X-ray imaging have at least a size of 64 × 64 pixels, which means a number of 4096 pixels has to be calibrated. Recent developments have even larger pixel counts [62, 6]. It is thus clear that this task has to be done automatically.

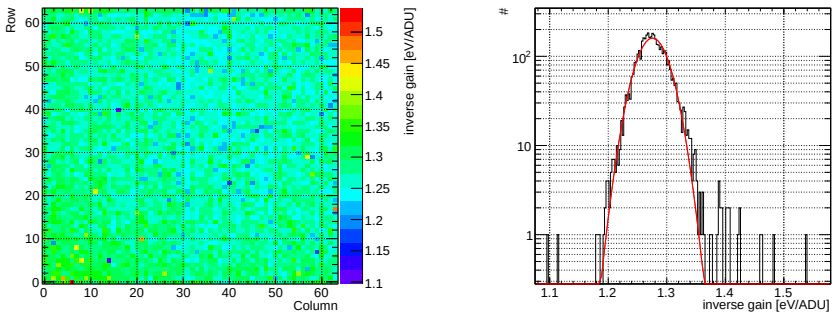

(a) gain map **(b)** map value histogram

Figure 3.36: An example gain map. The gain map shows the inverse gain values in eV/ADU as color coded values. The map value histogram reveals that most values are Gaussian distributed. The gain map has a dispersion, the variance divided by its mean, of 2 %.

The gain $g_{c,r}$ of a pixel is defined as the ratio of calibration signal $s_{c,r}$ to calibration energy E_c:

$$g_{c,r} = \frac{s_{c,r}}{E_c} \tag{3.42}$$

To determine the gain, a measurement with a monoenergetic source or source a with a distinctive line (e.g. an ^{55}Fe source) is performed, the determined peak position taken as the calibration signal and correlated with the known line energy.

This procedure has to be performed for each pixel of the DePFET matrix. The signals which can be attributed solely to a single pixel are SNG patterns. The algorithm thus creates histograms for each pixel, fills them with the found SNG events from the measurement, and finally tries to determine the calibration signal $s_{c,r}$ by applying a two stage Gaussian fit to the individual pixel histograms.

At first Gaussian fit is applied in which the mean of the Gaussian is fixed at the position of the maximum bin in the histogram. The maximum bin position serves as a first guess of the peak position. The $\pm 3\sigma$ range of the first fit then defines the fit range of the second, where the fit parameters are no longer fixed. The pixel signal $s_{c,r}$ is the mean of the final Gaussian fit.

Figure 3.37a shows a so-called column map, in which the pixel histograms for a single column of the matrix are shown together. Each row is an individual pixel histogram, the number of counts is color coded. The matrix was illuminated with an ^{55}Fe source, so the Mn-K$_\alpha$ and the K$_\beta$ peaks can be seen. The limits for all histograms were set externally to 6000 ADU to 8000 ADU. This ensures the algorithm is not distracted by e.g. a prominent noise peak.

Figure 3.37b shows such a pixel histogram and the two Gaussian fits. K_α and the K_β peak are marked by a red triangle. The first fit is shown in red, the second in green. The position of the peak is very well reproduced.

Because multiplication is computationally preferable to division, the gain map stores the *inverse gain value* $1/g_{c,r}$ for each pixel. Figure 3.36 shows an example. This way the energy of a pixel signal can be calculated by multiplying the signal value of a pixel with the respective inverse gain value:

$$E_c = s_{c,r} \cdot \frac{1}{g_{c,r}} \tag{3.43}$$

Details on this can be found in section 3.3.4.

For diagnostics, along with the gain map the algorithm stores additional information, such as whether the fit succeeded for a histogram and others, like the column maps and pixel histograms shown in figure 3.37. These can be evaluated afterwards to assess the gain map.

It is clear from the way the algorithm works that there has to be enough statistic within such a pixel histogram for the fit to succeed. From experience with calibration measurements a number of minimal 100 counts can be drawn as a rule of thumb.

As shown in section 3.1.2.2 the share of SNG events in the overall event count also depends on the pixel size. For small pixels the area where an absorbed photon creates SNG events is small compared to the total area, which prolongs

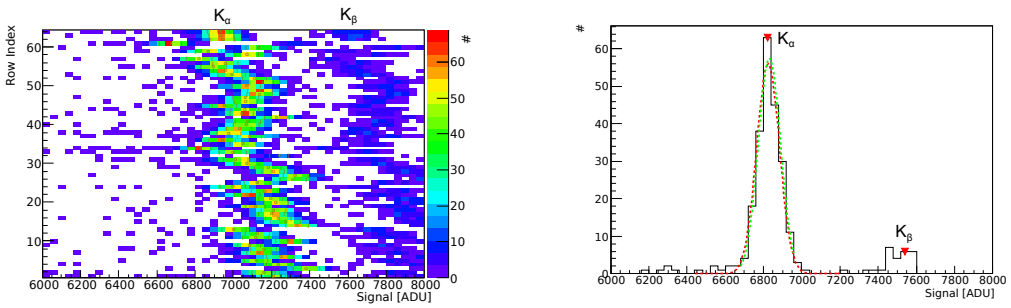

(a) column map **(b)** pixel histogram

Figure 3.37: Column map and pixel histogram. Both are diagnostic output of the gain map algorithm. The column map (a) shows the combined pixel histograms for a single column of the matrix. The histogram counts are shown color coded here. The pixel histogram (b) corresponds to a single line in a column map. The two fits applied to determine the position of the signal peak are shown. The matrix was illuminated with an ^{55}Fe source, so the K_α and K_β are visible.

the measurement time until enough SNG events per pixel have been gathered.

A remedy in such a case is to illuminate the detector from the front side. The charge cloud creation then takes place closer to the internal gate, so the charge cloud does not expand so much as in the case of back side illumination. This increases the share of SNG patterns.

The thicker and inhomogeneous layers of the processing side though worsen the peak to background, because of more incomplete charge collection, yet this is within acceptable limits. The larger problem with front side illumination is radiation damage in the interfaces and oxide layers which leads to threshold voltage shifts.

Therefore, new methods of calibration will have to be investigated, especially for large matrices like the ones designed for the IXO space mission (see section A.3) which will have a total pixel count of $1 \cdot 10^6$ (1024×1024 pixels).

Taking e.g. the mean of the gathered signals instead of doing a fit to the histogram may be a solution to cope with low statistics, iterative procedures which take not only SNG patterns into account could offer another way.

The algorithm described above is sufficient for laboratory conditions where a monoenergetic radiation source is available. It has been applied to calibrate the data from the measurements presented in chapter 4.

3.3.4 Calibration

Calibration of the pixel signals is done for each found pattern by multiplying the hit signals with the respective values stored in the gain map. For example, a DBL pattern which comprises two hits has the signal values s_1 and s_2, column indices c_1 and c_2, and the row indices r_1 and r_2. The coordinates of the two pixels in this pattern are thus $[c_1; r_1]$ and $[c_2; r_2]$.

The inverse gain values $1/g_1$ and $1/g_2$ for these pixels are retrieved from the gain map (see section 3.3.3) by looking up the respective coordinates there. For each signal an energy value e_i is calculated by simple multiplication.

$$e_i = s_i \cdot \frac{1}{g_i} \tag{3.44}$$

The total energy of the pattern E_{pat} is the sum of the energy values of the hits it comprises.

$$E_{\mathrm{pat}} = \sum_{i=1}^{N_{\mathrm{pat}}} e_i = \sum_{i=1}^{N_{\mathrm{pat}}} s_i \cdot \frac{1}{g_i} \tag{3.45}$$

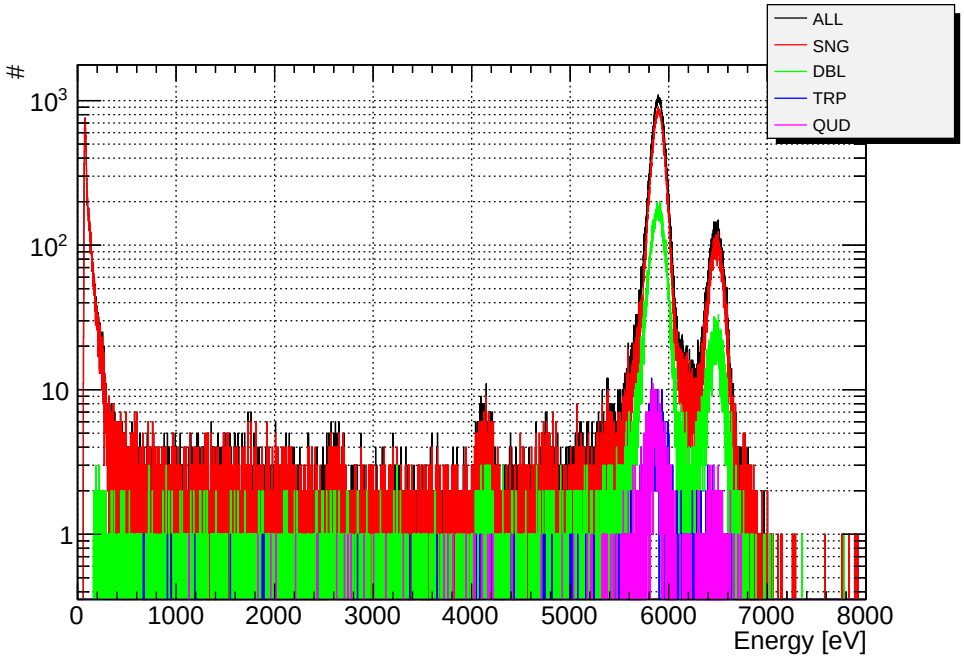

Figure 3.38: Calibrated histograms for SNG, DBL, TRP and QUD patterns, as well as their sum (ALL) for a measurement with an ^{55}Fe source. The Mn-K$_\alpha$ and K$_\beta$ can be seen.

with N_{pat} being the number of hits in the pattern, i.e. its multiplicity.

Figure 3.38 shows the calibrated spectra for valid SNG, DBL, TRP, and QUD patterns, and their combined spectrum (ALL). The measurement was performed with a Simbol-X quadrant detector matrix which has a pixel size of $500 \times 500\,\mu\text{m}^2$.

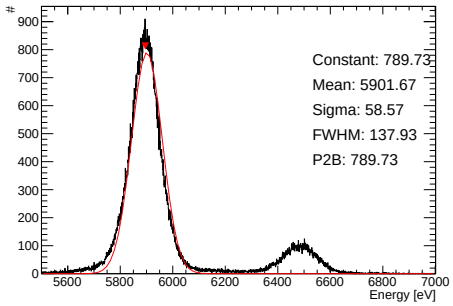

(a) SNG resolution

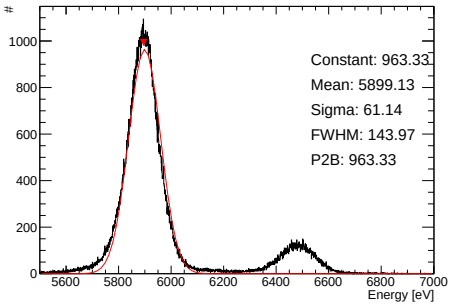

(b) ALL resolution

Figure 3.39: The energy resolution for SNG patterns (a) and for all valid patterns (b). The macropixel matrix shows an energy resolution of 137.93 eV for SNG patterns and 143.97 eV for all valid patterns at 5.9 keV.

The spectra were obtained by illuminating the detector matrix with an ^{55}Fe source, the Mn-K_α and K_β peak can be seen.

The spectra for SNG patterns and all valid patterns (ALL) from figure 3.38 can be used to determine the energy resolution of the detector. Figure 3.39 shows both spectra with a Gaussian curve fitted to it. From this fit, the energy resolution can be retrieved. This matrix shows an energy resolution of 137.93 eV for SNG patterns and 143.97 eV for *All Valids* (ALL) patterns at the energy of the Mn-K_α peak which is 5.9 keV.

3.3.5 Bad pixels

Some pixel in a matrix show erroneous behavior. This has to be identified and marked, such that patterns containing such pixels can be filtered out. Bad pixels are classified phenomenologically whether they are *bright*, *noisy*, or *dark*.

Bright pixel A *bright pixel* has an extraordinary offset. Whether a pixel is classified as bright is calculated from the residual offset map.

Noisy pixel A *noisy pixel* presents very high noise. They are calculated from the noise map.

Dark pixel A *dark pixel* has a very low gain. They are determined from the gain map. As the gain map stores the inverse value of the gain (compare to section 3.3.3), a low gain corresponds to a high value in the gain map.

Figure 3.40 shows the residual offset map, noise map, and the gain map of a DePFET matrix with a pixel defect. The defect can be clearly identified in the residual offset map (figure 3.40a) by the high residual offset.

The noise map (figure 3.40b) shows that the proximity of the pixel is affected, as well as the respective pixel column. The higher noise in the proximity of the erroneous pixel can be caused by charge injection from the defect. A defective DePFET pixel can affect its column e.g. if it is permanently switched on, thus disturbing the current flow from source to drain for the remaining pixels. Row defects are also possible, e.g. when the circuit path for the DePFET terminals (gate, cleargate and clear) is flawed.

The gain map (figure 3.40c) of the example only shows some pixels with low gain (high inverse gain values), visible as yellow and red spots distributed randomly over the matrix. As they are not connected locally to the defect, they

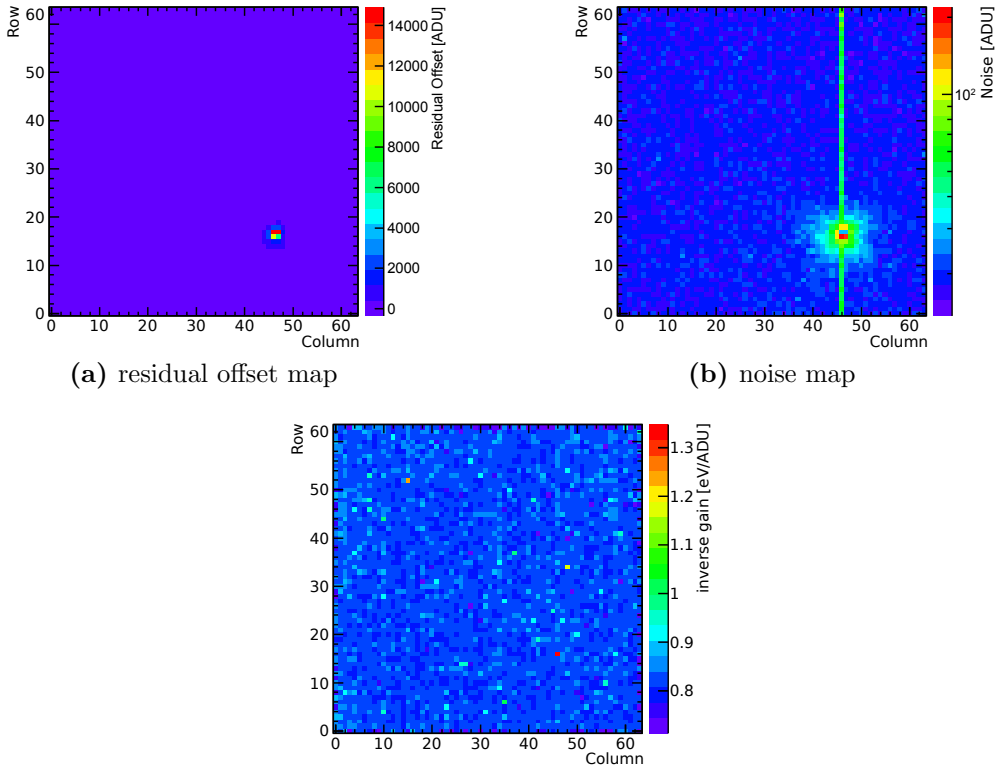

(a) residual offset map

(b) noise map

(c) gain map

Figure 3.40: Example of a detector matrix with a notable defect. The defective pixels can be clearly identified in the residual offset map (a) by their high residual offset. The noise map (b) shows that the pixel defect influences also its proximity and the related pixel column. The gain map (c) shows some pixels with low gain (high inverse gain values!) distributed randomly over the matrix.

are more likely caused by a failure when determining the gain map (compare to section 3.3.3).

There are two strategies for these maps to determine whether a pixel is marked as bad: The pixel value is compared either to a fixed user defined threshold, or to a threshold calculated from the respective map value histogram.

For the latter, the threshold is calculated from the mean μ and the variance σ of a Gaussian fit applied to the map value histogram. The threshold is equal to $\mu + \delta \cdot \sigma$ where δ is a user supplied parameter.

The default value for δ is 5, so for a Gaussian distribution of map values only the extreme outliers above the average matrix value are marked as bad.

Figure 3.41 shows the three pixel maps calculated from the maps presented in figure 3.40: The bright pixel map (figure 3.41a), the noisy pixel map (figure 3.41b), and the dark pixel map (figure 3.41c). These are merged into the *bad*

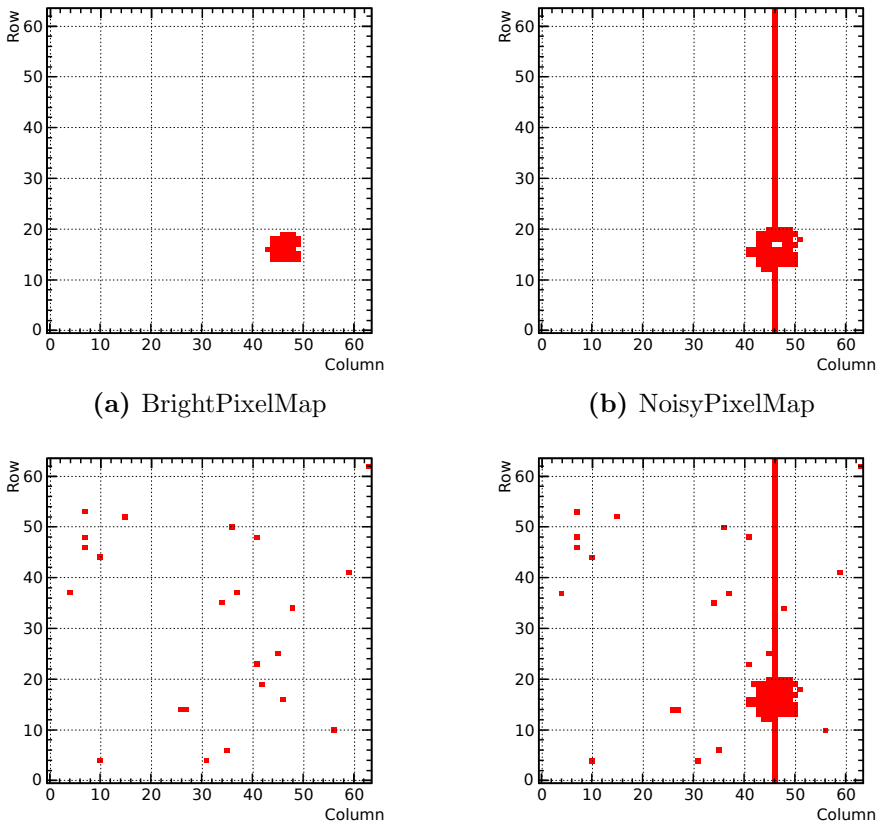

(a) BrightPixelMap **(b)** NoisyPixelMap

(c) DarkPixelMap **(d)** BadPixelMap

Figure 3.41: Bad pixel maps from the current example. The bright pixel map (a), noisy pixel map (b), and dark pixel map (c) are merged into the bad pixel map (d) which is used later to filter patterns.

pixel map (figure 3.41d), which is used later to mask pixels which the user does not want to be included in the analysis.

Optionally, pixels can be "defined" as bad by an *external bad pixel* map which is also merged into the bad pixel map. Such a map can be used e.g. to mask certain areas of the matrix.

In chapter 4 such an external bad pixel map was used to mask the non-illuminated areas of the detector.

3.3.6 Clear-correlation detection

A clear-correlation cluster comprises signals from a single pixel which spreads over consecutive frames. Therefore, a pattern with n components can contain n clusters. The first hit of a cluster is called the *precursor*, the other hits are called

successors. A pixel hit with no successor is a cluster with length 1. If a pixel shows no signal in a frame (i.e. it is below the event discrimination threshold), the frame is referred to as *empty* (for this pixel).

Because clear-correlations (see section 3.1.5) create a low energy background it is desirable to detect them, so the matrix can be biased optimally. Also tagging clusters in the measurement data and filtering them out can improve the spectra created later.

The cluster filtering traverses the list of events and checks for each whether their pixel components are part of a clear-correlation or not. If this is the case, it is added to this cluster, if not, it serves as a starting point for a new cluster.

For a single pixel, figure 3.42 shows different situations that can be encountered while scanning the data for clear-correlations and how they affect the clustering. The criteria whether a pixel belongs to a clear-correlation cluster are:

- The pixel coordinates match the cluster coordinates.
- The pixel hit signal is lower than the last signal in the cluster. Thus the signal values decline over the cluster (compare to figure 3.42b).
- The pixel signals are in consecutive frames (compare to figure 3.42c).
- The cluster does not consist of a negative signal (compare to figure 3.42d).
- The pixel hit signal is not negative (compare to figure 3.42e).
- The pixel hit signal is below a threshold value (compare to figure 3.42b). The threshold value can be used to tighten the second condition.

Each cluster found by the algorithm is numbered consecutively which gives them a unique id. For each event entry the ids of the single pixel components are stored, along with the length, the index (position within cluster) and other data useful for later analysis.

3.3.7 Misfit cluster detection

The algorithm for the detection of misfit clusters is quite similar to the detection of clear-correlations (section 3.3.6). In both cases one has to investigate the behavior of a pixel from frame to frame.

The found clusters are then marked for further analysis. As already stated in section 3.1.6, only negative misfit clusters can be detected while positive misfit clusters blend with the detector signals.

The criteria for a misfit cluster are

- The first pattern in the cluster contains a negative misfit hit, i.e. a negative signal.

- The second pattern in the cluster is covered by the first, the negative signal in the pixel is followed by a positive signal in the next frame.

Just like clear-correlation clusters, misfit clusters receive a unique id which is stored along with additional information about the cluster parallel to the information gathered at the event filtering (see section 3.3.2).

In contrast to clear-correlation clusters which can have arbitrary length, misfit clusters have a fixed length of two consecutive frames. However, the tagging as misfit cluster and clear-correlation is not exclusive. It is possible for the second pattern of a misfit cluster also to belong to a clear-correlation cluster.

A misfit cluster is created if charge is deposited during pixel readout (see section 3.1.6). A first order estimate on their frequency shall be made now. As only negative misfit clusters can be separated from other detector signals, the estimate is limited on those.

When a photon hits a pixel in the detector, a negative misfit cluster is created if the created charge is deposited within the time interval τ_{mft}, after the clear pulse and before the end of the second integration. The fraction n_{mft} of negative misfit clusters to all events is then given by the fraction of τ_{mft} to the overall time t_{frm} the shutter needs to traverse its sector on the matrix (compare to section 2.9).

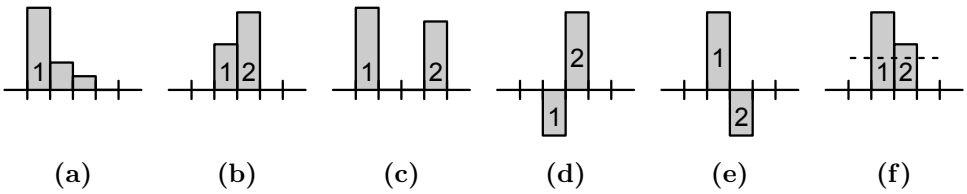

Figure 3.42: Different situations handled in the detection of clear-correlation clusters. The situations shown here are for a single pixel. The black line is the time axis, a frame is the region between the tick marks. A pixel signal in a frame is shown as a blue box. The number denotes the respective cluster, unnumbered signals belong to the cluster to their left. (a): A clear correlation cluster. (b): The signal height must decline over the cluster. (c): Pixel signals have to be in consecutive frames, to be clustered. (d) & (e) Negative signals (see section 3.1.6) are not clustered with other signals, they always form clusters on their own. (f): As an extra constraint, a threshold can be set. If the consecutive signal is above, it is not assigned to the cluster.

If the respective sector has N_{row} rows, the shutter needs

$$t_{\text{frm}} = N_{\text{row}} \cdot t_{\text{readout}} \tag{3.46}$$

for one pass. For the ASTEROID ASIC, t_{readout} is defined by equation 2.43. The fraction of negative misfit clusters is thus given by

$$n_{\text{mft}} = \frac{\tau_{\text{mft}}}{t_{\text{frm}}} = \frac{\tau_{\text{mft}}}{N_{\text{row}} \cdot t_{\text{readout}}} \,. \tag{3.47}$$

The matrix presented in chapter 4 is a 64×64 macropixel detector which was read out with a $t_{\text{readout}} = 6.85\,\mu\text{s}$. The time interval τ_{mft} for negative misfit clusters is 2.35 µs, which comprises the second integration period (1 µs) and the period of the plateau after the clear pulse[7].

With this, the equation 3.47 yields

$$n_{\text{mft}} = \frac{2.35\,\mu\text{s}}{64 \cdot 6.85\,\mu\text{s}} \approx 0.5\,\% \tag{3.48}$$

which is a small contribution to the spectrum, especially because the signal values are distributed between 0 and s, the respective signal value of the photon event (see section 3.1.6).

Figure 3.43 shows the rate of misfits of a measurement with a monoenergetic synchrotron light source (see chapter 4) at 1.9 keV. The misfit rate was determined by dividing the number of misfit clusters (detected with the algorithm above) by the number of all events found. Figure 3.43a shows the rate if only SNG patterns are considered, figure 3.43b if all valid patterns (ALL) are considered. The mean over the map is 0.5 % for SNG patterns which conforms with the estimate from equation 3.48.

The influence of the event discrimination threshold was neglected in equation 3.48. If the photon impinges short before the end of the second integration period, the negative signal created may be too close to 0 and thus discarded. This threshold effect reduces the effective τ_{mft}. However, if a photon hits the detector at the end of the clear pulse, it is possible that not all of the charge is removed from the internal gate. If the remaining charge is large enough, it can still create a negative signal below T_N and a positive above T_P (see section 3.3.2), i.e. create a negative misfit cluster. This effect would extend the effective τ_{mft}.

For a matrix with only one readout ASIC, the sector is identical to the whole

[7] The plateau has a length of 2.5 µs from which the 0.6 µs clear pulse and the pause before it (0.55 µs) has to be subtracted.

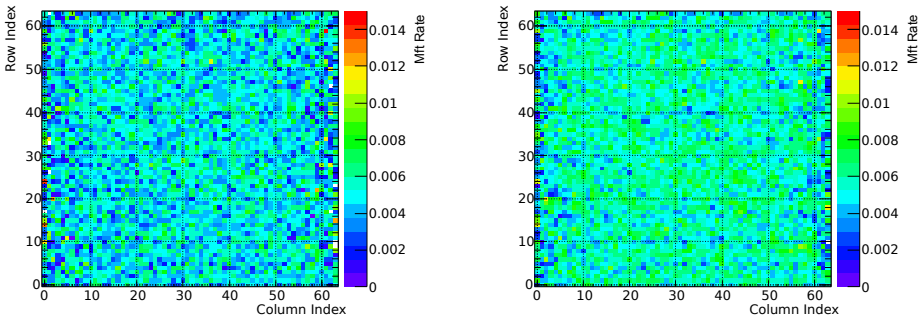

(a) SNG patterns **(b)** ALL patterns

Figure 3.43: Misfit rate distribution for a monoenergetic measurement at 1.9 keV. The misfit rate is the number of (negative) misfits per pixel divided by the number of overall events per pixel. (a): Only SNG patterns have been considered. The mean value over the matrix is 0.5 % with a variance of 0.2 %. (b): When taking all valid patterns into account, the mean rate over the matrix rises to 0.6 % with a variance of 0.1 %.

matrix. However, if the detector matrix is separated into hemispheres, N_{row} is of course half of the rows of the whole DePFET matrix. Especially when windowing is applied, i.e. only a small subarea of the matrix is read out, N_{row} is the number of rows within the window, which is small and t_{frm} accordingly shorter.

Thus, faster readout of the matrix, either by limiting the readout area or by using faster readout sequences (shorter t_{readout} and thus shorter τ_{mft}), increases the misfit probability for a photon event.

Comparing figure 3.43b to figure 3.43a shows that charge splitting influences the detected number of misfit clusters. Apparently, overlapping of patterns leads to fake misfit clusters detected by the algorithm. This has to be investigated, especially for readout methods for which misfit clusters are more prominent. For the matrix studied in chapter 4, the overall effect of misfit clusters is small and therefore neglected.

3.3.8 Generation of analysis results

The event filtering step (section 3.3.2) creates an *event list* in which each detected event is entered along with its information like position on matrix, pattern type, hit signal values, and so on. Steps like calibration, the detection of clear correlations (section 3.3.6), or misfit cluster detection (section 3.3.7) add additional information to the list of properties for each event.

These properties can be used to filter erroneous data coming from pixels

marked as "bad" (see section 3.3.5). Also filtering can be applied to investigate a subset of the event list, e.g. create a spectrum for each pattern type (see figure 3.38).

Creating a result out of data from the event list usually has the following approach:

- Traverse the event list
- For each event in the list decide whether it matches the filter conditions
- Perform additional calculations, if necessary, and enter event data into the result

For the generation of such results there is an extra step which allows to create several different results from the event list in parallel. This step implements a general method, which the user can use to create a customized set of histograms. This is done by using *spectrum factories*, *spectrum generators* and *spectrum filters*.

A spectrum factory is a container for an arbitrary number of filters and generators. A generator is comparable to a step (see section 3.2.2). It also states the results it produces, its parameters and dependencies needed. The same holds for spectrum filters, which also have dependencies and parameters except filters do not produce any results.

The dependencies and parameters of the filters and generators are collected by the step and handed over to the analysis instance for coherence checking.

The spectrum generation step can contain one or more spectrum factories, each with its generators and filters. When producing the designated spectra, the step has to be loaded with the parameters for its factories and the respective generators and filters. Afterwards, the step sets up access to the requested data from the event list.

This approach gives the analyst a great deal of flexibility. He can let the analysis software create the same histograms in different runs with a different filter set. Also several results can be created in a single pass through the event list. If each result was calculated by a dedicated step, there would be one pass for every result. For a large number of results and a large event list this can become time-consuming. Filters and generators have defined interfaces which makes it easy to implement new filters and generators and use them in the analysis.

Figure 3.44 shows a simplified schematic of the result generation process, which nevertheless displays the most important aspects of it.

The event list data is stored in so-called *trees*, a data structure provided by the ROOT framework. These trees can be combined to form a unified data set

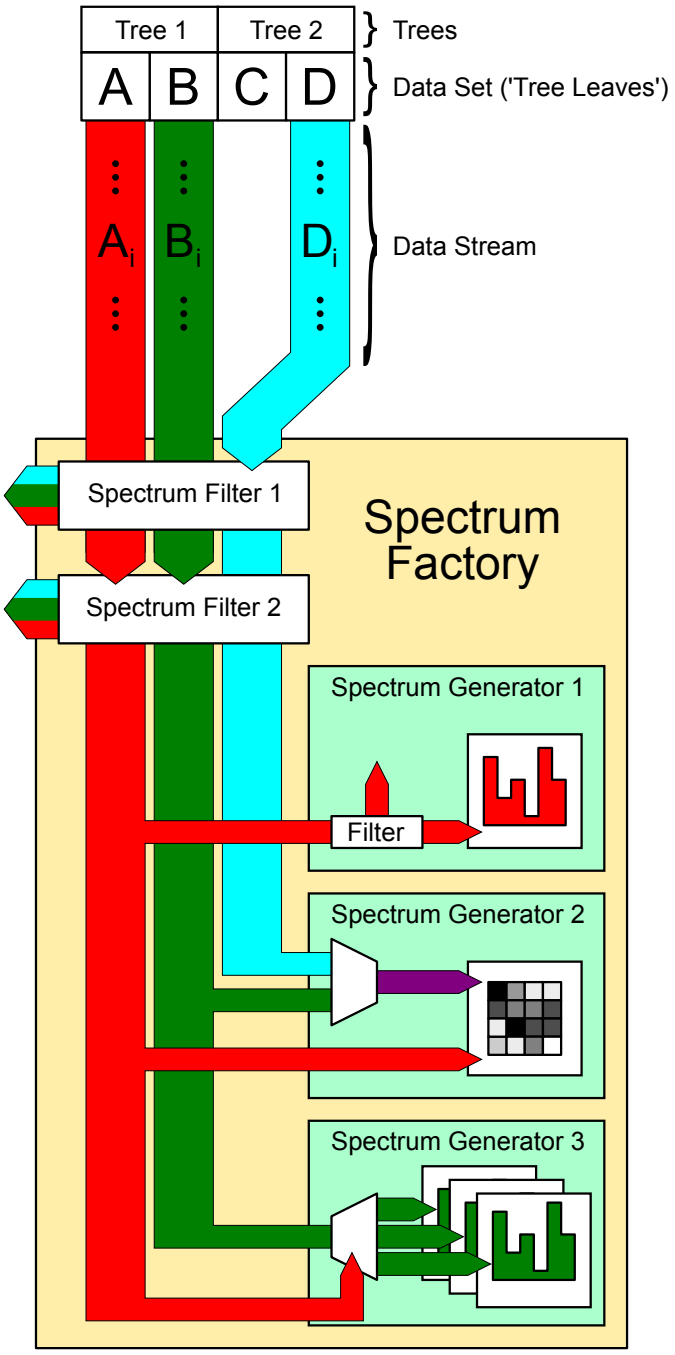

Figure 3.44: Overview of the spectra generation. The data stream is fed into spectrum factories, which filter the data and lead the stream to their spectrum generators. These can apply own filters to data variables (e.g. Spectrum Generator 1), do extra calculus on the data (e.g. Spectrum Generator 2), or use one variable to discriminate between another one (e.g. Spectrum Generator 3). See the text for a detailed explanation of the picture.

from their leaves, i.e. the variables stored in them. From this data set the needed ones are picked out and fed into a data stream which is lead to a set of *spectrum factories*.

Only a single spectrum factory is shown in figure 3.44. While the number of filters within a factory can be zero, i.e. no filtering applied) there has to be at least one generator associated with this factory.

The data stream in the example consists of the data variables A, B and D (C has not been selected). The spectrum factory first applies a number of filters (the number can be zero, i.e. no filtering applied then) to the data stream. The filters are daisy-chained, meaning data passing one filter is fed into the next.

As shown in figure 3.44, Spectrum Filter 1 takes variable D to decide whether to accept or discard the current data set, while Spectrum Filter 2 takes only A and B. The important thing is that the whole data set is discarded if a test is not passed. Data that has passed all filters is then led to the *spectrum generators* associated with the factory.

The generators are units that, like analysis steps, encapsulate an algorithm, take parameters and produce results. They can apply own filtering to the data coming in (see Spectrum Generator 1 in figure 3.44), use the data variables to calculate new values (see Spectrum Generator 2) or use one variable to discriminate between the values of another (see Spectrum Generator 3).

4. Detector response and quantum efficiency measurements

The Simbol-X quadrant matrix detector has at present with $3.2 \times 3.2\,\mathrm{cm}^2$ the largest active area of a DePFET matrix (see figure 2.32). Additionally it presents a detector with an extraordinary large pixel size of $500 \times 500\,\mu\mathrm{m}^2$. From this point of view it was of particular interest to

- to determine the homogeneity of the detector matrix with respect to parameters like offset, noise and gain,
- to study the charge collection within the macropixel,
- to investigate the linearity of the device,
- to determine the detection efficiency of the entrance window.

A macropixel matrix designed for the in the meantime abandoned space mission Simbol-X was exposed to monoenergetic and to polychromatic radiation in the radiometric laboratory of the *Physikalisch Technische Bundesanstalt* (PTB) at the electron storage ring BESSY II.

The measurements served in addition as a test run for later qualification and calibration measurements with the BepiColombo flight module. In the BepiColombo mission, a DePFET matrix will be used as focal plane array in the *Mercury Imaging X-ray Spectrometer* (MIXS) device, which will perform planetary X-ray fluorescence analysis (see section A.2 for details).

To decipher the X-ray fluorescence spectra that will be taken from planet Mercury it is vital to know the response of the detector to photons of different energies (linearity) as well as the distribution of properties like gain over the matrix (homogeneity). Also the detection efficiency, the probability for a photon to be registered when hitting the detector, is of importance when one wants to draw element abundances from X-ray fluorescence spectra.

Both detectors, the Simbol-X quadrant matrix and the BepiColombo matrix, are 64×64 macropixel DePFET detectors. The Simbol-X device has a larger pixel size (Simbol-X: $500 \times 500\,\mu\mathrm{m}^2$, BepiColombo: $300 \times 300\,\mu\mathrm{m}^2$) and a 50 nm

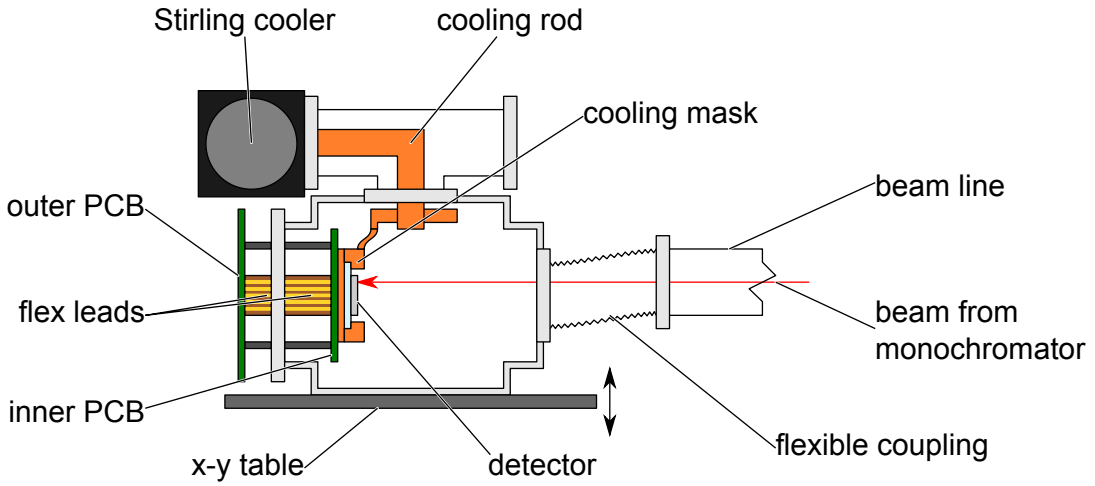

Figure 4.1: Schematic of the measurement setup used at BESSY II. The tank mounted on the x-y table houses the detector assembly described in section 2.10. It is attached to the beamline by a flexible coupling and can be moved with respect to the beam. For cooling, the device is fastened into a copper cooling mask and attached to a Stirling cooler via a copper rod.

Al entrance window processed directly upon the silicon bulk. The BepiColombo detector is planned to have an additional layer of silicon oxide and silicon nitride between Al and the bulk.

Moreover the campaign was an intensive test for the data analysis software package ROAn, which was described in chapter 3.

4.1 Measurement setup

BESSY II is the name of a 3rd generation synchrotron radiation facility. It is located in Berlin and operated by the *Berliner Elektronenspeicherring-Gesellschaft für Synchrotronstrahlung m.b.H.* (BESSY), hence the name. The synchrotron radiation from bending magnets of the 1.7 GeV BESSY II storage ring has a characteristic energy of 2.5 keV.

The measurements took place at the PTB radiometry laboratory at BESSY II. The PTB uses a plane grating monochromator [63] to provide monochromatic radiation of high spectral purity in the 40 eV to 1900 eV spectral range, and a four crystal monochromator [64] using InSb $\langle 111 \rangle$ and Si $\langle 111 \rangle$ crystals to provide radiation in the spectral range from 1.75 keV to 10 keV. Each monochromator has its own beamline in the PTB laboratory. An additional beamline provides undispersed, i.e. polychromatic, synchrotron radiation.

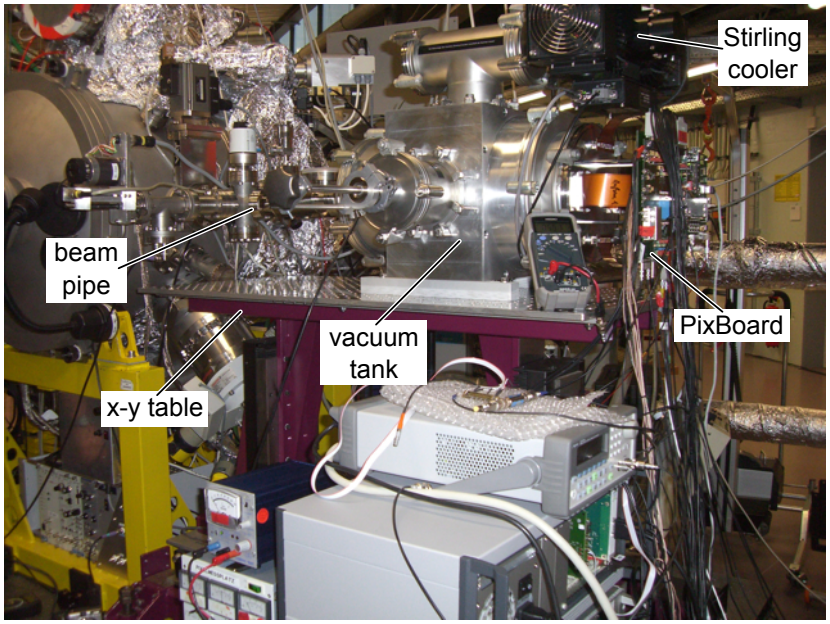

Figure 4.2: Picture of the measurement setup at the four crystal monochromator beamline in the PTB laboratory at BESSY II. The beam enters the detector coming from the left, through the tank visible at the image border. The cold head of the Stirling cooler is connected to the cooling mask of the detector via a copper rod within the t-fitting on top of the vacuum tank.

The measurement setup is shown in figure 4.1. It consisted of a vacuum tank which contained the setup described in section 2.10. The vacuum tank was attached to the beam pipe via a flexible connection and mounted on an x-y table which allowed the setup to be moved with respect to the beam pipe. The x-y table had a precision of 1 µm in each direction.

Opposite to the connection to the beamline was the flange carrying the inner PCB with the cooling mask and the outer PCB with the connectors to power supply and data acquisition. Inside the tank, the hybrid was fastened in a copper cooling mask which was connected to a cold head by a copper rod.

The cooler – a RICOR K535 Stirling cooler – was fastened to the tank via a t-fitting. It had two modes of operation: directly and remotely controlled. In directly controlled mode, the cooler cools down to the last set value (which is the factory default of 70 K, if it had been powered off) and can only be switched on or off.

In remotely controlled mode the cooler is connected to a PC via an RS232 cable. Via software the cooler can be switched on or off, the target temperature can be set, and its current status is displayed. The cooler keeps the programmed status even if the connection is lost.

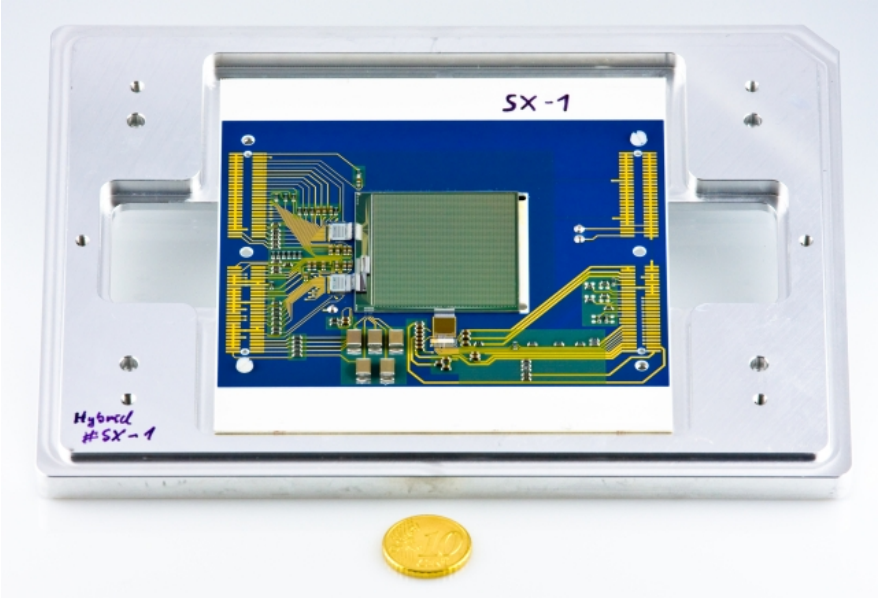

Figure 4.3: Picture of a Simbol-X DePFET macropixel prototype. The detector has a size of 64×64 pixels with a size of $500 \times 500\,\mu m^2$. The active area of the device is thus $3.2 \times 3.2\,cm^2$. Below, a ten-cent coin is shown for size comparison.

The temperature of the detector matrix could be monitored by the implanted temperature diode. It was connected to a voltmeter which measured the voltage drop over the diode.

The measurement setup comprised an acquisition PC and a PC for data analysis. The acquisition PC ran two programs, one for controlling the X-Board sequencer, another for data acquisition. The data acquisition program provides the possibility to observe the image of the DePFET matrix when not recording. This online display was used for beam spot assessment and alignment of start and end position of the scan patterns.

The acquisition PC was equipped with two 60 GB SAS[1] hard disks which provide fast access and were used to store the data of the ongoing measurement. The analysis PC had a 4 TB RAID 5 system for final data storage. Between measurements, the data from the acquisition PC was moved regularly to the analysis PC where also a preliminary data analysis took place.

The analog output of the readout ASIC was also fed into an oscilloscope, together with status signals coming from the X-Board sequencer. With these, the proper operation of the DePFET detector could be monitored.

Figure 4.3 shows a picture of a Simbol-X hybrid ceramic, a 64×64 macropixel

[1] SAS = **S**erial **A**ttached SCSI

detector with pixel size of $500 \times 500\,\mu m^2$. The active area of the detector thus had a size of $3.2 \times 3.2\,cm^2$. The hybrid was equipped with two Switcher IIb ICs and read out by an ASTEROID1.0 ASIC in source follower mode.

The measurement plan comprised different types of measurements: linearity and homogeneity, charge collection and quantum efficiency. The next sections describe how each of them was performed. Afterwards, the results are presented.

4.1.1 Linearity and homogeneity measurements

Several measurements from 100 eV up to 10 keV have been performed. Measurements from 1.7 keV to 10 keV took place at the four-crystal monochromator beamline, measurements from 100 eV up to 1900 eV at the plane-grating monochromator beamline. Table 4.2 shows an overview.

The measurements were performed at 5 different days in 2009: March 31st, April 1st, April 2nd, April 7th, and April 8th. The device was in permanent operation during two periods, the first from March 30th to April 2nd at the four-crystal monochromator and the second from April 6th to April 8th at the plane-grating monochromator.

The vacuum tank was kept evacuated during each measurement period, only vented when it was moved to another beamline.

Parameter	Value	Parameter	Value
$V_{\text{GATE ON}}$	−3.48 V	$V_{\text{GATE OFF}}$	5.0 V
$V_{\text{CLEARGATE ON}}$	3.5 V	$V_{\text{CLEARGATE OFF}}$	−3.6 V
$V_{\text{CLEAR ON}}$	19.0 V	$V_{\text{CLEAR OFF}}$	0.66 V
$V_{\text{RING BIAS}}$	−30 V	V_{BACKSIDE}	−60 V
$V_{\text{RING 1}}$	−3.5 V		
V_{DRAIN}	−5.0 V	I_{DRAIN}	8 mA
V_{BST}	−0.91 V	$V_{\text{REFERENCE}}$	−0.25 V
V_{DDS}	14.2 V		

Table 4.1: Detector parameter set at the BESSY II synchrotron facility. The table is divided into three parts. The upmost shows voltages concerning DePFET operation, the middle part comprises voltages related to depletion of the bulk, the lower part shows voltages and currents which concern the current source.

During each period, the detector voltages were applied permanently and kept constant after parameter optimization at the beginning of each of the two periods. Table 4.1 shows an overview of the most important detector parameters.

An exception was a small correction at the current source used to read out

the DePFET. The control voltage V_{BST} was changed to compensate a drift of the current. Apparently the drift was caused by temperature drift (see section 4.2.3).

The beam spot was much smaller than the detector size. Depending on the energy, beam spot sizes from 3×1 pixels to 15×5 pixels in x and y were obtained. At the double crystal monochromator the beam spot was smaller (3×1 pixels to 8×1 pixels) than at the plane-grating monochromator (9×5 pixels to 15×5 pixels).

These numbers represent a rough estimate of the FWHM of the individual beam spots. They were derived by observing the beam spot at the detector online monitor at the acquisition PC and estimating the FWHM in x and y from the image.

To illuminate the total detector area the tank containing the device was moved in x and y with respect to the beam, thus scanning the detector surface. Such a scan of the detector surface started with the beam spot in bottom left corner of the detector matrix (viewing at the beam through the detector). The x-y table was moved up stepwise to the next position. When reaching the top of the matrix, the table went down again, moved one step to the right, and started again moving up stepwise.

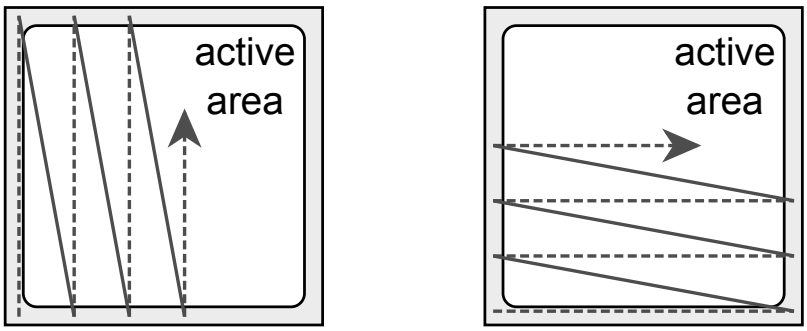

(a) vertical scan **(b)** horizontal scan

Figure 4.4: Applied scan patterns to achieve illumination of the whole detector matrix. Both patterns have been applied, no effect on the measurement results has been noted.

This pattern was applied at most of the measurements. An alternative pattern shown in figure 4.4b was applied to measurements taken on the April 7th to have a test whether the scan pattern has influence on the measurement results.

The beam spot remained at each position for 2.5 s to 5 s to accumulate enough statistics for the pixels in the illuminated area. The time interval between the scan positions was set depending on the momentary beam current in the storage

ring. Only the very first measurement was recorded with a 2.5 s time interval, the others had more than 4 s between step positions. The DAQ constantly recorded data while the beam scanned the matrix.

The step size in x and y was chosen such that a certain amount of overlap of the beam spots was ensured. The start and end position of a scan were chosen such that the border pixels were sufficiently illuminated.

The number of events collected in each pixel varied, depending on the beam intensity and the pixel position with respect to the beam track. The beam intensity of the electron storage ring decreases exponentially over time. After a period of approximately 10 h new electrons are injected into the ring to maintain a certain current level in the storage ring.

At the four-crystal monochromator the illumination of the total detector area took 1 h to 2 h because of the small beam spot size. The DAQ recorded data with a rate of approximately 48 GB/h. Having a storage capacity of 60 GB, the data had to be transferred to the storage server after this time. The measurements were paused then, to avoid interference of the data transfer to the DAQ[2].

To study the homogeneity of the gain it was sufficient to take only three measurements – at 10 keV, 5 keV and 2.5 keV – at the four-crystal monochromator where the whole matrix was illuminated. For the remaining measurements, the illumination was restricted to an area in the center of the matrix, containing approximately a quarter of the overall pixel count.

This procedure also saved time, first by reducing the scanning area, and second by reducing the amount of data per measurement, making less frequent pauses for data transfer necessary.

At the plane-grating monochromator beamline the beam spot size was bigger, i.e. less time was needed to scan the complete matrix, so the whole detector was illuminated in every measurement there.

The analog output of the readout ASIC could be monitored with an oscilloscope. To reduce the amount of pile-up events, the beam intensity was decreased until the oscilloscope image showed a homogeneous distribution of equal signals.

At the beginning of each measurement a short dark frame measurement without illumination was performed to monitor noise and offset.

In total, 52 measurements have been recorded in the energy range from 100 eV to 10 000 eV.

[2] e.g. data loss because of competing data streams to and from the hard disk

four-crystal monochromator		
ID	Energy [eV]	
090331_02	4997.0	F
090331_05	7496.8	F
090331_07	9990.6	F
090331_08	2499.1	F
090401_01	2100.5	P
090401_03	2999.0	P
090401_05	3998.2	P
090401_07	4999.3	P
090401_09	5998.3	P
090401_11	6996.9	P
090401_13	7993.9	P
090401_15	8993.6	P
090401_17	9006.5	P
090401_19	3498.9	P
090401_21	4500.0	P
090402_02	1819.4	P
090402_04	1859.2	P
090402_06	1759.3	P
090402_08	1998.9	P
090402_10	1839.2	P
090402_12	1859.2	P

plane-grating monochromator		
ID	Energy [eV]	
090407_02	1900.0	F
090407_03	1000.0	F
090407_06	1860.0	F
090407_08	1760.0	F
090407_10	1300.0	F
090407_12	1200.0	F
090407_14	1100.0	F
090407_16	1400.0	F
090407_18	1500.0	F
090407_20	1600.0	F
090407_21	1700.0	F
090408_02	1700.0	F
090408_04	1400.0	F
090408_06	1000.0	F
090408_08	900.0	F
090408_10	800.0	F
090408_12	700.0	F
090408_14	600.0	F
090408_16	500.0	F
090408_18	400.0	F
090408_20	310.0	F
090408_22	280.0	F
090408_24	200.0	F
090408_26	100.0	F
090408_28	450.0	F
090408_30	550.0	F
090408_32	650.0	F
090408_34	750.0	F
090408_36	850.0	F
090408_38	950.0	F
090408_40	1540.0	F
090408_42	1580.0	F

Table 4.2: Overview of the measurements at different beam energies. The left part shows the measurements at the four-crystal monochromator, the right those taken at the plan grating monochromator. The ID is composed by the measurement day (formatted *YYMMDD*) and a consecutive number for the run. "Missing" numbers are because of dark frame measurements which are not listed here. Also the charge collection measurements are not entered into this table. 'F' and 'P' in the third column indicates whether the matrix was **f**ully or **p**artially illuminated

4.1.2 Charge collection measurements

The matrix under test has a pixel size of $500 \times 500\,\mu m^2$. Each pixel has a set of 5 drift rings which guide the charge towards the DePFET in the pixel center. To investigate charge collection within the pixel area and its borders, an area of $1.5 \times 1.5\,mm^2$ in the center of the matrix was scanned with a 100 µm pencil beam in steps of 50 µm. The beam energy was 5 keV.

The x-y table moved to a new position every 7 s. When the position was reached, a trigger signal was issued by the x-y table. The trigger signal set a flag in a register, which was polled by the acquisition software every 500 ms. If found set, it paused polling and started a data recording. After recording, the flag was reset and the polling started again.

The data recording software was set to stop after acquiring 32 MB of data. With a frame rate of 2.4 kHz, this resulted in a measurement time of approximately 2 s and left a safety margin of around 5 s for the initialization and the termination of the recording process before the x-y table moved to the next position.

In total, 961 points were scanned, distributed on a 31×31 grid with 50 µm spacing in x and y between each position. This means an area of $1.5 \times 1.5\,mm^2$ (which corresponds to an area of 3×3 pixels) was scanned. The chosen size of the investigation area made sure that at least one pixel is completely within the scanning range.

The table positions were recorded in a file and provided by BESSY for later analysis. However, there was no calibration to calculate the beam position on the matrix from the table position. The absolute position of the area on the matrix had thus to be retrieved from the data afterwards (see section 4.2.5).

Both, the DAQ software and the x-y table accessed the register regardless of its state and were unaware of the other's status. This created a race condition between the DAQ and the x-y table. If the x-y table set the flag in the register before the DAQ had finished, the register was reset and the DAQ waits for the next flag. This way a trigger signal is lost.

This could happen if the data recording process took longer than 7 s, because of latencies in the system, e.g. concurrent access to the hard disk by another process. The only way to detect this was to check the file count at the end of the scan. Any number less than the expected number of 961 files means a trigger was missed. See section 4.2.5 how such a case was handled.

4.1.3 Detection efficiency measurements

The detection efficiency ε_{det} for the DePFET matrix is defined as the ratio of the number of photons N_{det} detected by the detector and the number photons N_{ph} impinging the detector:

$$\varepsilon_{\text{det}} = \frac{N_{\text{det}}}{N_{\text{ph}}} \tag{4.1}$$

An approach to determine the detection efficiency with respect to the photon energy experimentally is to take measurements at defined beam energies and to compare the number of photons detected to a reference measurement with a calibrated diode.

However, the measurements described in section 4.1.1 and listed in table 4.2 can not be used to determine the detection efficiency this way. Although the beam spot size was small compared to the active area size of the detector, it was too large for the PTB reference diode. Also the beam intensity used during the measurements (see section 4.1.1) was too low for the reference diode. Therefore, another approach to determine the detection efficiency was chosen.

To determine the detection efficiency, the detector was exposed to polychromatic radiation. These measurements took place in a separate measurement at April 26th.

The detection efficiency is then determined from this measurement by combining the detector-response model with the theoretical spectrum of the radiation

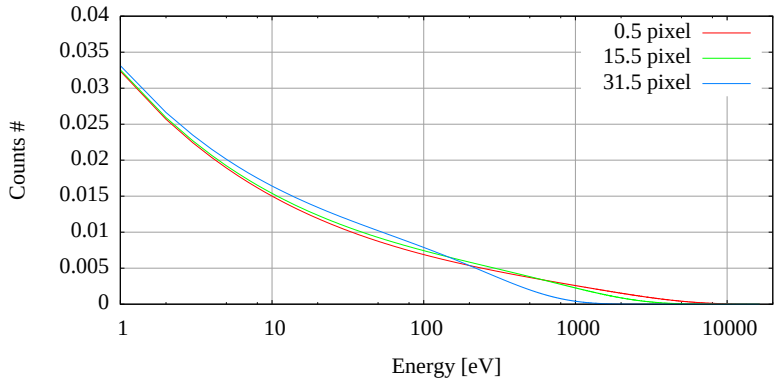

Figure 4.5: Different theoretical spectra for a single electron in the storage ring, calculated for a single $500 \times 500\,\mu\text{m}^2$ pixel. The spectra for a pixel depend on the absolute value of its offset to the horizontal plane. The offset of the first line next to the horizontal plane is 0.5 pixels, the offset of the outmost (32nd) is 31.5 pixels. At 1000 eV a difference in counts between the spectrum in the matrix center (0.5 pixel offset) and the one at the matrix border can be observed.

source and a detection-efficiency model and comparing this result to the experiment. This is explained in detail in section 4.2.7. The detector response to different photon energies is modeled by the response function presented in section 3.1.4, whose parameters are determined from the measurements at different beam energies (see section 4.2.6).

The PTB has a dedicated *Direct White Light* (DWL) beamline providing undispersed synchrotron radiation [65]. The respective spectrum the detector is exposed to follows a power law over the energy band of 100 eV to at least 10 keV [66].

Figure 4.5 shows the theoretical photon flux per electron volt and second, created by a single electron in the storage ring. These spectra were calculated for a single pixel ($500 \times 500\,\mu m^2$) at different offsets from the horizontal plane. The spectra are symmetrical to the horizontal plane, i.e. they depend only on the absolute value of the offset. The spectra were provided by M. Krumrey from BESSY.

For low energies the count rates for the individual offset values do not differ much. However, at higher energies the curve declines faster for higher offsets. This means, the closer to the horizontal plane the higher is the total photon flux, and the more high energy photons hit the detector. Parallel to the horizontal plane, the spectrum is homogeneous.

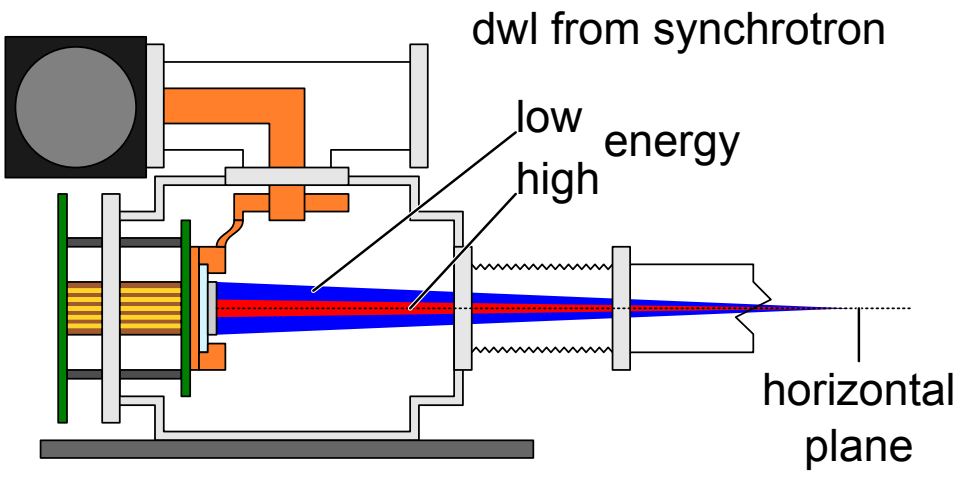

Figure 4.6: Setup used at the DWL beamline at the PTB laboratory. The tank is identical with the one described in figure 4.1. The detector is illuminated with undispersed synchrotron light from the storage ring. The photon energy and intensity is homogeneous in the horizontal plane but energy dependent in vertical direction. This is illustrated by the two colored areas for high and low energy photons.

The intensity of the spectrum scales with the number of photons in the storage ring. To reduce the number of photons and thus pile-up, the number of electrons in the storage ring was reduced. A measurement with only 3 electrons in the storage ring was taken.

Figure 4.6 shows a schematic of the setup. The detector setup is identical with the one described in figure 4.1. The synchrotron spectrum coming from the bending magnets is homogeneous in the horizontal plane. The distribution in vertical direction is energy dependent. The larger the distance the stronger the contribution of low energy radiation. In the picture this is illustrated by two lobes, one for high energy photons, the other for low energy photons.

For the measurements at the DWL beamline, the humidity in the measurement setup could be reduced by the vacuum pumps. Therefore, the setup was not affected by temperature drifts during the measurement period. The temperature setting of the RICOR K353 cold head was then set to 100 K which resulted in a stable temperature of 142 K measured by the on-chip temperature diode. Also, a better temperature monitoring had been installed in the acquisition setup.

4.2 Results

The next sections present the results of the different measurements. The data was processed with the offline analysis package presented in chapter 3. Offset and noise map for each measurement were calculated from the respective dark frame measurements which were taken regularly before the individual measurement run.

4.2.1 Homogeneity of the detector matrix

With an active area of $3.2 \times 3.2\,\mathrm{cm}^2$ the Simbol-X quadrant prototype currently presents one of the largest monolithic detectors of the HLL in operation. An important question at such dimensions is whether detector parameters like offset, noise and gain are homogeneous over the matrix area.

Offset Figure 4.7 shows an offset map of the matrix under test. The offset values range from 2772 ADU to 3865 ADU with a mean of 3298 ADU. The variance of the values of this offset map was determined to be 96 ADU.

The rightmost column (index 63) shows a lower offset, the second to last row (index 62) a higher offset compared to the rest of the matrix. Also the corners have slightly higher offsets. The deviations are probably due to inhomogeneities of the detector matrix. These offset specifics have no counterpart in the noise

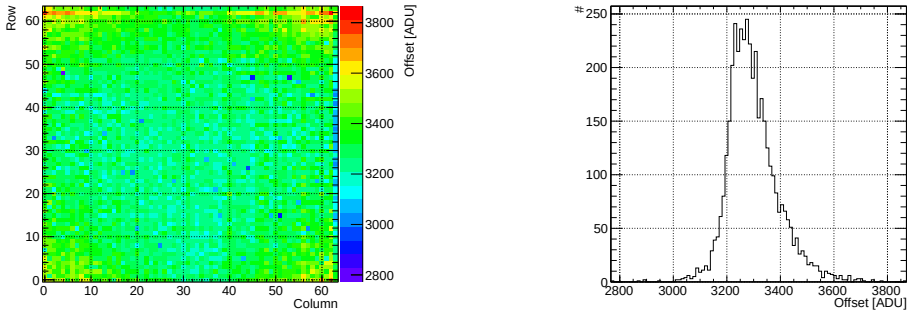

(a) offset map **(b)** map value histogram

Figure 4.7: Offset map of the matrix under test. The offset map has a mean of 3298 ADU. The rightmost column (index 63) shows a lower offset, the second to last row (index 62) and the corners a higher offset compared to the rest of the matrix. These deviations are probably due to inhomogeneities of the detector matrix, but are filtered out when offset correction is applied to the data.

map. Also the gain maps calculated from the various measurements do not show features which can be connected to them (compare to figure 4.10). Apparently, they are filtered out when correcting the offset.

Noise The noise map of the matrix under test, shown in figure 4.8, has a minimal and maximal noise of 9.2 ADU and 23.9 ADU respectively, with a mean noise of 11.8 ADU.

Figure 4.8b shows the map value histogram of the noise map; the data has been fitted with a Gaussian curve. The maximal noise value of 23.9 ADU is apparently a single outlier, otherwise the agreement with the Gaussian curve with a mean of 11.8 ADU and a variance of 0.9 ADU is very good.

The deviating values around 15 ADU are attributed to the region of higher noise (approximately 2 ADU above the mean) at the bottom center of the noise map. According to the ROAn coordinate system (see figure 3.26), this is the southern edge of the matrix below which the ASTEROID readout ASIC is located on the hybrid (compare to figure 4.3). Probably, this region on the noise map is caused by heat intake over the bond wires or infrared light emitted by the ASIC.

Characteristics Figure 4.9 shows the characteristic for offset and noise over the different measurements. The mean offset and noise for the matrix is shown, along with their variance over the matrix as error bars. The x-axis is a consecutive number for the individual dark-frame measurements.

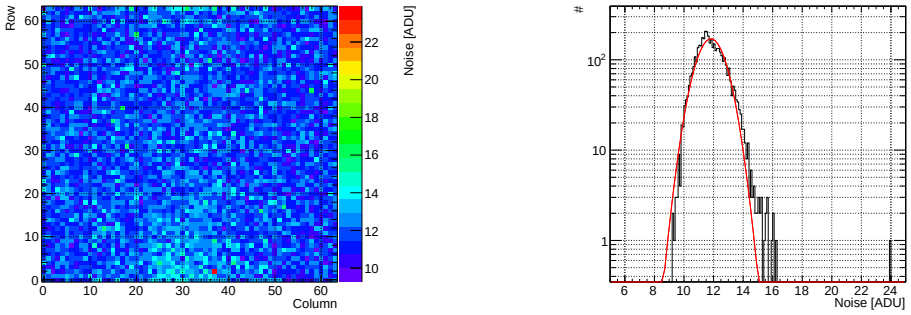

(a) noise map **(b)** map value histogram

Figure 4.8: Noise map of the matrix under test. The matrix has a Gaussian noise distribution with a mean noise of 11.8 ADU with a variance of 0.9 ADU. At the bottom center of the noise map shown in (a), some pixels show a slightly higher noise (+2 ADU) than the rest of the matrix. Also a deviation from the Gaussian distribution can be seen in (b) around 15 ADU. This is attributed to the readout ASIC which is located below this edge on the hybrid.

The offset changes over time for the first measurement days, which can be attributed to temperature drifts. The change in offset is strongest for the measurement days during which the largest temperature drifts occurred: March 31st, April 1st and April 7th (compare to section 4.13).

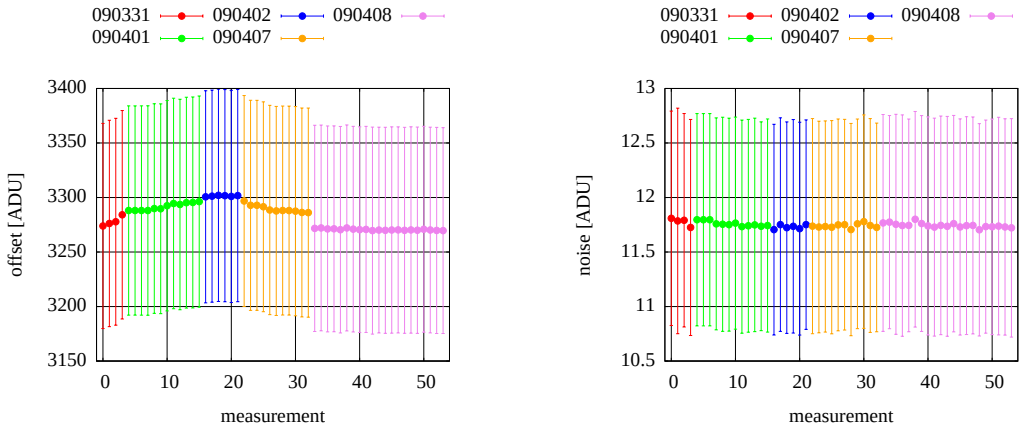

(a) offset characteristic **(b)** noise characteristic

Figure 4.9: Characteristic of offset and noise. The development of both values over time is shown, indicated by a consecutive number for each dark-frame measurement. For each measurement the mean value over the matrix shown. The error bars show the variance over the matrix of the offset or noise value respectively. The individual colors group measurements of the same day. The date is formatted *YYMMDD*.

For all measurements, the noise is stable at a mean value of 11.7 ADU and the standard deviation of approximately 1 ADU.

Gain Figure 4.10 shows gain maps derived at different energies (see section 3.3.3 for the definition of the gain map). The mean inverse gain of the matrix is noted below each gain map. The individual maps show a similar distribution and mean value.

For all measured energies from 100 eV to 10 000 eV, the dispersion of the inverse gain over the matrix (i.e., the variance of the values divided by their mean) is below 5 %. The matrix under test thus shows an excellent homogeneity with respect to gain.

To be less influenced by extreme outliers, variance and mean were calculated by putting all gain values into a histogram and applying a Gaussian fit. Outliers can be created when the automatic fit routine fails (see section 3.3.3), which is especially the case for energies below 1000 eV where the low energy background becomes more dominant (such values are visible as red squares e.g. in figure 4.10e).

Due to a flange with a too small inner diameter connecting the tank to the flexible coupling in the first measurements, the corners of the detector matrix were shaded. For the shaded areas no gain value could be determined, for these pixels the value determined for the respective column was entered into the map (compare section 3.3.3).

The small-diameter flange was used during the measurements at the four-crystal monochromator. As only the measurements at March 31st were full scans of the matrix (compare to table 4.2), the problem with the shaded corners only affects the gain maps for 2.5 keV, 5 keV, 7.5 keV and 10 keV. The flange was exchanged when switching the tank to the plane-grating-monochromator beamline.

Figure 4.11 shows the determined mean inverse gain (in eV/ADU) over the beam energy. The different measurement days are again shown color coded, the date is formatted *YYMMDD*. Only measurements where the matrix was fully illuminated are entered here, so there are no entries for April 1st and April 2nd. For most measurements the inverse gain is close to 1.27 eV/ADU.

For energies below 1000 eV, the inverse gain rises. For these energies the charge loss to the entrance window becomes more and more dominant (see section 3.1.4), resulting in a lower signal peak. As the inverse gain is defined as the quotient of the calibration energy and the signal peak value, this causes rising values of the inverse gain.

The values from April 8th are slightly above those from April 7th in the energy

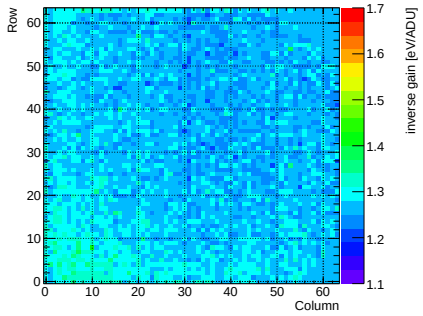

(a) 7.5 keV, 1.27 eV/ADU, 2 %

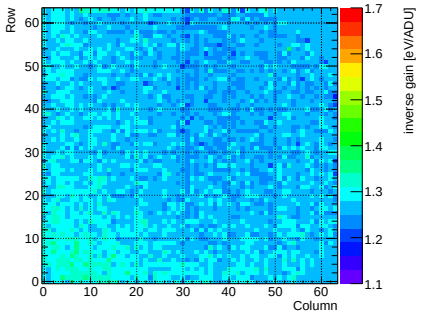

(b) 10 keV, 1.27 eV/ADU, 2 %

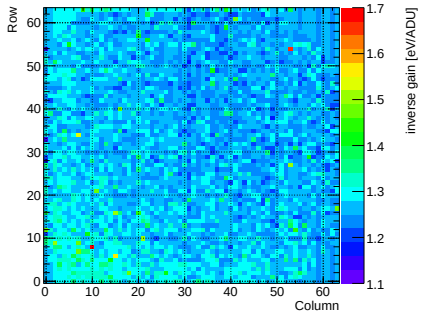

(c) 2.5 keV, 1.26 eV/ADU, 2 %

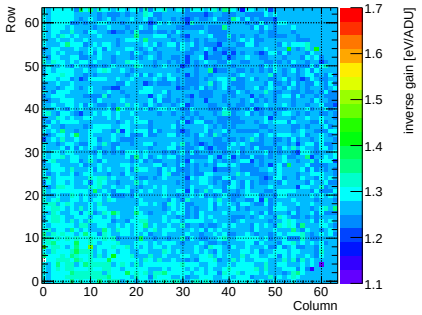

(d) 5.0 keV, 1.27 eV/ADU, 2 %

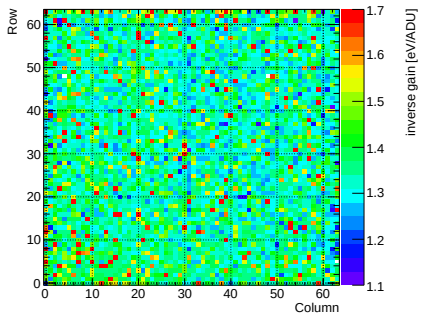

(e) 0.5 keV, 1.34 eV/ADU, 4 %

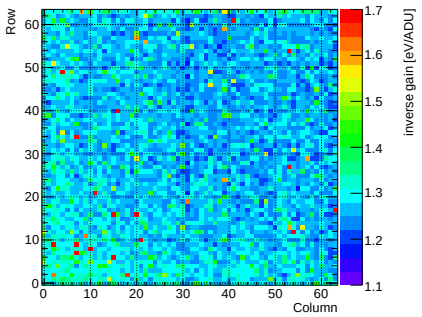

(f) 1.0 keV, 1.26 eV/ADU, 2 %

Figure 4.10: Gain maps derived from measurements at different beam energies. All gain maps show a similar distribution and average of the inverse gain. The color axis was fixed between 1.1 eV/ADU and 1.7 eV/ADU for better comparison. Below the gain maps the beam energy, the average inverse gain of the matrix, and the dispersion are stated. The gain dispersion over the matrix is below 5 % over the whole energy range. At 500 eV the peak shift due to incomplete charge collection becomes visible as a higher inverse gain. Extreme values, which show up as red dots in the maps, are most probable created by failed fits when calculating the gain map (see section 3.3.3).

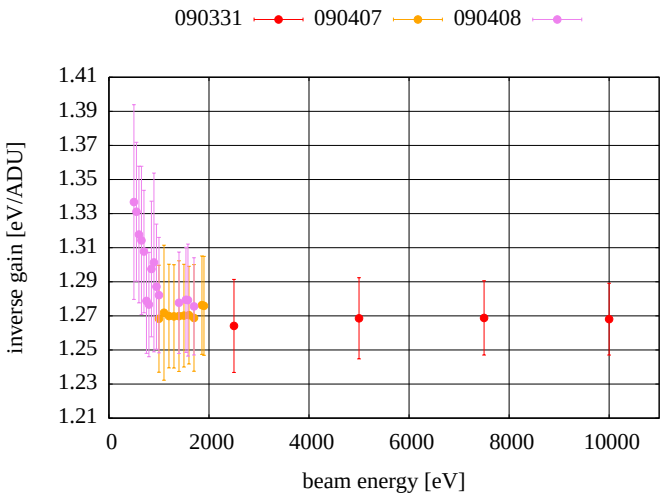

Figure 4.11: Characteristic of mean inverse gain over beam energy. The average value for the whole matrix is shown, the error bars show the variance of the values over the matrix. The different measurement days are shown color coded, the date formatted *YYMMDD*. Only measurements where the whole detector area was illuminated are considered here. The rising of the inverse gain for energies below 1000 eV can be explained by a shift of the signal peak due to charge loss to the entrance window. Above, the inverse gain is stable at 1.27 eV/ADU. The dispersion is below 5 % for all data points.

range from 1000 eV to 2000 eV. This shift can be attributed to temperature drifts (see section 4.2.3). A correction for these is presented in section 4.2.4.

4.2.2 Scan patterns

Figure 4.12 shows hit maps for SNG patterns from two measurements which had different scan patterns applied. The hit maps show the number of hits which were accumulated in each pixel during the measurement.

A hit map from a measurement with a vertical scan pattern performed at an energy of 5.0 keV is shown in figure 4.12a. The hit map has no counts in the corners due to shading by the flange with the smaller diameter (see above).

Figure 4.12b shows a hit map from a measurement with a horizontal scan pattern. The beam energy here was 1.0 keV. Because of the larger beam-spot size at the plane-grating monochromator, the scan paths are better visible in this hit map than in figure 4.12a which is from a measurement at the four-crystal monochromator.

The corresponding gain map for the measurement with the vertical scan pattern is shown in figure 4.10d, the one for the measurement with the horizontal

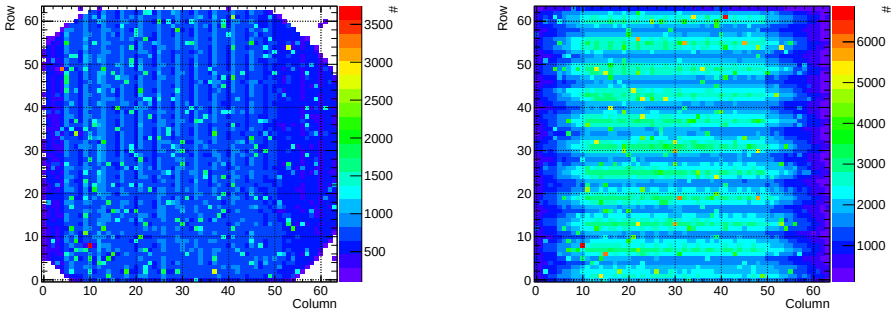

(a) vertical scan, 5.0 keV **(b)** horizontal scan, 1.0 keV

Figure 4.12: Two hit maps for SNG patterns from measurements with different scan patterns and energies. (a): Measurement at 5 keV, taken at the four-crystal monochromator. Because of a flange with a too small diameter in front of the detector its corners were shaded, so no hits are recorded there. (b) Measurement at 1 keV, taken at the plane-grating monochromator. The span between maximum and minimum number of SNG patterns per pixel is higher compared to (a), yet there is no effect on the respective gain maps (see figure 4.10d and figure 4.10f).

scan pattern in figure 4.10f.

The scan paths can be identified in the hit maps but not in the respective gain maps. There is no correction for the beam current when calculating the gain map. So, as long as enough hits are collected per pixel, there is no significant effect of the beam current on the gain map.

Due to overlap of the beam spots and the decreasing of the beam current in the storage ring, the number of hits per pixel varies over the matrix. However, in all measurements a minimum of approximately 100 hits per pixel (in the illuminated area) has been achieved.

4.2.3 Temperature drift

The cooler attached to the tank was first operated in the direct mode at a target temperature of 70 K. This target temperature could not be reached during the measurements. The cooler was connected to a PC and remotely controlled starting with the measurements of April 1st, but it was decided then to keep the setting for the target temperature for not to change the measurement environment.

As the cooler operated at its maximum capacity, the temperature was not optimally stabilized. Figure 4.13 shows the reconstructed temperature drift of the measurements for the two periods. The plots show the temperature difference to the measurement at 7.5 keV which was used for calibration (see below). The

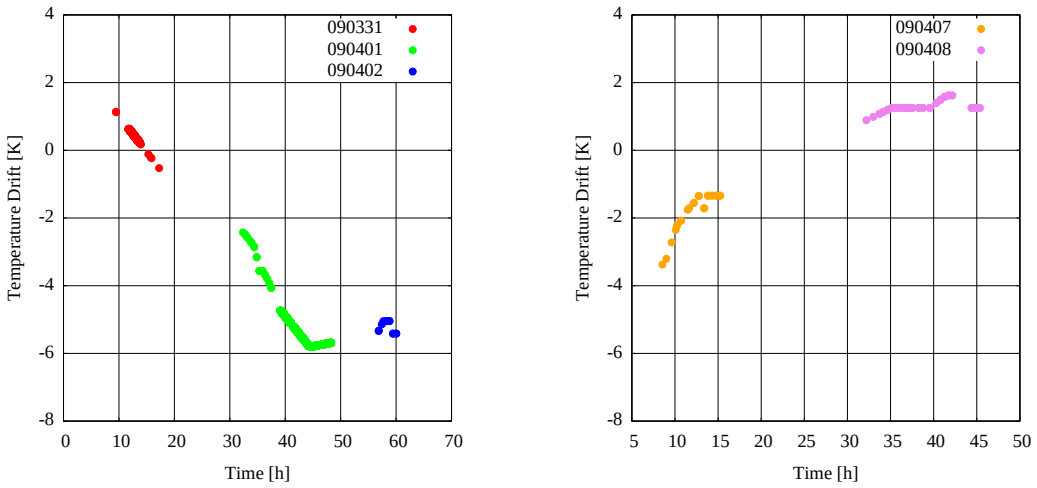

(a) Period 090331-090402 **(b)** Period 090407-090408

Figure 4.13: Reconstructed temperature drift. The measurement days (formatted *hi*) are shown color coded. The origins of the time axis are set arbitrarily to a point in time close to the first measurement of the respective period. The values were reconstructed by correlating the file creation dates of the recorded files with the temperature entries in the measurement log and linear interpolation. The temperature drift is calculated relative to the temperature of the measurement at 7.5 keV which was used as calibration. This reference temperature was 143 K.

temperature for this measurement was determined to be 143 K.

The origin of the time axis was set arbitrarily close to the first shown point in time of the respective measurement period. The different measurement days are shown color coded. The reconstruction was done by correlating the creation dates of the data files with the temperature log book entries and applying linear interpolation.

Probably humidity in the tank and bad vacuum led to icing at the copper rod, which connected the cold head to the cooling mask. This seemed to have created thermal bridges to the vacuum tank, which had the consequence that the cold head was not properly thermally insulated to the environment.

The effect of temperature differences were noticed after the measurement campaign during analysis of the peak positions of the calibrated detector signal with respect to the beam energy (see section 4.2.4, where also a correction for these effects is presented).

Later measurements confirmed a dependency on temperature when the ASTEROID ASIC was operated with a too low operation current [67]. This means a change in temperature changed the gain and pedestal of the ASIC.

4.2.4 Linearity of the detector matrix

The measurements at different beam energies were all calibrated with the gain map retrieved from the measurement at 7.5 keV. For each measurement a spectrum for the thus calibrated SNG patterns was created, and the position of the signal peak was determined by fitting a Gaussian curve to it and retrieving its mean value E_{peak}.

Figure 4.14 shows an evaluation of the found peak positions for SNG patterns over the beam energy E_{beam}. The error bars were set to 3σ of the respective fit. A straight line with slope 1.0 passes nicely through the data points. No strong deviations can be observed.

Figure 4.14 shows plots of the quotient $E_{\text{peak}}/E_{\text{beam}}$ of the determined peak energy E_{peak} and the beam energy E_{beam}. In figure 4.15a the data points belonging to different measurement days are shifted with respect to each other. For example, the values from April 1st are above those from March 31st in the same energy range. The same can be seen for the values from April 2nd, compared to those from April 7th and April 8th close to 2000 eV. These shifts can be attributed to the temperature drifts shown in section 4.2.3.

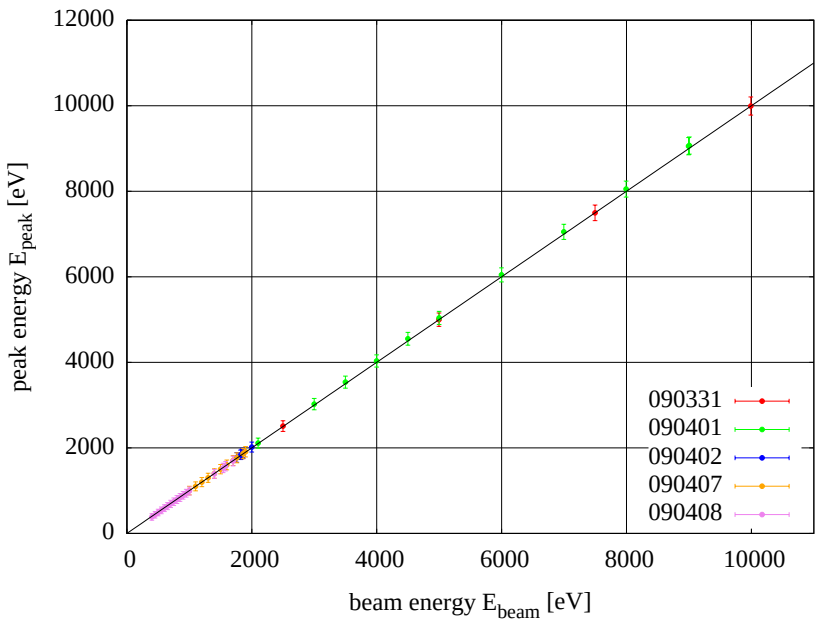

Figure 4.14: Peak positions over beam energy. The peak positions were determined by fitting a Gaussian curve to the peaks in the spectra for SNG patterns. The error bars mark the 3σ region around the found peak. No strong deviation from a straight line with slope 1.0 can be observed over the energy range.

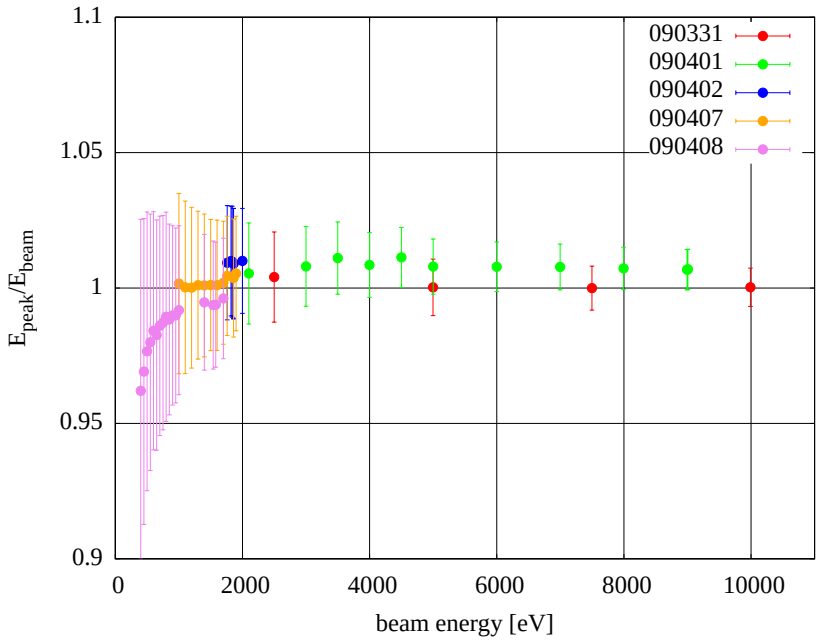

(a) without temperature correction

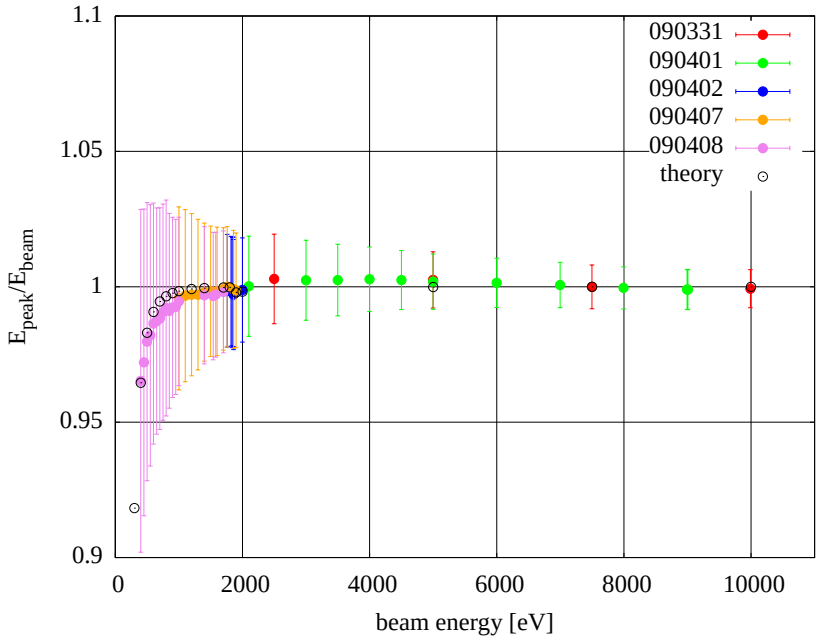

(b) with temperature correction

Figure 4.15: (a): Relative peak positions $E_{\text{peak}}/E_{\text{beam}}$, derived from measurements calibrated with a gain map derived from the measurement at 7.5 keV, (b): Same relative peak positions for measurements, now corrected for temperature drift. The error bars in both plots have been calculated from the peak sigmas.

By correlating the ratio $E_{\text{peak}}/E_{\text{beam}}$ to the temperature difference dT to the gain map measurement, a simple linear could be derived. Figure 4.16 shows the respective plot. The temperature difference dT is expressed in mV, because the temperature values were read from the voltmeter connected to the on-chip temperature diode. The measurement days are again shown color coded.

The measurements above 1000 eV, which are for the most part all except those from April 8th (090408), show a correlation to the temperature difference. Figure 4.13 shows that the temperature was quite stable for the measurements from April 8th compared to the other days. The deviation for the values from April 8th is attributed to the peak shift caused incomplete charge collection.

The linear correction was set to be 1.0 if the measurement was made at the same temperature as measurement the gain map was derived of (i.e. the one at 7.5 keV). The following formula was fitted to the data values above 1000 eV in

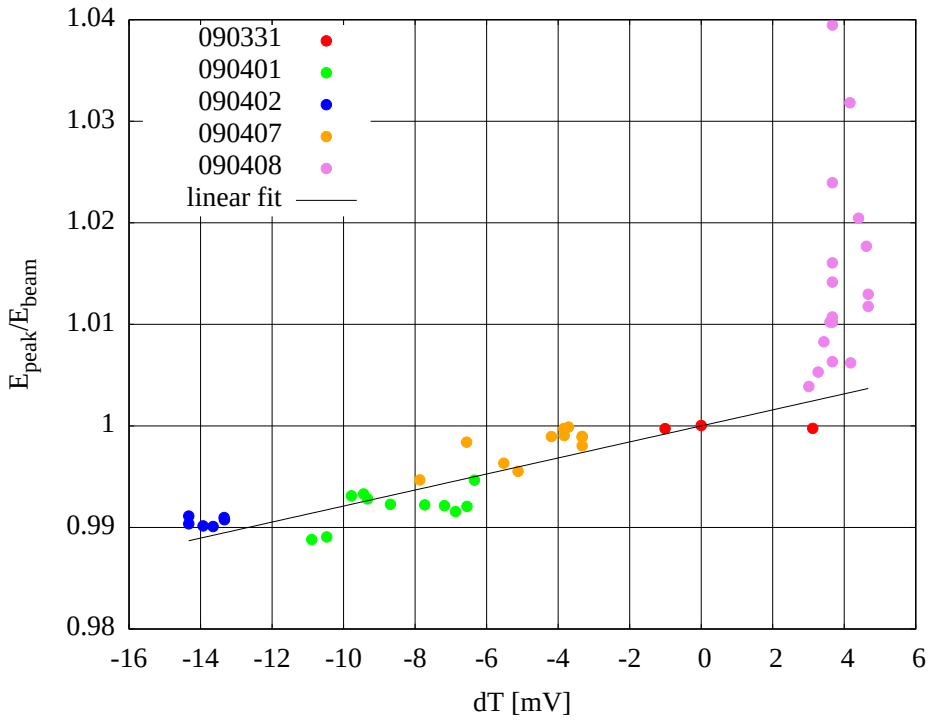

Figure 4.16: $E_{\text{peak}}/E_{\text{beam}}$ plotted over the temperature difference dT to the gain map measurement. Temperature is read as a voltage drop over the on-chip temperature diode, thus the difference is expressed in mV. Measurements above 1000 eV (at most all except 090408) show a correlation to dT. Measurement day 090408 comprises at most measurements below 1000 eV where the peak shift is dominated by incomplete charge collection (see section 3.1.4). Also, the temperature drift on this measurement day is rather small compared to the others (see figure 4.13).

figure 4.16:

$$\frac{E_{\text{peak}}}{E_{\text{beam}}} = 1.0 + a_1 \cdot dT \tag{4.2}$$

The fit returned $a_1 = 7.89\,\text{mV}^{-1}$ as result. This temperature correction was applied in the calibration routine described in section 3.3.4.

Figure 4.15b shows the same data with the linear temperature correction applied. The data shows no structures which could be connected to a measurement day. The temperature correction was applied to all measurements taken at both monochromator beamlines which were then used to define the detector model (see section 4.2.6).

The detector model, which has been fitted to the measurement data (see section 4.2.6), predicts that for small photon energies the peaks are shifted to lower energies due to charge loss at the detector surface. This peak shift is caused by the process of photon absorption and charge collection in the detector bulk, but not by a non-linearity of the device.

By applying the same fits as above to the theoretical detector model, the theoretical values shown as black circles in figure 4.15 can be derived. They show a good correspondence to the data, also at the low energy decline. Thus the DePFET matrix under test can be assumed as a linear device for the observed energy range.

4.2.5 Charge collection

Each measurement recorded during the pixel scan of the $1.5 \times 1.5\,\text{mm}^2$ area was subjected to the same offline analysis procedure. From each analysis, numbers like total count of different pattern types and the respective average energy are extracted.

Together with the position information from the x-y table, these figures can be composed to maps of the scanned area. The position of an entry in a map such created is determined by looking up the nth position in the list of positions for the nth measurement taken.

Figure 4.17 shows maps of the relative counts of SNG and DBL patterns. Here, *relative* means in respect of the overall count of valid multiplicities. The trenches in the SNG map and the walls in the DBL map correspond to the size of a pixel, i.e. $500 \times 500\,\mu\text{m}^2$. This can be used to pinpoint the position of the pixels of the scanning area. The border of the central pixel has been drawn into each map of figure 4.17

In total only 959 measurements have been recorded. This means two mea-

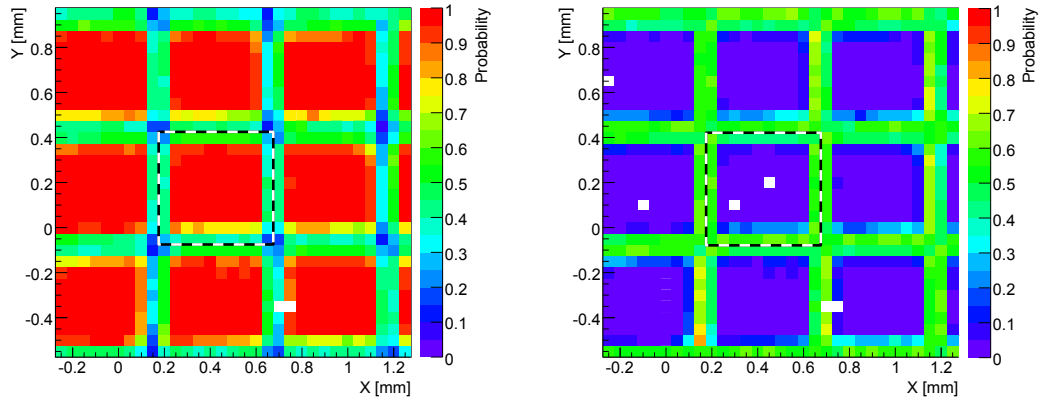

(a) SNG patterns **(b)** DBL patterns

Figure 4.17: Relative count maps for SNG and DBL patterns at a beam energy of 5 keV. Each entry has been normalized to the total number of valid patterns at the respective position. X and Y are the coordinates of the pencil beam. The trenches in (a), respectively the walls in (b) correspond to the pixel size of $500 \times 500\,\mu m^2$. The square marks the position of the central pixel of the 3×3 pixel patch.

surements were lost, apparently due to the race condition stated above (see section 4.1.2). To correct for this means two positions in the list have to be skipped. Which positions can be decided by regarding image of the resulting map.

The map in figure 4.17a shows two empty bins in the lower part. These correspond to the two lost measurements. The position of these to measurements was determined by skipping beam positions until the image of the trenches was properly aligned. The fact that all maps created from the data set show no artifacts that can be related to misalignment of the data proves this procedure as correct.

More important than the pattern ratio is the average energy collected in respect of the beam position. Figure 4.18 shows the respective maps for the two patterns. Here the average energy of all occurrences of the respective pattern recorded has been entered.

For the double map only positions which had a relative count of more than 5 % for DBL patterns were considered. Also the position of the central pixel derived above has been drawn into the maps.

Judging from the maps the collected average energy is close to the incident beam energy of 5 keV. This holds for SNG as well as for DBL patterns. So no charge loss within the pixel area was detected.

The vertical structures which show a lower energy signal that can be observed

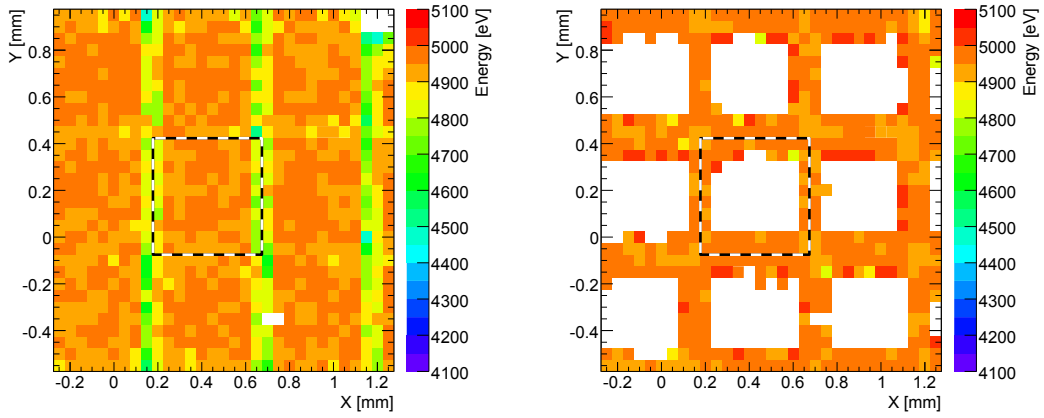

(a) SNG patterns **(b)** DBL patterns

Figure 4.18: Average charge maps for SNG and DBL patterns at a beam energy of 5 keV. The charge collection is without significant charge loss throughout the pixel area. The square marks again the position of the center pixel. The vertical structures are attributed to crosstalk in the multiplexer of the readout ASIC. Again, the square marks the position of the central pixel of the 3×3 pixel patch.

in figure 4.18a are attributed to crosstalk in the multiplexer of the readout ASIC (see section 3.1.2.5).

4.2.6 Fitting the detector response model

From the individual measurements at different beam energies spectra containing all valid multiplicities (SNG, DBL, TRP and QUD) were created. For their creation only the pixels from an area in the center (about a quarter of the size of the whole matrix) were considered, as this area was illuminated at all measurements.

A detector-response function was fitted to the spectra for all valid multiplicities to determine the value of its parameters. Before applying the fit, the bin count of the spectra was reduced from 16 384 to 2048 for smoothing. The bin width of the smoothed spectrum was then 8 eV, the bin error was recalculated accordingly.

The used function describes the detector response according to model presented in section 3.1.4. It comprises the parameters of the partial event model, S, c, l, and τ, which define the shape of the peak and the shoulder, and the detector noise σ_{det}. All these parameters are assumed to be energy independent. Also contained in the model are the escape rate k_{esc} and the flat-shelf rate k_{fs}, which are energy dependent parameters.

Additionally, a parameter $\varepsilon_{\text{corr}}$, which scaled the energy with a linearly, was introduced to compensate for remaining non-linearities (see section 4.2.6.4).

4.2.6.1 Model parameters

The fit for a single spectrum was done automatically using the χ^2-fitting routines offered by ROOT. A parallel fit of all spectra is not yet implemented in the ROAn software package. Therefore, the optimal parameter set has been determined manually.

To accomplish this, the individual spectra were at first fitted with all parameters set free. Then the found results were investigated and the most probable value for the energy independent values S, c, l and τ determined. Successively, these were fixed and the fits repeated to control the effect of the chosen value. This way iteratively the parameter set was pinned down. Table 4.3 shows an overview of the determined fit values.

Parameter	Value
S	0.38
c	0.8
l	0.08 µm
τ	0.09 µm
σ_{det}	15.1 eV

Table 4.3: Model parameter values. This parameter set was used when applying the model to measurements with polychromatic synchrotron radiation. The parameters were determined by fits to spectra obtained from monochromatic measurements at the four-crystal monochromator and the plane-grating monochromator beamline. Exception is the detector noise σ_{det}, which was derived from dark frame measurements.

Energy dependent values like escape rate k_{esc} and flat shelf rate k_{fs} were at first allowed to float. Then, the found fit values were modeled by functions so values for arbitrary energy values can be determined.

The value for electronic noise σ_{det} was determined from the calibrated noise map and set to 15.1 eV for all fits. As stated above, the complete data set has been calibrated with the gain map derived from the measurement at 7.5 keV in combination with the linear temperature drift correction (see section 4.2.4)

4.2.6.2 Escape rate

The escape rate k_{esc} was allowed to float during the fits. The found results were then modeled by an exponential function [50].

$$k_{\text{esc}} = \begin{cases} 0 & E \leq E_{\text{K}} \\ C_{\text{esc}} \cdot e^{-a_{\text{esc}} \cdot (E - E_{\text{K}})} & E \geq E_{\text{K}} \end{cases} \tag{4.3}$$

Here, $E_{\text{K}} = 1.84\,\text{keV}$ denotes the energy of the silicon K-edge, E the photon energy, and C_{esc} and a_{esc} the parameters describing the exponential function. Figure 4.19 shows the values for k_{esc} retrieved from fits and the modeling exponential function.

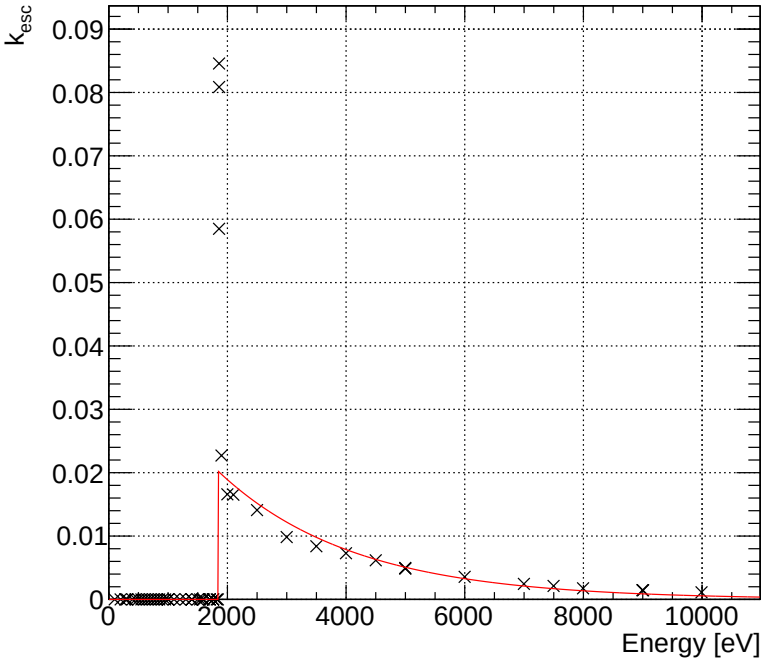

Figure 4.19: Fit values for the parameter k_{esc} and the modeling exponential function. The high values at the Si K-edge energy are created due to an overlap of the noise peak and the escape peak. They were not considered in the fit for k_{esc}.

The three high values around the Si K-edge energy are created due to an overlap of the noise peak with the escape peak, and were not considered in the fit.

The detector was illuminated by scanning the matrix with a beam spot much smaller than the matrix size (see section 4.1.1). This means, the large part of the matrix delivered only detector noise, which can lead to a certain amount of

noise hits (see section 3.1.2.1). For a beam energy equal to the energy of the Si K-edge, the escape peak would be at

$$E = E_{\text{beam}} - E_{\text{esc}} = 1840\,\text{eV} - 1740\,\text{eV} = 100\,\text{eV}\,. \tag{4.4}$$

The average noise of the matrix is 15.1 eV, which means the average threshold energy for event discrimination is around 75.5 eV (=5σ). At this distance, the escape peak and the noise peak still overlap.

The values determined from the modeling function were

$$\begin{aligned} C_{\text{esc}} &= 2.03 \cdot 10^{-2} \text{ and} \\ a_{\text{esc}} &= 4.38 \cdot 10^{-4}\,\text{eV}^{-1}\,. \end{aligned}$$

These values were then used to model the escape rate at arbitrary energies (see section 4.2.7).

4.2.6.3 Flat shelf

Like the escape rate, also the flat-shelf rate k_{fs} was allowed to float in the fits and then modeled by a function. Figure 4.20 shows the values and the modeling function.

The function modeling k_{fs} is an exponential function with an additional constant factor and an exponential to account for the behaviour for energies above the Si K-edge:

$$k_{\text{fs}} = A_{\text{fs}} + C_{\text{fs},1} \cdot e^{a_{\text{fs},1} \cdot E} + \begin{cases} 0 & E < E_{\text{K}} \\ C_{\text{fs},2} \cdot e^{a_{\text{fs},2} \cdot E} & E \geq E_{\text{K}} \end{cases} \tag{4.5}$$

The model function for k_{fs} is purely phenomenological, as no physical model was available which traced the fit values satisfactorily. For the fit only the energy range from 500 eV to 10 000 eV was considered. The values which gave the best fit of the modeling function to the parameter values were:

$$\begin{aligned} A_{\text{fs}} &= 8.54 \cdot 10^{-3} \\ C_{\text{fs},1} &= 0.150\,, \\ a_{\text{fs},1} &= -1.77 \cdot 10^{-3}\,\text{eV}^{-1}\,, \\ C_{\text{fs},2} &= 640.5 \text{ and} \\ a_{\text{fs},2} &= -5.48 \cdot 10^{-3}\,\text{eV}^{-1}\,. \end{aligned}$$

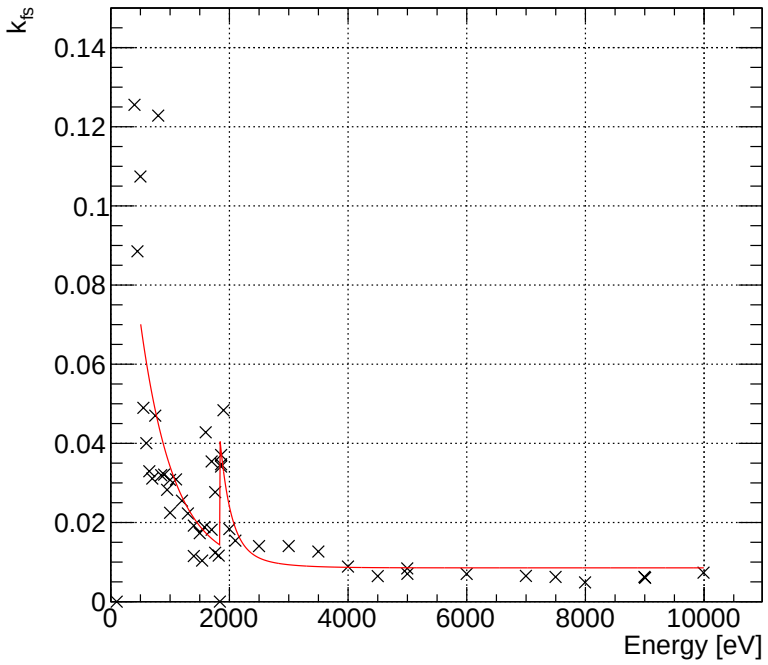

Figure 4.20: Fit values for the parameter k_{fs} and the modeling function. The model function is purely phenomenological.

Analog to k_{esc}, these values were used later to set k_{fs} at arbitrary energies.

4.2.6.4 Energy correction factor

To account for any remaining non-linearities, an energy correction factor $\varepsilon_{\mathrm{corr}}$ was introduced. With this factor the energy can be rescaled linearly by

$$E' = E \cdot \varepsilon_{\mathrm{corr}} \,. \tag{4.6}$$

Figure 4.21 shows the values for $\varepsilon_{\mathrm{corr}}$ retrieved from the fits. For energies above 500 eV, the energy correction is within $\pm 0.5\,\%$ around 1.0. Below 500 eV the spectrum gets more and more distorted due to effects of the CCE, according to the model (see section 3.1.4).

The effect of the energy correction factor is rather small: The values for $\varepsilon_{\mathrm{corr}}$ for energies below 500 eV result in a shifts below the bin width of 8 eV of the spectra. Above 500 eV, the strongest deviations of $\varepsilon_{\mathrm{corr}}$ are below the Si K-edge energy, where the shoulder of the peak becomes more pronounced.

For 2000 eV, a factor of $0.5\,\%$ means a shift of 10 eV which is in the order of the bin width of the spectra. For higher energies, the values of $\varepsilon_{\mathrm{corr}}$ are even

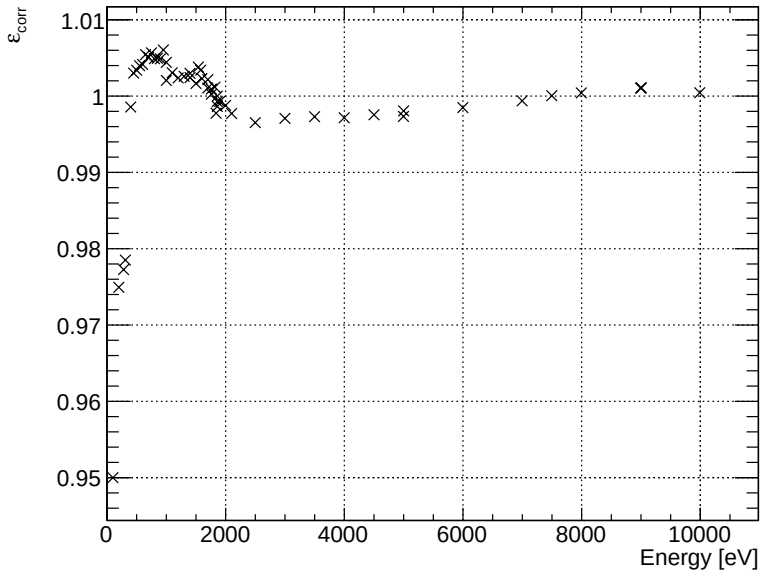

Figure 4.21: Energy correction factor $\varepsilon_{\text{corr}}$. The variations of the parameter are well within $\pm 0.5\,\%$ for most energies. The strong deviation at energies below 500 eV can be attributed to the strong distortion of the spectrum due to effects of the CCE function.

closer to 1.0, so the effect of the correction factor is even smaller there.

The energy correction factor was thus set to unity, when using the model to determine the detection efficiency (see section 4.2.7).

4.2.6.5 Fit results

Figure 4.22 shows spectra for all valid patterns with the fitted model function. Below each spectrum, the normalized residuals are displayed. These are calculated from the difference between model-function value and the histogram bin entry, divided by the respective bin error. The measurements shown in figure 4.22 were all taken at the four-crystal monochromator beamline.

Next to the main peak, the tail and the shoulder can be seen in the spectrum (compare to figure 3.15). Especially for lower energies (figure 4.22a and figure 4.22b) the onset of the shoulder can be clearly separated from the flat shelf in the spectrum. For higher energies (figure 4.22c and figure 4.22d) the shoulder merges with the flat-shelf background.

The detector-response model shows good agreement with the data, the normalized residuals are mostly within the range from -5 to 5. Larger values occur at energies around the main peak, indicating that either the detector noise is underestimated, or additional effects, which broaden the peak, exist and are not

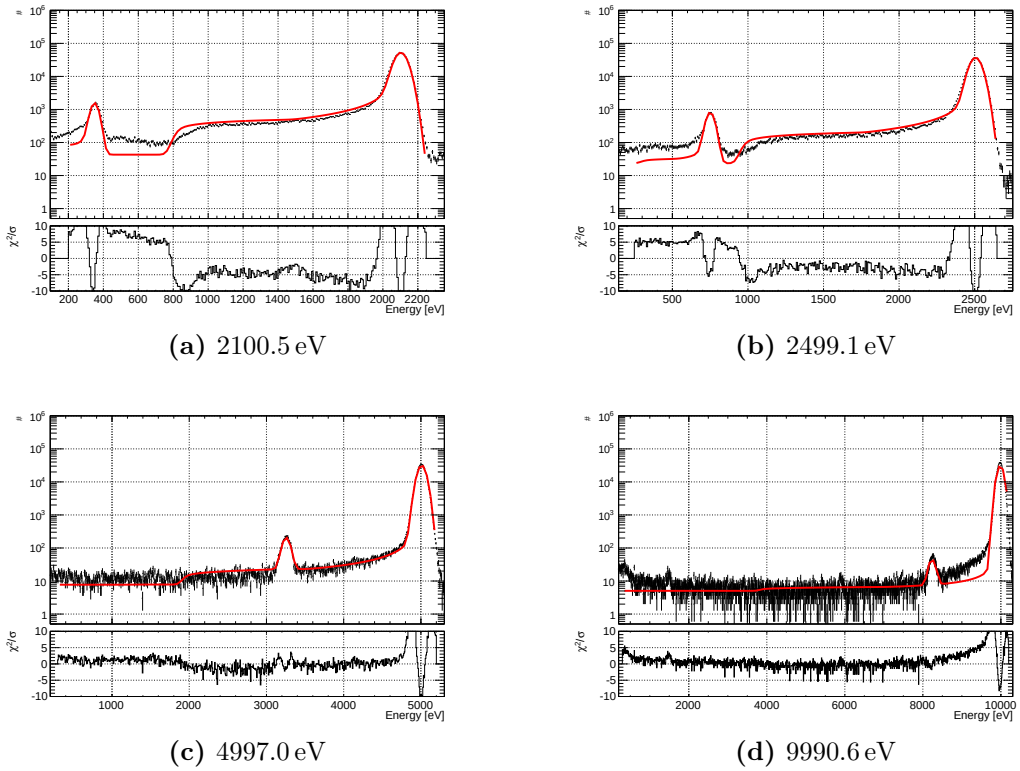

(a) 2100.5 eV **(b)** 2499.1 eV

(c) 4997.0 eV **(d)** 9990.6 eV

Figure 4.22: Fits of the detector model to spectra from measurements at different energies. The spectra were all taken at the four-crystal monochromator. The plot below each spectra shows the normalized residuals over the energy. DePFET spectrum features like shoulder and tail can be seen next to the main peak, especially at lower energies.

covered by the model. The differences between model and data are also stronger in the low energy range ($< 500\,\text{eV}$) in figure 4.22, indicating that the underground is not properly modeled.

In figure 4.22d a deviation of the model from the spectrum at the tail of the main peak can be observed. Such a deviation of the spectrum tail can also be observed in other spectra at beam energies above 5 keV.

By applying an energy cut to the measurement data and counting the respective hits per pixel related to all events in this energy region, a hit map can be created which shows the origin of these events.

Two examples, for 6.0 keV and 9.0 keV, are shown in figure 4.23. Both hit maps show a curved structure on the matrix with higher. These hit maps reveal that there are some pixels on the matrix which produce significantly more signals within the energy cut than the rest of the rest of the matrix.

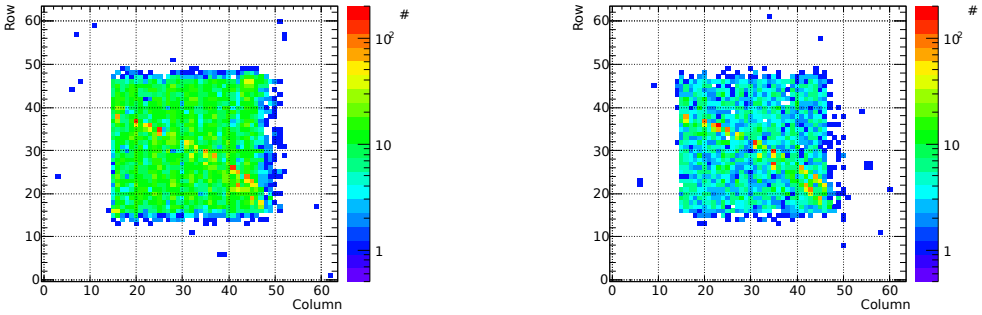

(a) $E_{\text{beam}} = 6.0\,\text{keV}$ **(b)** $E_{\text{beam}} = 9.0\,\text{keV}$

Figure 4.23: Hit maps created by counting hits per pixels for events within an energy range in the tail of the main peak, in which the spectrum shows deviation from the model function. The hit maps reveal a curved structure with higher counts. Only an area in the center of the matrix was illuminated, therefore the border pixels show no counts.

The cause for this localized effect is yet unknown, but the appearance bears resemblance to the circular structures already encountered previously in section 3.1.1 and section 3.1.5. The fact that this region appears for energies above 5 keV might hint for a dependence on depth, because the mean absorption depth also varies with photon energy.

In figure 4.24 spectra and the respective model function for energies from 310 eV to 1400 eV are shown. These measurements have been taken at the plane-grating-monochromator beamline. Also here, all valid patterns have been considered.

Because the beam energy is below the Si K-edge, the escape peak is missing. For low photon energies, the distortion of the spectrum due to incomplete charge collection becomes visible: The shoulder becomes more and more dominant (figure 4.24d) until it merges with the main peak (figure 4.24c).

There is also a deviation between model and spectrum at the tail of the main peak, visible in the spectra at 1000 eV and 1400 eV in figure 4.24. This can also be observed in figure 4.25a and figure 4.25b. In contrast to the deviation at energies above 5.0 keV, the deviations at the tail between model and spectrum are not localized on the matrix but homogeneously distributed. They are thus attributed to stray light from the plane-grating monochromator.

As already stated above, the measurements at the beamlines were performed with rather low intensity to avoid event pile-up. Therefore, the intensity was reduced drastically. At the plane-grating monochromator the shutter between

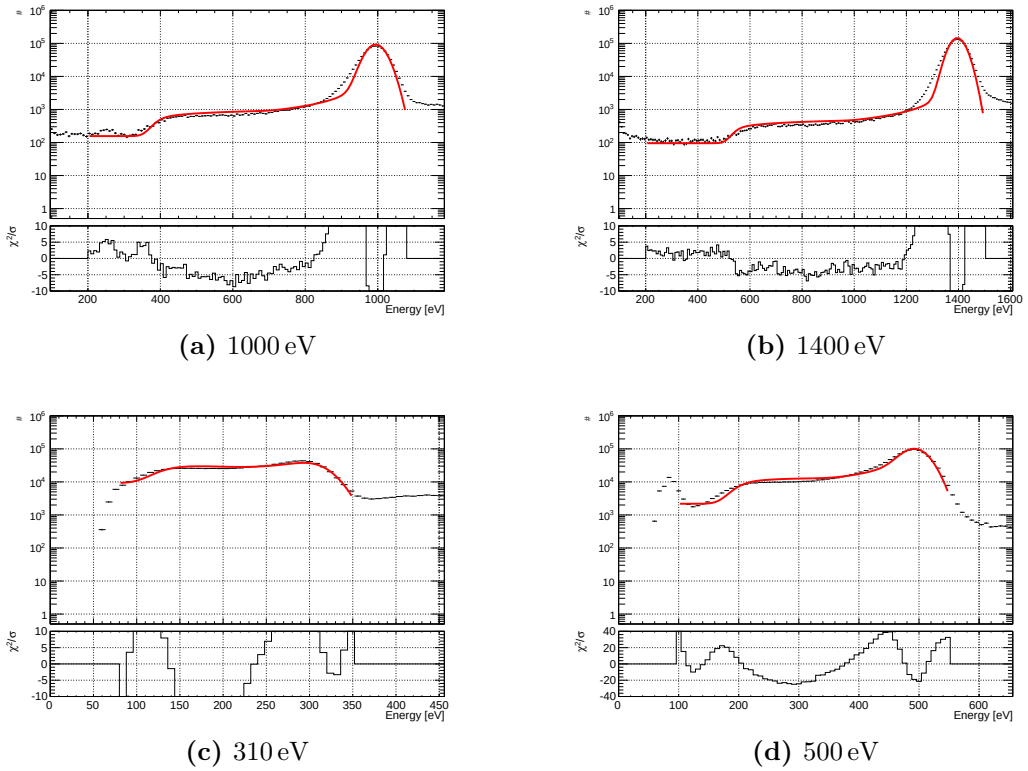

(a) 1000 eV **(b)** 1400 eV

(c) 310 eV **(d)** 500 eV

Figure 4.24: Fits of the detector model to spectra from measurements at different energies. The spectra were all taken at the plane-grating monochromator. The plot below each spectra shows the normalized residuals over the energy. Especially at energies below 500 eV the distortion of the spectrum becomes dominant. Peak and shoulder merge more and more as it can be seen in (c).

storage ring and monochromator was closed almost completely using only the minimal radiation coming through. Because of the strong dimming of the beam, stray light was expected to be dominant [68]. At the four-crystal monochromator the intensity was reduced by slightly tilting the monochromator crystals. Here, the problem with stray light was not present.

Figure 4.25 shows four measurements at energies below and above the Si K-edge. The data shown in the upper figures (4.25a and 4.25b) were taken at the plane-grating monochromator, those in the lower figures (4.25c and 4.25d) at the four-crystal monochromator. For each beamline, a measurement below (1.76 keV) and above (1.86 keV) the Si K-edge is shown.

The measurements at the different beamlines show similar spectra for the same energy. For both beamlines, the shoulder is much more pronounced at beam energies above the Si K-edge energy. The agreement of model and spectrum is

better for the measurements at the four-crystal monochromator. The deviation between model and spectrum at the main peak for the measurement at the plane-grating monochromator (figure 4.25a) is attributed to stray-light.

The spectra at 1.76 keV show a step in the flat-shelf background. Below 600 eV the model predicts a lower background than actually present in the spectra. Apparently, the model assumption of a homogeneous flat shelf below the main peak underestimates the influence of the Al entrance window at energies above the Al K-edge (1.56 keV).

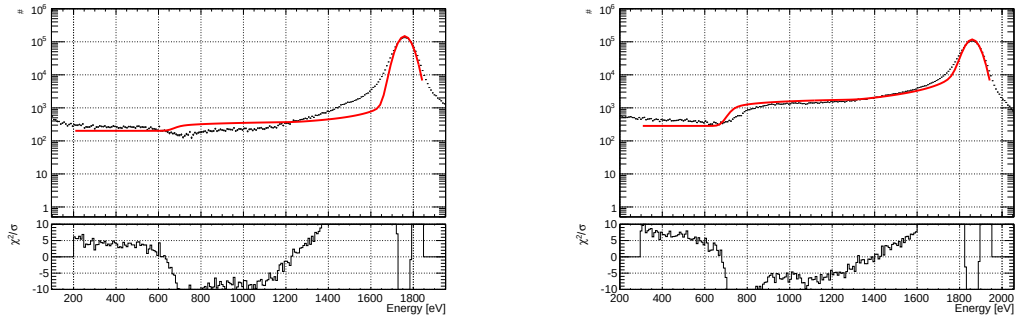

(a) 1.76 keV **(b)** 1.86 keV

(c) 1.76 keV **(d)** 1.86 keV

Figure 4.25: Fits of the detector model to spectra from measurements at energies below and above the Si K-edge. (a) and (b) were both taken at the plane-grating monochromator beamline. The deviation at the main peak are attributed to stray light. (c) and (d) were taken at the four-crystal monochromator beamline. Here, model and measurement show better agreement at the peak. Below the Si K-edge, the flat shelf at low energies is higher than predicted by the model.

4.2.7 Detection efficiency

If a photon is absorbed in the detector bulk, it creates a signal and is thus counted as detected. The signal height is irrelevant in this case. This means

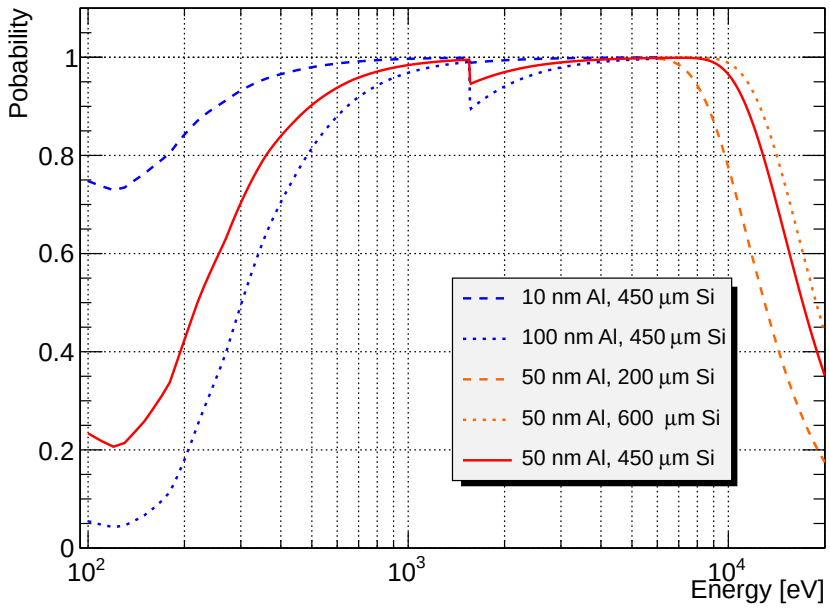

Figure 4.26: Theoretical detection efficiency over a range from 100 eV to 20 000 eV. The thick line corresponds to a 450 µm Si detector with 50 nm Al entrance window. The effect of different entrance window and wafer thicknesses is indicated by dashed and dotted lines. The entrance window has impact on the response to low energy photons, while the wafer thickness defines the limit for the detection efficiency for high energy photons. Data from [10].

the detection efficiency is governed by the transmission of the entrance window and the absorption of the silicon bulk. The detector has an aluminum entrance window directly processed upon the shallow p-implantation on the back side. There is no oxide or nitride layer, and no anti-reflective coating.

Figure 4.26 shows a plot of the theoretical detection efficiency over a range from 100 eV to 20 000 eV. The thick red line corresponds to a 450 µm Si detector with 50 nm Al entrance window which are the thicknesses for the device under test. According to this model the detector has a detection efficiency above 90 % for the energy range from 500 eV to 10 000 eV.

Indicated by dashed lines is the effect of a different entrance window and wafer thickness. The detection efficiency $\epsilon(h\nu)$ was calculated from the transmission and absorption probabilities for Al and Si:

$$\epsilon(h\nu) = \tau_{Al}(h\nu) \cdot [1 - \tau_{Si}(h\nu)] \tag{4.7}$$

The energy dependent values for the transmission τ in equation 4.7 are taken

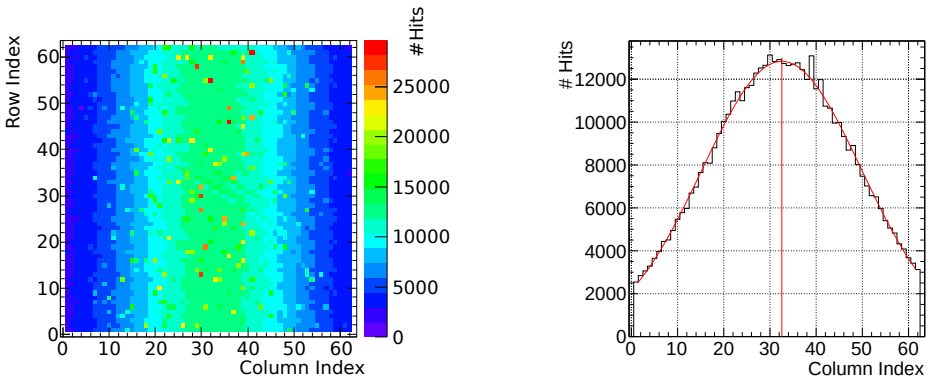

(a) hit map **(b)** hit map projection

Figure 4.27: From a measurement at the DWL beamline, the hit map for SNG patterns (a) and its projection over the column index (b) are shown. The projection displays the average number of hits for the respective column. The projection has been fitted with a Gaussian curve. The vertical line marks the mean of the fit, which is located at 32.6. This means the middle of the matrix is about one pixel below the horizontal plane.

from the Henke database [10]. Figure 4.26 shows that the entrance window has impact on the response to low energy photons (blue), while the wafer thickness defines the limit for the detection efficiency for high energy photons (orange).

To test this model the theoretical count rate $C(E)$ is calculated for a known photon flux $N(h\nu)$ and compared with the measurement. The count rate $C(E)$ of the detector is the convolution [65]

$$C(E) = \int N(h\nu) \cdot \epsilon(h\nu) \cdot P(h\nu; E) dh\nu \tag{4.8}$$

with $P(h\nu; E)$ being the detector model described in section 3.1.4 and which was fitted to the measurement data in section 4.2.6.

As described in section 4.1.3, the photon flux is homogeneous parallel to the horizontal plane and changes symmetrically with the distance in vertical direction. Figure 4.27a shows a hit map taken from a measurement with 3 electrons in the synchrotron ring.

The number of photons is maximal at the horizontal plane and declines with the distance. The combined spectrum has a Gaussian shape in vertical direction. The detector was aligned to have the horizontal plane at its center. As it was

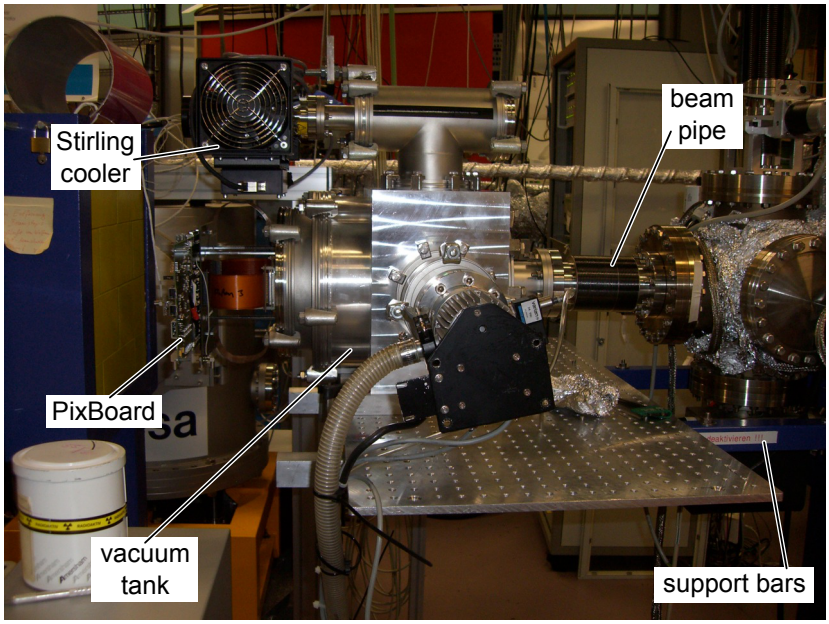

Figure 4.28: Image of the setup at the DWL beamline. The tank is fastened to the aluminum hole plate which is itself screwed to the two blue bars coming from the right. There was no direct support from underneath the tank, so the setup could bend down because of its weight.

turned by 90° the spectrum changes with the pixel column.

The detector has 64 pixel columns which are indexed from 0 to 63. This means the middle of the matrix is at $(63-0)/2 = 31.5$, i.e. at the edge between the pixel with column index 31 and column index 32. The Gaussian curve fitted to the profile in figure 4.27b has a mean of 32.6. This is an extra offset of approximately 1 pixel which has to be considered when calculating the photon flux for a certain pixel column.

The reason for this extra offset can be seen in figure 4.28 where the setup attached to the DWL beamline is shown. In contrast to the measurements at the monochromator beamlines where the tank was supported by the x-y table, here it was mounted on the aluminum hole plate which was fastened to two support bars.

There was no direct support from underneath the tank, so apparently the setup did bend slightly due to the weight of the tank. Other effects like tilt or a rotation of the matrix with respect to the beam axis were regarded negligible and thus not considered when calculating the photon flux.

The photon flux was calculated from the theoretical files provided by BESSY. These contained the flux $N(h\nu)_{\mathrm{BESSY}}$ for a single pixel at a certain offset from the

horizontal plane, created by a single electron per second in the storage ring (see figure 4.5). The number of electrons in the storage ring for the spectra presented below was determined to be $N_{e^-} = 3$ by a measurement with a calibrated diode at BESSY.

The photon flux $N(h\nu)$ hitting a pixel column is calculated by determining the column's offset from the horizontal plane and scaling the respective theoretical spectrum $N(h\nu)_{\mathrm{BESSY}}$ with the number of electrons N_{e^-} in the storage ring, the number of contributing pixels per column N_{pixels}, and the measurement time t_{meas}.

$$N(h\nu) = N(h\nu)_{\mathrm{BESSY}} \cdot N_{e^-} \cdot N_{\mathrm{pixels}} \cdot t_{\mathrm{meas}} \tag{4.9}$$

The measurement time t_{meas} for the plots shown here was determined from the number of frames in the measurement file multiplied with the integration time of 604.86 s.

Because the border pixels were not considered in the spectra, the number of contributing pixels was 62 per line, minus the number of bad pixels within. The number of bad pixels in the respective column was taken from the bad pixel map. The matrix only had a few bad pixels, so most of the pixel columns had 62 contributing pixels.

Figure 4.29 shows spectra for all valid patterns at different offsets to the horizontal plane. The spectrum is shown in black, in each spectrum the respective calculated theoretical detector count rate $C(E)$ is drawn in red. Below each spectrum the normalized residuals are displayed.

The result for a pixel column next to the horizontal plane (offset -0.5) is shown in figure 4.29a. The theoretical count rate for this pixel column shows good agreement with the spectra. The normalized residuals are well within the ± 5 range for the energy range from 500 eV to 10 000 eV. Within this energy range a slightly higher deviation around the Si K-edge energy (1.8 keV) is visible.

Figure 4.29b shows spectrum and model function for one of the two outmost pixel columns. Also here, the agreement between both is very good up to 2000 eV. Above this energy, the spectrum deviates from the model.

The reason for this is not yet understood. Pile-up does not show up in the other spectra, especially the one for the pixel column next to the horizontal plane (figure 4.29b) for which the photon flux is higher (see figure 4.5).

Figure 4.29c and figure 4.29d show spectra for two pixel columns with the same distance to the horizontal plane. Due to the symmetry of the DWL spectrum both pixel columns see the same photon flux $N(h\nu)$. The theoretical count $C(E)$ rate is thus the same and also matches both spectra equally well.

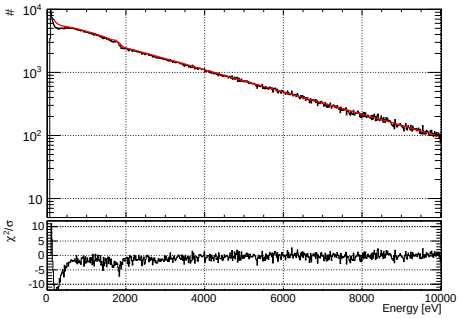

(a) Index 32, Offset −0.5

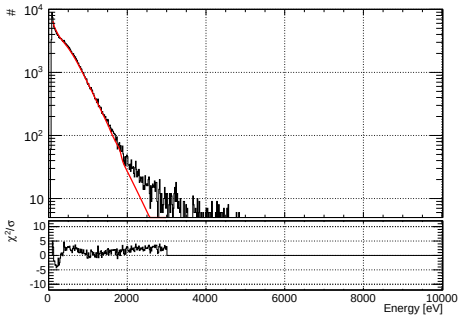

(b) Index 1, Offset −31.5

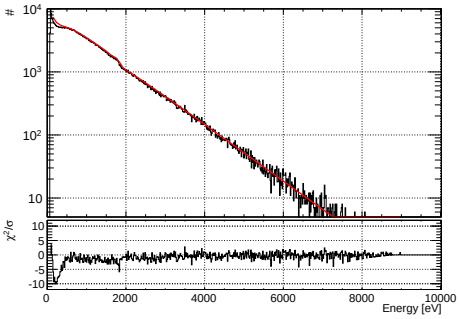

(c) Index 15, Offset −17.5

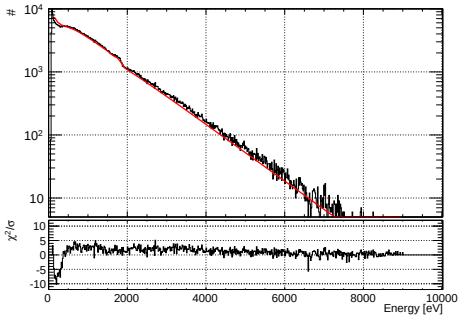

(d) Index 50, Offset 17.5

Figure 4.29: Comparison of calculated and measured DWL spectrum in the energy range from 0 eV to 10 000 eV. The theoretical curve is drawn in red. Below, the normalized residuals are shown which are below 5 for the energy range between 500 eV to 10 000 eV. The largest deviations between model and measurement are found below 500 eV. (a) shows the result for a pixel column next to the horizontal plane, (b) for one of the two outmost pixel columns. (c) and (d) show spectrum and model function for two pixel columns with the same offset to the horizontal plane.

Figure 4.30 shows different spectra from pixel columns between the horizontal plane and the matrix border. The rising contribution of high energy events to the spectrum with decreasing offset to the horizontal plane can be observed. Like for the spectra shown in figure 4.29, the normalized residuals are well between the ±5 range. The deviance is higher below the Si-K edge energy and becomes extreme below 500 eV.

The method presented here is a good way to determine the detection efficiency for a large-scale DePFET device such as the Simbol-X quadrant prototype over a large energy range. It shows that the detection efficiency is determined by the transmission in the entrance window and the absorption in the silicon bulk.

However, the resulting detection efficiency as a function of the photon energy relies on the correctness of the used models. The response function predicts a

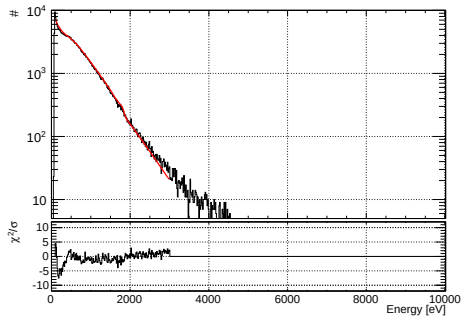

(a) Index 6, Offset −26.5

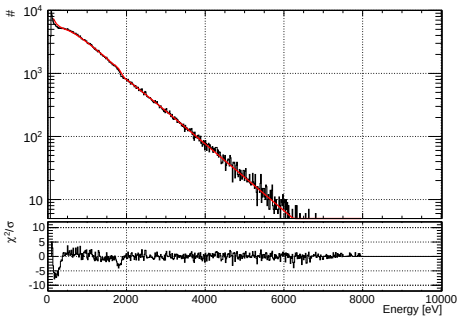

(b) Index 13, Offset −19.5

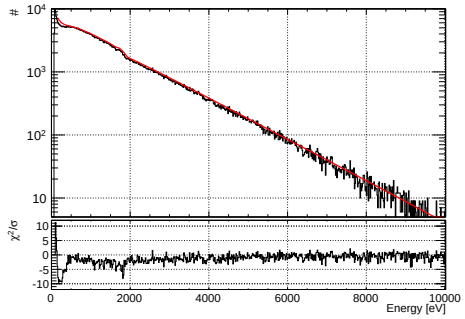

(c) Index 19, Offset −13.5

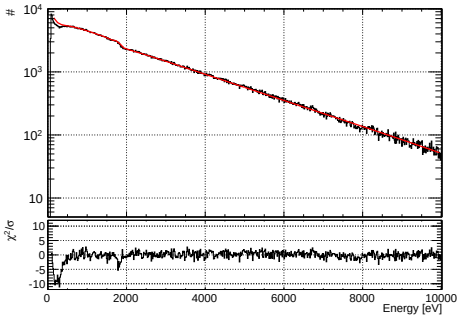

(d) Index 26, Offset −6.5

Figure 4.30: Comparison of calculated and measured DWL spectrum in the energy range from 0 eV to 10 000 eV. The theoretical curve in red, the spectrum in black. The share of high energy events becomes more and more prominent in the spectrum with falling offset.

contribution of low energy signals (shoulder and tail) due to incomplete charge collection which becomes dominant for lower photon energies (see section 3.1.4). The fits to the spectra from monoenergetic measurements shown in section 4.2.6, show that this is the case for energies of 500 eV and below. Also the contribution of the flat shelf to the spectrum is dominant for photon energies in this range.

The large deviation between the theoretical count rate $C(E)$ from the DWL spectra for energies below 500 eV. Especially the precision of the modeling of the low energy background, that means the flat shelf, has impact on the result of the theoretical count rate in the low energy region.

4.3 Summary

The characterization of the “Simbol-X quadrant” macropixel detector showed that detector parameters like noise and gain are distributed homogeneously over

the active area, even for such a large scale device with $3.2 \times 3.2\,\mathrm{cm}^2$ active area.

The offset showed some localized deviations, e.g. higher values in the corners, and a single line with higher offset values. However, these do not have effect on noise and gain of the matrix. Noise of the matrix was determined to be 15.1 eV or $4.1\,\mathrm{e}^-$.

Scans over the energy showed an excellent linear response of the detector matrix. The simple detector model developed reproduced the measured peak shapes with good agreement, despite the strong simplification of the flat shelf background.

From the detector model it can be deduced, that the deviation of peak positions for lower energies is mainly caused by incomplete charge collection close to the entrance window. In the current version, the flat shelf background is modeled by a phenomenological function. A physical model of the flat shelf background shall be implemented in future versions.

When scanning a 3×3 pixel patch of the detector matrix with a 100 µm pencil beam, no charge loss within the pixel area was detected. This showed that the charge collection within the $500 \times 500\,\mu\mathrm{m}^2$ pixel by the drift ring structure works, which is a good result for the BepiColombo matrices which have a smaller pixel size ($300 \times 300\,\mu\mathrm{m}^2$).

Comparison of polychromatic measurements with theoretic models of the count rate showed that the detection efficiency of the detector is determined by the transmission of the aluminum entrance window.

These results demonstrate the excellent DePFET pixel characteristics which are important for development and qualification of DePFET focal plane arrays for upcoming space missions like BepiColombo and IXO.

5. Conclusions and outlook

The measurement campaign at BESSY not only was an intensive study of the DePFET detector itself, but also a test for the DePFET data acquisition setup and the developed analysis software package ROAn.

The discovery of the temperature drifts lead not only to a better biasing of the ASTEROID ASIC, but also to improvements of the temperature logging means of the data acquisition setup.

Furthermore, the analysis demands of the BESSY measurement campaign led to improvements in the data analysis software ROAn. These comprise not only new algorithms but also improvements in stability and design of the underlying architecture. Due to the scripting ability of the analysis software, a large number of data files could be handled and information from different analysis runs gathered easily.

The BepiColombo mission is scheduled for launch in 2014. At present the flight modules are assembled. These will be qualified and tested in the same way as the Simbol-X prototype presented in section 4. The experiences made during the measurements and data analysis with the similar device also lay a good groundwork for the designated tests with the BepiColombo flight modules.

The analysis software package currently provides an already comprehensive set of analysis steps which are currently used to qualify next generation DePFET matrices at the HLL. Feedback from these applications continues to deliver new ideas and improvements which can be integrated easily, due to the modularity of its design.

In the future, the development of larger matrices and faster readout of the detectors will increase the data volume drastically. This will make on-board pre-processing necessary which reduces the data volume by pre-filtering the detector data in hardware. The analysis will have then have to cope with the such reduced data.

Readout of future DePFET matrices will also support windowing, i.e. selective readout of subareas on the matrix. Also such data will have to be analyzed.

With windowing, smaller parts of the DePFET matrix are read out faster, which means the occurrence of misfit clusters will become more prominent. The

effects on the spectrum and algorithms to correct these will have to be investigated.

The DePFET matrix presented in chapter 4 has a pixel size of $500 \times 500\,\mu m^2$. Peak shifts due to sub-threshold charge loss will be more articulated with smaller DePFET pixels, like they are proposed for the IXO wide field imager ($75 \times 75\,\mu m^2$). Correction algorithms are currently investigated and will be implemented.

Also, with smaller pixel sizes the number of SNG patterns reduces. As SNG patterns are used for pixel calibration, this results in longer calibration measurements. This makes the development of new calibration methods necessary.

At present, the data analysis software runs on a single processor only. Modern computers have multiple cores, which offers the possibility to parallelize algorithms. This can be used to speed up calculations and analysis. First steps into this direction are already investigated.

Thanks to its modular design, the developed analysis framework ROAn is capable of coping with the current analysis demands and flexible enough to be adapted to future tasks. This should ensure a longtime use at the HLL.

Bibliography

[1] Zedh. *EM spectrum*. URL: http://commons.wikimedia.org/wiki/File:EM_spectrum.svg.

[2] W. R. Leo. *Techniques for Nuclear and Particle Physics Experiments: a how-to approach*. Springer-Verlag, 1994.

[3] G. Lutz. *Semiconductor Radiation Detectors*. 2nd Edition. Springer-Verlag Berlin Heidelberg, 2007.

[4] L. Strüder. "Wide field imaging spectrometer for ESA's future X-ray mission: XEUS". In: *Nucl. Instr. Meth. Phys. Res. A* 436 (1999), pp. 53–67.

[5] P. Lechner et al. "The Low Energy Detector of Simbol-X". In: *Proceedings of SPIE* 7021 (2008), pp. 702110–1–702110–11.

[6] A. Stefanescu et al. "The Wide Field Imager of the International X-ray Observatory". In: *Nucl. Instr. Meth. Phys. Res. A* 624.2 (2010), pp. 533–539. DOI: 10.1016/j.nima.2010.05.049.

[7] J. Treis et al. "MIXS on BepiColombo and its DEPFET based focal plane instrumentation". In: *Nucl. Instr. Meth. Phys. Res. A* (2010). DOI: 10.1016/j.nima.2010.03.173.

[8] W. M. Yao et al. "Review of Particle Physics". In: *Journal of Physics G* 33.1 (2006).

[9] G. Lutz and J. Kemmer. "New Detector Concepts". In: *Nucl. Instr. Meth. Phys. Res. A* 253 (1987), pp. 365–377.

[10] B. L. Henke et al. "X-Ray Interactions: Photoabsorptions, Scattering, Transmission and Reflection at E=50–30000 eV, Z=1–92". In: *Atomic Data and Nuclear Data Tables* 54.2 (1993), pp. 181–342.

[11] A. C. Thompson and D. Vaughan, eds. *X-Ray Data Booklet*. 2nd Edition. Lawrence Berkeley National Laboratory, 2001. URL: http://xdb.lbl.gov/.

[12] M. O. Krause. "Atomic Radiative and Radiationless Yields for K and L Shells". In: *Journal of Physical and Chemical Reference Data* 8.2 (1979), pp. 307–327.

[13] C. Kittel. *Einfürung in die Festkörperphysik*. 9th Edition. R. Oldenburgverlag München Wien, 1991.

[14] S. M. Sze and K. K. Ng. *Semiconductor Devices – Physics and Technology*. 3rd Edition. John Wiley & Sons, 2007.

[15] P. Lechner. "Zur Ionisationsstatistik in Silizium". PhD thesis. Technische Universität München, 1998.

[16] R. C. Alig and S. Bloom. "Electron-Hole-Pair Creation Energies in Semiconductors". In: *Phys. Rev. Lett.* 35.22 (Dec. 1975), pp. 1522–1525. DOI: 10.1103/PhysRevLett.35.1522.

[17] U. Fano. "Ionisation Yield of Radiations. II. The Fluctuations of the Number of Ions". In: *Physical Review* 72 (1947), pp. 26–29. DOI: 10.1103/PhysRev.72.26.

[18] J. B. Johnson. "Thermal Agitation of Electricity in Conductors". In: *Physical Review* 32 (1928), pp. 97–109.

[19] H. Nyquist. "Thermal Agitation of Electric Charge in Conductors". In: *Physical Review* 32 (1928), pp. 110–113.

[20] K. Kandiah et al. "A physical model for random telegraph signal currents in semiconductor devices". In: *Journal of Applied Physics* 66.2 (1989), pp. 937–948. DOI: 10.1063/1.343523.

[21] W. Schottky. "Über spontane Stromschwankungen in verschiedenen Elektrizitätsleitern". In: *Annalen der Physik* 362.23 (1918), pp. 541–567. DOI: 10.1002/andp.19183622304.

[22] A. Bähr. "Experimenteller Betrieb neuartiger DEPFET-RNDR-Detektoren und mathematische Beschreibung der Mehrfachauslese". MA thesis. Hochschule für angewandte Wissenschaften in München, 2010.

[23] P. Klein. "Entwicklung, Bau und Test eines Halbleiter-Bildzellendetektors für den Einsatz in der Teilchenphysik". PhD thesis. Ludwig-Maximilians-Universität München, 1996.

[24] H. Spieler. *Introduction to Radiation Detectors and Electronics*. 1999. URL: http://www-physics.lbl.gov/~spieler/physics_198_notes_1999/index.html.

[25] R. Müller. *Rauschen*. Springer-Verlag Berlin Heidelberg, 1979.

[26] E. Gatti and P. Rehak. "Semiconductor Drift Chambers - An Application of a Novel Charge Transport Scheme". In: *Nucl. Instr. Meth. Phys. Res.* 225 (1984), pp. 608–614. DOI: 10.1016/0167-5087(84)90113-3.

[27] S. Wölfel. "Neuartige DePFET-RNDR-Detektoren im experimentellen Betrieb". PhD thesis. Universität Siegen, 2007.

[28] P. Lechner. personal communication.

[29] C. Guazzoni. "The first 25 years of silicon drift detectors: A personal view". In: *Nucl. Instr. Meth. Phys. Res. A* 624.2 (2010), pp. 247–254. DOI: doi:10.1016/j.nima.2010.06.005.

[30] N. Kimmel. "Analysis of the Charge Collection Process in Solid State X-Ray Detectors". PhD thesis. Universität Siegen, 2008.

[31] L. Strüder et al. "Development of Fully Depletable CCDs for High Energy Physics Applications". In: *Nucl. Instr. Meth. Phys. Res. A* 257.3 (1987), pp. 594–602.

[32] N. Meidinger et al. "eROSITA camera design and first performance measurements with CCDs". In: *Proceedings of SPIE*. Ed. by M. J. L. Turner and K. A. Flanagan. Vol. 7011. Proceedings of SPIE. SPIE. Marseille, France: SPIE, 2008, pp. 1–12. DOI: 10.1117/12.787793.

[33] R. Hartmann et al. "A high-speed pnCCD detector system for optical applications". In: *Nucl. Instr. Meth. Phys. Res. A* 568.1 (2006), pp. 118–123. DOI: 10.1016/j.nima.2006.05.229.

[34] P. Majewski. personal communication.

[35] J. Treis et al. "First results of DEPFET-based active-pixel-sensor prototypes for the XEUS wide-field imager". In: *Proceedings of SPIE*. Ed. by A. D. Holland. Vol. 5501. 1. Glasgow, Scotland, United Kingdom: SPIE, 2004, pp. 89–100. DOI: 10.1117/12.551536.

[36] S. Rummel. "Investigation of DEPFET as Vertex Detector at ILC - Intrinsic properties, radiation hardness and alternative readout schemes". PhD thesis. Technische Universität München, Apr. 2009.

[37] S. Rummel and L. Andricek. "The DEPFET active pixel sensor for vertexing at ILC and Super KEKB". In: *Nucl. Instr. Meth. Phys. Res. A* 623 (2010), pp. 189–191. DOI: 10.1016/j.nima.2010.02.191.

[38] M. Porro et al. “Spectroscopic performances of DePMOS detector/amplifier device with respect to different filtering techniques and operating conditions”. In: *Transactions on Nuclear Science* 16 (2005).

[39] L. Bombelli et al. “VELA: The CMOS Circuit Based on Fast Current Read-Out for X-Ray Spectroscopy With DePMOS”. In: *Transactions on Nuclear Science* 54.4 (2007), pp. 1359–1366. DOI: 10.1109/TNS.2007.901224.

[40] L. Bombelli et al. “First Readout of a 64 x 64 DEPFET Matrix With VELA Circuit”. In: *Transactions on Nuclear Science* 56.6 (2009), pp. 3789–3795. DOI: 10.1109/TNS.2009.2034519.

[41] L. Bombelli et al. “VELA: A fast DEPFET readout circuit for the IXO mission”. In: *Nucl. Instr. Meth. Phys. Res. A* 617.1-3 (2010), pp. 316–318. DOI: 10.1016/j.nima.2009.10.020.

[42] M. Porro et al. “Expected performance of the DEPFET sensor with signal compression: A large format X-ray imager with mega-frame readout capability for the European XFEL”. In: *Nucl. Instr. Meth. Phys. Res. A* 624.2 (2010), pp. 509–519. DOI: 10.1016/j.nima.2010.02.254.

[43] M. H. Ivan Peric Peter Fischer. “Spezikation des Switcher-Chips”.

[44] P. Fischer. “Switcher-S, a HV Switch ASIC for DEPFET Matrix Control”. 2009.

[45] M. Porro et al. “Performance of ASTEROID: a 64 channel ASIC for source follower readout of DEPFET matrices for X-ray astronomy”. In: (2008).

[46] M. Porro et al. “ASTEROID: A 64 channel ASIC for source follower readout of DEPFET arrays for X-ray astronomy”. In: *Nucl. Instr. Meth. Phys. Res. A* 617.1–3 (2010), pp. 351–357. DOI: 10.1016/j.nima.2009.10.040.

[47] W. Buttler et al. “Evolution in the criteria that underlie the design of a monolithic preamplifier system for microstrip detectors”. In: *Nucl. Instr. Meth. Phys. Res. A* 288.1 (1990), pp. 140–149. DOI: 10.1016/0168-9002(90)90479-P.

[48] J. Treis. personal communication.

[49] L. Strüder et al. “Large-format, high-speed, X-ray pnCCDs combined with electron and ion imaging spectrometers in a multipurpose chamber for experiments at 4th generation light sources”. In: *Nucl. Instr. Meth. Phys. Res. A* 614.3 (2010), pp. 483–496. DOI: 10.1016/j.nima.2009.12.053.

[50] M. Popp. "Untersuchung und analytische Modellierung der Systemantwort von pn-CCD Detektoren". PhD thesis. Ludwig-Maximilians-Universität München, 2000.

[51] K. Dennerl. *eROSITA/TRoPIC Detector Calibration*. Talk. Feb. 2008.

[52] J. Ballet. "Pile-up on X-ray CCD instruments". In: *Astron. Astrophys. Suppl. Ser.* 135.2 (1999), pp. 371–381. DOI: 10.1051/aas:1999179.

[53] G. W. Phillips and K. W. Marlow. "Automatic Analysis of Gamma-Ray Spectra from Germanium Detectors". In: *Nucl. Instr. Meth.* 137.3 (1976), pp. 525–536. DOI: 10.1016/0029-554X(76)90472-9.

[54] T. Eggert. "Die spektrale Antwort von Silizium-Röntgendetektoren". PhD thesis. Technische Universität München, 2004.

[55] F. Scholze and M. Procop. "Modelling the response function of energy dispersive X-ray spectrometers with silicon detectors". In: *X-Ray Spectrometry* 38.4 (2009), pp. 312–321. DOI: 10.1002/xrs.1165.

[56] W. T. Elam et al. "A new atomic database for X-ray spectroscopic calcualtions". In: *Radiation Physics and Chemistry* 63.2 (2002), pp. 121–128. DOI: 10.1016/S0969-806X(01)00227-4.

[57] R. Brun and F. Rademakers. "ROOT - An Object Oriented Data Analysis Framework". In: *Nucl. Instr. Meth. Phys. Res. A* 389 (1997), pp. 81–86.

[58] *ROOT | A Data Analysis Framework*. Dec. 2010. URL: http://root.cern.ch.

[59] B. Stroustrup. *The C++ Programming Language*. Addison-Wesley, 1997.

[60] *ROAn – A ROOT based Offline Analysis tool*. Dec. 2010. URL: http://www.hll.mpg.de/~pixana/.

[61] R. Andritschke et al. "Data analysis for characterizing PNCCDS". In: *Nuclear Science Symposium Conference Record*. Oct. 2008, pp. 2166–2172. DOI: 10.1109/NSSMIC.2008.4774781.

[62] A. Meuris et al. "Development and Characterization of new 256×256 Pixel DEPFET Detectors for X-ray Astronomy". In: *Nuclear Science Symposium Conference Record*. Nov. 2010.

[63] F. Scholze et al. "High-Accuracy EUV Metrology of PTB Using Synchrotron Radiation". In: *Proceedings of SPIE* 4344 (2001), pp. 402–413.

[64] M. Krumrey and G. Ulm. "High-accuracy detector calibration at the PTB four-crystal monochromator beamline". In: *Nucl. Instr. Meth. Phys. Res. A* 467/468 (2001), pp. 1175–1178.

[65] M. Krumrey et al. "Complete characterization of a Si(Li) detector in the photon energy range 0.9–5 keV". In: *Review of Scientific Instruments* 60.7 (1989), pp. 2287–2290. DOI: 10.1063/1.1140795.

[66] M. Popp. "Modeling the energy response of pn-CCDs in the 0.2-10 keV band". In: *Nucl. Instr. Meth. Phys. Res. A* 439.2–3 (2000), pp. 567–574. DOI: 10.1016/S0168-9002(99)00912-2.

[67] A. Stefanescu. personal communication.

[68] F. Scholze. personal communication.

[69] P. Ferrando et al. "Simbol-X: a formation flying mission for hard X-rays astrophysics". In: *Proceedings of SPIE* 5900 (2005), 59000P1–59000P10.

[70] P. Ferrando et al. "Simbol-X: a new generation hard X-ray telescope". In: *arxiv.org* (2003). DOI: 10.1117/12.521998.

[71] *ESA Science & Technology: BepiColombo*. 2010. URL: http://sci.esa.int/science-e/www/area/index.cfm?fareaid=30.

[72] G. Fraser et al. "The Mercury Imaging X-ray Spectrometer (MIXS) on BepiColombo". In: *Planetary and Space Science* 58 (2010), pp. 79–95. DOI: 10.1016/j.pss.2009.05.004.

List of used Acronyms

SDD *Silicon Drift Detector* 4

CCD *Charge-Coupled Device* 4

HLL *Halbleiterlabor* (german for 'semiconductor laboratory') 4

DePFET *Depleted P-Channel Field Effect Transistor* 4

IXO *International X-ray Observatory* 4

XEUS *X-ray Evolving Universe Spectroscopy* 4

MIP *Minimal Ionizing Particle* 8

FWHM *Full Width at Half Maximum* 17

FET *Field Effect Transistor* 27

ENC *Equivalent Noise Charge* 28

MOS *Metal-Oxide-Semiconductor* 26

NASA the *National Aeronautics and Space Administration* 36

MOSFET *Metal-Oxide-Semiconductor Field Effect Transistor* 39

IC *Integrated Circuit* 45

ASIC *Application Specific Integrated Circuit* 45

CMOS *Complementary Metal Oxide Semiconductor* 49

AMS *Austria Microsystems* 49

RAM *Random Access Memory* 49

S/H *Sample and Hold* 52

ADC *Analog-to-Digital Converter* 56

ESA the *European Space Agency* 59

PCB *Printed Circuit Board* 61

FPGA *Field-Programmable Gate Array* 63

PCI *Peripheral Component Interconnect* 63

ZIF *Zero Insertion Force* 65

ADU *Analog-to-Digital Unit* 68

DAC *Digital-to-Analog Converter* 68

DMA *Direct Memory Access* 69

DAQ *Data Acquisition* 70

FIFO *First In, First Out* 69

SGL *Scatter Gather List* 70

MBS *Multiple Buffer Structure* 70

CDF *Cumulative Distribution Function* 84

sng *Single*, i.e. a pattern which comprises one hit 86

dbl *Double*, i.e. a pattern which comprises two hits 86

trp *Triple*, i.e. a pattern which comprises three hits 86

qud *Quadruple*, i.e. a pattern which comprises four hits 86

all *All Valids*, comprises the valid forms of Singles, Doubles, Triples and Quadruples 145

oth *Other*, i.e. any pattern which is not one of the above 88

CCE *Charge Collection Efficiency* 99

ICC *Incomplete Charge Collection* 99

LED *Light Emitting Diode* 106

OOP *Object Oriented Programming* 116

PTB *Physikalisch Technische Bundesanstalt* (the Federal Institute of Physical and Technical Affairs) 155

MIXS *Mercury Imaging X-ray Spectrometer* 155

DWL *Direct White Light* 165

JAXA the *Japan Aerospace Exploration Agency* 214

List of Figures

List of Tables

A. DePFET missions

At the HLL several types of DePFET matrices have been developed to be used in different space missions. Each mission had different requirements to which the matrix was designed. DePFET detectors are planned to be used in several space missions. The following sections give a short presentation of each of them, depicting the detector requirements.

A.1 Simbol-X

Simbol-X was a hard X-ray mission which originated as a plan from the french (CNES[1]) and italian (ASI[2]) space agencies. The design envisioned a mirror spacecraft and a detector spacecraft in formation flying configuration creating an X-ray telescope with 20 m to 30 m focal length operating in the 0.5 keV to 80 keV range. Simbol-X will be the first mission using a focusing telescope at X-ray energies well above 10 keV where before only imaging systems using collimators and coded mask apertures have been available [5].

Simbol-X should investigate active galactic nuclei, the accretion discs around black holes which present the most violent regions in space. Also, the mission should measure the synchrotron spectrum of supernova remnants and the diffuse cosmic X-ray background. Unfortunately the mission was cancelled due to budget restrictions in March 2009. Because of this, the requirements for spacecraft and detector were never finally defined. The values presented below are taken from literature [70, 69].

The mirror-module carries a Wolter type I optic which focuses the X-ray radiation onto the detector module. Together, the telescope was planned to reach a resolution of 30 arch seconds half energy width and a sensitivity which is 100 times better than the one by the INTEGRAL space mission.

The focal plane assembly comprised a silicon low energy detector on top of a CdTe high energy detector. Both detectors have a sensitive area of $8 \times 8\,\mathrm{cm}^2$ and cover a field of view of 12 arch minutes. The low energy detector was planned to

[1] CNES = **C**entre **N**ational d'tudes **S**patiales

[2] ASI=**A**genzia **S**paziale **I**taliana

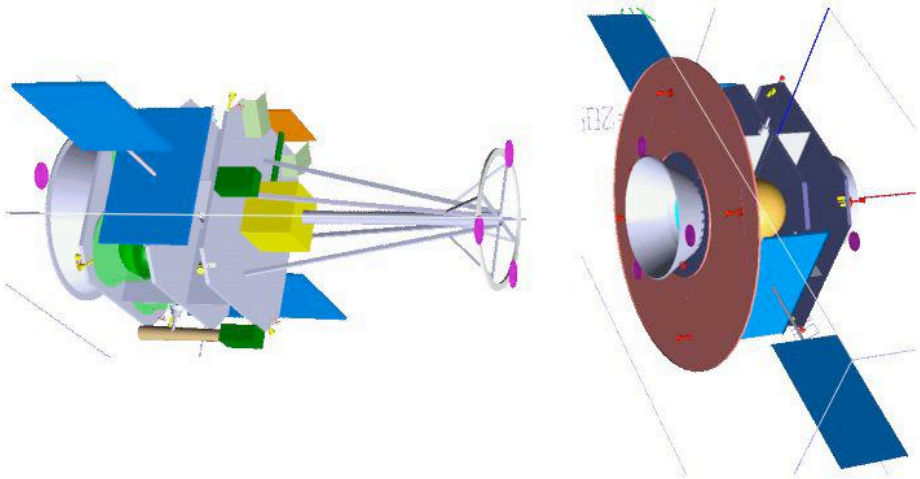

Figure A.1: The two spacecraft of Simbol-X: the detector module (left) and the mirror module (right). Picture from [69].

consist of a single wafer DePFET macropixel detector, divided into four quadrants. The pixel size was $500 \times 500\,\mu m^2$ the detector has a thickness of 450 µm. Together with the thermal filter in front of the mirrors and the optical light filter of the detector this results in a nominal energy range of the low energy detector of $\approx 0.5\,keV$ to 20 keV. The upper limit is hereby determined by the thickness of the detector.

The DePFET detector presented in section 4 was a quadrant prototype developed for this mission.

A.2 BepiColombo

BepiColombo is a joint space mission by ESA and the *Japan Aerospace Exploration Agency* (JAXA). It is destined for Mercury, which is the innermost and least explored planet in our solar system.

The spacecraft consists of two orbiters, the Mercury Magnetospheric Orbiter and the Mercury Planetary Orbiter. Their science objectives are [71]

- Origin and evolution of a planet close to the parent star
- Mercury as a planet: form, interior, structure, geology, composition and craters
- Mercury's vestigial atmosphere (exosphere): composition and dynamics

- Mercury's magnetized envelope (magnetosphere): structure and dynamics
- Origin of Mercury's magnetic field
- Polar deposits: composition and origin
- Test of Einstein's theory of general relativity

Among the 11 instruments on board the Mercury Planetary Orbiter to study the surface and geological composition of Mercury's crust is the MIXS. MIXS comprises two channels which have the same focal plane array, a 64×64 pixel DePFET detector with $300 \times 300\,\mu m^2$ pixel size.

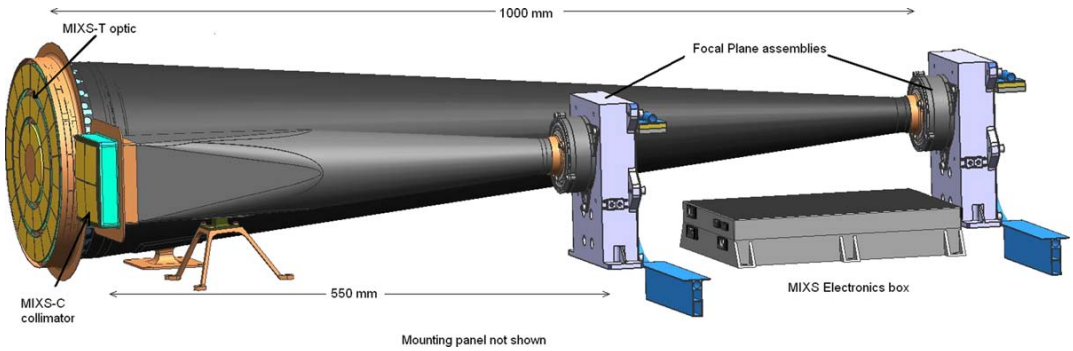

Figure A.2: Schematic view of the MIXS instrument. MIXS-C (foreground) has a simple collimator optic, which delivers a large scale footprint of the planet's surface at low solar X-ray intensity. MIXS-T (background) has a high resolution X-ray telescope, which is capable of resolving features in the sub-kilometer range, but requires higher solar X-ray fluxes. Both channels have the same focal plane assembly, a 64×64 DePFET macropixel detector with $300 \times 300\,\mu m^2$ pixel size.

Figure A.2 shows a schematic view of the instrument. The identical focal plane assemblies are on the right. The two instrument channels have different optics which define their lateral resolution. MIXS-T (telescope) can resolve surface features in the sub-kilometer range, but requires states of high solar activity. MIXS-C (collimator) can work also at quiet solar states, but delivers only a large scale footprint of the planet's crust.

With MIXS, scientist will study Mercury's surface composition using planetary X-ray fluorescence analysis. The sun's corona serves as a giant X-ray tube bombarding the planet's surface with X-ray photons. The fluorescence photons emitted back into space are measured by MIXS while orbiting the planet resulting in a map of Mercury's surface composition. The method is capable to probe

the upper few micrometer of the surface. The composition of deeper geological layers is investigated by other instruments.

Because the amount of iron in the planets crust is a crucial factor for the investigation of Mercury's planetary evolution, MIXS is required to be able to measure both, the Fe-L (0.7 keV) and Fe-K lines (6.40 keV and 7.06 keV). Especially, because the Fe-K lines are only excited in phases of high solar activity.

The energy resolution requirements are thus also 100 eV FWHM at 1 keV, with a maximal degradation to 200 eV at mission end. With this, the instrument is able to separate the Fe-L line from neighboring lines of Si [72].

These developed DePFET matrices for this mission show an energy resolution of 128 eV FWHM at 5.9 eV, taking into account all valid patterns, which is within the requirements [7].

The Mercury probe MESSENGER[3], which arrived at Mercury already in 2008 (orbit insertion scheduled on March 18th, 2011), has a similar instrument on board, XRS[4], consisting of three gaseous detectors detecting X-ray emissions in the range of1 keV to 10 keV. Compared to this, MIXS on BepiColombo will deliver much higher position and energy resolution [72].

A.3 IXO

The IXO mission is a merger of two abandoned missions, XEUS and Constellation-X. It is a planned joint mission of ESA, NASA and JAXA. The goal is to develop a successor to the successful X-ray telescopes XMM-Newton and Chandra.

Still in the planning phase, IXO is designed to carry several instruments to provide spectroscopy, imaging, timing, and polarimetry data on cosmic X-ray sources. Among the instruments, also a monolithic DePFET detector with 1024×1024 pixels and $100 \times 100\,\mu m^2$ pixel size is designated as focal plane array for the Wide-Field Imager.

The Wide-Field Imager shall cover a very large field of view of $18 \times 18\,ft^2$ with good spectral resolution (~ 125 eV at 5.9 keV), and good imaging resolution (fivefold oversampling of the mirror point spread function) in the energy range of 0.1 keV to 15 keV. This detector will then have a total size of $10.2 \times 10.2\,cm^2$, taking up the whole area of a 6 inch high purity silicon wafer [6].

For comparison, an XMM-Newton p-n CCD detector had a size of $6 \times 6\,cm^2$, a pixel count of 384×400 pixels, and was covering a single 4 inch wafer.

[3] MESSENGER=**ME**rcury **S**urface, **S**pace **EN**vironment, **GE**ochemistry and **R**anging

[4] XRS = **X**-**R**ay **S**pectrometer

B. The p-n junction

This section shows the calculation of potential and electric field in a p-n junction using the abrupt change approximation, which assumes that the doping profiles for acceptors and donors have sharp edges [14].

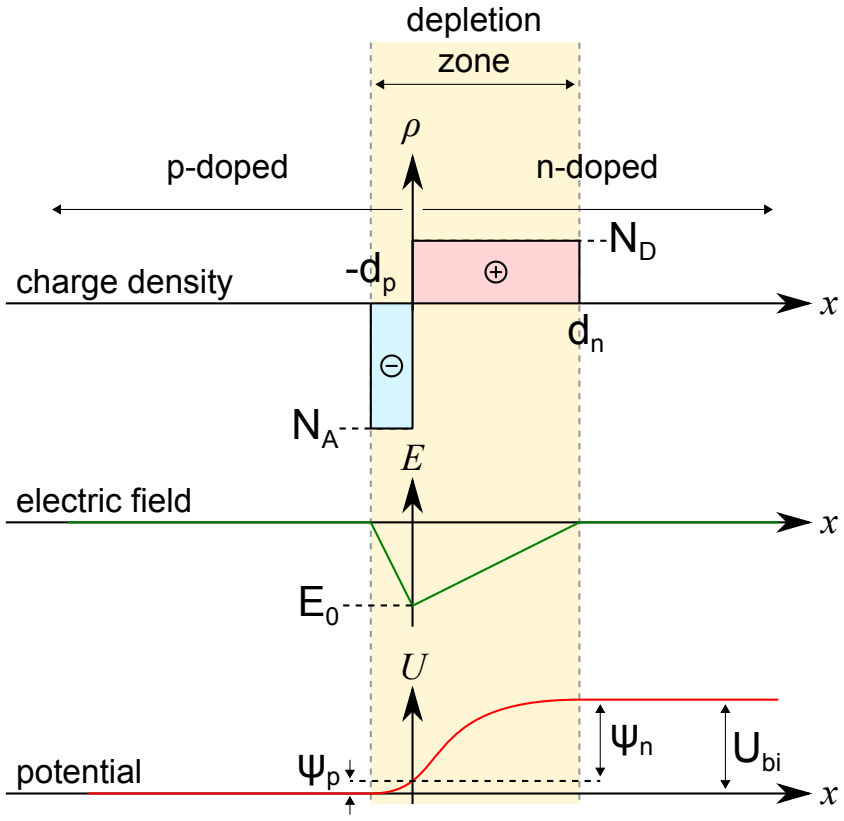

Figure B.1: Charge density, electric field and potential of an abrupt p-n junction in thermal equilibrium. Picture adapted from [14].

Electric field and potential at a p-n junction can be calculated from Poisson's equation:

$$-\Delta\psi = \nabla E = \frac{\rho}{\varepsilon_0 \varepsilon} \tag{B.1}$$

The charge density ρ is given by

$$\rho(x) = q(N_D(x) - N_A(x) + p_0 - n_0) \tag{B.2}$$

where q is the elementary charge and

$$\begin{aligned} n_0 &= n_i e^{\frac{q\psi}{kT}} , \\ p_0 &= n_i e^{\frac{q\psi}{kT}} . \end{aligned} \tag{B.3}$$

The concentrations of electrons and holes in the space charge region is negligible as compared to the ionized donor or acceptor atom density (depletion approximation) and so equation B.1 simplifies to

$$-\Delta\psi = \frac{q}{\varepsilon_0\varepsilon}(N_D(x) - N_A(x)) \tag{B.4}$$

with

$$N_A \cdot d_P = N_D \cdot d_N , \tag{B.5}$$

because the total negative charge per unit area in the p-side must be precisely equal to the total positive charge per unit are in the n-side, since in thermal equilibrium the electric field in the neutral regions is zero.

With the depletion approximation, the charge density can be expressed as

$$\rho(x) = \begin{cases} -qN_A & -d_P < x < 0 \\ qN_D & 0 < x < d_N \end{cases} \tag{B.6}$$

The electric field can be calculated by integrating equation B.1 with the above charge density inserted:

$$E(x) = \begin{cases} -\frac{q}{\varepsilon_0\varepsilon}N_A(x + d_P) & -d_P < x < 0 \\ \frac{q}{\varepsilon_0\varepsilon}N_D(x - d_N) & 0 < x < d_N \end{cases} \tag{B.7}$$

The maximum electric field E_0 is at $x = 0$ in (B.7) and is given by

$$E_0 = \frac{q}{\varepsilon_0\varepsilon}N_A d_P = \frac{q}{\varepsilon_0\varepsilon}N_D d_N \tag{B.8}$$

Integrating the electric field gives then the potential distribution:

$$\psi(x) = \begin{cases} \frac{q}{2\varepsilon_0\varepsilon}N_A(x + d_P)^2 & -d_P < x < 0 \\ \psi(0) + \frac{q}{\varepsilon_0\varepsilon}N_D(d_N - \frac{x}{2})x & 0 < x < d_N \end{cases} \tag{B.9}$$

The potentials across the regions are then given by

$$\psi_P = \frac{qN_A d_P^2}{2\varepsilon_0 \varepsilon} \tag{B.10}$$

$$|\psi_N| = \frac{qN_D d_N^2}{2\varepsilon_0 \varepsilon} \tag{B.11}$$

with the built-in voltage defined as

$$U_{bi} = \psi_P + |\psi_N| \,. \tag{B.12}$$

The width of the depletion zone can be derived from (B.12) and (B.5):

$$d_P = \sqrt{\frac{2\varepsilon_0 \varepsilon}{q} \frac{N_D}{N_A(N_A + N_D)} U_{bi}} \tag{B.13}$$

$$d_N = \sqrt{\frac{2\varepsilon_0 \varepsilon}{q} \frac{N_A}{N_D(N_A + N_D)} U_{bi}} \tag{B.14}$$

$$d_P + d_N = \sqrt{\frac{2\varepsilon_0 \varepsilon}{q} \frac{N_A + N_D}{N_A N_D} U_{bi}} \tag{B.15}$$

With an external bias voltage U (which is negative in the case of reverse bias) U_{bi} is substituted by $U_{bi} - U$. For a one-sided abrupt junction, the majority of the depletion region will be inside the lightly doped side. In the case of a p-implantation upon a n-type bulk, equation B.15 simplifies to

$$d = \sqrt{\frac{2\varepsilon_0 \varepsilon}{qN_D}(U_{bi} - U)} \tag{B.16}$$

C. The framesfile format

Originally, the framesfile format was developed as a data format for the XMM-Newton CCD camera. The names of the different fields within the file and frame headers stem from this. There exist different versions of the framesfile format which evolved from the original. They all adhere to a common layout described in the next section. The individual framesfile format layouts are presented at the end of this chapter.

Currently there are 3 format versions in use at the HLL, VERSION 5, VERSION 6 and the EXTENDED FORMAT (EXT in table C.1). The main difference between the formats are the maximum numbers of rows and columns supported.

Version	Min Col	Max Col	Min Row	Max Row
5	0	255	64	319
6	0	65535	0	65535
EXT	0	255	0	255

Table C.1: Overview of framesfile formats. For each format, the minimum and maximum number of columns and rows which can be stored is shown.

C.1 General layout

Figure C.1 shows a schematic of the general framesfile layout. A framesfile starts with the *file header* which is followed by the *frame records*. Each frame record consists of a *frame header* and the *frame data* itself. The headers contain fields giving additional information about the stored data, e.g. the size of the matrix, the current frame number, etc..

The layout shown in figure C.1 is common to all framesfile formats, but number and definition of the header fields can differ. Certain header fields are no longer in use in some framesfile formats. These are then marked as 'unused' in the tables below.

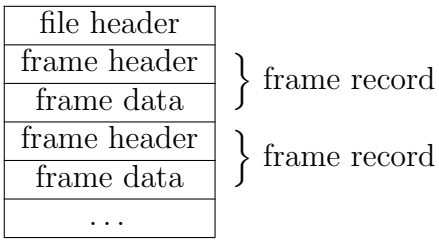

Figure C.1: General framesfile layout. This layout is common to all framesfile formats. The differences are in the way the header fields are used and defined.

C.2 Data types

In a framesfile, values are stored in a binary format. The size of the fields differ depending on the data type used. Table C.2 shows an overview of the data types and their size. The data type is also given in the tables of the sections below, which describe the layout of the file header and frame records of the individual framesfile formats.

Name	Size	Description
UChar	1 byte	unsigned integer value [0, 255]
UShort	2 byte	unsigned integer value [0, 65536]
UInt	4 byte	unsigned integer value [0, 4294967296]
Double	8 byte	double precision floating point value
String	variable	character string

Table C.2: Data types in the framesfile format. For the integer data types the respective range is shown as well. Strings are arrays of 8-bit ASCII characters. The length of strings in the framesfile format is either predefined by the format or can be deduced from field values in the file or frame headers.

C.3 Keywords

The current measurement setups use 14-bit ADCs for digitizing the pixel data and FPGAs to format the data stream. Each pixel value is stored as a 16 bit word, the remaining two bits are used for special keywords in the data stream (see table C.3). Except for the keywords for over- and underflows, values which have these two bits set normally should not show up in the frame data!

Another important issue when reading the framesfiles is *endianness* or *byte order*. The values given in table C.3 are shown in *little-endian notation*. When

Keyword	Meaning
0x4000	Underflow
0x8000	Underflow
0xBFFF	Overflow
0x7FFF	Overflow
0xFFFF	Frame start
0xFFFE	Line start

Table C.3: ADC keyword examples (in little-endian notation).

reading a framesfile the endianness has to be detected to process the different data types correctly. A mean for endianness detection are the first two fields in the file header which exist in all framesfile versions and always show the same values (that is 88 and 24). More information on endianness can be found in standard computer literature.

C.4 The 'version 5' format

File Header

The speciality in VERSION 5 format is the treatment of the row count N_{Row}. If N_{Row} is smaller than 64 a matrix with an actual row count of $N_{Row} + 256$ is assumed.

Byte	Description	Data type
1→2	Length of file header L_{FH} (=88)	UShort
3→4	Length of frame header L_{FrH} (=24)	UShort
5	XMM CCD number (unused)	UChar
6	Column count N_{Col}	UChar
7	Row count N_{Row}	UChar
8	Version number (=5)	UChar
9→88	File header comment	String

Table C.4: VERSION 5 format file header layout.

Frame Record

A frame record has a total length of $L_{FrH} = 24$ bytes for the header plus 2 bytes for each pixel in the frame. Thus the frame record length L_{FrR} is

$$L_{FrR} = (L_{FrH} + N_{Col} * N'_{Row} * 2) \text{ bytes}$$
$$= (24 + N_{Col} * N'_{Row} * 2) \text{ bytes}$$

with

$$N'_{Row} = \begin{cases} N_{Row} & \text{if } N_{Row} \geq 64 \\ N_{Row} + 256 & \text{if } N_{Row} < 64 \end{cases}$$

Byte	Description	Data type
1	Number of incomplete rows (unused)	UChar
2	Information flag (unused)	UChar
3	XMM CCD number (unused)	UChar
4	Subframe (unused)	UChar
5→8	Time stamp, seconds	UInt
9→12	Time stamp, microseconds	UInt
13→16	Frame counter	UInt
17→24	Temperature	Double
25→ L_{FrR}	Frame data array	UShort

Table C.5: VERSION 5 format frame header layout.

C.5 The 'version 6' format

File Header

Byte	Description	Data type
1→2	Length of file header (=88) (unused)	UShort
3→4	Length of frame header (=24) (unused)	UShort
5	XMM CCD number (unused)	UChar
6	not used	UChar
7	not used	UChar
8	Version number (=6)	UChar
9→88	File header comment	String
89→90	Column count N_{Col}	UShort
91→92	Row count N_{Row}	UShort
93→1024	VERSION 6 format header comment	String

Table C.6: VERSION 6 format file header layout.

In VERSION 6 format, the values for column and row count are stored after the comment field. The fields for column and row count used in VERSION 5 format are ignored. The total file header length is set to 1024 bytes.

NB: The file header length of a VERSION 6 format framesfile is 1024, although the length field in the file header is set to 88. Also the length of the frame header is (despite the value given in the file header) 64 and not 24!

Frame Record

A frame record in VERSION 6 format has a total length of $L_{FrH} = 64$ bytes for the header plus 2 bytes for each pixel in the frame. Thus the frame record length L_{FrR} is

$$\begin{aligned} L_{FrR} &= (L_{FrH} + N_{Col} * N_{Row} * 2) \text{ bytes} \\ &= (64 + N_{Col} * N_{Row} * 2) \text{ bytes} \end{aligned}$$

Byte	Description	Data type
1	Number of incomplete rows (unused)	UShort
2	Information flag (unused)	UShort
3	XMM CCD number (unused)	UShort
4	Subframe (unused)	UShort
5→8	Time stamp, seconds	UInt
9→12	Time stamp, microseconds	UInt
13→16	Frame counter	UShort
17→24	Temperature	Double
25→26	Number of incomplete rows	UShort
27→28	Subframe	UShort
29→64	Frame header comment	String
65→ L_{FrR}	Frame data array	UShort

Table C.7: VERSION 6 format frame record layout.

C.6 The 'extended' format

The EXTENDED format has a file header which is of the same size as a frame record ($L_{FH} = L_{FrR}$). This is achieved by appending a comment field of variable

length to the original comment field, the EXTENDED format comment.

File Header

Byte	Description	Data type
1→2	Length of file header (=88) (unused)	UShort
3→4	Length of frame header L_{FrH} (=24)	UShort
5	XMM CCD number (unused)	UChar
6	Column count N_{Col}	UChar
7	Row count N_{Row}	UChar
8	Version number (=64 for extended)	UChar
9→88	File header comment	String
89→ L_{FrR}	EXTENDED format comment	String

Table C.8: EXTENDED format file header layout.

The EXTENDED format comment has a length L_{ExC} such that the total file header length is the same as the length of a frame record L_{FrR}.

$$L_{ExC} = (L_{FrH} + N_{Col} * N_{Row} * 2 - 88) \text{ bytes}$$

NB: The real length of the file header L_{FH} is not 88 but equal to L_{FrR}!. The length of file header and frame header, L_{FH} and L_{FrH}, are always 88 and 24 bytes respectively. These numbers can be used to detect the endianness of the file.

Frame Record

A frame record has a total length of $L_{FrH} = 24$ bytes for the header plus 2 bytes for each pixel in the frame. Thus the frame record length L_{FrR} is

$$\begin{aligned} L_{FrR} &= (L_{FrH} + N_{Col} * N_{Row} * 2) \text{ bytes} \\ &= (24 + N_{Col} * N_{Row} * 2) \text{ bytes} \end{aligned}$$

NB: The condition that the file header has to have the same length as a frame record puts a lower limit to the pixel count of the device. The minimal length of the file header L_{FH} is 88 (in this case the EXTENDED comment has length 0).

Byte	Description	Data type
1	Number of incomplete rows (unused)	UShort
2	Information flag (unused)	UShort
3	XMM CCD number (unused)	UShort
4	Subframe (unused)	UShort
5→8	Time stamp, seconds	UInt
9→12	Time stamp, microseconds	UInt
13→16	Frame counter	UShort
17→24	Temperature	Double
25→ L_{FrR}	Frame data array	UShort

Table C.9: EXTENDED format frame record layout.

From this the minimal pixel count $N_{Pix} = N_{Col} * N_{Row}$ can be derived:

$$\begin{aligned} L_{FrR} &= L_{FH} = 88 \text{ bytes} \\ L_{FrR} &= L_{FrH} + N_{Col} * N_{Row} * 2 \text{ bytes} \\ L_{FrR} &= 24 \text{ bytes} + N_{Pix} * 2 \text{ bytes} \\ \Rightarrow N_{Pix} &= (88 - 24)/2 = 32 \end{aligned}$$

Matrices with a pixel count less than 32 cannot be saved in the EXTENDED format.

D. Orientation of DePFET chips on hybrid ceramics

For DePFET readout steering ASICs and readout ASICs are used. The steering ICs – the Switchers – activate one row of a matrix, the readout IC – usually an ASTEROID chip – reads out the pixels of the active row and serializes the data.

The active row moves continuously over the matrix. After the last row it jumps back to the first row and restarts. This way of readout is called *rolling shutter*. The data of a complete readout of a matrix are called *frame*.

During readout, the two-dimensional image of the detector is converted into a one-dimensional data stream. The position of a pixel signal in the data stream depends on the run direction of the active row and the multiplexer. Figure D.1 illustrates this: The pixel marked green has the address 6 or 16, depending on the configuration.

Data analysis evaluates the individual frames and stores results like offset, noise and gain as two-dimensional histograms. It is important to reconstruct pixel positions correctly, not only to obtain a correct image, but also to relate

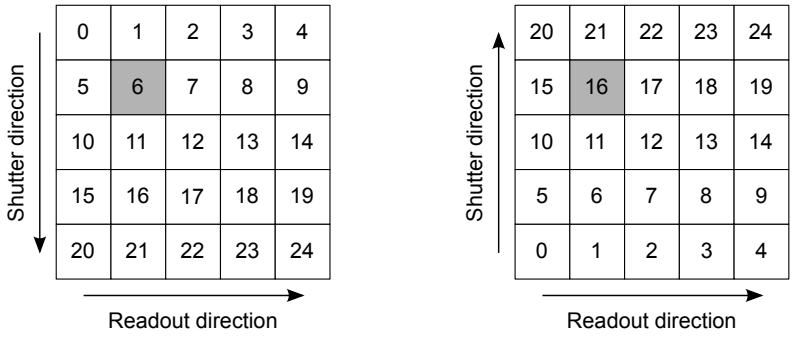

Figure D.1: Matrix in two different readout modes. In (a) and (b) the switcher chips are programmed with opposite run directions. The numbers show the index of the respective pixel in the one-dimensional data stream. Depending on the configuration the same two-dimensional position of a pixel in the matrix (marked grey) has a different index in the one-dimensional data stream.

regional effects in the detector image to the correct position on the detector matrix.

For this it is important to store the run directions of switcher and readout ICs. As a side effect, possible influences of the run directions on detector data can be studied later.

D.1 Matrix readout

The Switcher ICs support two run directions, UP and DOWN, named after the order of activation of their output pads:

- UP: Activation in raising order, e.g. from 0 to 63,
- DOWN: in falling order, e.g. from 63 to 0.

Figure D.2 shows the pad numbering of switcher and readout chips schematically. Note that the switcher chips are numbered in raising order from right to left when viewed from the opposite edge, the readout chips from left to right!

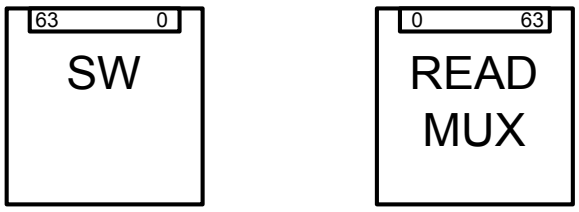

(a) switcher chip **(b)** readout chip

Figure D.2: Schematic of pad numbering at switcher and readout ASICs. The switcher chips have a pad numbering which runs in the opposite direction than the one of the readout ASIC.

The readout chips cannot change their readout direction. The sample and hold cells are addressed by the multiplexer in raising order from 0 to 63. Visualized this means the pads are addressed from left to right when viewed from the edge opposite to the pads.

However, the run direction in respect of the matrix can change with the positioning of the readout chip. If the readout chip is at the bottom edge of the matrix the pixel columns are addressed from left to right, if it is positioned at the top edge the pixel columns are addressed from right to left.

D.2 Offline data analysis

The DePFET data analysis uses the convention that a pixel identified by its index i in the data stream has an address $[c, r]$ in the pixel matrix where the numbering of columns and rows goes from left to right, respectively from bottom to top. The column index c and row index r is calculated from the index i by

$$\begin{aligned} c &= i \mod C \\ r &= \left\lfloor \frac{i}{R} \right\rfloor \end{aligned} \tag{D.1}$$

where C and R are the column and row count respectively. In this system the pixel with index 0 is located in the lower left corner as shown in figure D.3.

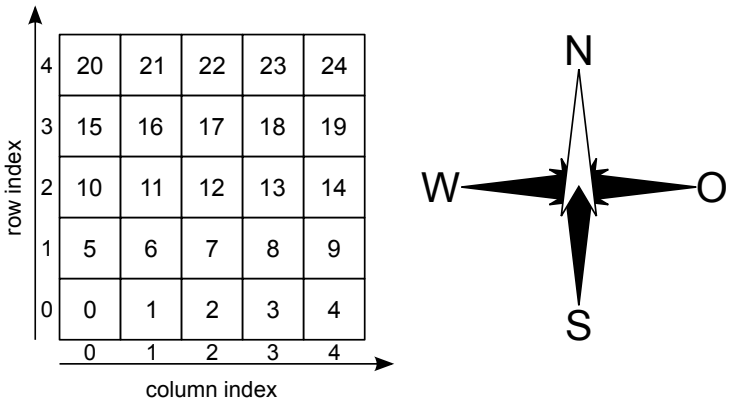

Figure D.3: The coordinate system in ROAn.

The real orientation of the detector in the experiment environment can be arbitrary and is not of special interest. More important is to have an anchor point relative to which the detector orientation is known.

For directions in respect of the matrix – e.g. run directions of switcher and readout chips, naming of patterns, ...– the offline analysis uses the cardinal points NORTH, SOUTH, EAST and WEST.

To help with the orientation of the different matrices, here are some rules of thumb:

- The direction of view is through the detector onto the source. The detector is illuminated on its back side.

- The readout chips are usually positioned on the north-south line.

- The gate-switcher is located in the east.[1]
- On hybrids with a single readout chip, this is located in the south

As the data has to be converted from raw format to frames file format in any case, it was convenient to sort the pixels as well during this step. This way the analysis has to deal only with one configuration.

D.3 Switcher configuration files

The switcher configurations for a certain matrix readout are stored in a text file, usually named after the run direction of the gate switcher. The two directions, UP and DOWN, signalize the addressing order of the output pads (UP from 0 to 63, DOWN from 63 to 0). One has to take heed that, if the clear switcher is on the opposite side of the matrix, it has to be programmed with the opposite run direction as the gate switcher to have the rolling shutter move over the matrix.

D.4 Detector hybrid ceramics

The next sections show an overview of the available detector hybrid ceramics at the HLL. The positions of the steering and readout chips with respect to the matrix are shown along with their orientation in the common coordinate system. Also a table matching the switcher run directions with the shutter run direction and the respective configuration file is supplied.

D.4.1 XEUS hybrid

The 64×64 matrices are read out by a single ASIC and use two steering chips. The readout chip is in the south, the gate switcher in the east, the clear switcher in the west (see figure D.4).

configuration file	gate	clear	shutter	readout
run_direct_down	DOWN	UP	NORTH	EAST
run_direct_up	UP	DOWN	SOUTH	EAST

Table D.1: Run directions for the XEUS hybrid.

[1] If the switchers are on opposite sides, this puts the clear switcher in the west

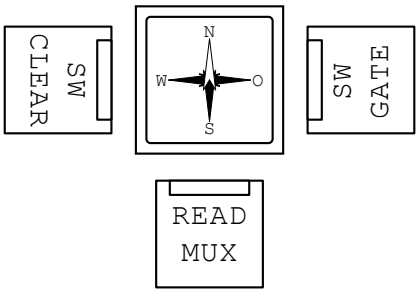

Figure D.4: XEUS matrix hybrid.

D.4.2 Simbol-X quadrant hybrid

Like the XEUS matrices also the Simbol-X quadrants have 64×64 pixels and a single readout ASIC. The switcher chips are here located both on the east side of the matrix.

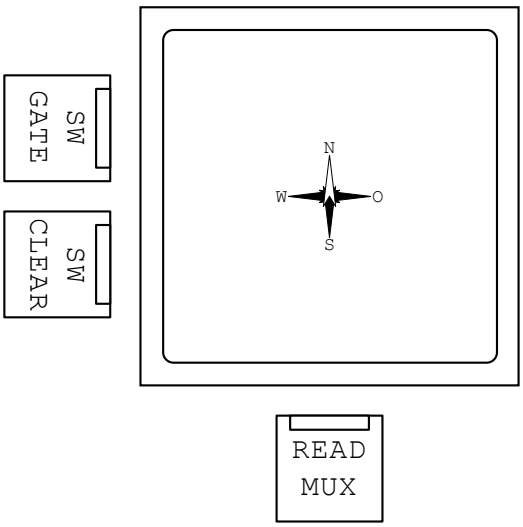

Figure D.5: Simbol-X quadrant hybrid.

configuration file	gate	clear	shutter	readout
run_direct_down	DOWN	DOWN	SOUTH	EAST
run_direct_up	UP	UP	NORTH	EAST

Table D.2: Run directions for the Simbol-X quadrant hybrid.

D.4.3 BepiColombo hybrid

The matrices designated for the BepiColombo mission are 64×64 pixels and separated in two hemispheres, NORTH and SOUTH. Each has its own set of one readout and two switcher chips.

The switchers for each hemisphere have 64 channels but only 32 of them are actually bonded to the matrix. During readout it is important that in each hemisphere there is one active row. Therefore, the switchers must not access their unconnected pads. This results in only one possible readout mode.

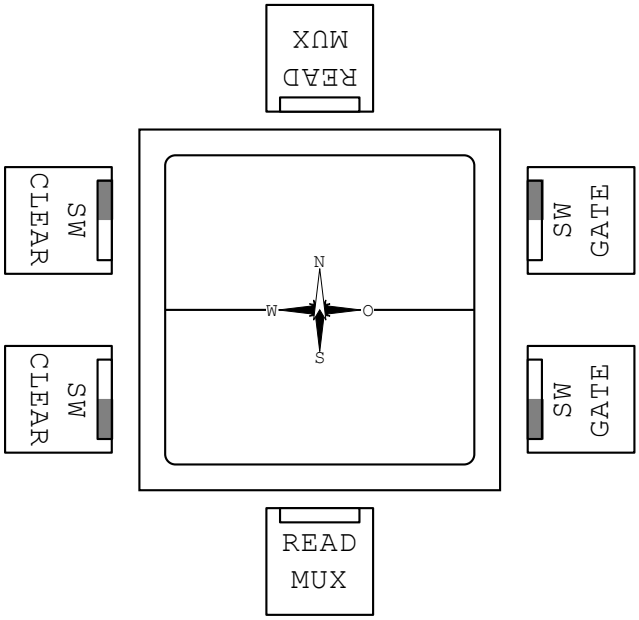

Figure D.6: BepiColombo matrix hybrid. The switcher chips only use the pads from the inner area (marked light), i.e. the switcher is reset after having traversed half of its pads. The unused pads must not be addressed as this creates undefined states in the matrix. Therefore, only one readout mode is possible.

hemisphere	gate	clear	shutter	readout
north	DOWN	UP	NORTH	WEST
south	UP	DOWN	SOUTH	EAST

Table D.3: Run directions for the BepiColombo matrix hemispheres.

E. Proof for the formula for noise clear correlation clusters

The noise of a DePFET detector is assumed to be a Gaussian curve with mean $\mu = 0$ and standard deviation σ. The probability for a noise event with the energy E is given by the probability density function

$$P(E) = \frac{1}{\sigma\sqrt{2\pi}} e^{-\frac{1}{2}\left(\frac{E}{\sigma}\right)^2} \tag{E.1}$$

The probability for a noise event above an energy E_T and below an energy E_1 is given by the integral over the probability density function

$$P(E_1 \geq E_0 \geq E_T) = \int_{E_T}^{E_1} P(E_0)\, dE_0 = \Phi\left(\frac{E_1}{\sigma}\right) - \Phi\left(\frac{E_T}{\sigma}\right) = \Phi_1 - \Phi_T \tag{E.2}$$

where Φ is the cumulative distribution function

$$\Phi = \frac{1}{\sqrt{2\pi}} \int_{-\infty}^{x} e^{-\frac{1}{2}t^2}\, dt \tag{E.3}$$

and

$$\Phi_l^i = \Phi^i\left(\frac{E_l}{\sigma}\right) = \left[\Phi\left(\frac{E_l}{\sigma}\right)\right]^i \tag{E.4}$$

is used as an abbreviation for powers of Φ at energy E_l.

The probability of a noise clear correlation cluster of length n and a maximum energy E_n is given by the probability of having a noise event with energy E_{n-1} followed by a noise clear correlation cluster of length $n-1$ and the maximum energy E_{n-1}. This then has to be integrated over all possible values $[E_T; E_n]$.

$$P(E_n \geq \cdots \geq E_0 \geq E_T) = \int_{E_T}^{E_n} P(E_{n-1}) \cdot P(E_{n-1} \geq \ldots \geq E_0 \geq E_T)\, dE_{n-1} \tag{E.5}$$

The probability for cluster with length $n-1$ is calculated in the same way, which leads to a recursive pattern. The result of the integration can be summed up in

the formula

$$P(E_n \geq \cdots \geq E_0 \geq E_T) = \frac{1}{n!} \left[\Phi_n - \Phi_T\right]^n \tag{E.6}$$

E_n is the upper limit for the first signal in the cluster. For a pure noise clear correlation cluster the value of E_n is infinity and thus $\Phi(E_n/\sigma) = 1$. The same can be assumed for noise clusters which follow normal signals because the signal height is much higher than the threshold. Therefore

$$P(CCLen = n) = P(\infty \geq \cdots \geq E_0 \geq E_T) = \frac{1}{n!} \left[1 - \Phi_T\right]^n \tag{E.7}$$

Proof by mathematical induction

Auxiliary calculation

$P(E)$ is the derivative of $\Phi(E/\sigma)$:

$$\Phi'\left(\frac{E}{\sigma}\right) = \frac{d}{dE}\Phi\left(\frac{E}{\sigma}\right) = P(E) \tag{E.8}$$

With the formula for partial integration

$$\int_a^b u \cdot v' \, dx = \left[u\, v\right]_a^b - \int_a^b u' \cdot v \, dx \tag{E.9}$$

and using $u = g^n$ and $v' = g'$ (where g is an arbitrary function) we get

$$\int_a^b g^n \cdot g' \, dx = \left[g^n \, g\right]_a^b - \int_a^b n \cdot g^{n-1} \cdot g' \cdot g \, dx = \left[g^{n+1}\right]_a^b - n \cdot \int_a^b g^n \cdot g' \, dx \tag{E.10}$$

which can be resolved to

$$\int_a^b g^n \cdot g' \, dx = \frac{1}{n+1} \left[g^{n+1}\right]_a^b \text{ (valid for } n \geq 0) \tag{E.11}$$

Thus

$$\int_{E_A}^{E_B} P(E) \cdot \Phi^n \, dE = \frac{1}{n+1} \left[\Phi^{n+1}\right]_{E_A}^{E_B} = \frac{1}{n+1} \left(\Phi_B^{n+1} - \Phi_A^{n+1}\right) \tag{E.12}$$

The proof

n=1 For $n = 1$ we get equation (E.2). Equation (E.6) delivers the same result:

$$P(E_1 \geq E_0 \geq E_T) = \frac{1}{1!} \left[\Phi_1 - \Phi_T\right]^1 = \Phi_1 - \Phi_T \tag{E.13}$$

n=2 For $n = 2$ we get by direct calculation

$$\begin{aligned} P(E_2 \geq E_1 \geq E_0 \geq E_T) &= \int_{E_T}^{E_2} P(E_1) \cdot P(E_1 \geq E_0 \geq E_T)\, dE_1 \\ &= \int_{E_T}^{E_2} P(E_1) \cdot (\Phi_1 - \Phi_T)\ dE_1 \\ &= \int_{E_T}^{E_2} P(E_1) \cdot \Phi_1\, dE_1 - \Phi_T \cdot \int_{E_T}^{E_2} P(E_1)\, dE_1 \end{aligned} \tag{E.14}$$

which simplifies with help of equation (E.12) to

$$\begin{aligned} P(E_2 \geq E_1 \geq E_0 \geq E_T) &= \frac{1}{2}\left[\Phi^2\right]_{E_T}^{E_2} - \Phi_T \cdot (\Phi_2 - \Phi_T) \\ &= \frac{1}{2}\left(\Phi_2^2 - \Phi_T^2\right) - \Phi_T \cdot \Phi_2 - \Phi_T^2 \\ &= \frac{1}{2}\Phi_2^2 - \Phi_T \cdot \Phi_2 - \frac{1}{2}\Phi_T^2 \\ &= \frac{1}{2}\left(\Phi_2 - \Phi_T\right)^2 \end{aligned} \tag{E.15}$$

which is the same result as delivered by the formula.

Inductive step It will be now proven that if the formula is right for $n-1$ it also holds for n:

$$P(E_n \geq \cdots \geq E_0 \geq E_T) = \int_{E_T}^{E_n} P(E_{n-1}) \cdot P(E_{n-1} \geq \cdots \geq E_0 \geq E_T)\, dE_{n-1} \tag{E.16}$$

Inserting the formula for $n-1$

$$\begin{aligned} P(E_n \geq \cdots \geq E_0 \geq E_T) &= \int_{E_T}^{E_n} P(E_{n-1}) \cdot \frac{1}{(n-1)!}\left(\Phi_{n-1} - \Phi_T\right)^{n-1}\ dE_{n-1} \\ &= \frac{1}{(n-1)!}\int_{E_T}^{E_n} P(E_{n-1}) \cdot \left(\Phi_{n-1} - \Phi_T\right)^{n-1}\ dE_{n-1} \end{aligned} \tag{E.17}$$

and expanding with the binomial theorem

$$(a-b)^n = \sum_{k=0}^{n} \binom{n}{k} a^{n-k} \cdot (-1)^k b^k \tag{E.18}$$

leads to

$$\begin{aligned} P &= \frac{1}{(n-1)!}\int_{E_T}^{E_n} P(E_{n-1})\cdot\sum_{k=0}^{n-1}\binom{n-1}{k}\Phi_{n-1}^{n-1-k}\cdot(-1)^k\Phi_T^k\,dE_{n-1} \\ &= \frac{1}{(n-1)!}\sum_{k=0}^{n-1}\binom{n-1}{k}\int_{E_T}^{E_n} P(E_{n-1})\cdot\Phi_{n-1}^{n-1-k}\,dE_{n-1}\cdot(-1)^k\Phi_T^k \end{aligned} \tag{E.19}$$

The integral in equation (E.19) can be simplified by using equation (E.12) from the auxiliary calculations above. Therefore

$$\begin{aligned} P &= \frac{1}{(n-1)!}\sum_{k=0}^{n-1}\binom{n-1}{k}\frac{1}{(n-1-k)+1}\left[\Phi_{n-1}^{(n-1-k)+1}\right]_{E_T}^{E_n}\cdot(-1)^k\Phi_T^k \\ &= \frac{1}{(n-1)!}\sum_{k=0}^{n-1}\binom{n-1}{k}\frac{1}{n-k}\left[\Phi_{n-1}^{n-k}\right]_{E_T}^{E_n}\cdot(-1)^k\Phi_T^k \end{aligned} \tag{E.20}$$

The binomial coefficient can be drawn together with the fraction

$$\binom{n-1}{k}\frac{1}{n-k} = \frac{(n-1)!}{k!\cdot(n-1-k)!)\cdot(n-k)} = \frac{(n-1)!\cdot n}{k!(n-k)!\cdot n} = \binom{n}{k}\frac{1}{n} \tag{E.21}$$

simplifying the probability equation further

$$\begin{aligned} P &= \frac{1}{(n-1)!}\sum_{k=0}^{n-1}\binom{n}{k}\frac{1}{n}\left(\Phi_n^{n-k}-\Phi_T^{n-k}\right)\cdot(-1)^k\Phi_T^k \\ &= \frac{1}{n!}\sum_{k=0}^{n-1}\binom{n}{k}\left(\Phi_n^{n-k}\cdot(-1)^k\Phi_T^k-(-1)^k\Phi_T^n\right) \end{aligned} \tag{E.22}$$

By adding the identity

$$0 = \binom{n}{n}\left(\Phi_n^0\cdot(-1)^n\Phi_T^n-(-1)^n\Phi_T^n\right) \tag{E.23}$$

to the sum, the upper limit can be extended to n:

$$\begin{aligned} P &= \frac{1}{n!}\sum_{k=0}^{n}\binom{n}{k}\left(\Phi_n^{n-k}\cdot(-1)^k\Phi_T^k-(-1)^k\Phi_T^n\right) \\ &= \frac{1}{n!}\left\{\sum_{k=0}^{n}\binom{n}{k}\Phi_n^{n-k}\cdot(-1)^k\Phi_T^k-\sum_{k=0}^{n}\binom{n}{k}(-1)^k\Phi_T^n\right\} \end{aligned} \tag{E.24}$$

The right sum evaluates to 0 because of the identity

$$\sum_{k=0}^{n} \binom{n}{k} (-1)^k = 0 \tag{E.25}$$

leaving the other sum which is a binomial formula

$$P = \frac{1}{n!} \left\{ \sum_{k=0}^{n} \binom{n}{k} \Phi_n^{n-k} \cdot (-1)^k \Phi_T^k \right\} = \frac{1}{n!} \left(\Phi_n - \Phi_T \right)^n \tag{E.26}$$

The final result is the formula given in equation (E.6).

□

F. Acknowledgements

I would like to express my thanks to the following people:

- Prof. Dr. Günther Hasinger, for accepting me as his doctoral candidate despite his change to the IPP.
- Prof. Dr. Lothar Strüder, for all his efforts to make my work at the HLL possible.
- Dr. Johannes Treis, for being my supervisor and for the Hitchhiker's Guide to the Thesis.
- Dr. Petra Majewski, for relentless proofreading, useful tips and remarks.
- Alexander Stefanescu, as well for relentless proofreading, but also for xtraordinary kool coding designs.
- Dr. Robert Andritschke, for his valuable contributions to ROAn, UNIX support, and for sharing his insights into the world of data analysis and the spectrum of science.
- Dr. Peter Lechner, for proofreading and useful images.
- My fellow grad students, for good office atmosphere, tips and tricks.
- The staff at the HLL, for their excellent work in producing the detectors.
- The PTB staff at BESSY, for their support during the measurements.
- Alex, Chris, Christoph, Tommy & Eric – Thank you for the music!
- John Krauth, for lifting my mood.
- Dr. Silvana Siebert, for her dedicated support, her (different) opinion, and proofreading.
- Last but not least: My parents, Helga and Dr. Werner Lauf, for their tremendous support over all these years.